# THESE

Pour l'obtention du Grade de
DOCTEUR DE L'ECOLE NATIONALE SUPERIEURE DE MECANIQUE ET D'AEROTECHNIQUE
(Diplôme National – Arrêté du 25 mai 2016)

Ecole Doctorale :
Sciences et Ingénierie en Matériaux, Mécanique, Energétique

Secteur de Recherche : Energétique, Thermique et Combustion

Présentée par : Maksym SLOBODENIUK

**********

ANALYTICAL AND EXPERIMENTAL STUDY OF HEAT AND MASS TRANSFER IN PULSATING HEAT PIPES FOR NON-GRAVITY FLIGHT APPLICATIONS

**********

Directeur de thèse : Yves BERTIN
Co-encadrant : Vincent AYEL, Rémi BERTOSSI

**********

Soutenue le 20 Janvier 2022

devant la Commission d'Examen

**********

## JURY

Président et rapporteur:
COLIN Catherine, Professeur, INP/IMFT
Rapporteur :
MARENGO Marco, Professeur, Université de Brighton
Membres du jury :
CANEY Nadia, Ingénieure de recherche, CEA/LITEN
BERTIN Yves, Professeur, Institute Pprime, ISAE-ENSMA
BERTOSSI Rémi, Maitre de conférences, IPSA
AYEL Vincent, Maitre de conférences, Institute Pprime, ISAE-ENSMA

*To my parents.*

*For their endless love, support and encouragement.*

# Acknowledgements

This scientific and personal journey, called PhD thesis, was impossible without help and influence of people surrounding me. First of all, I would like to express my gratitude to all people who helped me during the development of my thesis, in particular my thesis supervisors Vincent Ayel, Remi Bertossi and Yves Bertin for this great chance to contribute in science advancement and for weightless experience during parabolic flights. I am grateful to Vincent for trusting me completely, for encouraging me and for supporting all my ideas; Remi for his interest, his great availability and motivation; Yves for his warm welcome in the lab, his humanity and advises.

I would also like to thank reviewers of my thesis and jury members, Prof. Colin, Prof. Marengo and Dr. Caney who took the time to read this manuscript and provide very important comments and ideas for future research.

I would like to thank all people in the lab, in particular a lot of thanks to Catherine L. without whom everything would stop in all lab and to Cyril for his great technical skills and scientific advices. Many thanks to people from the technical team, without whom it was impossible to build the prototypes. Thanks to Christophe, Catherine F., Nicolas P., Jean-Christophe, Yann…

My former students, Flavien, Karthik, Antoine and Raji, also deserve my gratitude for all work realized during their internships. Without their contribution, it would be impossible to obtain all the results of proper quality.

I would like to thank my colleagues and friends from the lab for good moments and hours of discussions about life, culture and research. Special thanks to my friend Flavio for his support and best Italian food in my life.

I would like also to thank my friends from Marseille for first introduction in French society. Many thanks to Carlito for friendship and breaking my language barriers, to Alex for his humor, to Eddy for his kindness, support and help.

Спасибо моим местным друзьям и близким с которыми мы говорили на родном языке. Спасибо за задушевные разговоры и частицу чего-то родного и очень недостающего. Спасибо за поддержку, особенно в последние месяцы.

Также я хочу поблагодарить моих одесских друзей за нашу дружбу, их поддержку, отзывчивость и готовность подменить меня дома в трудные минуты. Спасибо за мощную мотивацию, пусть даже не намеренную. Спасибо Борису К. за нестрандартный педагогический подход и умение направить.

Конечно, я хочу выразить признательность моей семье. В первую очередь спасибо моим родителям за проявленное терпение и упорство во время моих «трудных периодов», спасибо за их поддержку за все эти годы. Спасибо бабушкам и дедушкам, которые всегда желали мне лучшего и мечтали об ученом внуке. Пусть даже они не поймут и строчки в этой работе, этот путь был пройден благодаря им и для них.

# Contents

# List of Figures

# List of Tables

# Nomenclature

## Abbreviations

| | |
|---|---|
| BHM | Bottom heated mode |
| CLPHP | Closed loop pulsating heat pipe |
| CPL | Capillary pumped loop |
| ESA | European Space Agency |
| FPHP | Flat pulsating heat pipe |
| FPPHP | Flat plate pulsating heat pipe |
| FR | Filling ratio |
| HP | Heat pipe |
| ISS | International Space Station |
| LHP | Loop heat pipe |
| NCG | Non-condensable gas |
| OLPHP | Open loop pulsating heat pipe |
| PFC | Parabolic Flight Campaign |
| PHP | Pulsating heat pipe |
| TMS | Thermal management system |
| TS | Thermosiphon |

# Symbols

| | |
|---|---|
| $A$ | Area [$m^2$] |
| $Bo$ | Bond number |
| $Ca$ | Capillary number |
| $c_p$ | Specific heat capacity [$J.kg^{-1}.K^{-1}$] |
| $d$ | Diameter [m] |
| $dh$ | Liquid column difference [m] |
| $F$ | Force [N] |
| $Fr$ | Froude number |
| $g$ | Gravity acceleration [$m.s^{-2}$] |
| $Ga$ | Garimella number |
| $h_{lv}$ | Latent heat of vaporization [$J.kg^{-1}$] |
| $L$ | Length [m] |
| $m$ | Mass [kg] |
| $N$ | Number |
| $P$ | Pressure [Pa] |
| $Q$ | Heat load [W] |
| $q$ | Heat flux [$W.m^{-2}$] |
| $R$ | Radius [m] |
| $Re$ | Reynolds number |
| $Rth$ | Thermal resistance [$K.W^{-1}$] |
| $S$ | Area [$m^2$] |
| $T$ | Temperature [$^oC$; K] |
| $t$ | Time [s] |
| $u, U$ | Velocity [$m.s^{-1}$] |

| | |
|---|---|
| $V$ | Volume [$m^3$] |
| $We$ | Weber number |
| $x$ | Position [m] |
| $Z$ | Compressibility factor |

## Greek symbols

| | |
|---|---|
| $\rho$ | Density [$kg.m^{-3}$] |
| $\Delta$ | Difference |
| $\lambda$ | Thermal conductivity [$W.m^{-1}.K^{-1}$] |
| $\mu$ | Dynamic viscosity [Pa.s] |
| $\sigma$ | Surface tension [$N.m^{-1}$] |
| $\tau$ | Wall shear stress [Pa] |

## Subscripts

| | |
|---|---|
| *ad* | Adiabatic |
| *cond* | Condenser |
| *cool* | Cooling |
| *driv* | Driving |
| *eff* | Effective |
| *ev* | Evaporator |
| *l* | Liquid |
| *sat* | Saturation |
| *v* | Vapor |
| *vis* | Viscosity |

# PART I

## MOTIVATIONS AND TECHNOLOGY OVERVIEW

# Chapter 1

## Introduction

Integration of high power and high performance electronic devices in modern spacecraft system with heat generation of hundreds of watts per square centimeter crucially increases needs in high performance, low weight, energy efficient and reliable thermal management systems. Due to these specific demands, two-phase heat rejection devices are preferable for space applications. However, pumped cooling devices, despite their capability to remove high heat fluxes, require supplemental equipment, as well pumping subsystem (usually consisting in moving parts), extension reservoir etc., which lead to additional energy consumption, increase in weight and size and, as a consequence, reliability loose. Heat pipes, as one of the most widely used passive two-phase thermal dissipation technology both for terrestrial and aerospace applications, cannot manage with extra high heat fluxes and long distance heat transportation despite their reliability and well developing [1.1]. Capillary Pumped Loops (CPLs) and Loop Heat Pipes (LHPs) are devoid of these disadvantages (heat removal capability could be at least two orders magnitude higher than for conventional heat pipes), but CPLs need exhaust and time-consuming starting process [1.2]. Despite the existence of high efficient passive cooling solutions, engineering society is still in search of simple, low cost, high performance and reliable heat transfer technologies.

During last few decades, research and engineering studies on a new passive two-phase heat transfer device with simple structure, called Pulsating Heat Pipe (PHP) or Oscillating Heat Pipe (OHP), have experienced a great development. Simple structure of the PHP is represented by a single curved capillary tube or channel (to ensure domination of surface tension forces on gravitational ones), which is folded back to make itself parallel and partially filled with liquid to reach saturation conditions [1.3]. Liquid distributes inside the channels in chaotic form, forming alternating chains of liquid plugs and vapor slugs. Evaporator and condenser are usually placed on the opposite sides of PHP (adiabatic zone between them) which leads to differences in saturation conditions between two zones and

pressure driving displacement of the liquid-vapor pairs along the channels as a result. Consequently, heat transfer process, related to PHP operation, consists of both latent and sensible heat forms, which allow increasing thermal performance. Simple design without any porous structures, moving parts and sub-systems coupled with high heat transfer performance makes PHP a very promising technology for future exploitation onboard space apparatuses.

However, considering available works in literature, complex mechanisms of thermo-hydrodynamic processes inside PHP is not fully studied and any precise suitable design recommendations are still not available, together with the contradictory believes of researchers [1.4; 1.5]. Therefore, this technology needs further investigations related to the understanding improvement of the phenomena inside the PHP.

This thesis has been realized in the context of two successive research projects funded by European Space Agency – INWIP and TOPDESS - which are dedicated to the development of the high efficient and passive thermal management technologies for the space applications.

The first project - **In**novative **Wi**ckless Heat **P**ipe Systems for Ground and Space Applications (INWIP) – aims at designing, manufacturing and testing innovative wickless heat pipes with enhanced performances and reliability for both space and ground applications.

Based on the research consortium experience and fields of interests, research work is focused on the numerical and experimental investigations of three two-phase heat transfer devices: wickless hybrid thermosiphons, grooved heat pipes and pulsating heat pipes. Parametric studies of these systems include the performance evaluations of the several working fluids, functionalized surfaces (hydrophobic and hydrophilic), gravity influence (different orientations during on-ground tests and reduced gravity during parabolic flights). This project is a first preparatory step for the further systematic experimentation on the Thermal Platform1 TP1 onboard the International Space Station, investigating particular grooved and pulsating heat pipes filled with ordinary and self- rewetting fluids.

The second project – **T**w**o**-**P**hase Passive Thermal **De**vices for Deployable **S**pace **S**ystems (TOPDESS), continues developing the research work started through the previous ESA MAP INWIP project, but this time with the ambitious purpose of dealing with

deployable and/or flexible two-phase wickless devices for developing the applicative aspects. Nevertheless, the deployability or flexibility of such systems will not be studied in this thesis. We will mainly focuses on heat and mass transfer inside flat-pate pulsating heat pipes. In particular, tests of the improved version of the Flat Plate PHP, developed during the INWIP project, should be done in order to meet the following objectives:

- The high-speed grayscale and infrared visualizations of the entire channel array for an accurate detection of the liquid-vapor interfaces and measurements the liquid bulk temperature (to determine the local heat transfer coefficient);
- A parametric study concerning the wettability of the fluid/metal couple, by using different surface coatings (oxidation, etc.) and/or fluid thermophysical properties by adding specific substances such as alcohols (self-rewetting fluids) or surfactants.

Therefore, the main purposes of this thesis are to characterize the heat transfer performance of the flat plate pulsating heat pipe operating under normal and reduced gravity, understanding the two-phase flow behavior inside the FPPHP and increasing the heat transfer characteristics using working fluids with different transport properties.

**References**

[1.1] Hengeveld D., Mathison M., Braun J., Groll E., Williams A., 2010. Review of Modern Spacecraft Thermal Control Technologies, HVAC&R Res. 16.

[1.2] Bugby D., Wrenn K., Wolf D., Kroliczek E., Yun J., Krein S. and Mark D., 2005. Multi-evaporator hybrid loop heat pipe for small spacecraft thermal management. Proc. IEEE Aerospace Conf.

[1.3] Akachi H., Polašek F., Štulc P., 1996. Pulsating heat pipes. Proc. 5th Int. Heat Pipe Symp.

[1.4] Tang X., Sha L., Zhang H. and Ju Y., 2013. A review of recent experimental investigations and theoretical analyses for pulsating heat pipes. Front. Energy. 7, 161-173.

[1.5] Bastakoti D., Zhang H., Li D., Cai W., Li F. and 2018. An overview on the developing trend of pulsating heat pipe and its performance, Appl. Therm. Eng. 141, 305-332.

# Chapter 2

## Two-Phase Cooling Systems for Ground and Space Applications

To better introduce the pulsating heat pipe and describe motivation of this work, a short overview of the existing thermal management devices is presented in this chapter. As shown in Fig. 2.1, recent cooling solutions can be classified in the four main categories as a function of the amount of rejected heat flux and surface superheat [2.1]:

- Natural convection;
- Gas forced convection;
- Liquid forced convection;
- Two-phase cooling.

It seems that two-phase cooling devices have several advantages compared to the standard single-phase cooling systems:

- First, a fluid's latent heat of vaporization can be a few orders of magnitude larger than the specific sensible heat;
- Second, the maximal rejected heat flux in regards to the surface superheat is a one order of magnitude higher for two-phase systems compared to the liquid forced convection and at least three orders of magnitude higher than gas forced convection;
- Finally, recent electronic devices require thermal management systems (TMS) capable to reject heat fluxes densities higher than 100 $W/cm^2$.

Thus, this part will focus on two-phase cooling solutions and a main attention will be paid to the high performances they represent.

Any cooling solution of a space electronic equipment is based on the design features that determine compactness, low power consumption and weight, as well as a decrease in the cost of the product. Thus, the choice by the designer of the thermal management system type is guided by the applications they aim for. So, understanding not only the principles of functioning of various types of TMS, but also, more importantly, their functional limitations,

as well as the necessary and sufficient conditions that determine the stable operation of the TMS is of major interest.

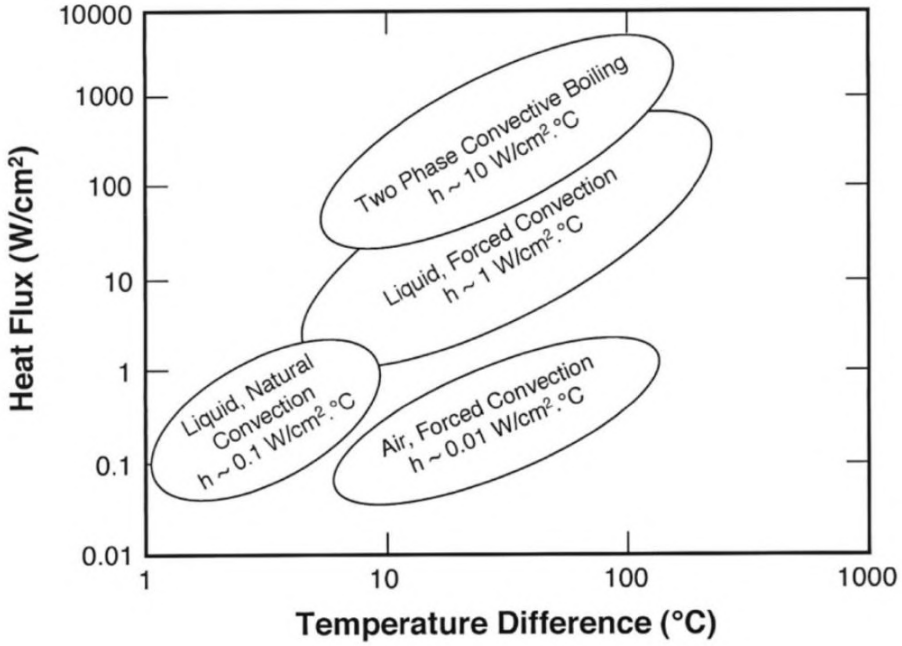


Figure 2.1. Comparison of the various thermal management approaches [2.1].

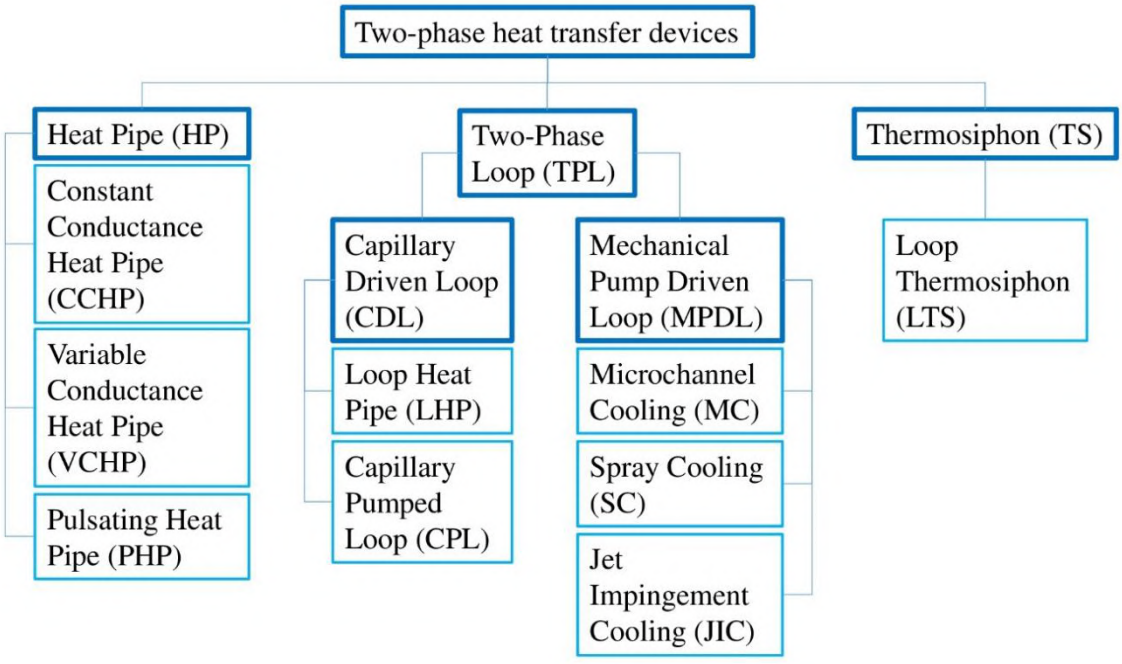


Figure 2.2. Classification of the two-phase heat transfer devices [2.2; 2.3].

There are numerous different approaches of the TMS classification mainly caused by the development of recent TMS solutions. For a general understanding of the types and

location of the two-phase heat transfer systems, it is proposed to consider the classification according to the principle of their functioning, shown in Fig. 2.2. Based on this classification, latter devices will be described in this chapter.

## 2.1. Mechanical Pump Driving Loops

### *2.1.1. Microchannel Heat Sink*

The microchannel heat sinks were initially proposed as single-phase systems by Tuckerman and Pease in 1981 for the high-performance microprocessors cooling [2.4]. The primary component of a microchannel cooler (i.e. Microchannel Heat Sink) is shown in Fig. 2.3. Electronic devices are typically attached to the bottom side of the microchannel heat sink under the ribs in the central part. Open top side is usually covered by a planar plate with the inlet and outlet ports. With appropriate driving pressure, the fluid is driven through the microchannels and heat is transferred from the electronic component through the microchannels into the fluid.

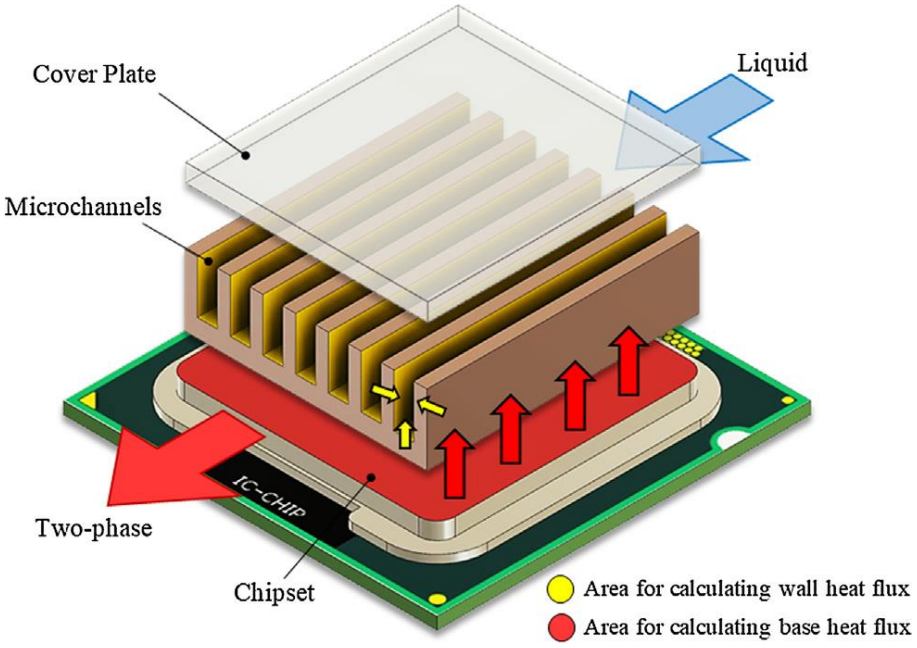


Figure 2.3. Typical microchannel heat sink with parallel channels [2.5].

During two last decades, two-phase microchannel systems have attracted much attention as a method for high-heat flux electronic cooling. It has been shown that flow through large surface area (related to the device volume) microchannels boosts the heat transfer coefficient in single-phase flow; additional gains in the heat transfer coefficient can

be obtained by allowing the liquid to vaporize along the walls of the microchannel [2.6]. These systems also possess the advantages like compactness and minimal coolant usage that make them attractive for electronics cooling applications.

### *2.1.2. Spray and Jet-Impingement Cooling Systems*

The mechanism of the Spray Cooling could be seen in Fig. 2.4. Here, fluid is introduced to a nozzle located opposite to the heated surface. With appropriate driving pressure (provided by a pump), the fluid leaving the nozzle breaks up into individual droplets that deposit on the hot surface. The fluid forms a film on the surface and heat is transferred both by sensible mode (at the moment of the droplets deposition) and latent mode (occurring during the film evaporation).

Along with the other potential benefits of two-phase cooling, spray cooling can provide a uniform heat flux and temperature across the heating surface. Usually, spray coolers also provide low flow rate requirements due to the precise fluid-delivery and heat removal mechanism. Despite all these advantages, spray cooling is considered excessively complex and unfeasible for many applications [2.7].

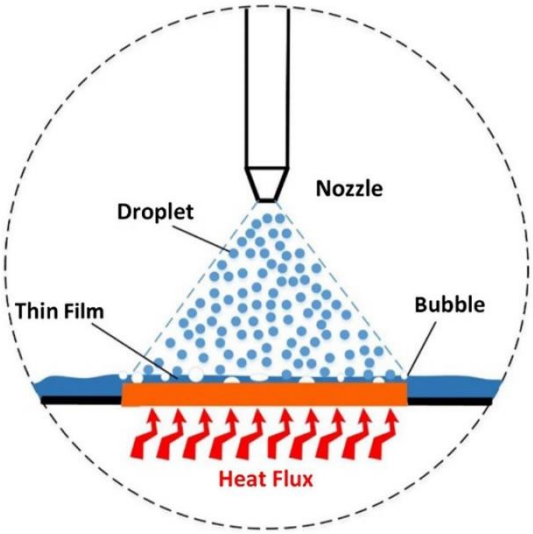


Figure 2.4. Schematic view of the spray cooling process [2.8].

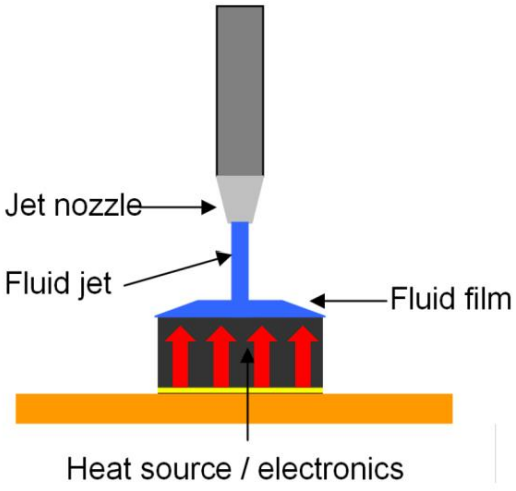


Figure 2.5. Schematic of the jet-impingement cooler [2.9].

Jet Impingement could be divided in the three following basic forms: free jet (liquid jet in a vapor or gaseous ambient), submerged jet (liquid jet in a liquid ambient), and confined jet (liquid jet confined between the nozzle and heat source).

A free jet-impingement cooling is usually used for two-phase applications. The primary components of this approach can be seen in Fig. 2.5. A continuous jet of the fluid is forced through a jet nozzle that impinges on the heated surface. With the applied heat, film evaporation occurs on the surface removing heat from the surface. Previous research works have shown that heat transfer coefficient is significantly higher near the jet flow than around it [2.10]. Thus, the concentration of the heat transfer coefficient and associated heat removal within the impingement zone could provoke significant temperature gradients within the device. This non-uniformity of temperature can cause thermal stress in electronics and their potential failure.

## 2.2. Passive Two-Phase Cooling Devices

### *2.2.1. The Thermosiphon*

Thermosiphon is a high performance passive two-phase gravity-assisted heat transfer device (Fig. 2.6), which was firstly proposed in 1838 by Perkin [2.11]. At the beginning of the XX$^{th}$ century, a thermosiphon, called the Perkin's tube, was used as a heater in baking ovens. After, during Second World War, high demand in such devices as cooling system for gas turbine blades, significantly increased. In USSR thermosiphons were widely used in Long's thermal piles during construction in permafrost regions. From 1980, thermosiphons have been used in different applications, as well solar heating, construction, metallurgy, power electronic cooling etc. due to their simple structure, low cost and high performance.

Usually, the thermosiphon is made of an evacuated sealed smooth or grooved tube, closed from both sides and partially filled with a working fluid at ~20% of filling ratio (an optimal value) [2.12]. Conventional thermosiphon is composed of evaporation, adiabatic and condensation sections (Fig. 2.6). As a gravity assisted device, the condenser should be located above the evaporator to allow the return of liquid condensate from condenser to evaporator.

The heat flux from the source, applied to the evaporator (located on the bottom side of the tube), provokes boiling in the fluid volume. Generated vapor moves to the condensation zone thanks to the density and pressure difference between the evaporation and condensation zones. Condensed vapor flows back to the evaporator in the form of liquid film on the wall of the thermosiphon thanks to gravity assistance.

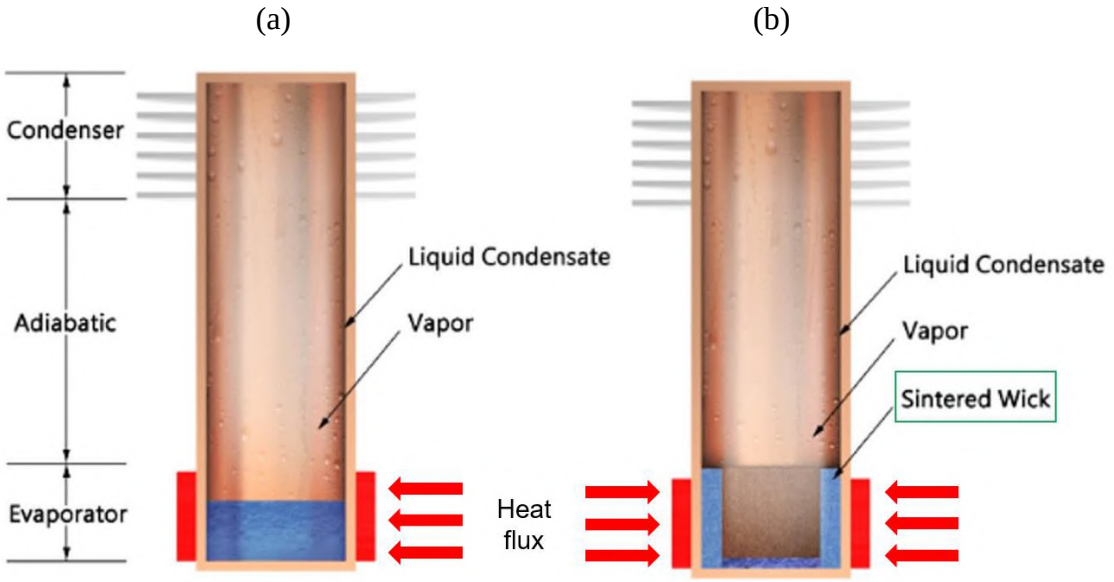


Figure 2.6. Thermosiphon schematic representation [2.13].

The thermosiphon is a one of the most effective passive two-phase heat transfer devices, but heat transfer rate strongly depends on the geometrical parameters, fluid properties and filling ratio but also on the orientation. Performances of the thermosiphon are significantly affected by the inclination angle – operation failure could be reached in the horizontal position or in position with the evaporator located above the condenser.

Sometimes, high applied heat fluxes lead to reach the boiling crisis and dry-spots generation on the evaporator wall resulting in heat transfer performances degradation. To prevent this phenomenon, sintered wick deposition on the evaporator walls could be used to homogenize the fluid distribution (Fig. 2.6b) [2.13].

Another way to improve performances of such two-phase heat transfer devices consists in the use of the gravity assisted natural circulation two-phase loop, also called Closed Loop Thermosiphon – a particular version of the thermosiphon, described above. As for conventional thermosiphon, this system consists of the condenser located above the evaporator and connected via two tubes, called “riser” and “down-comer”. Generally speaking, the terms “riser” and “down-comer” describe the fluid flow direction through these connection tubes. As shown in Fig. 2.7, in the bottom side of the closed loop thermosiphon, boiling in the fluid volume occurs and vapor flows through the left tube (“riser”) to the condenser. After condensation, the working fluid flows to the evaporator through the right tube (“down-comer”).

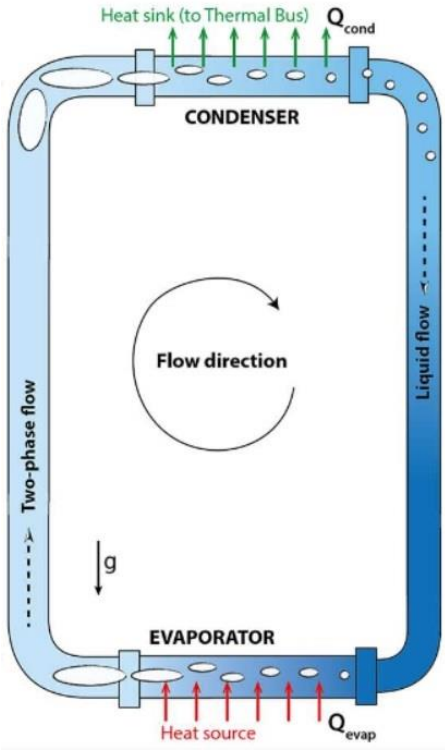


Figure 2.7. Schematic of a thermosiphon loop [2.14].

The main difference of the Closed Loop Thermosiphon from the conventional thermosiphon is the separation of the paths of the upward two-phase liquid/vapor flow and the descending condensate flow. This modification of the thermosiphon allows to significantly increase heat transfer performances of the device.

### *2.2.2. The Heat Pipe*

The passive two-phase heat transfer device capable to work with different orientation (even, for some cases, opposite to gravity vector) have been developed in the middle of the XX$^{th}$ century. First concept of the device, later called Heat Pipe, has been proposed by Gaugler [2.15] in the context of the refrigeration machines with the evaporator located above the condenser. Almost twenty years later, in the framework of the American Space Program, Grover re-introduced the heat pipe as a device very similar to the device of Gaugler [2.16].

Typical heat pipe (Fig. 2.8a) looks almost identical to thermosiphon – including evacuated sealed tube with the same evaporation, adiabatic and condensation zones and partially filled with working fluid. However, a main difference between these two devices is in the way the liquid returns from the condenser to the evaporator – contrary to the

thermosiphon, the heat pipe is not a gravity-assisted device and liquid returns to the evaporator thanks to a capillary structure (also called the "wick"), usually deposited on the walls along the heat pipe. The capillary structure could be in a form of the sintered powder, open grooves and mesh structure or their combinations, as presented in Fig. 2.8b. The driving force, which moves the liquid from the condenser to the evaporator, is caused by the capillary pressure difference between advancing and receding menisci at the opposite sides of the heat pipe.

(a) (b)

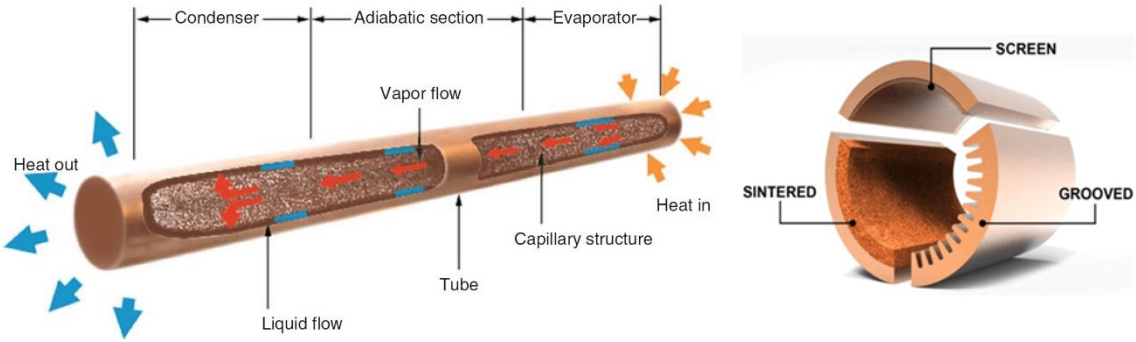


Figure 2.8. (a) Heat pipe working principle [2.17] and (b) types of capillary structures [2.18].

The heat pipe has a wide range of applications due to its gravity independence and wide range of the construction materials. Today, heat pipes are widely used in terrestrial and space applications in the thermal management systems. Compatibility with a wide range of fluids allows operation from the cryogenic (using helium as a working fluid) to the extreme temperatures (filled with liquid metals).

### *2.2.3. The Variable Conductance Heat Pipe*

Some applications need to guarantee a constant temperature of the heat source whatever the heat flux value is. Obviously, evaporator temperature of the thermosiphon and heat pipe strongly depends on the applied heat flux: for this reason, a Variable Conductance Heat Pipe, presented in Fig. 2.9, has been developed.

Unlike the heat pipe, the variable conductance heat pipe uses a reservoir, filled with a non-condensable gas to modulate the device conductance. The working principle of the VCHP is

very similar to the conventional heat pipe, except the varying length (and effective heat transfer surface) of the condenser.

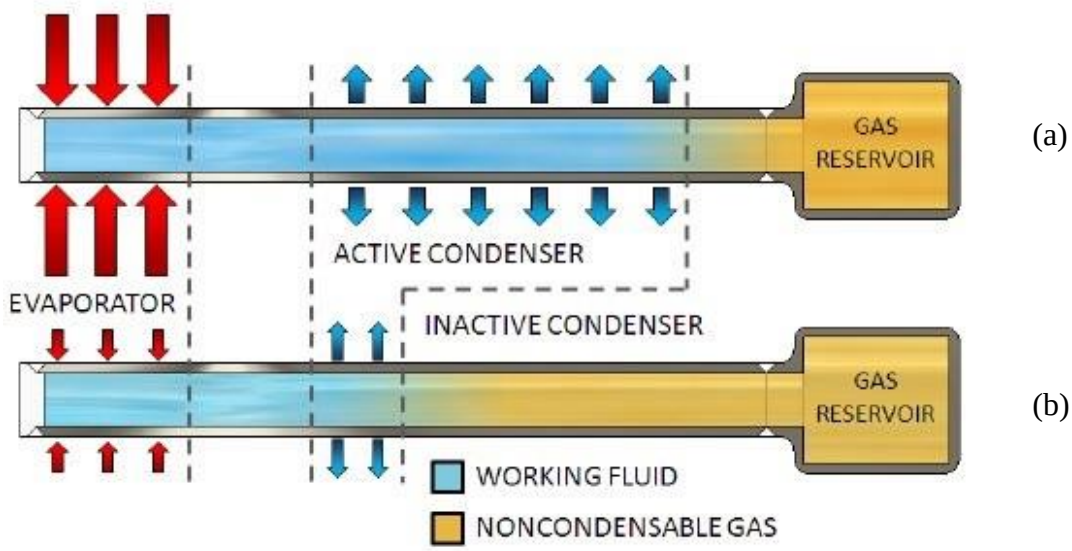


Figure 2.9. The working principle of a variable conductance heat pipe [2.19].

As seen in Fig. 2.9b, with low heat load (or without it), non-condensable gas fills a significant part of the heat pipe, preventing an optimal heat transfer rate. But increase of the temperature on the evaporator surface leads to the vapor pressure rise and moves the non-condensable gas into the reservoir, liberating a larger condenser surface area to interact with the vapor, resulting in a higher condensation rate (see Fig. 2.9a). So, heat transfer rate could be passively controlled to keep the cooling device at a relatively constant temperature in the range of ±1 $^{o}$C [2.20].

Despite an advantage of the variable conductance heat pipe in the temperature control, the design and fabrication of such device is more difficult and costly comparing to the one of conventional heat pipe.

### *2.2.4. The Micro Heat Pipe*

The miniaturization of electronic components and higher and higher heat generation have led to the introduction of the concept of a Micro Heat Pipes by Cotter in 1984 [2.21]. The micro heat pipe is defined as a heat pipe in which the mean curvature of the liquid vapor interface is comparable in magnitude to the reciprocal of the hydraulic radius of the total flow channel. Typically, micro heat pipes have convex but cusped cross sections to keep a

capillary pumping in the corners, with hydraulic diameter in range of 10 to 500 μm. The typical micro heat pipe and its profiles are shown in Fig. 2.10.

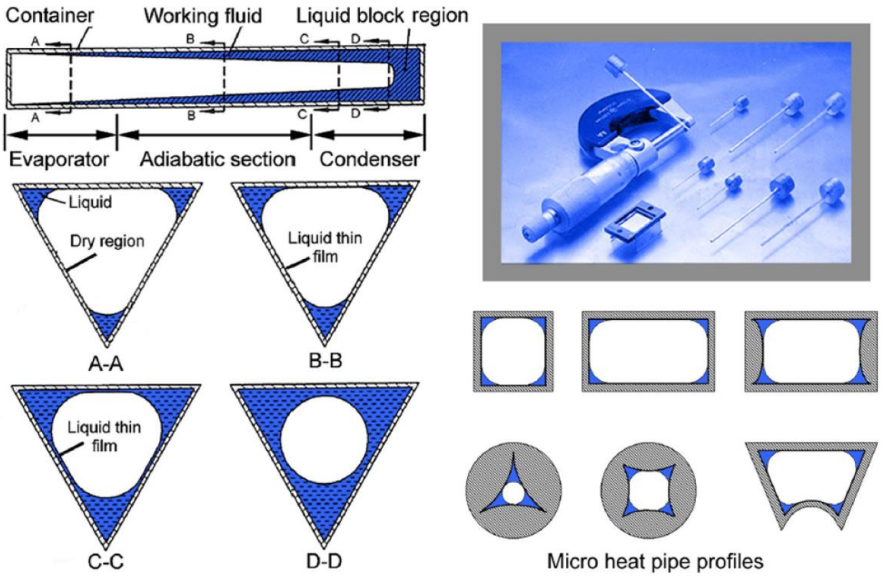


Figure 2.10. Cross-section geometries of the micro heat pipes [2.22].

In analogy with conventional heat pipes, micro heat pipes have also evaporator, adiabatic and condensation zones. The working principle is very similar to the heat pipe with the open grooves – central part of the micro heat pipe occupied by a vapor, but corners (grooves) filled with liquid which flows from the condenser to the evaporator thanks to the capillary pressure difference.

Micro heat pipes are able to transfer radial heat flux densities up to the 90 W/cm$^2$ in horizontal inclination and up to 150 W/cm$^2$ for vertical orientation with the condenser located above the evaporator [2.23]. But, due to the variation of the liquid cross section with the decrease of the menisci radii along the capillary flow, the liquid pressure losses become very high and increase much faster than the driving capillary pressure (increasing with decreasing radii). Thus, the remove heat and the transport distance of these systems remain very low compared to the others (a few Watts and centimeters only).

### *2.2.5. The Loop Heat Pipe and Capillary Pumped Loop*

Last few decades, the increase of the demands in the heat transfer devices capable to work with long distances and under different gravity conditions have been observed. Despite the capillary pumping effect inside the conventional heat pipe, the length increase leads to

the augmentation of the pressure losses in the liquid flow, which provoke a significant heat transfer degradation due to lower working fluid flow rate to the evaporator. Thus, a lot of attention has been brought to the novel two-phase loops, combining the benefits of the closed looped thermosiphon and conventional heat pipe, as well high heat transfer rate, low hydraulic resistance and ability to work under different gravity conditions. As a result, two types of two-phase loops have been developed in the second part of the $XX^{th}$ century.

First presented two-phase loop was a Capillary Pumped Loop, developed by Stenger in 1966 for NASA on-orbit spacecraft missions [2.24]. Later, in 1972, a little different device, called Loop Heat Pipe, has been developed in the former USSR [2.25].

The main physical principle of operation is the same as that of heat pipes, but the vapor and liquid paths are here separated (Fig. 2.11). At the evaporator, a porous wick acts as a capillary pump. The liquid evaporates by absorbing a heat flow from the evaporator. The vapor flows to the condenser through the vapor line and condenses in the condenser. The condensate returns to the evaporator through the liquid line. The control reservoir helps to absorb fluctuations and fluid expansion that may occur during loop operation. The reservoir also modulates the operating conditions of the loop, temperature and saturation pressure in particular. It is the position of the reservoir relative to the evaporator that leads to the distinction between the two types of two-phase loops: Loop Heat Pipe (Fig. 2.11a) and Capillary Pumped Loop (Fig. 2.11b).

Two-phase capillary pumped loops have several advantages compared to the conventional heat pipe. The porous wick provides thermal insulation and hydraulic separation (hydraulic lock) between liquid and vapor phases, preventing phase change on the vapor-liquid interface; they increase the design flexibility thanks to the separation of the evaporator and condenser; the capillary structure is present just in the evaporator which drastically reduces pressure losses and increases the capillary limit, and the separation of liquid and vapor lines prevent shearing of liquid particles by vapor flow (entrainment limit). Despite these advantages, capillary pumping loops are complicated to be systematically implemented due to reservoir separation from the evaporator and necessarily presence of the temperature control heater.

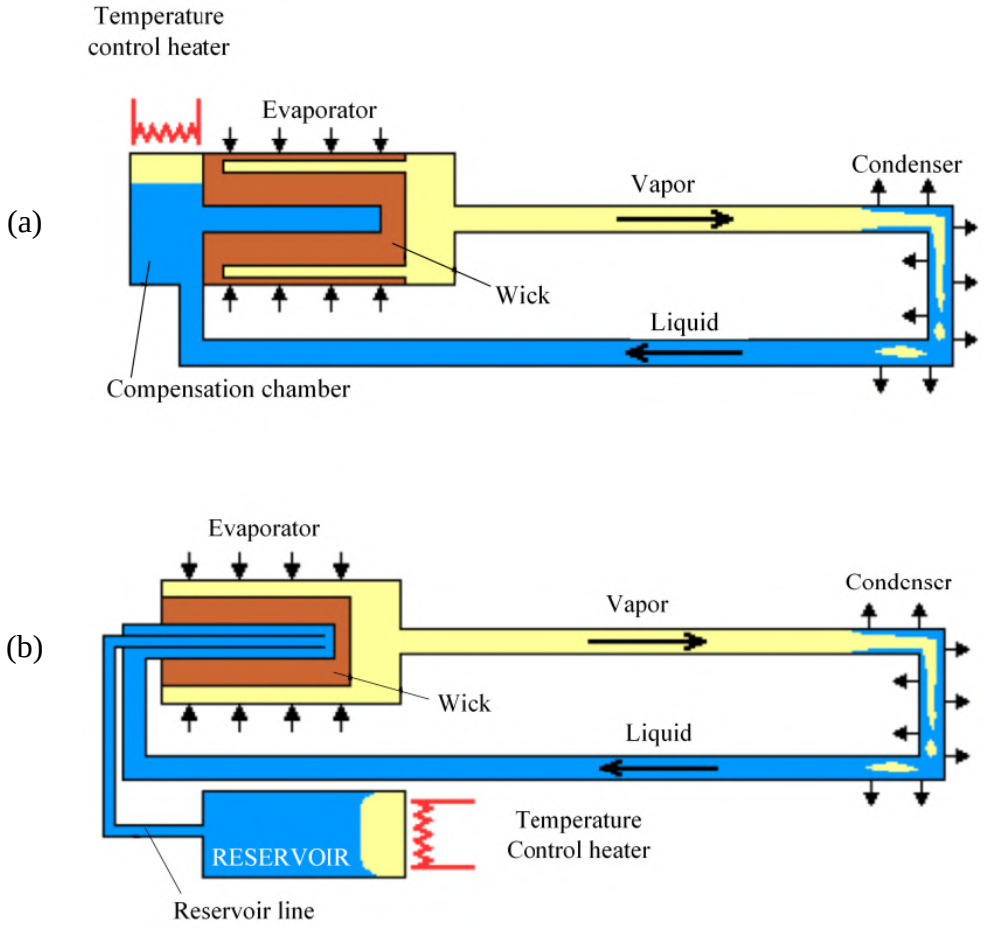


Figure 2.11. Schematic working principle of the loop heat pipe (a) and capillary pumped loop (b) [2.26].

### *2.2.6. The Pulsating Heat Pipe*

The first concept of the Pulsating Heat Pipe has been proposed in 1971 by Smirnov [2.27]. The proposed pulsating heat pipe, described in Fig. 2.12, consists of two reservoirs (evaporator and condenser), connected by a capillary tube to ensure vapor liquid separation in the slug form. The evaporator and connecting tube are initially filled with working fluid, the condenser is partially filled with non-condensable gas and liquid, as shown in Fig. 2.12 (stage 1). Evaporation, caused by the applied heat load, leads to the pressure gradient generation and following liquid pushed to the condenser by piston effect, provoking compression of the passive gas (Fig. 2.12, stage 2). Then liquid evaporates and connection tube is filled only with vapor. Simultaneously, when vapor gets in the condenser, it condensates on the internal surface of this zone, provoking a local decrease of pressure. At the same moment, depending on the pressure distribution in the various sections of the

device, the potential energy, stored in the volume of passive gas compressed in the condenser, will push the liquid back to the evaporator – returning to the initial conditions.

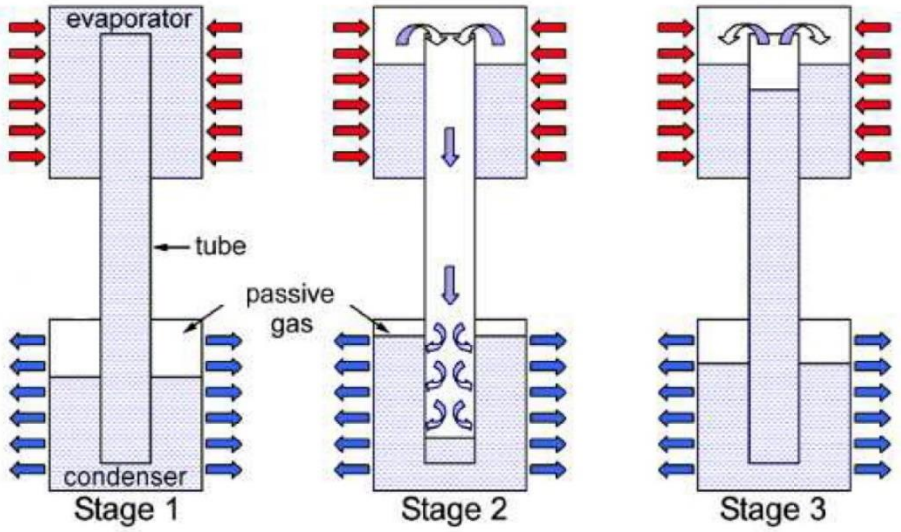


Figure 2.12. Single-channel pulsating heat pipe [2.27].

Despite the singe-channel pulsating heat pipe introduction in 1971, this concept was not used until the end of the XX$^{th}$ century. In 1990, Akachi [2.28] introduced a new concept of pulsating heat pipes. Relatively new, this type of heat pipe represents a unique serpentine capillary tube bended in few/many turns from hot to cold sources, and partially filled with a working fluid at liquid/vapor saturation state (Fig. 2.13). The fluid at saturation state is alternately distributed in the form of liquid plugs and vapor bubbles inside the tube, due to surface tension forces in the tube of capillary dimension.

The physical principle of the PHP is based on the phase change induced motions of working fluid from evaporator to condenser. With heat power applied, the volume of the vapor bubbles increases in the evaporation zone, generating outward forces. The opposite phenomena occurs in the condensation zone – vapor bubble volume decreases with heat rejection, generating inward forces. These two forces induce the motion of the all fluid from the evaporator to the condenser. Due to the exploitation of both sensible and latent heat transfer modes, PHP shows a high heat transfer capability, compared to classical heat pipes. In addition, PHP has a simple structure and the ability to operate under different gravity levels and different positions. However, the complexity of the physical phenomena inside pulsating heat pipes creates a big challenge in applications design.

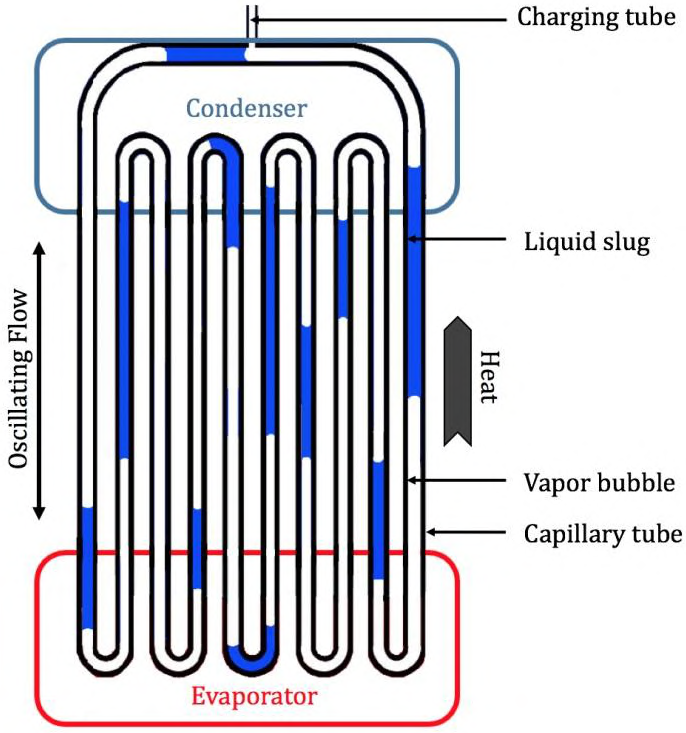


Figure. 2.13. Basic construction of a closed looped pulsating heat pipe [2.29].

A detailed presentation and overview of this system will be drawn in Chapters 3 and 4 of this document.

## 2.3. Conclusions

A brief review of the most efficient two-phase thermal management approaches has been done in this chapter. The comparison of these system regarding heat transfer capability presented in table 2.1. Active cooling solutions (pump forced liquid circulating loops) ensure the high-performance heat rejection, uniform surface temperature and gravity independent operation. Despite these advantages, complexity of physical phenomena involved in the system and high power consumption for the fluid pumping represents a big challenge to use such systems in space applications.

Passive two-phase systems could operate stably with high level of heat rejection without supplementary energy consumption. Unfortunately, a more simple and stable device – the thermosiphon - could not operate without gravity assistance, which makes this type of device not applicable for space application. Other passive two-phase systems are successfully used

for the space missions during last few decades. However, new challenges in the TMS for space electronic cooling need the more efficient and simple devices.

Table 2.1. Comparison the two-phase cooling solutions.

| **Technology** | **Maximum Heat Flux** [$W.cm^{-2}$] | **Total Power** [kW] |
|---|---|---|
| Two-Phase Microchannel [2.30] | 250 | - |
| Two-Phase Spray / Jet [2.30] | 1820 | - |
| Thermosiphon / Loop Thermosiphon [2.31] | 100 | 10 |
| Heat Pipe [2.32] | 100 | 0.2 |
| Loop Heat Pipe [2.33] | 900 | 10 |
| Capillary Pumped Loop [2.34] | 100 | 10 |
| Pulsating Heat Pipe [2.35] | 30 | 5 |

The pulsating heat pipe stands out thanks to its high performance, simple structure and ability to work under different gravity conditions. However, despite its advantages in terms of simplicity and heat transfer, its large-scale development is not yet very relevant, unlike other two-phase technologies such as the capillary pumped loops or the thermosiphon, more mature from a technological point of view. Certain aspects related to the operation of the pulsating heat pipes are not yet fully understood due to relatively novel technology and physical complexity. In further chapters, some experimentations will be led on given PHP – in ground and space conditions – to try to better understand the physical phenomena and the induced performances of such devices.

**References**

[2.1] Mudawar I., Bharathan D., Kelly K. and Narumanchi S., 2009. Two-Phase Spray Cooling of Hybrid Vehicle Electronics. IEEE TRANSACT. COMPONENTS PACK. TECH. 32, 501-512.

[2.2] ECSS Secretariat, 2010. Qualification of two-phase heat transport systems. The Netherlands, Noordwijk.

[2.3] Khairnasov S. M., 2015. The use of heat pipes in thermal control system for electronics: current situation and prospects. Tech. Design Electron. Equip. 2, 19-33.

[2.4] Tuckerman D. B. and Pease R. F. W., High-performance heat sinking for VLSI. IEEE Electr. Dev. Let. 2, 126-129.

[2.5] Al-Zaidi A. H., Mahmoud M. M and Karayiannis T.G., 2019. Flow boiling of HFE-7100 in microchannels: Experimental study and comparison with correlations. Int. J. Heat Mass Trans. 140, 100–128.

[2.6] Kadam S. and Kumar R., 2014. Twenty first century cooling solution: Microchannel heat sinks. Int. J. Therm. Sci. 85, 73-92.

[2.7] Visaria M. and Mudawar I., 2009. Application of Two-Phase Spray Cooling for Thermal Management of Electronic Devices. IEEE Trans. Comp. Pack. Tech. 32.

[2.8] Wang J.-X., Li Y.-Z. and Li G.-C., 2019. Ground-Based Near-Space-Oriented Spray Cooling: Temperature Uniformity Analysis and Performance Prediction. J. THERMOPHYS. H. TR. 33, 617-626.

[2.9] Wang J-X., Guo W., Xiong K. and Wang S.-N., 2020. Review of aerospace-oriented spray cooling technology. Progress Aerospace Sci. 116, 100635.

[2.10] Monde M., 1987. Critical Heat Flux in Saturated Forced Convection Boiling on a Heated Disk with an Impinging Jet, ASME J. Heat Transf. 109, 991–996.

[2.11] Perkin A.M., 1898. Mode of heating buildings and evaporating fluids. Specification of Letters Patent, No 888.

[2.12] Feldman K.T. Jr. and Srinivasan R., 1984. Investigation of heat transfer limits in two-phase closed thermosiphon. Proc. 5th Int. Heat Pipe Conf., Tsukuba, Japan.

[2.13] https://celsiainc.com/technology/thermosiphon/

[2.14] Lamaison N., Marcinichen J., Szczukiewicz S., Thome J. and Beucher P., 2016. Passive Thermosyphon Cooling System for High Heat Flux Servers. Interfac. Phen. H. Transf. 3, 369-391.

[2.15] Gaugler R.S., 1944. Heat transfer device. United States Patent, No 2350348.

[2.16] Grover G.M., 1963. Evaporation-condensation heat transfer device. United States Patent, No3229759..

[2.17] Zohuri B., 2016. Heat Pipe Design and Technology. Springer.

[2.18] https://celsiainc.com/wp-content/uploads/2016/05/heat-pipe-wick-types.png

[2.19] Tarau C., Anderson W. and Peters C., 2012. Thermal Management System for Long-Lived Venus Landers. 9th Ann. Int. Energy Conv. Eng. Conf., San Diego, California.

[2.20] Anderson W., Hartenstine J., Tarau C., Sarraf D. and Walker K., 2011. Pressure Controlled Heat Pipes. Proc. 41st Int. Conf. Env. Sys., Portland, USA.

[2.21] Cotter T.P., 1984. Principles and prospects for micro heat pipes. Proc. 5th Int. Heat Pipe Conf., Tsukuba, Japan.

[2.22] Groll M. and Khandekar S., 2002. Micro heat pipes. Chapter 2.13.8, Heat Exchanger Design Book.

[2.23] Hopkins R., Faghri A. and Khrustalev D., 1999. Flat Miniature Heat Pipes with Micro Capillary Grooves. J. Heat Trans. 121, 102-109.

[2.24] Stenger F.J., 1966. Experimental feasibility study of water-filled capillary-pumped heat transfer loops. NASA TM-X-1310.

[2.25] Maidanik Y.F., 2005. Loop heat pipes. Appl. Therm. Eng. 25, 653-657.

[2.26] Chen X., Ye H., Fan X., Ren T. and Zhang G. Q., 2016. A review of small heat pipes for electronics. Appl. Therm. Eng. 96 , 1-17.

[2.27] Smirnov G. F. and Savchenkov G. A., 1971. Pulsating Heat Pipe. USSR Patent, No504065.

[2.28] Akachi P. and Polasek F., 1996. Pulsating heat pipes. Proc 5th Int. Heat Pipe Symp., 208–217.

[2.29] Barba M., Bruce R., Bonelli A. and Baudouy B., 2017. Experimental study of Large-scale cryogenic Pulsating Heat Pipe, IOP Conf. Series: Mat. Sci. Eng. 278, 012156.

[2.30] Agostini B., Fabbri M., Park J. E., Wojtan L., Thome J. and Michel B., 2007. State of art of high heat flux cooling technologies. Heat Trans. Eng. 28, 258–281.

[2.31] Cao J., Zheng Zh., Asim M., Hu M., Wang Qi., Su Yu., Pei G. and Leung M., 2020. A review on independent and integrated/coupled two-phase loop thermosyphons. Appl. Energy 280, 115885.

[2.32] Accorinti F., 2020. Two-Phase Power Electronics Cooling Solution Design in Air Context Answering to the Objectives of the Hybrid Aircraft 2035. PhD Thesis.

[2.33] Aono Y., Watanabe N., Ueno A. and Nagano H., 2021. Development of a loop heat pipe with kW-class heat transport capability. Appl. Therm. Eng. 183, 116169.

[2.34] Dupont V., Legros J.-C., Oost S. V., Barremaecker L., 2013. Experimental investigation of CPL pressurized with NCG inside a centrifuge up to 10 G. Proc. 17th Int. Heat Pipe Conf., 303–310.

[2.35] Marengo M., and Nikolayev V., 2018. Pulsating Heat Pipes: Experimental Analysis, Design and Applications. Encyclopedia Two-Phase Heat Transf. Flow IV, 1-62.

# Chapter 3

## Fundamental Mechanisms of the PHP Operation

In this chapter will be given a detailed description and analysis of the thermo-hydrodynamic working principles of the pulsating heat pipe, their types and differences. Due to the particular shape of the channels in the flat plate pulsating heat pipes studied in this thesis, peculiarities of the flow in rectangular capillary channels will be also discussed.

### 3.1. Pulsating heat pipe working principles

Beyond the different geometries and dimensions, according to the arrangement of the tube, pulsating heat pipes could be first categorized into the two principal configurations, according to [3.1], presented in Fig. 3.1:

- Closed Loop Pulsating Heat Pipe (CLPHP), formed by the serpentine channel looping, allowing the fluid oscillation and circulation operations;
- Open Loop Pulsating Heat Pipe (OLPHP), where a serpentine channel is not looped (not connected), keeping two ends closed.

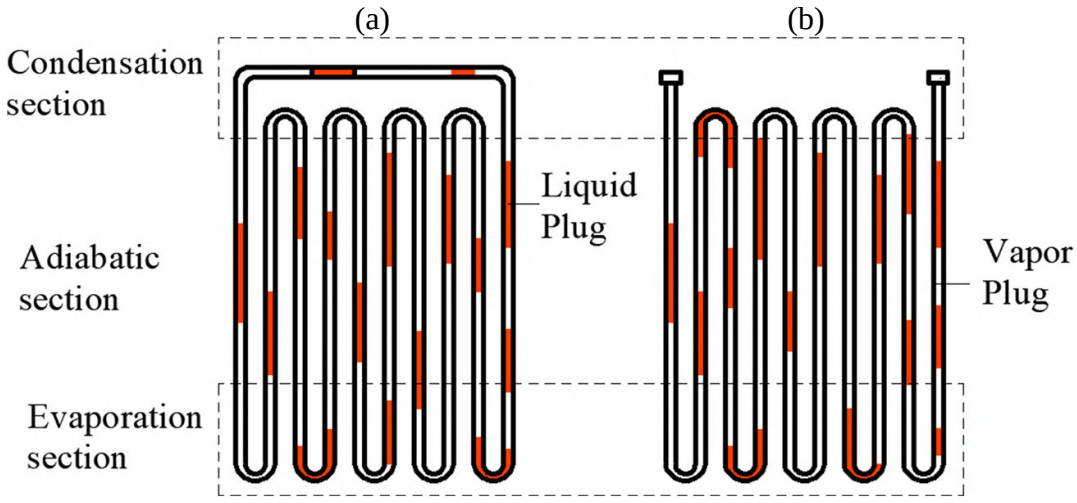


Figure 3.1. Schematic representation of the different PHP configurations [3.1]: (a) Closed Loop Pulsating Heat Pipe, (b) Open Loop Pulsating Heat Pipe.

However, up to now, several other characteristics can be used to categorize the PHPs: tubular or flat plate design, 2D or 3D structure, etc. The principal difference between tubular and flat plate pulsating heat pipes requires to be specified due to the direct influence on the device operation. If tubular PHP can be presented as a tube bended into a serpentine (Fig. 3.2a), the flat plate PHP can be defined as: a flat plate with engraved/machined (or obtained by additive/etching manufacturing) single, generally square or rectangular channel forming a serpentine between one or more hot sources and one or more cold sources (Fig. 3.2b). This plate is sealed with a smooth plate cover to confine the channel.

(a) (b)

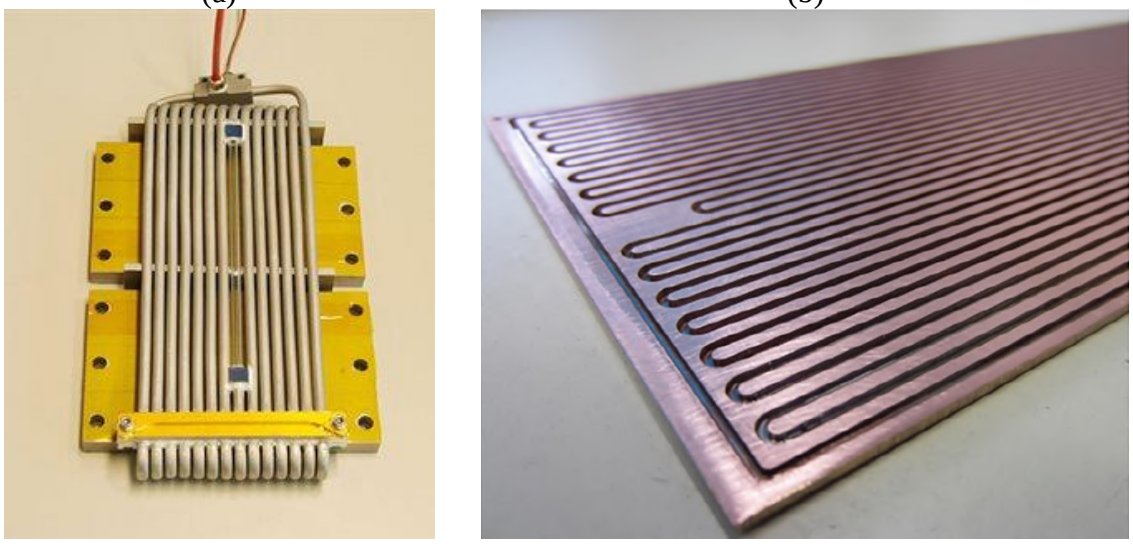

Figure 3.2. Difference between (a) tubular [3.2] and (b) flat plate PHP.

The main parameter that distinguish flat plate device from tubular one is the geometrical continuity between channels leading to very low transverse thermal resistance: thermal spreading occurs and tends to strongly decrease the thermal gradients between channels. This causes homogenization of the pressure differences in the channels, which are the main drivers of oscillations under slug flow regime, particularly in horizontal inclination [3.3].

Even with these construction differences, all PHP types have common characteristics, in their general structure and, more important, in their operation. These basic characteristics can be summarized by:

- A unique channel bent in a serpentine with at least a few “U-turns”. This channel could be with connected ends (CLPHP) or not (OLPHP). The channel surface remains smooth – no additional treatment is necessary;

- Channel is partially filled with working fluid, which is compatible with pulsating heat pipe material and corresponds to the necessary thermophysics demands;
- Presence of at least one evaporation zone (hot source - heat absorption) and one condensation zone (cold source - heat rejection);
- Acceptable presence of the adiabatic zone between evaporator and condenser, but not required.

In addition to previously mentioned criteria for PHP performance, the correct operation of the device is insured by the initial liquid distribution inside the PHP in the form of the liquid plugs and vapor slugs chain. This distribution is insured by the capillary forces domination on gravitational forces and leads to the complete transverse tube blocking by the liquid plug which separates neighboring vapor slugs. The meniscus region exists on both ends of each liquid plug, caused by the interaction forces at the solid/liquid/vapor interfaces. Depending on the surface properties and vapor slug length, the meniscus can be surrounded by thin liquid film. In case of isothermal conditions – no heat load and no heat rejection – liquid and vapor phases exist at equilibrium at saturation pressure which corresponds to the device temperature. With heat applied, the fluid flows in a capillary tube in the form of the motion of both liquid plugs and vapor slugs (Taylor flow). This flow configuration with forces affecting the fluid flow, and corresponding heat transfer mechanisms, are shown in Fig. 3.3.

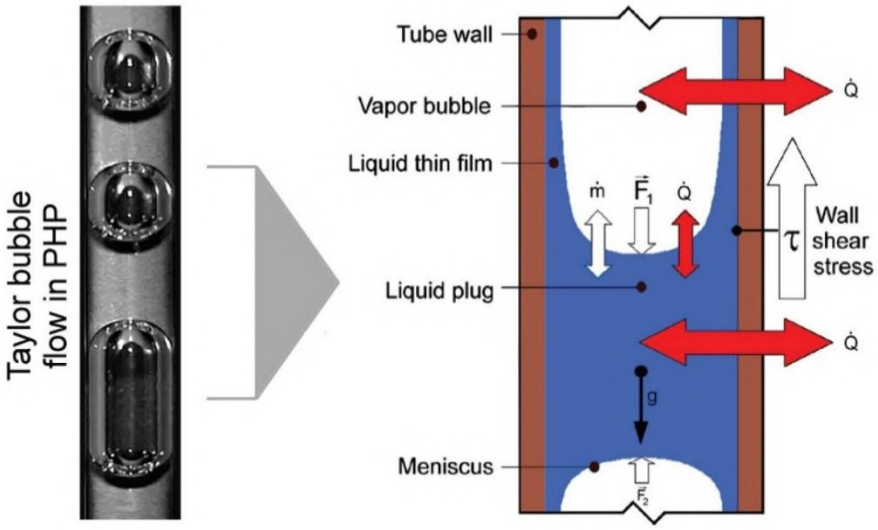


Figure 3.3. Taylor bubble chain in a vertical tube (left), the forces acting on the liquid plug and transfer processes in the single-cell scale (right) [3.4].

But device performance and operation strongly depend on the continuous non-equilibrium conditions inside the system. So, pulsating heat pipe operation can be described with the local thermodynamic states for different zones, as shown in Fig. 3.4.

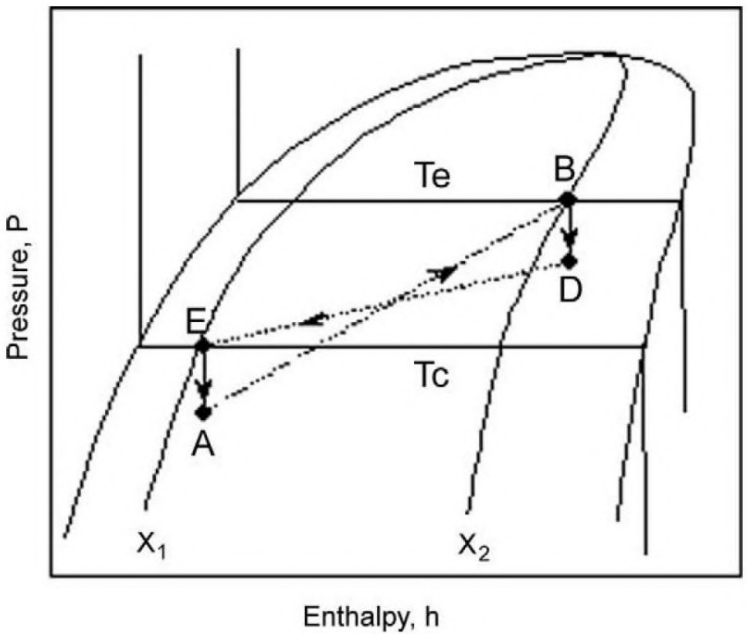


Figure 3.4. Pressure-enthalpy diagram of the PHP operation [3.6].

According to Khandekar et al. [3.6], initial temperature and vapor quality in the evaporator and condenser zones are known (or can be assumed); consequently the state at the outlets of the evaporator and condenser are known too. If "point A" can be considered as a starting at the evaporator inlet, the following explanations can be given to the involved thermodynamic transformations:

A→B: (outlet of evaporator): constant pressure heat input combined with an isentropic compression due to bubble expansion;

B→D: isenthalpic pressure decrease in the adiabatic section;

D (inlet of condenser) →E (outlet of condenser): due to the complicated nature of the thermodynamic process between the condenser inlet and outlet, it can be simplified to constant pressure condensation with negative isentropic work;

E→A: an isenthalpic pressure drop in the adiabatic section completes the cycle;

Because of the numerous assumptions made in this description, thermodynamic analysis is insufficient to study real PHP system, but it helps to a better understanding of the PHP operation.

### 3.2. Physical phenomena in PHP.

Pulsating heat pipe is a high-performing device with a very simple design, as was mentioned in previous chapter. Despite these advantages, understanding of PHP operation is still quite complex and requires intensive investigations: many parameters (design, fluids, filling ratio, inclination etc.) influence the device operation. In general, these parameters can be classified in few groups:

- Design parameters
  - Open or closed loop configuration
  - Device material and type (tubular PHP or flat plate PHP)
  - Channel diameter and shape (alternate or not)
  - Number of turns
  - Length of the evaporation, adiabatic and condensation zones
  - Presence of valves (check valves or Tesla valves)
- Working fluid properties
- Operational parameters
  - Filling ratio
  - Inclination and/or gravity level
  - Heat load
  - Heat sink heat transfer coefficient and temperature

First of all, the main task of a heat transfer device is high efficient thermal transport and stable operation. So, from this point of view, higher thermal conductivity of the PHP material is always an advantage. On the other side, pulsating heat pipe exploits both sensible and latent heat of the working fluid, which influences are greatly higher than material heat conduction, especially in cases with long adiabatic zone. Value of effective thermal conductivity ($\lambda_{eff} = \dot{Q}L/[A_t(T_{ev} - T_{cond})]$ with, respectively, $\dot{Q}$ the applied heat load, $L$ a characteristic length between hot and cold sources, At the PHP solid transverse cross section and $(T_{ev} - T_{cond})$ the temperature difference between evaporator and condenser zones) for conventional pulsating heat pipes classically goes up to 10 $kW.m^{-1}.K^{-1}$ [3.7] and up to 20 $kW.m^{-1}.K^{-1}$ for cryogenic PHPs [3.8].

*3.2.1. Diameter influence on the liquid distribution inside PHP*

Due to the strong dependency of the flow pattern from capillary forces, one of the main parameters influencing the pulsating heat pipe operation is the channel diameter. Indeed, surface tension forces become predominant when channel diameter becomes smaller and two-phase flow changes into a slug-plug -or Taylor- flow pattern, defined as the basis of the PHP operation.

The scientists and engineers who worked on mini- and microchannel heat transfer also tried to classify the channels, based on their diameters and/or on the possibility of the existence of a Taylor flow inside them. A few main classifications for the transition from macroscale to microscale flows, based on the hydraulic diameter, have been proposed during few last decades. First, Mehendal et al. [3.9] recommended a size-based classification as follows:

- Microchannels ($D$ = 1–100 μm)
- Mesochannels ($D$ = 100 μm to 1 mm)
- Macrochannels ($D$ = 1–6 mm)
- Conventional channels ($D$ > 6 mm)

Later, Kandlikar [3.10] implemented the following classification, based on the channel diameter range and more reliable:

- Microchannels ($D$ = 50–600 μm),
- Minichannels ($D$ = 600 μm to 3 mm)
- Conventional channels ($D$ > 3mm)

Unfortunately, transition criteria based just on channel dimensions do not reflect the influence of channel size on the physical mechanisms and do not take into account fluid properties. A more general definition should address to the interaction of different forces, as well gravitational, interfacial and viscous ones.

If a vapor slug is introduced in a vertical channel with a small diameter (smaller than a critical value defined below thanks to Eq. (3.1)-(3.3)), the bubble will not rise up by buoyancy. This means that liquid plugs and vapor slugs can be formed without stratification.

Fig. 3.5 and 3.6 schematically present the fluid distribution inside vertically oriented PHPs with different diameters under adiabatic and operating condition. Two cases in Fig.

3.5 depict the fluid distribution for the device with channel diameter much higher (a) and slightly higher (b) than critical one (from Eq. (3.1)). Initially, under adiabatic conditions, all liquid phase is accumulated in the bottom part of the device due to stratification. During operation, the effect of surface tension reduces, working fluid stratifies by gravity and the device with higher channel diameter works in the thermosiphon mode (Fig. 3.5a) – liquid boils in the evaporation zone, vapor flows to the condenser, where it condensates and returns into the evaporator along the tube inner walls thanks to gravity forces. Unlike previous case, if the channel diameter is decreased (Fig. 3.5b), the flow circulates with large liquid plugs and most of the liquid sticks to the wall – the device operates as a bubble pump thanks to buoyancy.

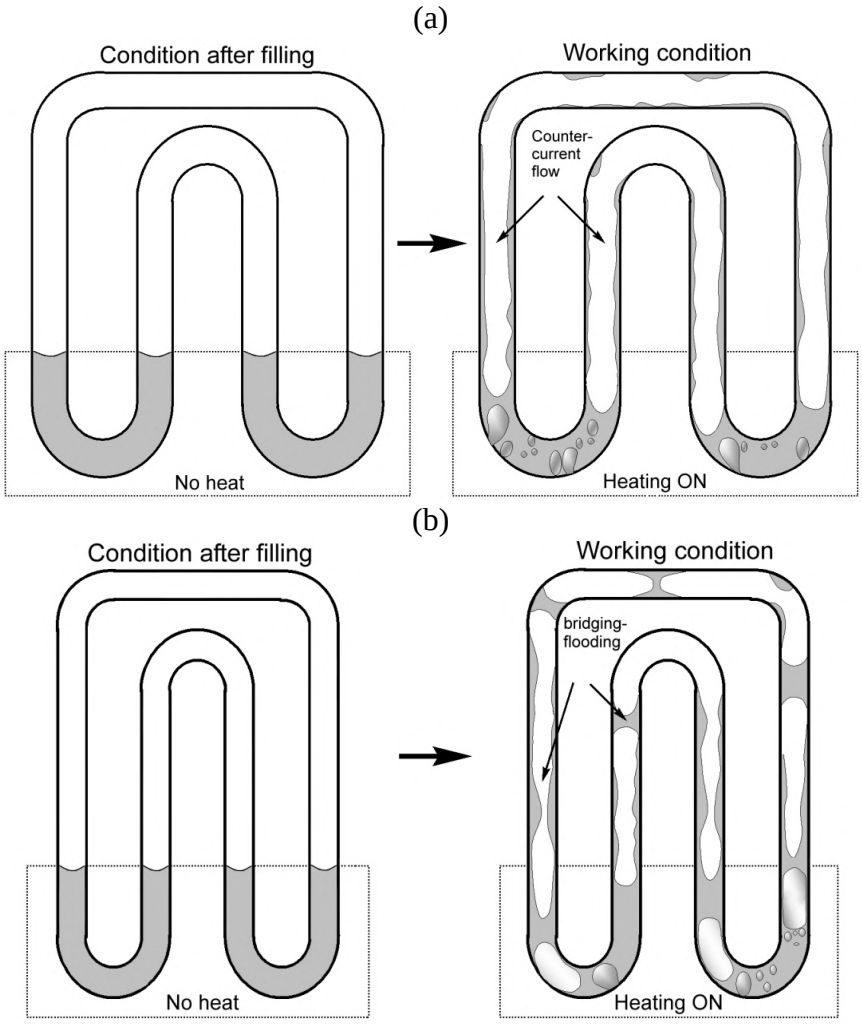


Figure 3.5. Effect of channel diameter on fluid distribution inside the circular tube under adiabatic and operation conditions: diameter (a) much and slightly (b) higher than critical one [3.5].

If channel diameter becomes lower than a critical value, the surface tension forces dominate and stable slug/plug liquid-vapor distribution along the channel is formed, as shown in Fig.3.6a. This type of flow ensures the continuous and effective heat and mass transfer inside the PHP. On the other hand, if channel diameter becomes much lower than critical value (Fig. 3.6b), the slug-plug flow is maintained, but the oscillations are limited by the significant influence of the surface and viscous forces.

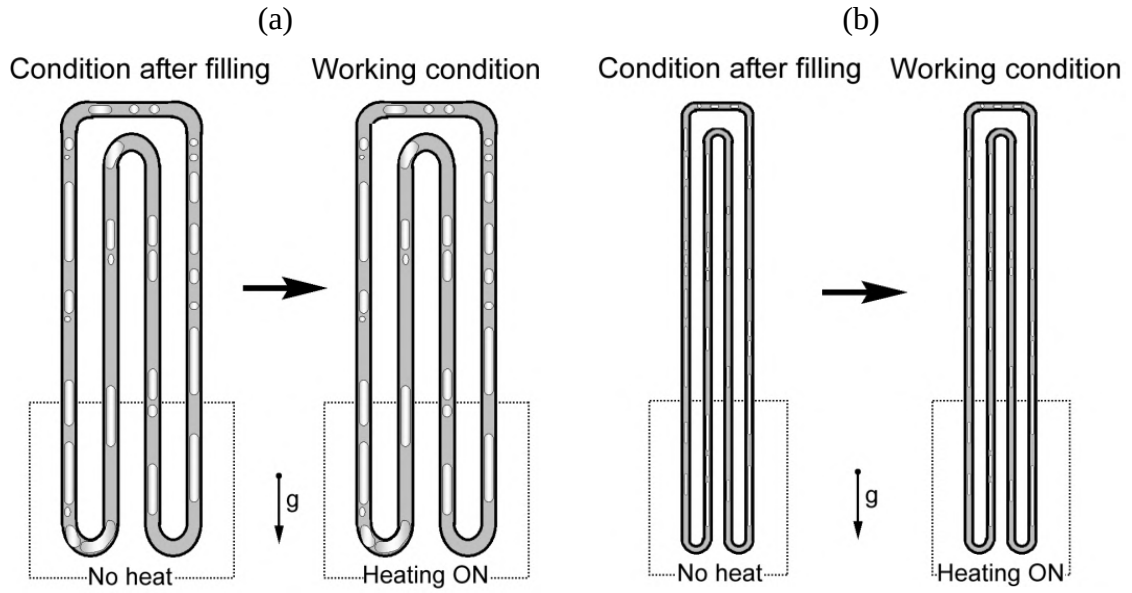


Figure 3.6. Effect of channel diameter on fluid distribution inside the circular tube under adiabatic and operation conditions: diameter (a) slightly and (b) much lower than critical one [3.6].

All these configurations have been classified thanks to dimensionless numbers describing the ratio between capillary and other influences forces (gravity, inertial, viscous forces). Originally, Hosoda et al. [3.11] proposed to use dimensionless Bond number ($Bo = (\rho_l - \rho_v) g D^2/\sigma$), representing the ratio between capillary and gravity forces, to identify the diameter range, providing the transition to slug-plug flow. A critical dimeter based on Bond number can be calculated as follows:

$$D_{\mathrm{cr,Bo}} = 2\sqrt{\frac{\sigma}{g(\rho_{\mathrm{l}} - \rho_{\mathrm{v}})}} \tag{3.1}$$

It has to be noted that this criterion has been widely used in the literature for PHP design. However, as discussed by Mameli et al. [3.12], this criterion is obviously not applicable for conditions where gravity acceleration is no more relevant or applicable in such equation, like

high accelerations or microgravity conditions. From the knowledge of velocity of the liquid plugs and vapor slugs motions (around 0 – 1 m.s$^{-1}$ for PHPs), liquid inertia has been accepted as a predominant force between the two phases due to the higher density of the liquid phase. From this point, a new criterion based on the Weber number, based on the ratio between inertial and capillary forces ($We = \rho_l U_l^2 D/\sigma$), has been proposed by Gu et al. [3.13] and defines a new critical diameter from the critical value known as *We,cr* = 4:

$$D_{\mathrm{cr,We}} = \frac{4\sigma}{\rho_{\mathrm{l}} U_{\mathrm{l}}^2} \tag{3.2}$$

Initially related to the microchannel two-phase flow, and based on Garimella number *Ga* ($Ga = Re\sqrt{Bo}$), a more relevant criterion has been proposed later by Harichian and Garimella [3.14] to define the diameter limitation for reduced gravity fields, from the found critical value of *Ga* = 160:

$$D_{\mathrm{cr,Ga}} = \sqrt{\frac{160\mu_{\mathrm{l}}}{\rho_{\mathrm{l}} U_{\mathrm{l}} \sqrt{\frac{\sigma}{g(\rho_{\mathrm{l}}-\rho_{\mathrm{v}})}}}} \tag{3.3}$$

According to presented criteria, the above mentioned simplified explanation of the diameter effect can be classified quantitatively.

### *3.2.2. Fluid flow and heat transfer in PHP*

Considering the fluid distribution pattern inside the PHP, the motion of the liquid plug could be described by momentum equation (Eq. (3.4)). The main forces acting on the slug-plug flow system originate from the surface tension, viscosity, inertia, tangential shear stresses and the force associated with the disjoining pressure at the molecular level. So, the integrated momentum equation for a moving liquid plug of length *Ls* over the channel with cross-section area *S* is given by:

$$\frac{d(m_l u_l)}{dt} = [(P_r - P_a) - \Delta P_c \pm \rho_l g dh]S - (F_\tau + F_{turns}) \tag{3.4}$$

where $m_l$ represents the liquid plug mass ($m_l = S{\cdot}Ls$) and $u_l$ the liquid slug velocity. $\Delta P_c$ is the capillary pressure drop arising from hysteresis between advancing ($\theta_a$) and receding ($\theta_r$) contact angles during the motion of the plug ($\Delta P_c = (2\sigma/R)\cdot(-\cos(\theta a) + \cos(\theta r))$). This additional resistance is additive and gets amplified if several slugs are simultaneously located in a channel (see Fig. 3.7). The cumulative pressure gradients damp oscillations and,

when contact angle hysteresis is too large, an excessive number of liquid plugs may rapidly block the flow, especially if the driving force is not sufficient [3.4]. The term $\rho_l gdh$ represents gravity pressure drop, which can be positive, negative or equal to zero according to the inclination of the tube and the direction of the liquid plug motion. $F_\tau$ represents the viscous shear stress term (classically, $F\tau = \Lambda(L_s/D)S(\rho_l u_l^2)/2$ where $\Lambda = 64/Re$ *is* the Poiseuille flow friction factor for established laminar flow) and $F_{turns}$ is a supplementary force caused by the singular pressure drop during plugs enters inside the curved part of the tubes [3.15]. For liquid plugs of high length-to-diameter ratio ($L_s/D \gg 1$), the viscous shear stress terms becomes dominant compared to the capillary forces. Finally, the term $(P_r - P_a)$ means the main driving agent of the liquid plug motion and presents the pressure difference between vapor bubbles surrounding the liquid plug. Detailed description of the vapor thermodynamic state and pressure evolution caused by heat and mass transfer can be found in [3.3] and [3.15].

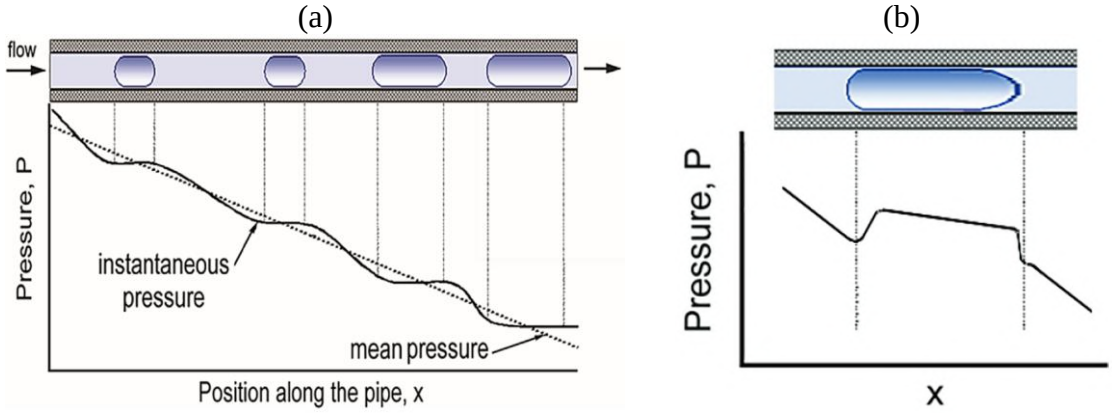


Figure 3.7. Pressure drop in Taylor bubble flow assuming (a) no pressure in individual bubbles and (b) liquid plug advancing angle lower than π/2 [3.4].

There are a lot of contradictions in the heat transfer mechanismes inside pulsating heat pipe: it was repeatedly established that liquid evaporation/condensation contributes mainly as a means to slug-plug flow motion and the main part of heat is transferred by the sensible heat of the liquid plugs flowing from evaporator to condenser and vice-versa. Recently, the predomination of the latent heat transfer in pulsating heat pipes has been experimentally proven (between 55% and 80% of rate compared to sensible one) (Fig. 8.a) [3.16; 3.17].

Infrared measurements of the single vapor slug flow in a capillary channel heated by Joule effect (Fig. 3.8b) showed that the external temperature of the tube wall cooled only by classical convective cooling (single liquid liquid flow) increases transiently with time (Fig.

3.8c) [3.18]; in the region named "close to the meniscus", experimental temperature slightly decreases and separates from the numerical curve (after 3.6 s); the third zone corresponds to the liquid thin film evaporation phase: a sudden drop of the wall temperature is observed, followed by a plateau. The wall temperature in this area seems to be almost constant in time due to high heat transfer rate (the temperature minimal value is very close to the vapor saturation temperature).

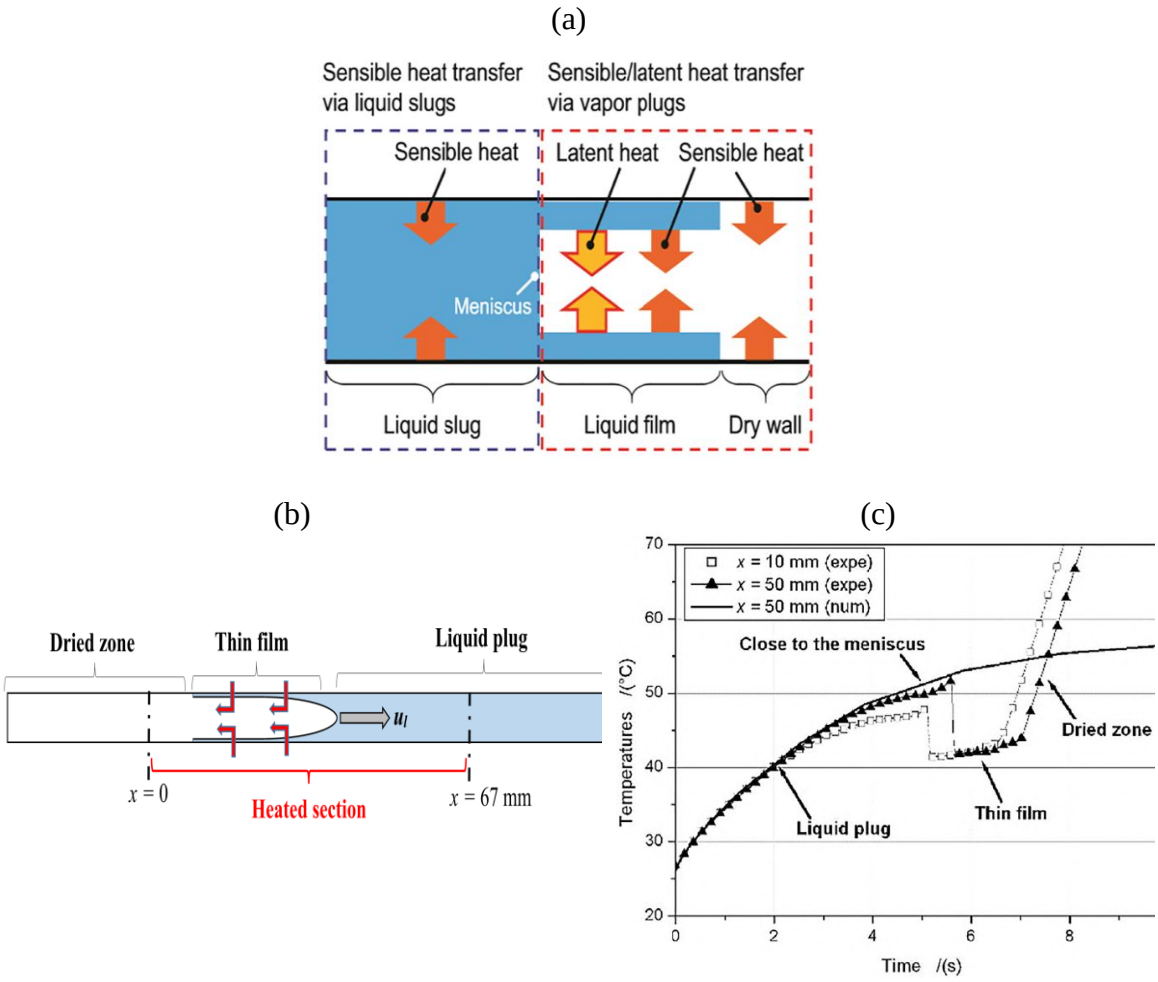


Figure 3.8. Sensible and latent heat transfer near meniscus region: (a) schema [3.17]; (b) evaporating thin film in heated copper tube and (c) infrared temperature profile [3.18].

The last zone corresponds to the sharp linear temperature increase ("dried zone") due to complete liquid film evaporation and sensible heat transfer with vapor. These results confirm the above-mentioned assertion that latent heat transfer via the liquid films accounts for a considerable portion of the total heat transfer rate a very high efficiency of pulsating heat pipes.

*3.2.3. Peculiarities of slug-plug flow in channels with rectangular shape*

Due to specific production methods, the flat plate pulsating heat pipes are most of the time manufactured with milled channel with sharp angles (rectangular, triangular, trapezoidal etc.). These sharp angles induce capillary pressure imbalance between the edges and the corners and, as follows, non-symmetrical cross-sectional fluid distribution. The capillary pressure gradient induces the liquid flow along the channel even in dry-out conditions or with non-moving bubbles (no liquid deposition on the walls). Such efficient self-induced transport mechanism of liquid by the capillary effect is naturally absent in circular tubes.

The schema of a bulk meniscus with thick capillary films in the corners and dried edges of a vertical square channel, during evaporation, is illustrated in Fig. 3.9. The experimental comparison on the self-induced evaporation of n-hexane in capillary channels with square and circular cross-section, open to stagnant ambient air, confirmed a tendency indicating that evaporation in a channel with corners can be several orders of magnitude faster than in a circular channel with the same dimensions. From other side, prediction of the liquid film length and thickness and following modelling of the heat transfer became a very complicated task.

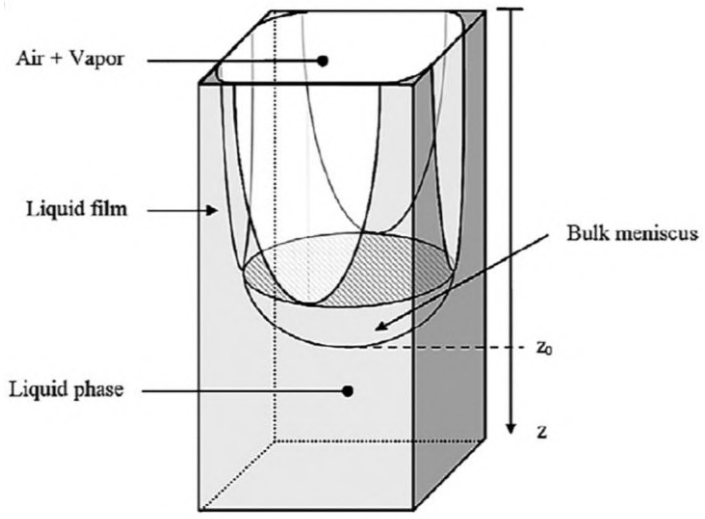


Figure 3.9. Liquid film distribution in a vertical rectangular square channel [3.19].

*3.2.4. Influence of orientation on the two-phase flow pattern inside FPPHP*

The observations of the hydraulic behavior inside flat plate pulsating heat pipes are still limited but enough for the qualitative comparison of the fluid flow regimes occuring in different device orientations.

In vertical position (bottom heated mode, BHM), different modes can be observed depending on the operating conditions. For example, with low filling ratios (below 20%), the device can operate like an interconnected looped thermosiphon [3.20]. In this mode, vapor rises through the center of the channel and the condensed liquid returns to evaporator in a form of liquid film falling along the corners. Same effect was observed also with heat load augmentation [3.5]. Such operation is a result of the channel shape (with sharp angles) and was not observed in previous studies with circular-shaped channels [3.21]. This trend was confirmed even for a filling ratios close to 50% and could be caused by capillary pressure inbalance in the channel corners [3.22, 3.23].

Sometimes, the annular flow was prevalent in the central and lateral channels and distributed along the whole length of the FPPHP, and the excess liquid was trapped in adjacent channels, without contributing in heat transfer (dotted yellow rectangles in Fig. 3.10a). Indicated by flashes waves, Fig. 7a shows some instabilities at the liquid/vapor interfaces caused by liquid-vapor counter flow. This phenomena became more obvious with channel diameter increase (related to the critical diameter).

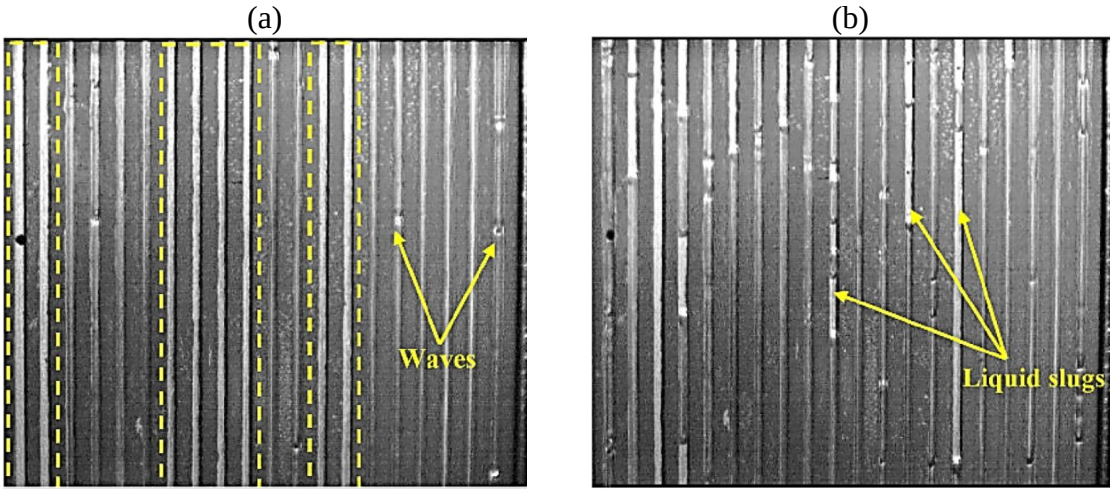


Figure 3.10. Visualization of the fluid flow in adiabatic section: (a) annular flow, Q = 40 W and (b) semi-annular flow, Q = 100 W (copper FPPHP, 2×2 mm$^2$, ethanol, FR = 50%, BHM) [3.22].

According to [3.20], higher filling ratios lead to the transition from thermosiphon mode to pulsating slug-plug flow regime. The same effect was observed for heat load increase – the flow pattern inside the FPPHP became a mix between classical thermosiphon annular (counter-current) flow in some channels and capillary slug-plug flow in others. In this case, liquid plugs are moving from the evaporator (Fig. 3.10b), with a random and rapid velocity [3.22]. This flow pattern change leads to the thermal characteristics improvement by the sensible heat contribution in overall heat transfer.

The flow pattern in horizontal position can be only slug-plug (if the internal diameter is small enough to prevent liquid stratification) due to absence of the gravity forces influence.

Despite the reported stable and efficient FPPHP operation in horizontal position [3.3], sometimes unstable operation and low thermal performance, caused by intermittently long-term stopover phenomena (momentary stops of flow oscillations) or even early dry-out of the evaporator, was observed during device operation, tested in horizontal orientation [3.21, 3.24, 3.25, 3.26]. The insufficient pressure perturbations from one channel to another can cause this operational stops.

Succesive photos of a FPPHP (8 turns, 2×2 $mm^2$, water) tested in horizontal position at 30 W of heat load are presented in Fig. 3.11 [3.24]. Oscillations occur only for short time periods and completely stopped at steady-state. Such operation can be explained by the thermally linked neighboring channels – thermal equilibrium in the neighboring channel leads to the driving pressure diminution, unlike tubular PHP with naturally separated channels.

In dried-out configuration, long liquid slugs are accumulated in the cold edge of the channels (condenser zone), forming U-shaped liquid columns of approximately the same length, as shown in Fig. 3.11c. Due to liquid accumulation on one end of the device, the channels in the evaporator zone are totally occupied by vapor exposed to dried wall without liquid film, resulting in vapor superheating. In this conditions heat transfer from evaporator to condenser are done mainly by conduction with relatively poor thermal performance compared to the normal operation. When the fluid starts to flow, both ends of a U-shape liquid column oscillate in opposite directions. If the amplitude of oscillations is sufficient, liquid flow into the evaporator and vapor flow into the condenser occur, completing the circulation cycle.

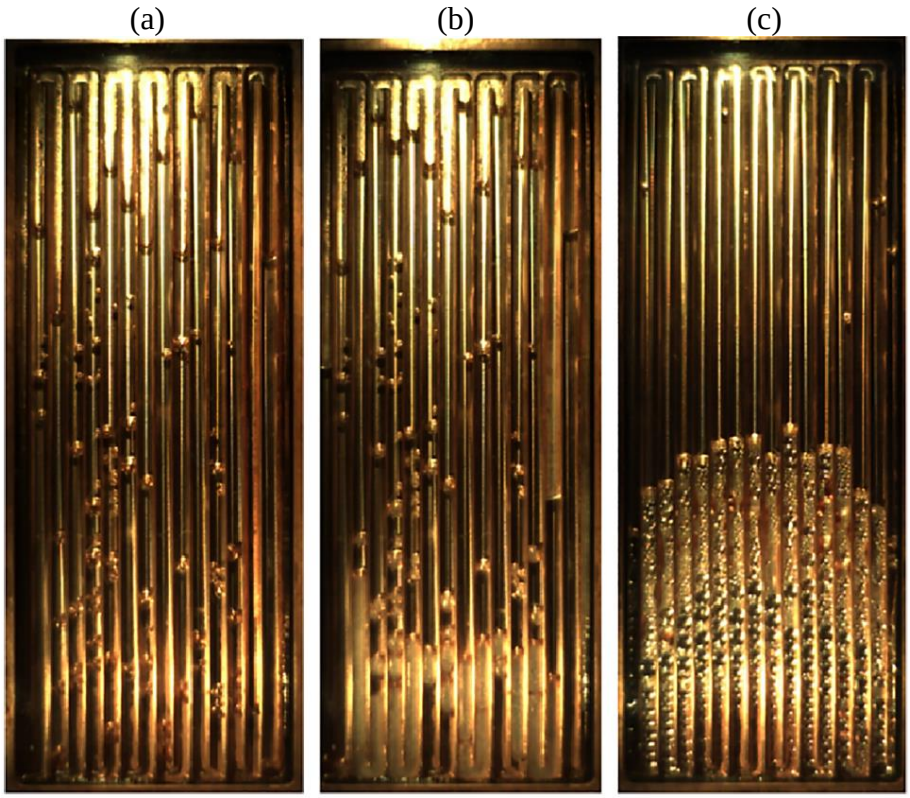


Figure 3.11. High speed visualization of the FPPHP operating in horizontal position (a) initial state; (b) after 1 min of heating; (c) steady-state operation (2×2 $mm^2$, Q = 30 W, water, FR = 70%) [3.24].

### 3.3. Conclusions

The fundamental operational principles of the pulsating heat pipes, as well peculiarities of the flat plate devices and their differences, and main influencing parameters, have been discussed in this chapter. Despite the fact that physical mechanisms of conventional (tubular) pulsating heat pipe operation are well known, particular and contradictory phenomena occur in flat plate devices due to the thermal link between channels and their specific shape (sharp angles presence leads to the liquid film distribution thanks to capillary pressure unbalance between corners and edges of the transverse cross section).

The operation of an oscillating heat pipe depends on a complex combination between different parameters, since they are all more or less coupled to each other. The current level of knowledge (especially on FPPHPs) does not yet allow to create an engineering recommendations to be used in industrial level or create an adequate modelling tool.

So, a review on the experimental and numerical studies, intended to shed light on the different parameters influencing the pulsating heat pipe operation, will be presented in the following section.

**References**

[3.1] Zhang D., He, Z. and Jiang E., 2021. A review on start-up characteristics of the pulsating heat pipe. Heat Mass Trans. 57, 723–735.

[3.2] https://www.brighton.ac.uk/advanced-engineering/research-projects/novel-hybrid-heat-pipe-for-space-and-ground-applications.aspx

[3.3] Ayel V., Slobodeniuk M., Bertossi R., Romestant C. and Bertin Y., 2021. Flat plate pulsating heat pipes: a review on the thermohydraulic principles, thermal performances and open issues. Appl. Thermal Eng. 197, 117200.

[3.4] Khandekar S., Panighahi P.-K., Lefevre F. and Bonjour J., 2010. Local hydrodynamic of flow in a Pulsating Heat Pipe: a review. Fr. Heat Pipes 1, 1–20.

[3.5] Khandekar S., 2004. Thermo hydrodynamics of closed loop pulsating heat pipes. PhD thesis, Stuttgart University.

[3.6] Khandekar S., Groll M., Charoensawan P. and Terdtoon P., 2002. Pulsating Heat Pipes: Thermo-fluidic Characteristics and Comparative Study with Single Phase Thermosyphon. Proc. 12th Int. Heat Trans. Conf., Grenoble, France.

[3.7] Marengo M., and Nikolayev V., 2018. Pulsating Heat Pipes: Experimental Analysis, Design and Applications. Encyclopedia Two-Phase Heat Transf. Flow IV, 1-62.

[3.8] Natsume K., Mito T., Yanagi N. and Tamura H., 2012. Development of cryogenic oscillating heat pipe as a new device for indirect/conduction cooled superconducting magnets. IEEE Transact. Appl. Superconduct. 22, 4703904.

[3.9] Mehendal S. S., Jacobi A. M. and Shah R. K., 2000. Fluid flow and heat transfer at micro- and meso-scales with application to heat exchanger design. Appl. Mech. Rev. 53, 175–193.

[3.10] Kandlikar S., 2002. Two-Phase Flow Patterns, Pressure Drop, and Heat Transfer during Boiling in Minichannel Flow Passages of Compact Evaporators. Heat Transf. Eng. 23, 5-23.

[3.11] Hosoda M., Nishio S. and Shirakashi R., 1990. Meandering Closed-Loop Heat Transport Tube (Propagation Phenomena of Vapor Plug). Proc 5th ASME/JSME Joint Th. Eng. Conf., New York, USA.

[3.12] Mameli M., Catarsi A., Mangini D., Pietrasanta L., Fioriti D., La Foresta M., Caporale L., Miche N., Marengo M., Di Marco P. and Filippeschi S., 2018. Large Diameter Pulsating Heat Pipe for Future Experiments on the International Space Station: Ground and Microgravity Thermal Response. Proc. 19th IHPC, Pisa, Italy.

[3.13] Gu J., Kawaji M. and Futamata R., 2004. Effects of Gravity on the Performance of Pulsating Heat Pipes. J. Thermophys. Heat Transf. 18, 370-378.

[3.14] Harichian T. and Garimella S., 2010. A comprehensive flow regime map for micro-channel flow boiling with quantitative transition criteria. Int. J. Heat Mass Transf. 53, 694-702.

[3.15] Nikolayev V. and Marengo M., 2018. Pulsating Heat Pipes: Basics of Functioning and Numerical Modeling. Encyclopedia. Two-Phase Heat Transfer Flow IV, 63-139.

[3.16] Jo J., Kim J. and Kim S.-J., 2019. Experimental investigations of heat transfer mechanisms of a Pulsating Heat Pipe. En. Conv. Manag. 181, 331–341.

[3.17] Kamijima C., Yoshimoto Y., Abe Y., Takagi S. and Kinefuchi I., 2020. Relating the thermal properties of a micro Pulsating Heat Pipe to the internal flow characteristics via experiments, image recognition of flow patterns and heat transfer simulation, Int. J. Heat Mass Tr. 163, 120415.

[3.18] Ayel V., Bertossi R., Mehta B., Chauris N., Romestant C. and Bertin Y., 2015. Evaporation of a thin liquid film in a heated capillary tube: experimental results and discussion on the related physical phenomena. IX Minsk Int. Sem. “Heat Pipes, Heat Pumps, Refrigerators, Power Sources”, Minsk, Belarus.

[3.19] Chauvet F., Cazin S., Duru P. and Prat M., 2010. Use of infrared thermography for the study of evaporation in a square capillary tube. Int. J. Heat Mass Transf. 53, 1808–1818.

[3.20] Yang H., Khandekar S. and Groll M., 2009. Performance characteristics of Pulsating Heat Pipes as integral thermal spreaders, Int. J. Th. Sc. 48 (2009) 815–824.

[3.21] Khandekar S., Schneider M., Schafer P., Kulenovic R. and Groll M., 2002. Thermofluiddynamic study of flat-plate cosed-loop Pulsating Heat Pipes. Microsc. Thermophys. Eng. 6, 303–317.

[3.22] Ayel V., Romestant C., Bertin Y., Manno V. and Filippeschi S., 2014. Visualization of flow patterns in flat plate Pulsating Heat Pipe: influence of hydraulic behavior on thermal performances. Heat Pipe Sc. Tech.: Int. J. 5, 377–384.

[3.23] Markal B. and Varol R., 2020. Thermal investigation and flow pattern analysis of a closed loop pulsating heat pipe with binary mixtures, J. Braz. Soc. Mech. Sc. Eng. 42, 1–18.

[3.24] Chien K.-H., Lin Y.-T., Chen Y.-R., Yang K.-S. and Wang C.-C., 2012. A novel design of pulsating heat pipe with fewer turns applicable to all orientations. Int. J. Heat Mass Tr. 55, 5722–5728.

[3.25] Jun S. and Kim S.-J., 2018. Experimental study on thermal characteristics of Pulsating Heat Pipes, Joint 19th IHPC / 13th IHPS, Pisa, Italy.

[3.26] Ayel V., Araneo L., Marzorati P., Romestant C., Bertin Y. and Marengo M., 2018. Visualization of Flow Patterns in Closed Loop Flat Plate Pulsating Heat Pipe Acting as Hybrid Thermosyphons under Various Gravity Levels. Heat Transf. Eng.

[3.27] Ayel V., Pietrasanta L., Lalizel G., Romestant C., Bertin Y. and Marengo M., 2019. Thermo-Hydraulic Analysis of Semi-Transparent Flat Plate Pulsating Heat Pipes Tested in 1 g and Microgravity Conditions. Microgravity Sci. Tech. 31, 403–415.

# Chapter 4

## Parameters Influencing on the PHP Thermal Performance

In previous chapter, the global mechanism of the PHP functioning was presented; influence of some geometrical parameters (channel shape/diameter; tubular/flat plate) and device orientation on flow and heat transfer behavior inside was discussed. Besides already discussed studies in last part, the influence of the fluid thermophysical, operating conditions and geometrical parameters on the pulsating heat pipe thermal transport characteristics is required. The comparison of the parameters influence on the thermal performances (based on the operational temperatures and thermal resistances) of tubular and flat plate pulsating heat pipes will be done in following chapter.

### 4.1. Channel diameter and shape

As previously mentioned, the internal diameter of the PHP directly influences the device operation due to the fluid distribution along channel, relating to the interfacial interaction with the PHP channel walls and gravity viscous effect. Fig. 4.1 presents a comparison of the thermal resistance of three PHPs with different channel diameters and with water and ethanol as working fluids (filling ratio FR = 50%) from [4.1]. It is clear that the thermal resistance decreases with increasing inner diameter for the water-charged PHPs (Fig. 4.1a). However, the opposite trend is shown by the ethanol-filled PHP (Fig. 4.1b): thermal resistance increasing with increase of the channel diameter. Authors [4.1] found similar results for the same PHPs, filled with other filling ratios and operated with different evaporator lengths.

However, not only channel diameter influences pulsating heat pipes operation, but also the channel shape does: it directly affects the menisci shape and fluid distribution around the vapor slug. Fig. 4.2a shows a unitary cell of two similar flat plate PHPs with the same channel diameters, but with different shapes (square or circular) and fluid distribution around the channels [4.2]. In the case of square channels, the liquid will tend to accumulate in the corners, giving rise to capillary action generated due to sharp angle corners, and the menisci

will recede if the filling ratio is lower. Unlike square channel, the liquid uniformly distributes along the perimeter of the circular channel. Moreover, the square channel has around 27% larger perimeter length than circular one, which means a larger wall-to-fluid heat exchange area.

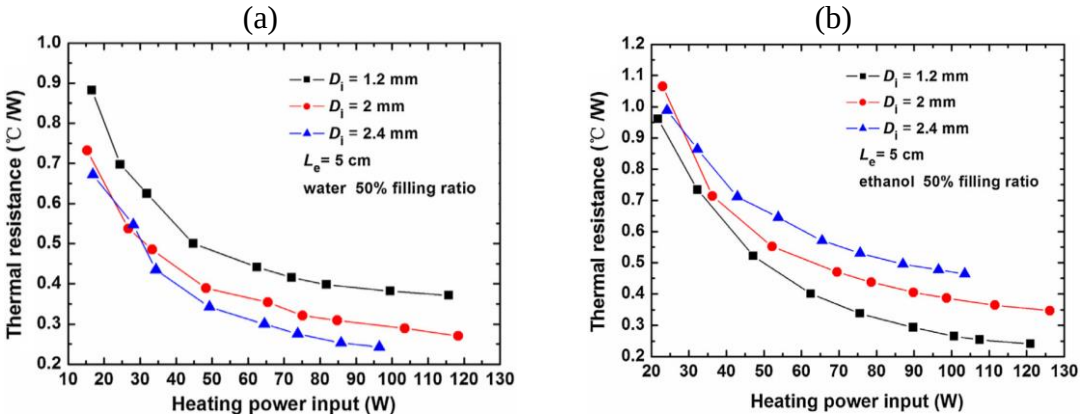


Figure 4.1. Effect of channel diameter on the PHP thermal performances for different working fluids: (a) water and (b) ethanol (FR = 50%, vertical BHM, $T_{cond}$ = 25 $^{o}$C) [4.1].

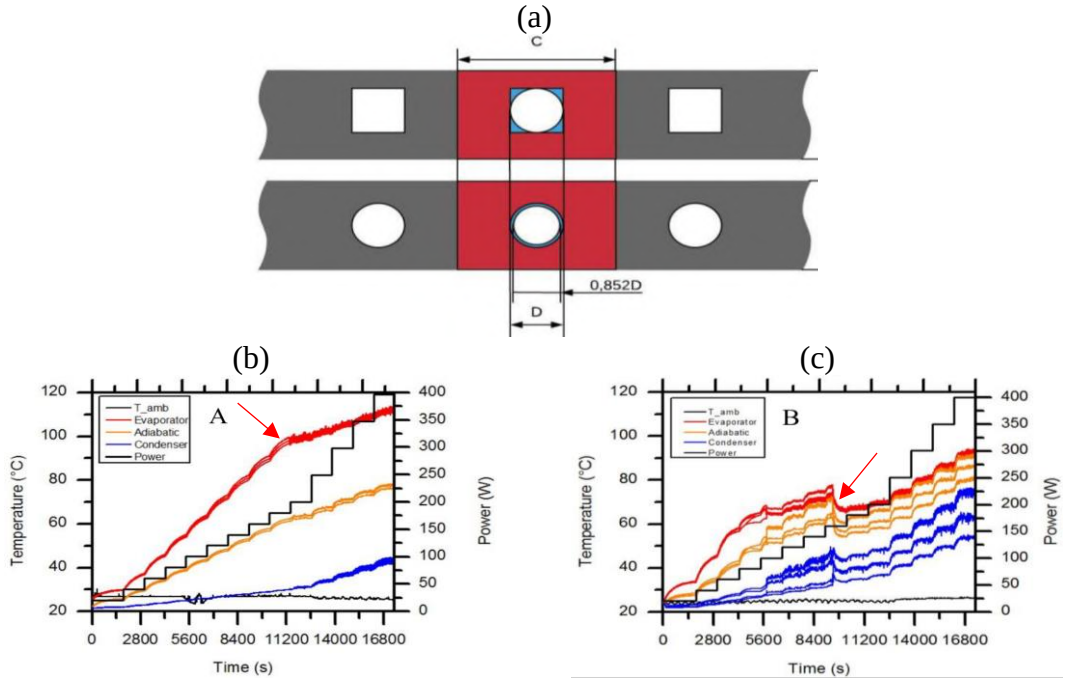


Figure 4.2. (a) Scheme of the fluid distribution inside squire and circular channels at FR=22%; temperatures histories at different heat power inputs for: (a) circular cross-section and (b) square cross-section (D = 3.18 mm, water, FR = 60%, vertical BHM, $T_{cond}$ = 20 $^{o}$C) [4.2].

Fig. 4.2b and 4.2c illustrate the temperatures behavior for both PHPs (circular and square cross-sections) as functions of time for different heat power input levels. The start-up (red flash in Fig. 4.2b) of the circular cross section PHP is observed since 200 W applied heat power; but, for the square cross section PHP, it happens earlier at 80 W applied power (red flash in Fig. 4.2c). A second activation was observed at 160 W, accompanied by the evaporator and adiabatic temperatures decrease, and condenser temperature increase. From this heating power level, the amplitude of the oscillations decreases. In addition, thermal resistances of PHP with circular channel are quite higher than thermal resistances for square channel PHP, starting from 80 W heat applied power (Fig. 4.3).

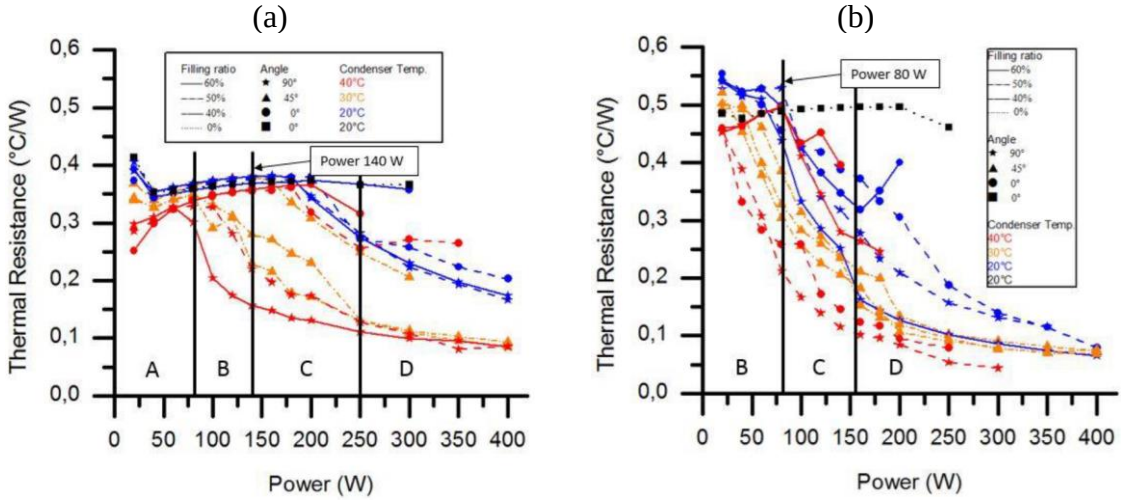


Figure 4.3. Thermal resistance for (a) circular and (b) square cross section PHPs (D = 3.18 mm, water, $T_{cond}$ = 20 $^{o}$C) [4.2].

## 4.2. Orientation

Due to the PHP's basic operational principles, device orientation is one of the most important parameters influencing the performance and operation stability. It is known that gravity assists the liquid reflow to the evaporator for device positioned in vertical or favorably inclined orientation with condenser located above the evaporator. However, in opposite orientation, with evaporator located above condenser, the gravity forces are directed away from the evaporator, which means that the driving pressure forces should be high enough to ensure the liquid flow. There is particular case on which the gravity almost not influences the fluid flow: *i/e* in horizontal orientation. In this position gravity force is directed perpendicular to the flow.

In order to understand the orientation influence on PHP operation, many studies have been done for PHPs tested with different geometrical parameters and different fluids. According to previous studies [4.3; 4.4; 4.5], the PHP operates with best thermal performance in vertical bottom heated mode (also called "favorable orientation"), but change of inclination angle does not influence significantly the device operation, until the horizontal position for which the heat transfer efficiency drastically decreases (Fig. 4.4).

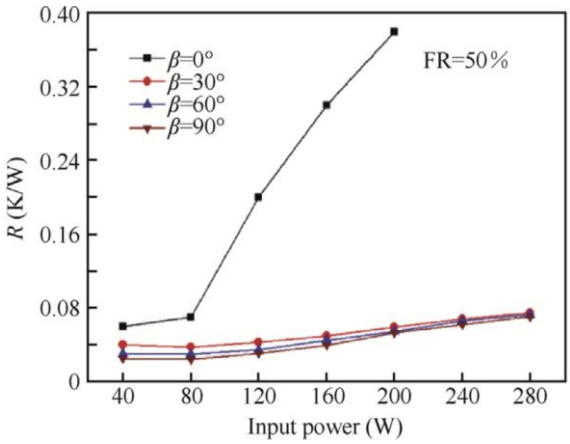


Figure 4.4. Effect of inclination angle on the PHP thermal resistance: (a) conventional PHP (D = 2 mm, ammonia, FR = 50%, $T_{cond}$ = 28 °C) [4.4].

### 4.3. Lengths of the PHP respective zones

There are not a lot of available literature on the influence of evaporator, condenser and adiabatic lengths on pulsating heat pipes thermal transport characteristics. However, the length of PHP does not affect just the working fluid amount, but also the fluid flow inside the tubes, and so heat transfer performances. On one hand, it is clear that the length of each section of the device (evaporation, adiabatic and condensation) affects pulsating heat pipe operation in their own way. For example, decreasing evaporator and condenser lengths leads to the local heat transfer efficiency diminution due to a lower heat transfer area. On the other hand, it is known that condensation heat transfer rate in pulsating heat pipes is lower than evaporation ones. Due to the wickless structure, PHP is not subjected to the entrainment limit, but the boiling limit might occur and manifest itself by an unacceptable overheating of the evaporator due to the lack of cooling working fluid, tending to an eventually dry-out. Thus, heat transfer area of the condenser needs to be high as much possible [4.6]. Concerning adiabatic zone, its length mostly influences the flow behavior inside the channel – the longer

the channel the higher flow resistance caused by viscous forces, which requires highest driving pressure to overcome the flow resistance.

Qu et al. [4.1] have tested closed loop pulsating heat pipe to find an optimal evaporator-to-condenser length rate. Fig. 4.5a shows the evolution of the thermal resistance of a pulsating heat pipe formed of a seven centimeters long condenser (over a total length of 22 cm) and filled with water and ethanol at FR = 50%. Evaporator lengths varies from 3 cm to 7 cm by step of 2 cm. Among all of the evaporator lengths, the largest thermal resistances of the PHP appears for the lowest 3 cm length, indicating that the over-short evaporator length makes the device work at a low efficiency. Thermal resistance curves clearly show the best performances of both PHP (filled with water and ethanol) for the 7 cm-length evaporator. Obtained results look very different from tests performed by Charoensawan and Terdtoon [4.7], where authors found that lowering the evaporator length improved thermal performances for all tested channel diameters, working fluids and filling ratios. This results can possibly be caused by the comparison of the evaporator length among PHPs with different total lengths, contrary to Qu's tests carried out with constant PHPs length.

(a) (b)

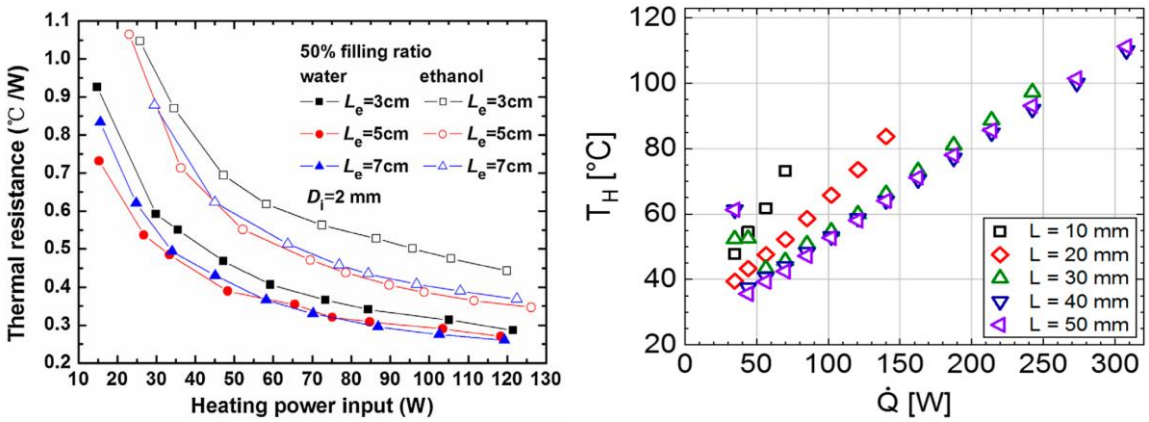


Figure 4.5. Influence of the (a) evaporator (FR = 50%, vertical BHM, $T_{cond}$ = 25 ºC) [4.1] and (b) condenser (1.5×1.5 mm$^2$, acetone, FR = 50%, horizontal, $T_{cond}$ = 20 ºC) [4.8] lengths on the PHP thermal performance.

Winkler et al. [4.8] evaluated influence of the condenser plate length on the PHP thermal behavior in the context of dry-out probability decreasing. As shown in Fig. 4.5b, increasing the condenser plate width delayed the occurrence of dry-out for PHP tested in horizontal position. Moreover, the larger condenser area leads to evaporator temperature decrease, probably due to higher condensation rate and closer to evaporator liquid formation.

The question that rises from these last two results is whether the increasing performances come from the increase of the evaporator length, the condenser length or from the decreasing adiabatic length.

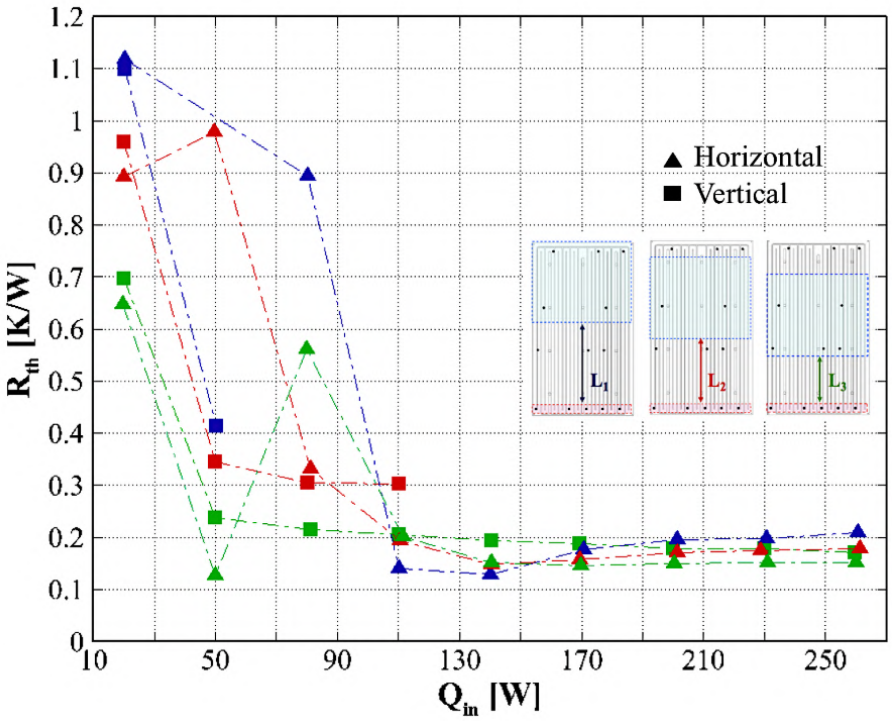


Figure 4.6. Adiabatic length influence on the PHP thermal resistance (1.6×1.7 mm$^2$, ethanol, FR = 50%, $T_{cond}$ = 20 ºC) [4.9].

To answer to such question, Pagnoni et al. [4.9] have studied the adiabatic section length influence on PHP operation. Authors changed adiabatic length making the condenser move into the evaporator direction (Fig. 4.6) and found that adiabatic length plays an important role on the PHP behavior and performances: thermal resistance decreases with decreasing adiabatic length. Moreover, with the minimal distance (green curves), thermal resistance is almost similar for horizontal and vertical positions – gravity does not seem to significantly affect thermal performances.

The influence of the length of each PHP section on its operation and heat transfer performance is obvious, but almost unstudied. The absence of relevant studies on this topic creates a huge interest for future works.

### 4.4. Number of turns

By default, pulsating heat pipe is a closed or coupled tube with several numbers of turns. Parallel channels quantity increase leads to the increase the PHP volume capacity and heat transfer area in evaporation and condensation zones. Moreover, thermal performances becomes almost independent from orientation with higher numbers of turns [4.10].

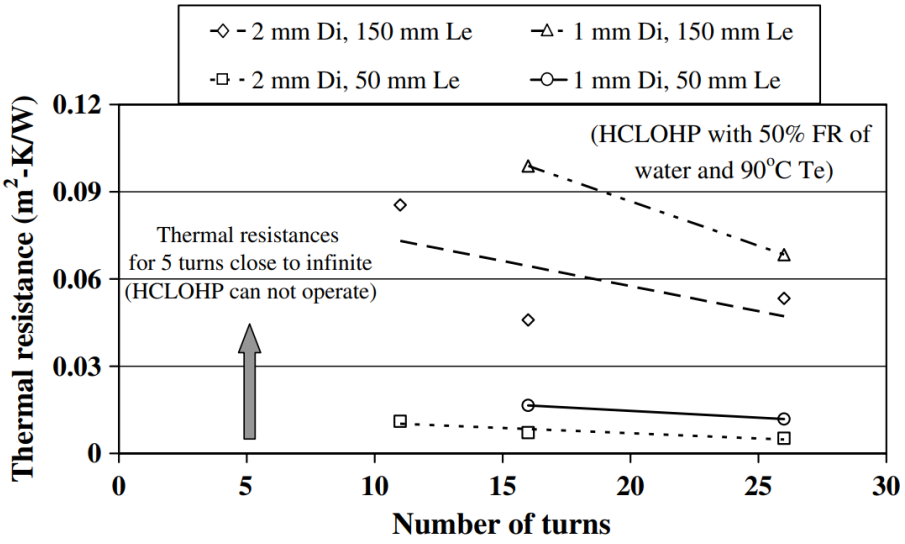


Figure 4.7. Influence of the number of turns on PHP performance (water, horizontal, $T_{cond}$ = 25 °C) [4.7].

Charoensawan and Terdtoon [4.7] tested PHPs with different channel diameters (1 mm and 2 mm) and evaporator lengths (50 mm and 150 mm), water with filling ratio of 50% was used as working fluid (Fig. 4.7). Tests have been performed for the PHPs with 5, 11, 16 and 26 turns. For a 50 mm long evaporator with number of turns up to 26, the thermal resistance slightly decreased. So, the thermal resistance significantly reduces as the number of turns increased and so heat performances are enhanced. However, the best performance of all PHPs was obtained for the maximum number of 26 turns, which enhances the fluid motion. On the opposite, operation failed for all tested PHPs with the smallest number of turns (5 turns).

### 4.5. Filling ratio

Since the pulsating heat pipe operation is based on the oscillatory movement of the liquid-vapor pairs (plugs and slugs), the necessary condition is to have enough liquid inside

the PHP that allows this two-phase distribution. The ratio between the volume of liquid phase, being inside the PHP, and the total inner volume of the channel is called "filling ratio" (FR). Considering the following two extreme cases: 0% and 100% of filling ratio, it becomes obvious that, in the first case (FR = 0), if there is no fluid inside PHP, the latter will operate in dry mode which means pure conduction heat transfer; but if PHP is filled with 100% of liquid, and knowing that the liquid is incompressible, there will be no place for bubbles formation, so the PHP operates in the single-phase thermosiphon mode. Thus, the filling ratio range from 10% to 90% is considered as a true range for the PHP operating as a pulsating device [4.11].

Despite numerous studies on the filling ratio influence, it remains impossible to clearly define the optimal value because the optimal filling ratio strongly depends on operating conditions, such as orientation, working fluid properties, distance between evaporator and condenser, their respective lengths, etc. Most of the time, a FR value close to 50% has been found by researchers, but with a variation in range depending on every operating conditions. At the same time, an optimal charge ratio exists for each PHP setup; for many typical experiments (circular cross-section in a planar array with less than 20 parallel channels), the optimum filling ratio has been found of around 40% [4.12].

Fig. 4.8 describes the effective thermal resistances of a PHP (1 mm diameter, 150 mm length, 20 turns) charged with ethanol (Fig. 4.8a, FR = 50, 70, 85%) and acetone (Fig. 4.8b, FR = 10, 35, 50, 70, 85%), and tested in vertical position (BHM). There are different lowest thermal resistances with different heat inputs and filling ratios. For the PHP charged with ethanol, the lowest thermal resistance at low heat load has been found for FR = 50% and the highest for FR = 85%; but for higher heat loads, PHP charged at FR = 70% has shown the best thermal performances. Similarly to the case with ethanol, PHP charged with acetone operates better at lower heat loads with filling ratio of 35% and presents worst thermal performances for FR = 85%. But at higher heat loads, the PHP has shown better performances at FR = 70%.

Yang et al. [4.13] evaluated filling ratio influence on the thermal performance of two PHPs (1 mm, and 2 mm, internal diameters) operated in vertical (BHM and THM), and horizontal orientations and filled with ethanol as working fluid (see Fig. 4.9a). For horizontal and vertical THM orientations, the optimum filling ratio was of about 50% – 65%. In vertical BHM position, the optimum filling ratio was of about 40-70%, and 15 % was found for

lower heat load, corresponding to a minimum thermal resistance. This is attributed to the gravity assisted thermosiphon mode of operation, *i.e.* the device does not act as a PHP in this situation, but as an interconnected array of closed two phase thermosiphons. However, with heat load increase, filling ratio has to be increased and the device starts to perform in self-excited thermally driven oscillating/pulsating mode. In this case, the maximum thermal performance is not very sensitive to FR in the range between 40% and 70%.

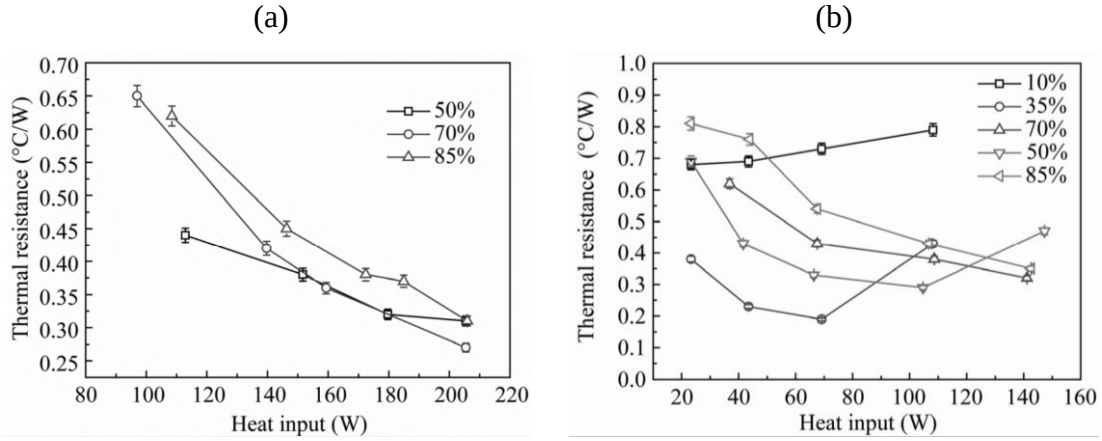


Figure 4.8. Thermal resistance for PHP tested in vertical position and filled at different ratios with (a) ethanol and (b) acetone (1×1 mm$^2$, BHM, $T_{cond}$ = 11 °C) [4.14].

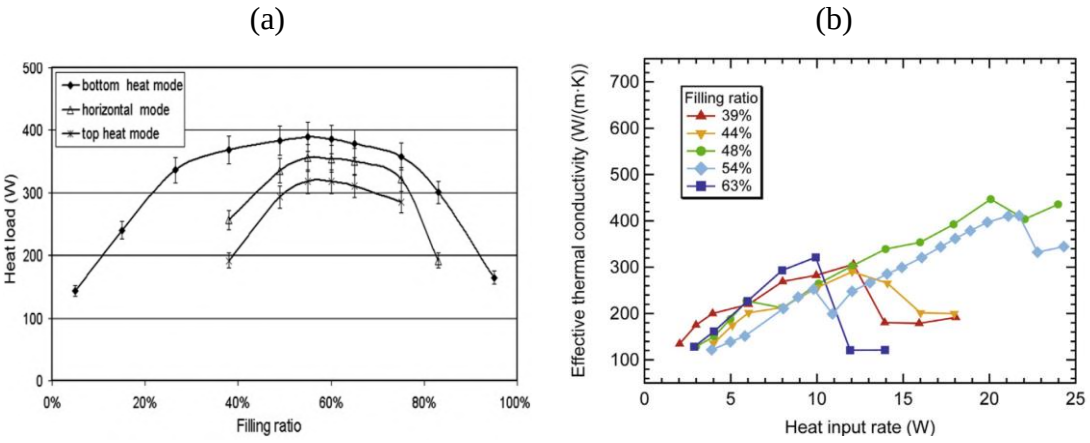


Figure 4.9. Influence of the filling ratio on the PHP thermal performance with (a) 2 mm (ethanol, $T_{cond}$ = 20 °C) [4.13] and (b) 0,35 mm (FC-72, BHM, $T_{cond}$ = 20 °C) [4.15] of internal diameters.

Finally, Kamijima et al. [4.15] evaluated the filling ratio influence on micro-FPPHP with channel internal diameter of 0.35 mm and filled with Fluorinert FC-72. For low heat input (up to 10 W), the thermal conductivity of micro-PHP increases with the filling ratio increase (Fig. 4.9b) but, the effective thermal conductivities for FR = 39%, 44%, and 63%

decrease when heat load exceeds 10 W, indicating the occurrence of the dry-out. The micro-FPPHP filled at FR = 48% and 54% can operate till almost 25 W with continuous effective thermal conductivity increase. The optimal FR in this case tends to increase the heat power range of operation.

However, filling ratio is also related to the liquid plugs and vapor plugs proportions: on one hand, with low filling ratios, the liquid plugs are shorter and wall friction force is smaller leading to easier oscillations. But continuous channel wall rewetting in the evaporator becomes more difficult and dry-out appears more frequently. On the other hand, high filling ratio leads to higher friction forces, that means the necessity in higher pressure difference between neighboring vapor slugs to drive the flow [4.16]. It can be concluded that the optimal filling ratio is the result between liquid and vapor plugs distribution and respective lengths in the device, depending on operating conditions.

### 4.6. Working fluid

First of all, the working fluid should correspond to all design, project and safety demands, *i.e.* satisfy the requirements related to the material – fluid compatibility, PHP channel diameter, working temperatures, pressure etc. But from the operational point of view, the fluid should have high value of the slope of vapor-liquid saturation line ($(dp/dT)_{sat}$) [4.17] to ensure stable liquid-vapor pairs oscillations inside PHP. Kearney et al. [4.18] tested PHPs filled with ethanol, Novec 649 and Novec 7200 (their liquid/vapor saturation slopes are shown in Fig. 4.10a in comparison with water). Based on the $(dp/dT)_{sat}$ values and experimental results, it seems that Novec 649 is the best working fluid (from the three tested) to ensure stable operation of PHP (Fig. 4.10b). To confirm this, the temperature differences between evaporator and condenser are presented in Fig. 4.10b for PHPs filled with ethanol and Novec 649 (FR=30%). It is clearly shown that, in horizontal inclination, the PHP filled with ethanol showed worse performance than with Novec 649; moreover, PHP filled with Novec 649 continued its operation till 0.8 $W.cm^{-2}$ of heat flux, while PHP filled with ethanol failed at 0.6 $W.cm^{-2}$. In vertical orientation, PHP filled with Novec 649 again showed better thermal performances than with ethanol.

Later, based on previous investigations and numerous assumptions, Kim and Kim. [4.19], proposed a figure of merit for the working fluid selection related to their micro FPPHP (80×35×1.7 $mm^3$, D=0.67 mm).

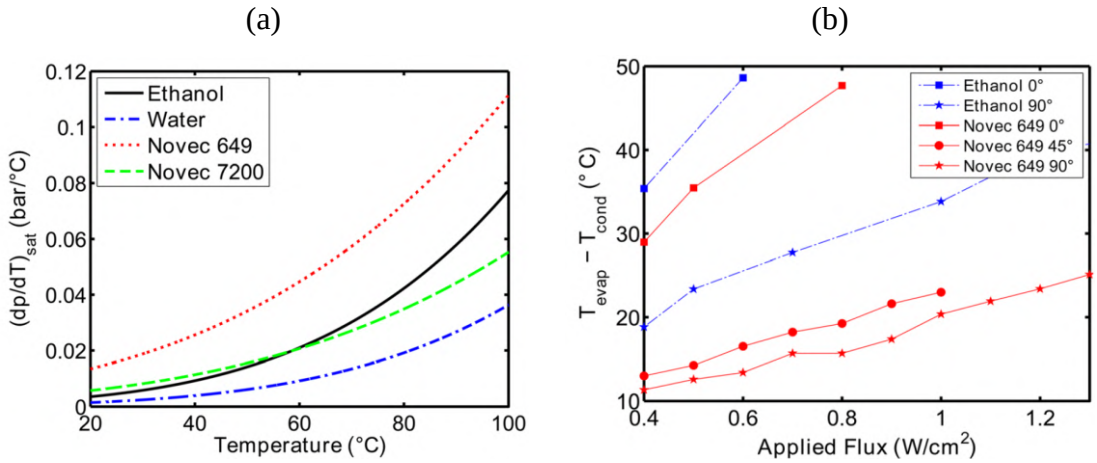


Figure 4.10. (a) $(dp/dT)_{sat}$ as function of temperature for various working fluids and (b) temperature difference between evaporator and condenser (1.55×1.9 mm$^2$,FC-72, FR = 30%, $T_{cond}$ = 18 $^o$C) [4.18].

Assuming that a thin liquid film surrounds each vapor bubble, vapor is in saturation state, and pressure can be expressed using the Clapeyron equation and the ideal gas law corrected with compressibility factor *Z*:

$$P_v = \left(\frac{\partial P}{\partial T}\right)_{sat} \frac{ZRT_{sat}^2}{h_{lv}} \tag{4.1}$$

Previously, it was noted that pressure difference between two vapor slugs surrounded a liquid plug ($P_r$ - $P_a$) is a main driver for oscillation motion in PHP. As the experimental time-average temperature difference between two vapor slugs is less than 2 °C [4.19], the terms of Eq. (4.1) can be assumed to be equal to the values corresponding to the average saturation temperature of the two vapor plugs and can be evaluated at $T_{sat} = (T_{sat,r} + T_{sat,a})/2$. Then, the driving pressure for the fluid motion (from Eq. (3.4)) can be simplified as follows:

$$\Delta P_v = (P_r - P_a) \approx 2\left(\frac{\partial P}{\partial T}\right)_{sat} \frac{ZRT_{sat}}{h_{lv}} (T_{sat,r} - T_{sat,a}) \tag{4.2}$$

Assuming that slug-plug motion in PHP is a fully developed laminar flow, the viscous friction of vapor is negligible and fluid velocity is related to the sensible heat transfer rate due to the motion of liquid slug ($u_l \approx Q_{sens}/\rho_l c_{pl} S(T_{ev} - T_{cond})$ where $Q_{sens}=\gamma_{sens}Q$ is experimentally obtained with sensible heat transfer rate, related to total heat transfer), the frictional pressure drop is determined as follows:

$$\Delta P_\tau = 32\mu_l \left(\frac{L_s}{D^2}\right) u_l \left(\frac{\gamma_{sens} Q}{\rho_l c_{pl} S(T_{ev} - T_{cond})}\right) \tag{4.3}$$

Since the figure of merit is proportional to the ratio of driving pressure $\Delta P_v$ on the frictional pressure drop $\Delta P_\tau$ (see Eq. (4.5)), the latter has to be calculated::

$$\frac{\Delta P_v}{\Delta P_\tau} = \frac{\left(\frac{\partial P}{\partial T}\right)_{sat} ZRT_{sat}(T_{sat,r}-T_{sat,a})}{16h_{lv}\mu_l\left(\frac{L_s}{D^2}\right)}\left(\frac{\rho_l c_{pl} S}{\gamma_{sens}}\right)\left(\frac{T_{ev}-T_{cond}}{Q}\right) \tag{4.4}$$

Based on the juxtaposition of curves for inversed pressure ratios and thermal resistance values (Fig. 4.11a), the figure of merit can be extracted from the pressure ratio. The thermal resistance of a PHP can be estimated by assuming that the driving pressure for the fluid motion (Eq. (4.2)) is the same with the frictional pressure drop of the liquid slug (Eq. (4.3)) as follows:

$$R_{th} = \left(\frac{T_{ev}-T_{cond}}{Q}\right) = \left[\frac{\rho_l c_{pl}\left(\frac{\partial P}{\partial T}\right)_{sat} ZRT_{sat}}{h_{lv}\mu_l}\right]^{-1}\left(\frac{16L_s\gamma_{sens}}{SD^2(T_{sat,r}-T_{sat,a})}\right) \tag{4.5}$$

where the first term of right-hand side combines all fluid thermophysical properties from the pressure ratio, while the second term corresponds to the residual term. The term inside the brackets representing the figure of merit:

$$M_{PHP} = \frac{\rho_l c_{pl}\left(\frac{\partial P}{\partial T}\right)_{sat} ZRT_{sat}}{h_{lv}\mu_l} \tag{4.6}$$

Variation of the proposed figure of merit as a function of operation temperature is presented in Fig. 4.11b for different working fluids. It qualitatively predicts the thermal performance of PHPs filled with different working fluids. Based on the graphics Fig. 4.11a-b, R-134a is the best working fluid, studied by Kim and Kim.

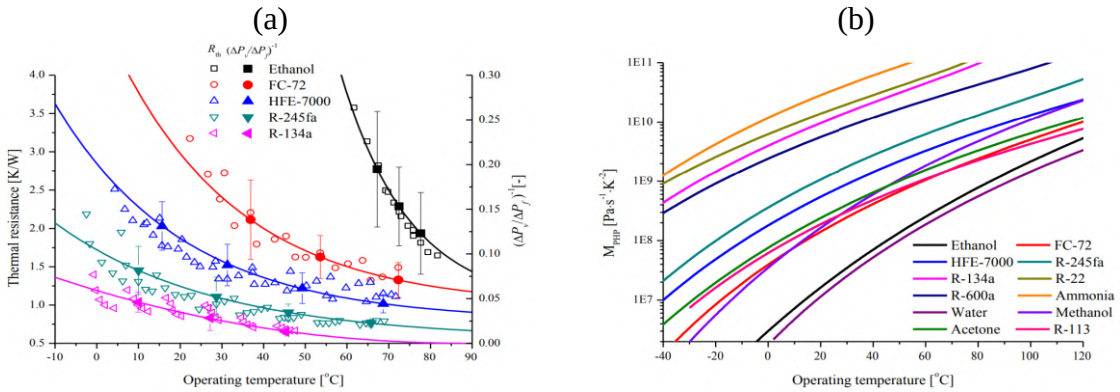


Figure 4.11. (a) Comparison of the thermal resistance of the MPHPs with the inverse of the pressure ratio (Eq. (4.4)) at various operating temperatures; and (b) change in the values of the proposed figure of merit (Eq. 4.6) for micro-FPPHP with operating temperature and working fluid (1×0.5 mm$^2$, FR = 50%, BHM) [4.19].

However, if analysis provided by authors is suitable for their PHP under tested parameters and has a good agreement with experimental results, the best thermal performance for larger pulsating heat pipes was obtained with water as a working fluid. Therefore, it can be concluded that the figure of merit can finally be proposed as an initial qualitative guideline for working fluid selection to be used in micro PHP. Anyway, validation of proposed approach needs much more approbations with different geometries.

### *4.6.1 Binary mixtures*

Passive heat transfer enhancement, based on fluid modification, is one of the more practical techniques thanks to its easily implementation and low cost. As mentioned above, the PHPs operation behavior and performance are greatly influenced by the working fluid properties. Some of them directly affect both flow behavior and thermal performances. However, it is possible to change the properties of the different fluids by mixing them in various volume ratios to improve the performances of PHPs. During the last decade, authors studied PHPs operation with classical binary mixtures in different proportions, as well water-acetone, water-ethanol, ethanol-acetone [4.20; 4.21; 4.16], and even immiscible water-HFE7100 mixtures [4.22] and pentane/heptane/methanol mixtures [4.23]. Authors reported the positive influence of some mixtures on their PHP start-up and dry-out delay. However, authors also concluded on the dominating importance of the filling ratio, mixing ratio and binary mixture type on the PHP operation. A more detailed information can be found in the review paper of Ayel et al. [4.24].

Results for a PHP with channel diameter of 2 mm tested with water, methanol, acetone and their mixtures, at FR = 50%, obtained by Pachghare and Mahalle [4.25], are presented in Fig. 4.12. It can be seen that the PHP filled with water-methanol mixture (Fig. 4.12a) gives better thermal performance than both pure working fluids, especially water. It is also clear that, during starting at low heat loads (from 10 W to 30 W), the thermal resistance of the pure working fluid drastically varies and, with heat load augmentation, the thermal resistance curves converge for all fluids. However, after 80 W of heat load, water-methanol binary mixture filled PHP dries out.

In the case of water-acetone mixture (Fig. 4.12b), the PHP presents lower thermal resistance than with pure water, but higher than with pure acetone. Heat load augmentation

does not provoke the dry-out at high heat fluxes. This configuration does not seem interesting in that it only leads to intermediate thermal performances between both pure fluids.

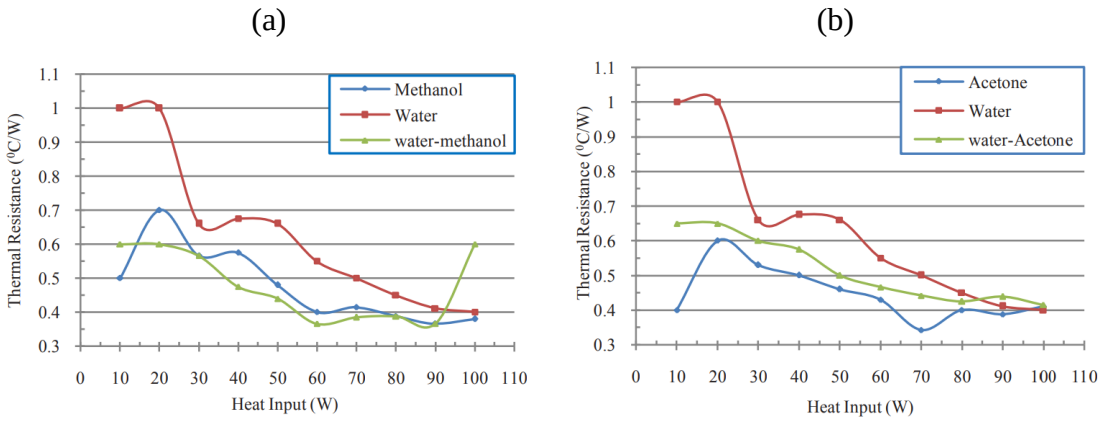


Figure 4.12. The binary mixture influence on the PHP performance: (a) methanol-water and (b) acetone-water mixtures (D = 2 mm, FR = 50%, BHM) [4.25].

*4.6.2. Self-Rewetting Fluids*

Heat transfer degradation of PHPs often happens due to partial or full dry-out of the evaporator zone, particularly when using water as working fluid: while very performing through its thermophysical properties, its bad wettability, compared to other fluids, generally plays a negative role on heat and mass transfer in such systems. In order to overcome this problem, binary aqueous mixtures, based on the addition of a low quantity of high-weight alcohols, also called Self-Rewetting Fluid (SRWF), could improve wettability and rewet the heat transfer surface. Abe et al. [4.26] measured the surface tension of alcohols and their aqueous mixtures and concluded that SRWFs surface tension decreases with increasing concentration and become more hydrophilic. Moreover, above a certain threshold temperature, the surface tension increases when temperature rises (Fig. 4.13): it would be conducive for the colder fluid moving spontaneously toward the heated side. Therefore, as shown in Fig. 3.16a, the self-rewetting fluid can flow from colder region towards the higher temperature one on the channel inner surface thanks to the Marangoni effect.

It is known that, in confined two-phase flows, the long vapor slugs are not always surrounded by liquid films, leading to the generation of a dry patch on the heated surface. But, with SRWF, this phenomenon can be prevented and the evaporation heat transfer can be improved in the PHP, as schematically shown in Fig. 4.14b. This phenomenon causes a

rapid increase in vapor pressure in the heating section due to high concentration of evaporated heavy alcohol within.

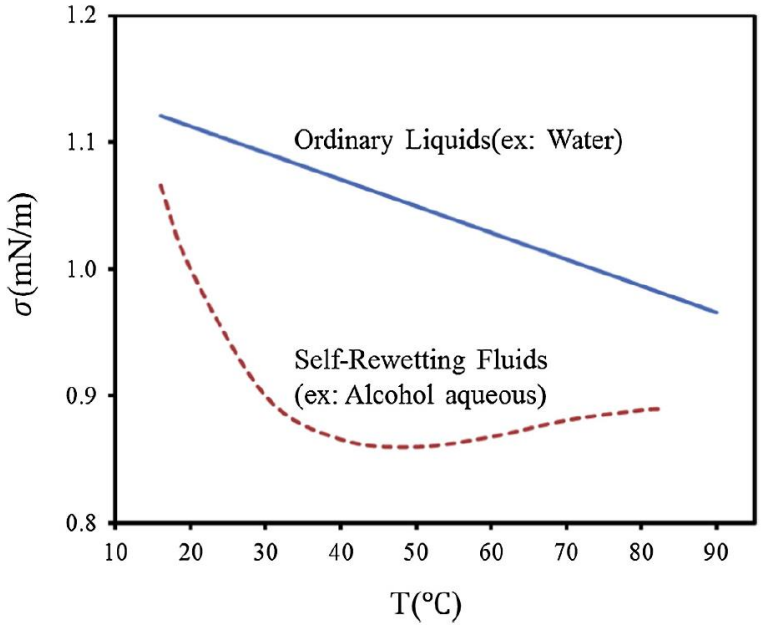


Figure 4.13. Definition of self-rewetting fluid [4.27].

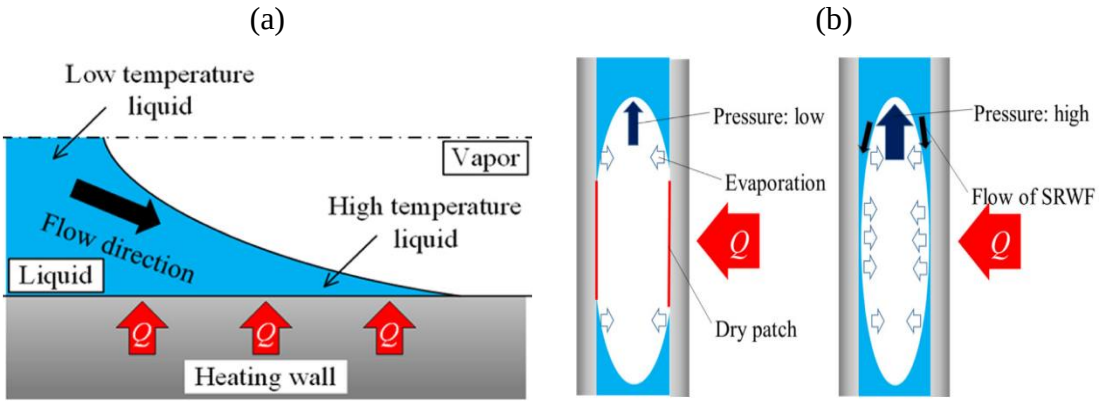


Figure 4.14. Behavior (a) and heat transfer enhancement mechanism (b) of the binary fluid [4.28].

Fumoto et al. [4.29] tested an aluminum flat plate pulsating heat pipe filled with butanol and pentanol water-based mixtures. Their experiments showed that the self-rewetting fluid generally improves the heat transfer characteristics of the PHP: the temperature difference between the heater and evaporator section of the pulsating heat pipe was reduced, resulting in lower thermal resistance of the device compared with the water-filled PHP.

Cecere et al. [4.30] compared the flow behavior inside copper flat plate pulsating heat pipe filled with water and water-butan-2-ol solution (SRWF). For the same operating

conditions, in the FPPHP filled with water, the channel walls surrounded by vapor slugs were dried (Fig. 4.15a). But, in the case of SRWF, the thin liquid film along the channel walls are clearly visible, as shown in Fig. 4.15b. Despite this, the thermal performance of the PHP tested in vertical BHM orientation and filled with SRWF was a little worse than with pure water.

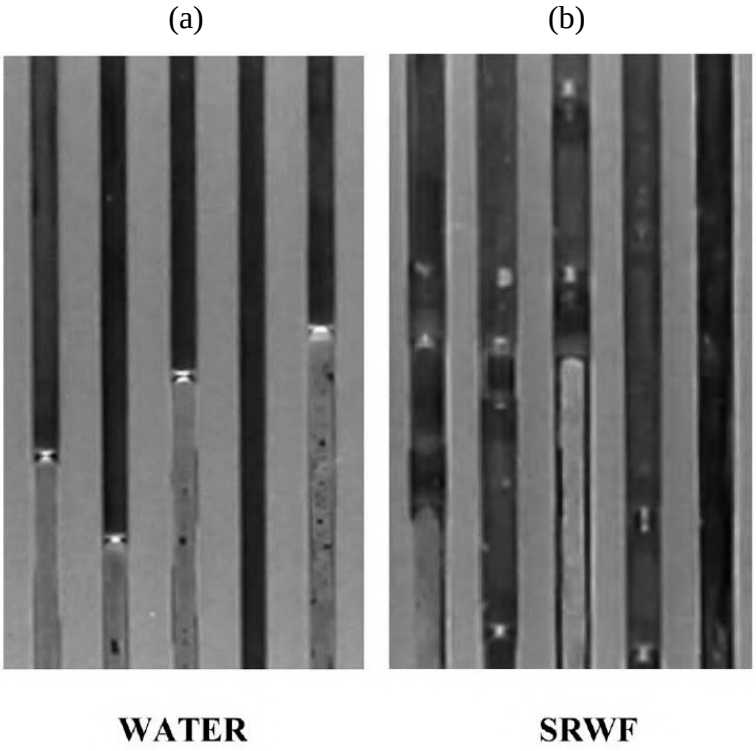


Figure 4.15. Flow regime inside flat plate pulsating heat pipe filled with water and 4%-butan-2-ol/water mixture (SRWF) [4.30].

On the other hand, under microgravity, the PHP filled with SRWF operated much better than with pure water: the maximum evaporator temperature rise during transient microgravity phases for SRWF-filled PHP was of around 11 K at 200 W of applied power, whereas but this temperature difference was of around 30 K for water. This happened due to stopover phenomena for water-filled PHP, during which all liquid phase was accumulated in the condenser section and the absence of gravity forces did not push the liquid phase towards the evaporator. Almost the same trends in thermal performance were obtained in [4.31]: in vertical BHM mode, PHP filled with water operated better than with butan-2-ol-water solution, especially for low heat loads. With heat load augmentation, the thermal resistances became almost equal. But, in horizontal orientation, the PHP filled with water and tested at 20 $^{o}$C of condenser temperature did not operate at heat loads higher than 100

W, and SRWF-filled device operated in all heat loads range (from 50 W to 200 W). Moreover, the thermal resistances for pure water were at least three times higher than for SRWF.

Based on this literature survey, an attempt will be made to clarify some questions, related to the different parameter influence on the flat plate pulsating heat pipe, especially in the microgravity conditions.

### *4.6.3. Surfactants*

The positive effect of the fluid modification has been described above, but zeotropic binary mixtures are characterized by significant changes in boiling temperatures and transport properties. So, it is almost impossible to selectively change specific properties like, for example, surface tension, which directly influences liquid/surface wettability – very important feature influencing boiling and evaporation heat transfer.

In pharmaceutic and cosmetic industries, particular substances, called “surfactants”, are widely used to stabilize creams, foams etc. and prevent fluids segregation by the interfacial tension reduction on the interface between two immiscible liquids.

Borrowing this approach, a very little rate of surfactant added to a working fluid can significantly decrease the total surface tension (Fig. 4.15a) and improve the channel walls wetting of the working fluid while keeping other thermophysical properties constant, as well density, saturation temperature, viscosity (Fig. 4.15b), latent heat of vaporization etc.

In literature, using of the surfactant aqueous solutions as working fluids generally lead to better PHP operation and also prevent from dry spots formation [4.32]. Wang et al. [4.33] used sodium stearate surfactant solutions with concentrations of 10, 20 and 40 ppm, and found that the thermal resistance values of the PHP with 40 ppm of surfactant has significantly been decreased compared to pure water. Bastakoti et al. [4.34] tested the PHP filled with cetyltrimethyl ammonium chloride (CTAC) surfactant solution and found a lower thermal resistance compared to the one obtained with pure water. Bao et al. [4.35] observed that the presence of surfactant had a positive effect on lower start-up, higher dry-out and heat fluxes compared to pure water. Should be noted that all these tests were done for the PHP operated in BHM.

(a) (b)

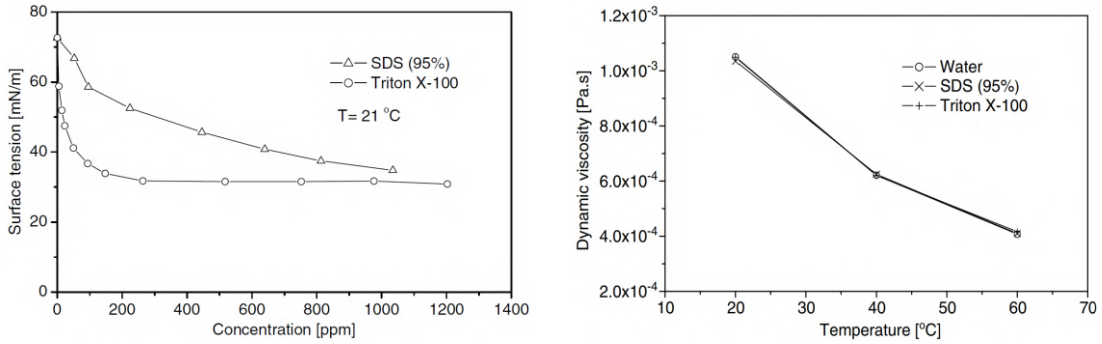


Figure 4.16. (a) Surfactant concentration influence on the measured equilibrium surface tension and (b) variation of the measured dynamic viscosity versus temperature [4.36].

Despite the positive influence of the surfactants on the PHP thermal performances, rare periods of foam generation inside the tube occur (Fig. 4.17a). The foam temporally blocks the channel, impedes the fluid circulation and decreases device performances. Later, bubbles present in the foam collapse into vapor bubbles, as shown in Fig. 4.17b [4.37].

(a) (b)

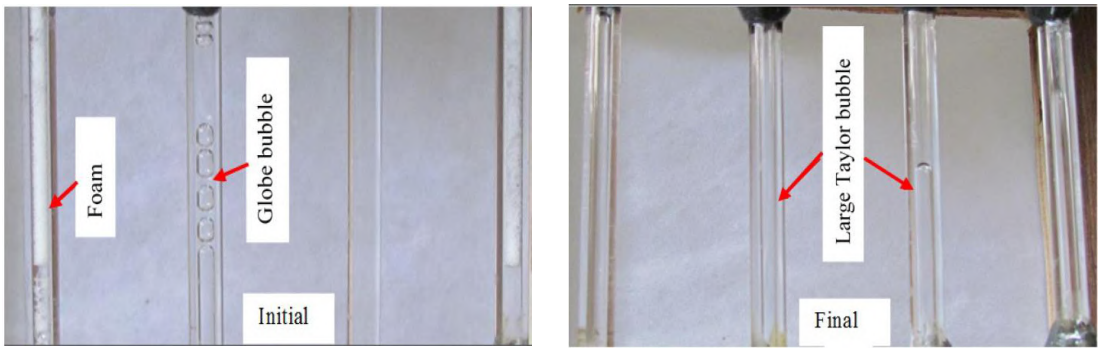


Figure 4.17. Bubble distribution inside transparent PHP filled with water – surfactant solution [4.37]

However, testing their device in horizontal orientation, Ayel et al. [4.38] found unstable PHP operation with water/Tween 20 and water/Tween 40 solutions: the device operated quite better than one filled with water, but often sudden and great evaporator temperature rises happened (up to 50 K higher than average operational temperature). The foam generation and temporary channel blockage can also explain this phenomenon.

### 4.7. Microgravity experiments on pulsating heat pipes

The gravity directly influences the two-phase fluid dynamics (during pool boiling, flow boiling and boiling in confined space) and, as a consequence, on the device thermal performance and, finally, makes existed prediction tools unusable for space applications [4.39]. Therefore, it is necessary to perform experiments directly in microgravity conditions.

As discussed in the Chapter 2, heat pipes with capillary structure are widely used in space applications since the second part of 20$^{th}$ century. Despite their proven operation, the thermal performance of conventional heat pipes is severely degraded in weightless environment [4.40] compared with ground conditions.

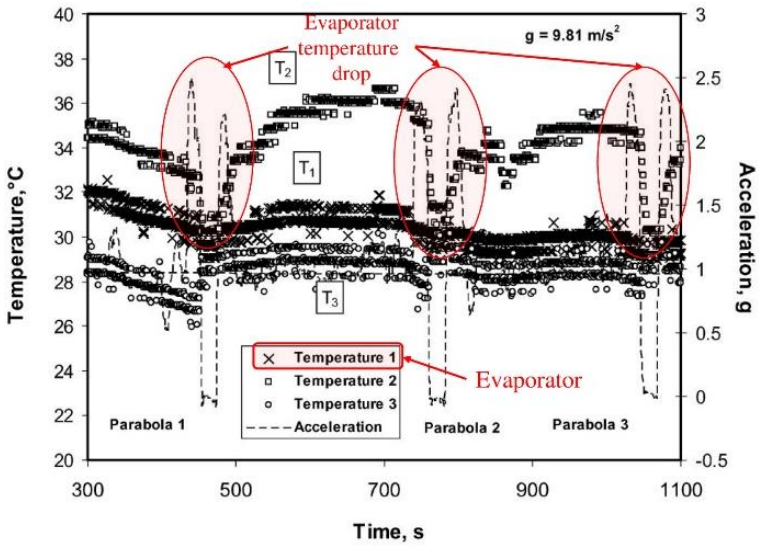


Figure 4.18. Temperature histories for FPPHP (1×1 mm$^2$, R-114, FR = 50-70%, $T_{cond}$ = 10 $^o$C) tested by Gu et al. [4.41].

First microgravity tests of pulsating heat pipes have been performed by Kawaji et al. [4.42; 4.41; 4.43] by conducting the experiments during parabolic flights trajectories. They have tested two similar aluminum flat plate pulsating heat pipes with inner channel, consisting of a single continuous channel with 1×1 mm$^2$ cross section, laid out in a serpentine with 48 turns at both ends. The heat pipes were charged with refrigerant R-114. These two PHP differed in the evaporation zone configuration: the first with evaporator placed in the center and condenser on the edge of device; and the second with evaporator and condenser located on the opposite sides of PHP. The authors found that the optimal PHP operation

performance occurred during microgravity conditions (Fig. 4.18) and concluded that the PHPs can operate satisfactory under long-term microgravity.

Later (during last decade), Mameli et al. [4.3] tested a PHP consisting in a copper tube (D = 1.1 mm) bent into a planar serpentine of 32 parallel channels. The dielectric fluid FC-72 was used as working fluid. The ground-based and parabolic flight tests were performed to validate the orientation and gravity influence on PHP operation. Orientation change from vertical to horizontal led to the evaporator temperature increase and its oscillation amplitude augmentation. Onset of the microgravity periods are characterized by the evaporator temperature increase until end of parabola (Fig. 4.19, left). End of parabola and gravity restoration led to the temperature drop, caused by the gravity assistance of the fluid flow.

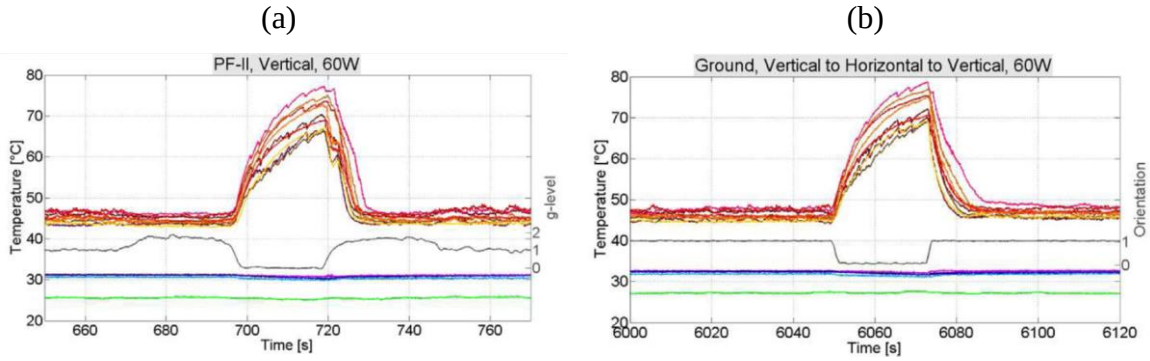


Figure 4.19. (a) Flight tests in vertical position compared with (b) ground dynamic tests (D = 1.1 mm, FC-72, FR = 50%, $T_{cond}$ = 30 °C) [4.3].

In addition, authors simulated the absence of the gravitational force influence on the fluid flow inside the PHP by the device rotation from vertical to horizontal position and from horizontal to vertical with time interval of 20 seconds (duration of one parabola). Resulting these operations, temperature behavior for microgravity looks very similar to the ground-based one.

In the work of Mangini et al. [4.44], authors tested an aluminum tubular pulsating heat pipe (D = 3 mm) consisting in a planar serpentine with five turns at the evaporator zone. The device was also filled with FC-72 (50% of filling ratio). On ground, in vertical position, the PHP operates like a closed loop two-phase multi-evaporator thermosyphon (*i.e.* with internal diameter higher than critical one for FC-72 (at temperature range 20 – 80 °C), calculated thanks to Bond number). Tests in horizontal orientation showed that the device works as a pure conductive medium: no fluid motion was observed. On the other hand, parabolic flight

tests reveal that the device operated in a complete different mode during microgravity phases: the images recorded in the condenser zone, together with the pressure signal, showed a transition from thermosyphon mode to slug flow pattern. In some cases the hyper-gravity period led to the elimination of partial dry-outs restoring the correct operation until the occurrence of the next microgravity period.

Recently, Mameli et al. [4.45] designed a closed loop pulsating heat pipe with 3D configuration for tests to be performed onboard of International Space Station. This PHP consists in annealed aluminum tube (D = 3 mm) bent in 14 U-turns in the evaporation zone and filled with FC-72 at filling ratio of 50%. Authors performed microgravity tests (parabolic flights) to characterize PHP operation and demonstrated the ability of the device to operate satisfactorily in space. Firstly, absence of stop-over periods during microgravity phases have been found, contrary to previous experiments conducted for PHP with lower number of turns [4.44]. After, authors proposed to use wavelet analysis of the pressure signals for flow velocity prediction [4.46]. This is an important step towards the characterization of PHP behavior and towards the validation of analytical and numerical PHP models. Moreover, in some cases, developed method could eliminate the necessity in visualization and relating equipment.

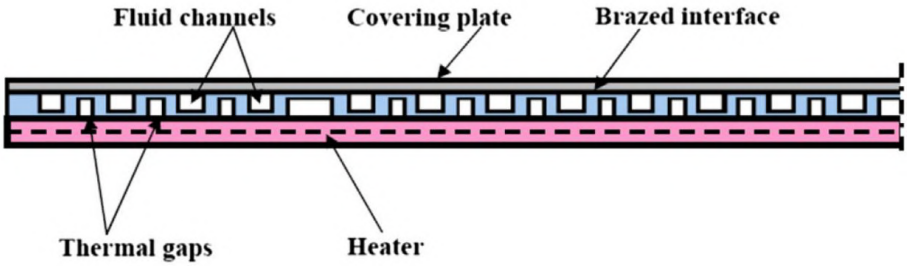


Figure 4.20. Cross-sectional view of the PHP with separating grooves [4.5].

In parallel to researches form previous authors on tubular pulsating heat pipes tested under microgravity conditions, Ayel et al. [4.5] performed an experimental campaign for a flat plate pulsating heat pipe onboard Novespace Zero-G aircraft. This FPPHP consisted a copper plate (200×120×2 $mm^3$) in which a rectangular serpentine groove (1.6×1.7 $mm^2$) is milled, forming 12 U-turns in the evaporation zone (24 parallel channels). To form the closed channel, milled plate was covered with a second thin copper plate. Separating grooves were engraved on the backside of the FPPHP ("thermal gaps") to minimize transverse conduction between adjacent channels (Fig. 4.20).

This PHP have been tested during ESA 62nd parabolic flight campaign with FC-72 (FR = 50%) in two initial positions: vertical and horizontal. During normal gravity periods, PHP operation corresponding to ground conditions and transition to microgravity allowed to find the operational difference.

(a) (b)

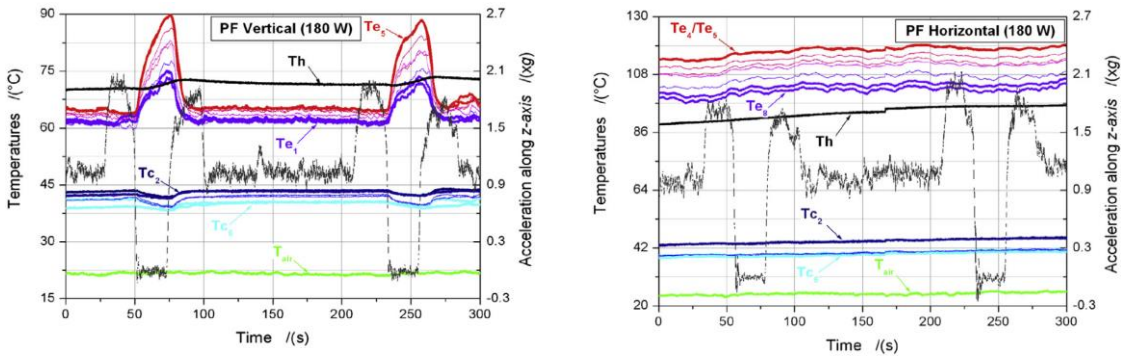


Figure 4.21. Transient temperatures response of the FPPHP subjected to the two successive parabolic trajectories: (a) vertical and (b) horizontal orientations (1.6×1.7mm, FC-72, FR = 50%) [4.5].

As shown in Fig. 4.21, during normal gravity, the FPPHP works more efficiently in vertical orientation than in horizontal. The thermal behavior of the pulsating heat pipe tested in vertical orientation is greatly influenced by the change of gravity levels, due to distinct thermal performances markedly varying from one case to the other. The occurrence of annular flow patterns in vertical BHM is (most) probably the cause of such behaviour, compared to slug flow pattern in horizontal orientation or under microgravity conditions. Note that, on Fig. 4.21b, the FPPHP tested in horizontal inclination doesn't seem to be influenced by changes of gravity levels, proving that such a system can be an efficient candidate for thermal control in different space applications.

The influence of the channel diameter on the thermal behavior and fluid flow inside flat plate pulsating heat pipes have been studied for four semi-transparent devices by Ayel et al. [4.47; 4.48; 4.49] during ESA 64th PFC. Each tested FPPHP was made of copper plate with engraved square channels with diameters range from 1.5 to 3 mm, and 11 U-turns in the evaporator zone. A borosilicate glass was glued on the grooved side of the copper plate to allow visualizations. The refrigerant FC-72 was used as working fluid (FR = 50%). Initially, FPPHPs were installed in vertical position (BHM). During normal gravity periods, the FPPHP with highest channel diameter showed the best thermal performance. Microgravity

onset led to the flow regime change into slug-plug for all channel diameters. Dry-out periods were observed with following overall fluid motion reactivations phases. PHPs with 2.5 mm and 3 mm channel diameters showed almost the same thermal performance, but PHPs with lower diameters operated with less efficiency.

Recently, Ando et al. [4.50; 4.51] performed on-orbit tests of a flat plate pulsating heat pipe with check valves and filled with HFC-134a at filling ratio of 45%. They found successful operation of their PHP with heat transfer performance matching to preliminary ground tests. No failure or performance degradation were observed for almost four years of operation. However, some start-up difficulties were seen under certain initial conditions. Further analysis indicated that there is a risk of start-up with most check valves positioned close to the evaporation zone. However, if all check valves are located near the condenser section, liquid slugs could be supplied to the evaporator section even if the liquid was localized in the condenser section, and the start-up is successful. Later, Taft and Irick [4.52] showed stable operation of their PHP filled with butane during six weeks of space flight.

## 4.8. Conclusions

Review of the basic research studies on pulsating heat pipes operation under different conditions, i.e. geometrical parameters, orientations, working fluids, and gravity, concerning the device thermal behavior has been done in present chapter. Currently, pulsating heat pipes are considered as a very promising thermal management technology. Since first device introduction by Akachi [4.10], numerous experimental and theoretical studies have focused on the influence of different parameters on pulsating heat pipe operation and performance: channel shape and diameter, number of turns, device orientation, filling ratio, working fluid thermophysical properties and even microgravity. Some authors focused on the fluid motion inside the PHP to better understand the physics of the liquid-vapor pair motions.

Nevertheless, the influence of many other parameters is still not clear or sometimes contradictory. Numerous studies on space applications of pulsating heat pipes have been done, but still with no any precise design recommendation.

Based on this literature survey, an attempt will be made to clarify some questions, related to the different parameters influence on the flat plate pulsating heat pipe, especially operating under microgravity conditions.

**References**

[4.1] Qu J. and Wang Q., 2013. Experimental study on the thermal performance of vertical closed-loop oscillating heat pipes and correlation modeling. Appl. Energy 112, 1154-1160.

[4.2] Facin A., Betancur L., Mantelli M., Florez J-P. and Coutinho B-H., 2018. Influence of channel geometry on diffusion bonded flat plate Pulsating Heat Pipes. Joint 19th IHPC and 13th IHPS, Pisa, Italy.

[4.3] Mameli M., Araneo L., Filippeschi S., Marelli L., Testa R. and Marengo, M., 2014. Thermal response of a closed loop pulsating heat pipe under a varying gravity force. Int. J. Thermal Sci. 80, 11-22.

[4.4] Zhihu X. and Wei Q., 2014. Experimental study on effect of inclination angles to ammonia pulsating heat pipe. Chin. J. Aeronautics 27, 1122-1127.

[4.5] Ayel V., Araneo L., Scalambra A., Mameli M., Romestant C., Piteau A., Marengo M., Filippeschi S. and Bertin Y., 2015. Experimental study of a closed loop flat plate pulsating heat pipe under a varying gravity force. Int. J. Thermal Sci. 96, 23–34.

[4.6] Bastakoti D., Zhang H., Li D., Cai W. and Li F., 2018. An overview on the developing trend of pulsating heat pipe and its performance. Appl. Thermal Eng. 141, 305–332.

[4.7] Charoensawan P. and Terdtoon P., 2008. Thermal performance of horizontal closed-loop oscillating heat pipes. Appl. Therm. Eng. 28, 460-466.

[4.8] Winkler M., Rapp D., Mahlke A., Zunftmeister F., Vergez M., Wischerho E., Clade J., Bartholomé K. and Schäfer-Welsen O., 2020. Small-Sized Pulsating Heat Pipes/Oscillating Heat Pipes with Low Thermal Resistance and High Heat Transport Capability. Energies 13, 1736.

[4.9] Pagnoni F., Ayel V., Romestant C. and Bertin Y., 2018. Experimental Behaviors of Closed Loop Flat Plate Pulsating Heat Pipes: a Parametric Study. Joint 19th IHPC and 13th IHPS, Pisa, Italy.

[4.10] Akachi P. and Polasek F., 1996. Pulsating heat pipes. Proc 5th Int. Heat Pipe Symp., 208–217.

[4.11] Khandekar S., Schneider M., Schafer P., Kulenovic R. and Groll M., 2002. Thermofluiddynamic study of flat-plate cosed-loop Pulsating Heat Pipes. Microsc. Thermophys. Eng. 6, 303–317.

[4.12] Zhang Y. and Faghri A., 2008. Advances and Unsolved Issues in Pulsating Heat Pipes. Heat Transf. Eng. 29, 20–44.

[4.13] Yang H., Khandekar S. and Groll M., 2009. Performance characteristics of Pulsating Heat Pipes as integral thermal spreaders, Int. J. Th. Sc. 48 (2009) 815–824.

[4.14] Shi W. and Pan L., 2017. Influence of Filling Ratio and Working Fluid Thermal Properties on Starting up and Heat Transferring Performance of Closed Loop Plate Oscillating Heat Pipe with Parallel Channels. J. Therm. Sci. 26, 73-81.

[4.15] Kamijima C., Yoshimoto Y., Abe Y., Takagi S. and Kinefuchi I., 2020. Relating the thermal properties of a micro Pulsating Heat Pipe to the internal flow characteristics via experiments, image recognition of flow patterns and heat transfer simulation, Int. J. Heat Mass Tr. 163, 120415.

[4.16] Han X., Wang X., Zheng H., Xu X. and Chen G., 2016. Review of the development of pulsating heat pipe for heat dissipation. Renew. Sustain. Energy Rev. 59, 692–709.

[4.17] Khandekar S., Groll M., Charoensawan P. and Terdtoon P., 2002. Pulsating Heat Pipes: Thermo-fluidic Characteristics and Comparative Study with Single Phase Thermosyphon. Proc. 12th Int. Heat Trans. Conf., Grenoble, France.

[4.18] Kearney D. and Griffin J., 2014. An Open Loop Pulsating Heat Pipe for Integrated Electronic Cooling Applications. J. Heat Transf. 136, 081401.

[4.19] Kim J. and Kim S. J., 2020. Experimental investigation on working fluid selection in a micro pulsating heat pipe. Energy Conv. Management 205, 112462.

[4.20] Zhu Y., Cui X., Han H. and Sun S., 2014. The study on the difference of the start-up and heat-transfer performance of the pulsating heat pipe with water-acetone mixtures. Int. J. Heat Mass Transf. 77, 834–842.

[4.21] Caihang L., Zhuang H., Yongwang Y. amd Si Z., 2015. Experimental study on thermal performance of pulsating heat pipe with ethanol-acetone mixtures. Int. J. Heat Tech. 33, 185–190.

[4.22] Xu R., Zhang C., Chen H., Wu Q. and Wang R., 2019. Heat transfer performance of pulsating heat pipe with zeotropic immiscible binary mixtures. Int. J. Heat Mass Transf. 137, 31–41.

[4.23] Markal B. and Varol R., 2020. Thermal investigation and flow pattern analysis of a closed loop pulsating heat pipe with binary mixtures, J. Braz. Soc. Mech. Sc. Eng. 42, 1–18.

[4.24] Ayel V., Slobodeniuk M., Bertossi R., Romestant C. and Bertin Y., 2021. Flat plate pulsating heat pipes: a review on the thermohydraulic principles, thermal performances and open issues. Appl. Thermal Eng. 197, 117200.

[4.25] Pachghare P. R. and Mahalle A. M., 2013. Effect of pure and binary fluids on closed loop pulsating heat pipe thermal performance. Proc. Eng. 51, 624 – 629.

[4.26] Abe Y., Iwaski A. and Tanaka T., Thermal management with self-rewetting fluids. Microgravity Sci. Tech. 16, 148–152.

[4.27] Wu S., Lee T., Lin W. and Chen Y., 2017. Study of self-rewetting fluid applied to loop heat pipe with PTFE wick. Appl. Therm. Eng.119, 622–628.

[4.28] Fumoto K., Sasa M., Okabe T., Savino R., Inamura T. and Shirota M., 2019. Research on heat transfer performance of the open-loop micro pulsating heat pipe with self-rewetting fluids. Microgravity Sci. Tech. 31, 261-268.

[4.29] Fumoto K., Kawaji M. and Kawanami T., 2010. Study on a pulsating heat pipe with self-rewetting fluid. J. El. Pack. 132, 031005.

[4.30] Cecere A., De Cristofaro D., Savino R., Ayel V., Sole-Agostinelli T., Marengo M., Romestant C. and Bertin Y., 2018. Experimental analysis of a flat plate pulsating heat pipe with self-rewetting fluids during a parabolic flight campaign. Acta Astronautica 147, 454-461.

[4.31] Slobodeniuk M., Martineau F., Ayel V., Bertossi R., Romestant C. and Bertin Y., 2020. Thermal performance of flat plate Pulsating Heat Pipe using aqueous alcohol solutions. 28th Fr. Therm. Eng. Conf., Belfort, France.

[4.32] Semenov A. A., Peschenyuk Y. A. and Vozhakov I. S., 2021. Application of Aqueous Solutions of Surfactants in Pulsating Heat Pipe. J. Eng. Thermophys. 30, 58-63.

[4.33] Wang X.H., Zheng H.C., Si M.Q., Han X.H. and Chen G.M., 2015. Experimental investigation of the influence of surfactant on the heat transfer performance of pulsating heat pipe. Int. J. Heat Mass Transf. 83, 586–590.

[4.34] Bastakoti D., Zhang H., Cai W., Li F., 2018. An experimental investigation of thermal performance of pulsating heat pipe with alcohols and surfactant solutions. Int. J. Heat Mass Transf.117, 1032–1040.

[4.35] Bao K., Wang X., Fang Y., Ji X., Han X. and Chen G., 2020. Effects of the surfactant solution on the performance of the pulsating heat pipe. Appl. Therm. Eng. 178, 115678.

[4.36] Cheng L., Mewes D. and Luke A., 2007. Boiling phenomena with surfactants and polymeric additives: A state-of-the-art review. Int. J. Heat Mass Transf. 50, 2744–2771.

[4.37] Kumar M., Kant R., Das A. K. and Das P., 2015. Effect of surface tension of the working fluid on the performance of a closed loop pulsating heat pipe. Proc. 23rd N. Heat Mass Transf. Conf. 1st Int. ISHMT-ASTFE Heat Mass Transf. Conf., Thiruvananthapuram, India.

[4.38] Ayel V., Slobodeniuk M., Bertossi R., Karmakar A., Martineau F., Romestant C., Bertin Y. and Khandekar S., 2021. Thermal performances of a Flat-Plate Pulsating Heat Pipe tested with water, aqueous mixtures and surfactants. Int. J. Therm. Sci.

[4.39] Narcy M. and Colin C., 2015. Two-Phase Pipe Flow in Microgravity with and without Phase Change: recent progress and future prospects. Interfac. Phenom. Heat Tr. 3, 1-17.

[4.40] Prager R., Nikitkin M. and Cullimore B., 2002. Heat pipes. Spacecraft Thermal Control Handbook, 489-522.

[4.41] Gu J., Kawaji M. and Futamata R., 2004. Effects of Gravity on the Performance of Pulsating Heat Pipes. J. Thermophys. Heat Tr. 18, 370-378.

[4.42] Kawaji M., 2003. Studies of Vibration-Induced Multi-Phase Fluid Phenomena and Pulsating Heat Pipe Performance under Microgravity. ASME/JSME 2003 4th Joint Fluids Summer Eng. Conf., Honolulu, Hawaii, USA.

[4.43] Gu J., Kawaji M. and Futamata R., 2005. Microgravity performance of micro pulsating heat pipes. Microgravity Sci. Tech. 16, 181–18.

[4.44] Mangini D., Mameli M., Georgoulas A., Araneo L., Filippeschi S. and Marengo M., 2015. A pulsating heat pipe for space applications: Ground and microgravity experiments. Int. J. Thermal Sci. 95, 53-63.

[4.45] Mameli M., Catarsi A., Mangini D., Pietrasanta L., Michè N., Marengo M., Di Marco P. and Filippeschi S., 2019. Start-up in Microgravity and Local Thermodynamic States of a Hybrid Loop Thermosyphon/Pulsating Heat Pipe. Appl. Thermal Eng. 158, 113771.

[4.46] Perna R., Abela A., Mameli M., Mariotti A., Pietrasanta L., Marengo M. and Filippeschi S., 2020. Flow characterization of a pulsating heat pipe through the wavelet analysis of pressure signals. Appl. Thermal Eng. 171, 115128.

[4.47] Ayel V., Araneo L., Marzorati P., Romestant C., Bertin Y. and Marengo M., 2018. Visualization of Flow Patterns in Closed Loop Flat Plate Pulsating Heat Pipe Acting as Hybrid Thermosyphons under Various Gravity Levels. Heat Transf. Eng.

[4.48] Ayel V., Pietrasanta L., Lalizel G., Medrinal B., Romestant C, Bertin Y. and Marengo M., 2018. Thermo-hydraulic analysis of semi-transparent Flat-Plate Pulsating Heat Pipes tested under normal and microgravity regimes. Joint 19th IHPC and 13th IHPS, Pisa, Italy.

[4.49] Ayel V., Pietrasanta L., Lalizel G., Romestant C., Bertin Y. and Marengo M., 2019. Thermo-Hydraulic Analysis of Semi-Transparent Flat Plate Pulsating Heat Pipes Tested in 1 g and Microgravity Conditions. Microgravity Sci. Tech. 31, 403–415.

[4.50] Ando M., Okamoto A., Tanaka K., Maeda M., Sugita H., Daimaru Y. and Nagai H., 2018. On-orbit demonstration of oscillating heat pipe with check valves for space application. Appl. Therm. Eng. 130, 552–560.

[4.51] Ando M., Okamoto A. and Nagai H., 2021. Start-up and heat transfer characteristics of oscillating heat pipe with different check valve layouts. Appl. Therm. Eng. 196.

[4.52] Taft B. and Irick K., 2019. ASETS-II OSCILLATING HEAT PIPE SPACE FLIGHT EXPERIMENT: THE FIRST SIX MONTHS ON ORBIT. Front. Heat Mass Transf. 24.

# PART II

## FLAT PLATE PULSATING HEAT PIPE EXPERIMENTAL STUDIES

# Chapter 5

## Experimental Set-up for Ground and Parabolic Flight Tests

As mentioned in the previous chapter, gravity significantly affects the two-phase flow inside pulsating heat pipes, especially during conditions with gravity field absence. Furthermore, gravity absence makes difficult (and sometimes impossible) to use ground-developed models and correlations to precisely predict the flow regime inside the channels and, as a consequence, heat transfer performances. Therefore, there is a strong demand on experimental validation of developed models in microgravity conditions. So, for these reasons an experimental rack has been developed to allow flat plate pulsating heat pipe tests under normal and microgravity condition.

In this chapter, detailed description of the experimental system and tests sections used for the flat plate pulsating heat pipes investigation during on-ground and several parabolic flight tests will be reported. Likewise, architectural differences between tested FPPHPs, the cooling systems for on ground and parabolic flight tests will be described. Then, the main measurement techniques and data treatments, as well uncertainty analysis will be presented.

### 5.1. The Parabolic Flight

Nowadays, several approaches are available for microgravity environment simulation and scientific tests performing, as well drop tower, parabolic flights, sounding rockets or experiments on-board satellites and the International Space Station (ISS). The comparison of these approaches in the context of the gravity level *vs.* duration is resumed in Fig. 5.1.

The parabolic flights have been chosen as a compromise between duration (around 20 seconds per parabola), accessibility (few campaigns per year) and opportunity to perform controlled experiments: researchers are able to interact with the experimental system and change parameters during experiments if necessary. Furthermore, in comparison with other “ground-based” microgravity simulation environment (drop tower and sounding rocket),

parabolic flights do not impose very strong limitations related to the device mass and volume, so experiments could be more flexible.

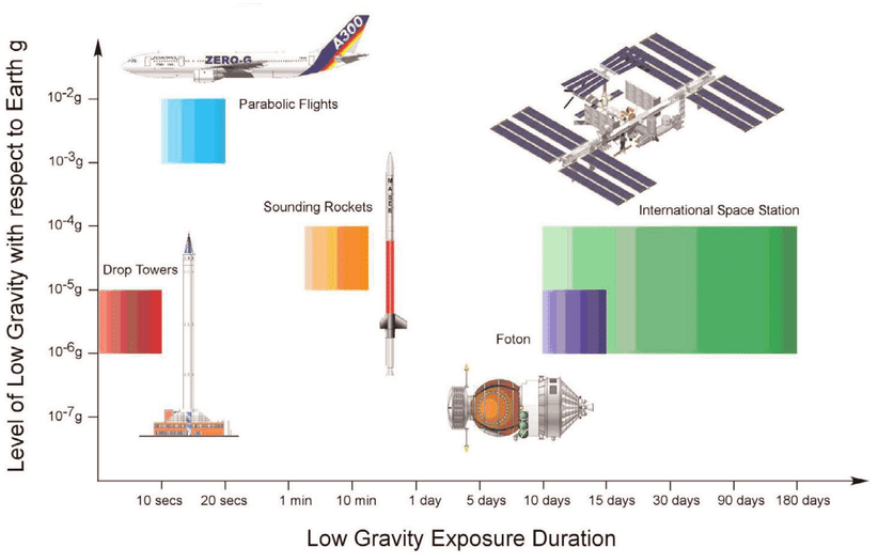


Figure 5.1. Available reduced gravity platforms for scientific approaches [5.1].

As shown in Fig. 5.2, an aircraft (Airbus A310 ZERO-G) flies from steady horizontal flight to following maneuvers:

- The aircraft climbs up to 50° (pull-up phase) for about 20 seconds and, during this phase, acceleration levels (perpendicular to the aircraft floor) is almost two times higher than Earth gravity: between 1.6*g* and 2*g*;
- Powers of all engines are reduced for about 20 seconds just for air drag compensation and aircraft follows a free fall ballistic trajectory (a parabola), that corresponds to the microgravity phase;
- The aircraft dives down to 42° (pull-out phase) during around 20 seconds with acceleration rises between 1.8g and 2g (same as for the pull-up phase);
- The aircraft returns to a steady horizontal flight.

All these maneuvers are combined in sequences of five parabolas with intervals of around two minutes between two consecutive parabolas. The interval between the parabola's groups is about five minutes, depending of the flight itinerary.

One day of flight allows to reach thirty parabolas plus one for adjustment in six sequences of five successive parabolas. The residual accelerations sensed by experimental

set-ups attached to the aircraft floor structure are typically in the order of 0.01$g$ during the microgravity phases.

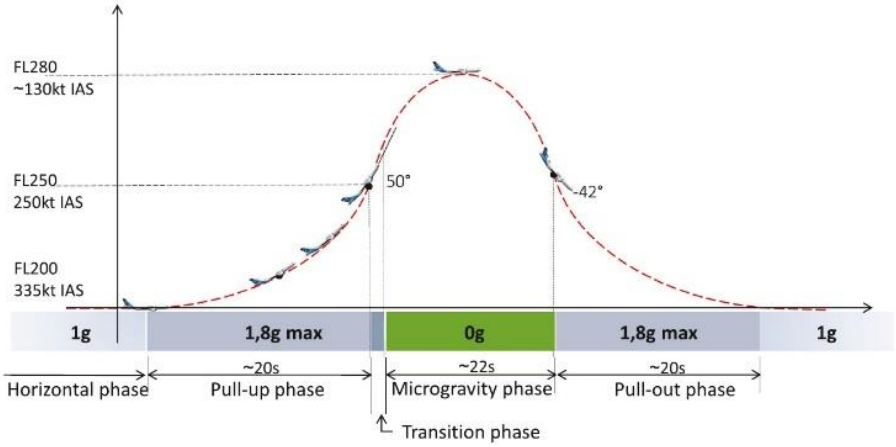


Figure 5.2. Parabolic flight trajectory [5.2].

## 5.2. The Experimental set-up

Based on the technical requirements of the Zero-G Flights operator (Novespace) and on the scientific demands, the experimental system has been developed and built in order to respond to flat pulsating heat pipe investigations during on-ground and parabolic flight tests. Used experimental set-up consisted of two main parts: command and test racks (Fig. 5.3). The test rack has been designed in order to allow thermohydraulic investigations of the FPPHPs which could be easily removed from the base and replaced by others between flight days. Besides test section, the experimental rack consists of data acquisition module, high-speed camera with external LED module, infrared camera, synchronization module and hydraulic loop (cooling subsystem).

(a) (b)

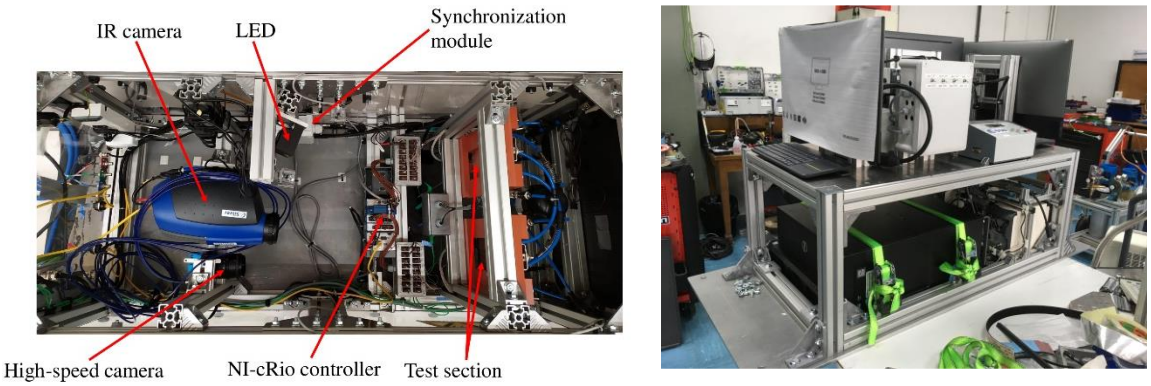


Figure 5.3. Parabolic flight experimental system: (a) top view of the test rack and (b) command rack.

Since the experimental rack mostly consists in data acquisition equipment and test section, the command rack is used for test manipulations and includes all control, security and power equipment: three PCs (one for Labview® Software data acquisition management, and the two others for high speed -and IR- cameras control), two DC power sources assuring the FPPHP evaporator heating, two DC power sources for DAQ system and synchronization module, accelerometer, gear pump controller and security box.

### *5.2.1. The Test Section*

The data obtained during 64$^{th}$, 69$^{th}$, 71$^{st}$ and 74$^{th}$ ESA Parabolic Flight Campaigns are used for the analysis in the present work, as well from ground tests for the FPPHPs used in 71$^{st}$ and 74$^{th}$ ESA PFCs. Because FPPHPs used during all these tests have different geometrical and fluid/solid thermophysical properties, it seems necessary to present each test section in chronological order.

#### *5.2.1.1. 64$^{th}$ ESA Parabolic Flight Campaign*

Despite the fact of analyzing videos of two-phase flows inside only two out of four tested FPPHPs, an experimental investigation on four one-side transparent flat plate pulsating heat pipes with different channel diameters (1.5, 2, 2.5 and 3 mm) was performed during 64$^{th}$ ESA PFC (only data for the FPPHPs with channel diameters of 1.5 mm and 3 mm will be analyzed in chapter 7). All four tested PHPs were made from a copper substrate with a length of 204 mm and varying plate width/thickness (corresponding to the channel diameter). A unique groove with a rectangular shape was machined in this plate forming a serpentine with 11 U-turns on one side (evaporator zone) or 22 parallel channels. Copper plate was covered by a borosilicate cover plate on the grooved side, forming the entire device (Fig. 5.4). The sealing of the grooved copper plate with borosilicate plate was realized thanks to glue deposition between them (with thickness of 0.5 mm). An elastic silicon glue (NUSIL® CV7 2289 1P) was used to overcome the possible deformation caused by the thermal expansion differences between copper and borosilicate ($3.3\times10^{-6}$ $K^{-1}$ for borosilicate and $17\times10^{-6}$ $K^{-1}$ for copper). Unfortunately, this kind of glue is porous and air permeation inside the PHP from ambient is possible, due to very low internal pressure, compared to atmospheric one. Since the presence of non-condensable gases strongly influences the PHP operation, a containment channel connected to a high-volume vacuumed

reservoir was provided ("Extension vacuum reservoir", Fig. 5.4). This kind of test cell modification keeps the functioning area of the device "protected" from ambient air permeation.

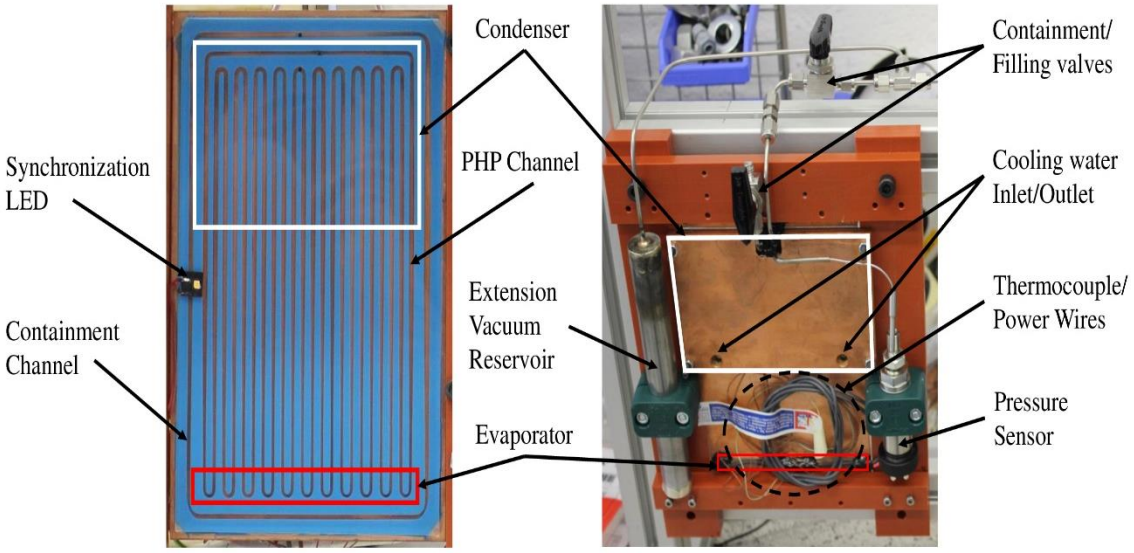


Figure 5.4. Copper-Borosilicate FPPHP used for 64$^{th}$ ESA Parabolic Flight Campaign.

A heating wire with diameter of 1 mm was embedded in a copper plate (height of 10 mm and width equal to evaporation zone of each PHP) which was brazed on the back side of the PHP to provide heat supply to evaporator.

A second massive copper plate (10 mm thickness, 100 mm height and width equal to the device one) with machined serpentine channel through which the cooling liquid circulates, was soldered on the back top-side of the PHP and used as a cold source for heat rejection (condenser).

*5.2.1.2. 69$^{th}$ ESA Parabolic Flight Campaign*

Later, in the context of the ESA project INWIP and preparation of the forecast FPPHP tests onboard the ISS, the dimensions of the test cell have been modified respecting installation requirements – 200 mm high and 80 mm wide – provided at the time by ESA specifications for integration in ISS Heat Transfer Host 1.

Based on the previous experience, and in the purpose of having a thermal expansion coefficient as close as possible to borosilicate – or sapphire – ones, together with a high value of thermal conductivity, molybdenum was chosen as material for pulsating heat pipe

metallic plate and sapphire glass as a cover plate (thermal expansion coefficients: $3.2\times10^{-6}$ $K^{-1}$ for sapphire and $5\times10^{-6}$ $K^{-1}$ for molybdenum; and thermal conductivity of 138 $W.m^{-1}K^{-1}$ for molybdenum). In analogy with copper-based flat plate pulsating heat pipes, tested during 64th ESA PFC, a unique serpentine groove of rectangular shape (depth of 2.5 mm and width of 3 mm) was milled in the molybdenum plate ($200\times80\times3$ $mm^3$). Regarding the changes in width of the device (restricted to 80 mm), the number of U-turns in the evaporator was also reduced down to seven (or 14 parallel channels).

Grooved molybdenum plate was covered with a sapphire plate ($80\times200\times5$ $mm^3$) using rigid epoxy glue to guarantee perfect sealing at the plate boards, and between adjacent channels relative to one-another. The thickness of the glue layer was set at 0.5 mm (same than for the previous case), providing a depth of the channel of 3 mm, giving them square shape which corresponds to the chosen hydraulic diameter of 3 mm. Epoxy glue could be used here thanks to the same levels of thermal expansion of both materials: indeed, although rigid, compared to elastic –silicon-type- glues, this type of glue turns out to be perfectly leak-proof, particularly to air permeation. Photograph and scheme of the developed FPPHP can be seen in Fig. 5.5.

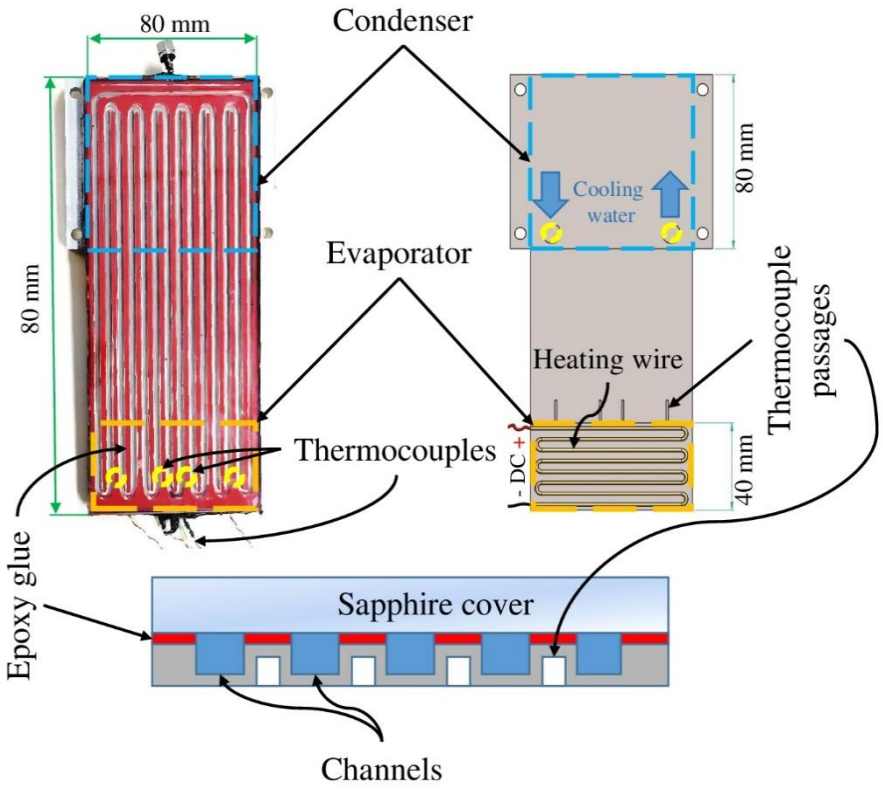


Figure 5.5. Molybdenum-Sapphire FPPHP for 69th ESA Parabolic Flight Campaign.

Heating of the evaporator zone was provided via engraved molybdenum plate (80×40×3 $mm^3$) glued on the bottom back side of the FPPHP with a serpentine groove of 1.5×1.5 $mm^2$. Stainless still coated Ni-Chrome heating wire (Thermocoax® Type NcAc15) was crimped into the groove of the heating plate. Heat rejection from the condenser was realized via molybdenum block (100×80×10 $mm^3$), also glued on the top back side of FPPHP, with milled rectangular shape serpentine channel through which cooling water circulates.

*5.2.1.3. 71st and 74th ESA Parabolic Flight Campaigns*

The flat plate pulsating heat pipes tested during 71st and 74th ESA PFCs are very similar to the previous one tested during ESA 69th PFC. The new FPPHP is composed of a rectangular copper plate (80×200×3.5 $mm^3$) in which a unique groove with square shape (3 mm deep and 3 mm wide) is milled. This groove forms a closed loop serpentine with 8 U-turns in the evaporator zone. The plate with milled channels (Fig.5.6, right) was covered with a thin copper plate (80×200×1 $mm^3$) using solder with silver addition to guarantee perfect sealing at the plate boards, and between adjacent channels relative to one-another. The filling / evacuation and pressure ports were also welded on the opposite sides of the FPPHP. Assuming the thickness of the soldering junction as negligible, the depth of the channel remains equal to 3 mm.

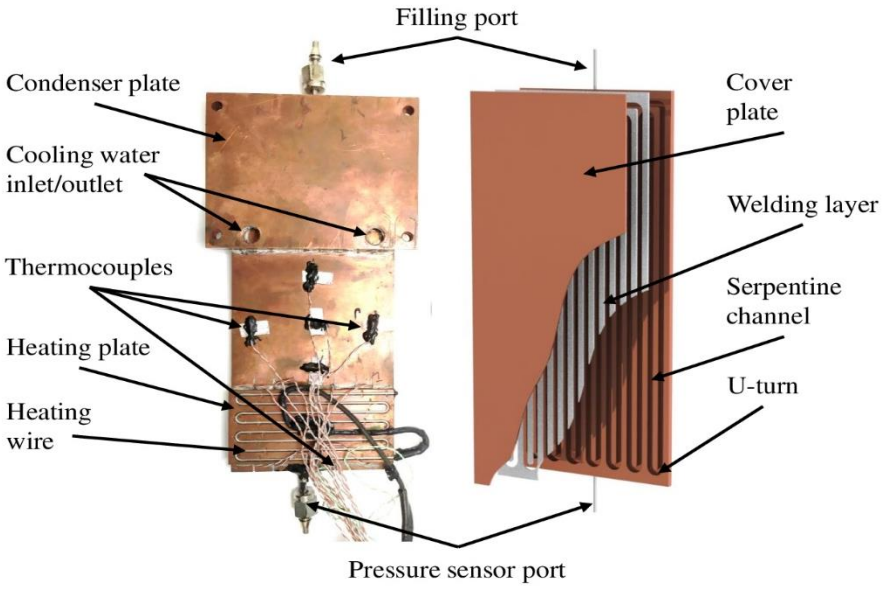


Figure 5.6. Copper-Copper FPPHP for 71st and 74th ESA Parabolic Flight Campaigns.

A cross-section cut of a manufactured copper sample can be seen in Fig. 5.7: it clearly shows almost invisible interface between grooved and cover plates. Moreover, any change in channel shape or their blockage due to solder occurrence inside them have not been observed. Note that a cleaning process was systematically done after welding in order to eliminate all the solder flux residue used during brazing.

Figure 5.7. Cross-section cut of a welded flat plate PHP sample.

Evaporator heater is composed of a copper plate (80×40x1.5 $mm^3$) with milled serpentine channel in which is inserted a heating wire (Thermocoax® Type NcAc15, 1 mm external diameter). This plate was soldered on the bottom-back side of the FPPHP. The condenser cooling plate (80 mm high and 100 mm wide), cooled by a cooling liquid which circulates inside the serpentine channel milled inside, was soldered on the top-back face of the FPPHP plate.

Temperature measurements in the evaporator zone were provided by T-type thermocouples installed in grooves (milled on the back side of the FPPHPs, on the ribs between adjustment channels). Pressure values inside the FPPHP were acquired thanks to the pressure sensor connected to the port at bottom rib of the device. These means of the data extracting are the same for all tested PHPs.

### *5.2.2. The filling Procedure*

After test cell manufacturing, the system needs to be partially filled with liquid with the required quantity. The latter is determined by the filling ratio (FR), corresponding to the volume of fluid injected into the device compared to the total internal volume of the channel (see chapter 4). Previous literature survey and past laboratory work have shown that the optimal value of the PHP filling ratio has been generally found close to 50%. On this basis, a first step consists in preparing the filling reservoir with the required quantity of the fluid. As all procedures have been performed at room temperature ($T_{room} \approx 20$ °C), the required mass of fluid can be calculated as follows:

$$m_{l,fill} = \rho_l(T_{room})V_{tot} \times \frac{FR}{100} \quad (5.1)$$

where $V_{tot}$, and $\rho_l$, are respectively the internal volume of the PHP (defined during device conception) and the fluid density at $T_{room}$. After fluid mass calculation, the filling reservoir isvacuumed down to less than 0.03 mbar with a molecular pump of a Axiden® ASM 142 leaks detector. After evacuation, the filling reservoir was weighed and filled with the previously prepared liquid (with a small higher amount than calculated). For water as working fluid, the following steps are: measuring the liquid mass inside the reservoir; heating the reservoir above 125 °C to ensure continuous liquid boiling inside and to dissolve gases separation; after boiling (and external wall temperature verification to be sure that the internal pressure becomes above atmospheric one), a first degassing is done by opening the valve under an extractor hood; then, the reservoir is immersed into a cryostat bath and cooled at -20 °C; once turned into solid phase, a vacuum pump is connected to the reservoir for 30 second to evacuate all residual vapor and non-condensable gases (NCG). This set of procedures (heating-cooling-evacuating) is repeated three times before pulsating heat pipe filling. For other working fluids, the solidification process was not performed, but only cooling the reservoir before heating it again. The last action in reservoir preparation is the liquid saturation pressure verification – a pressure sensor is connected to the reservoir set into the thermostat bath, which allows to control temperature inside the reservoir. If the saturation pressure curve is equal to the theoretical one (Fig. 5.8), then it is assumed that there are no NCGs inside the reservoir or with negligible quantity.

After saturation pressure verification, the pulsating heat pipes can be filled: the FPPHP is connected to the filling sub-system, consisting in a rotary vacuum pump, a leak detector and a filling reservoir, schematically presented in Fig. 5.9. All three components are connected by a Swagelok® valve to a T-connection and are used respecting the manipulation priority. The first step is to evacuate residual liquid and/or gases from the device, and create the vacuum inside it with the rotary vacuum pump, connected to the FPPHP (opening valves V0 and V1). Once the device empty and vacuumed (the valves V0 and V1 are closed), leaks tests of all connections and PHP interfaces (both glued and soldered) have been performed thanks to Pfeiffer Adixen ASM 142 helium-sensible leaks detector (opening valves V0 and V2). If the value of the helium permeation in the system is lower than $10^{-9}$ mbar.ls$^{-1}$ for the glued PHP and $10^{-10}$ mbar.ls$^{-1}$ for the soldered one, the device can be filled with earlier predefined working fluid.

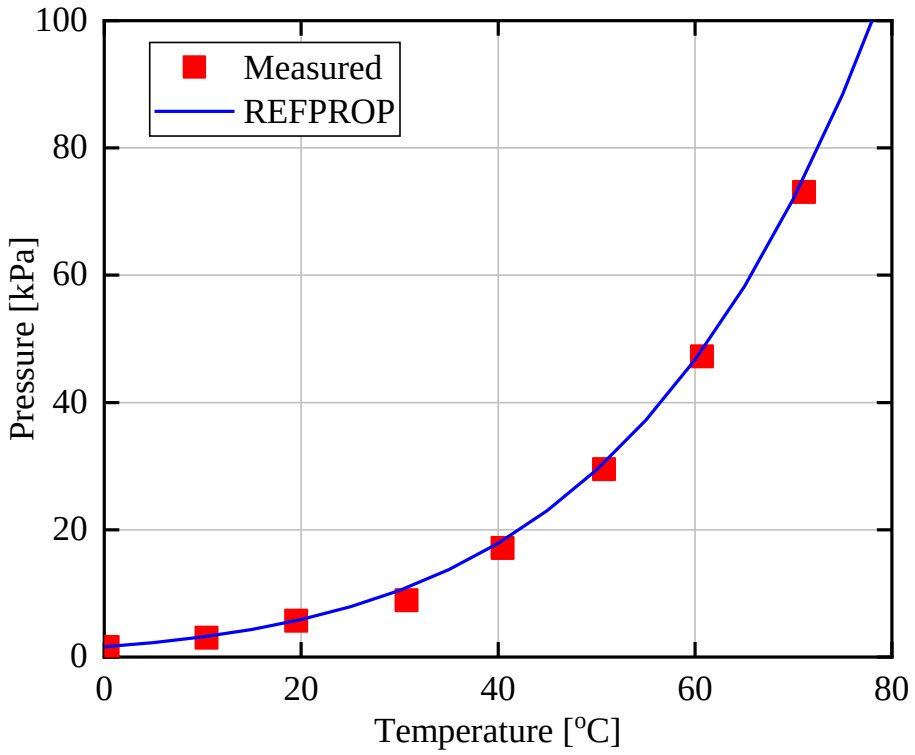


Figure 5.8. Validation of the filling fluid saturation pressure (ethanol).

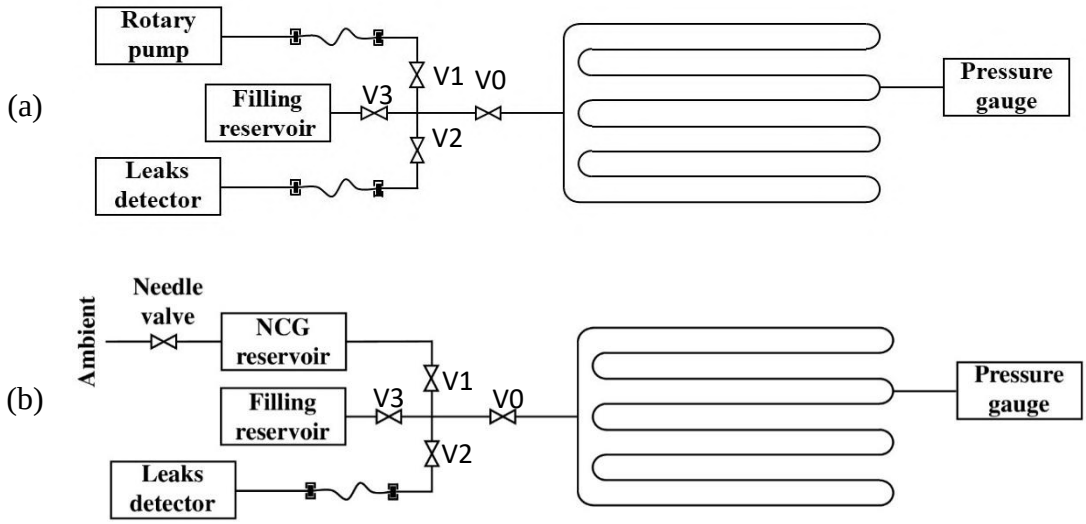


Figure 5.9. (a) Filling scheme of the pulsating heat pipe and (b) modified scheme for filling with NCG.

Before final step of filling procedure (fluid introduction inside the FPPHP), all valves are closed, the device condenser temperature is set at 5 °C and the filling reservoir is heated up to 100-130 °C (depending on the fluid saturation pressure) to reach internal pressure higher than 2 bars. All fitting and tubing are also heated to prevent condensation of the fluid

inside them. Finally, the two valves between reservoir (V3) and the FPPHP (V0) are opened, then the fluid penetrates into the PHP thanks to gravity assistance (reservoir installed above FPPHP) and pressure difference between reservoir and FPPHP.

To fill PHP for tests with non-condensable gases presence, the rotary pump needs to be replaces by the NCG reservoir (500 $cm^3$ of volume) connected to the ambient through needle valve (valve V1 is closed) after residual liquid evacuation and before leaks detection. Then, vacuum pump of leaks detector used for NCG reservoir vacuuming (needle valve, valves V0, V2 are closed). After this, previously, described procedure of leaks detection can be done. If system is leaks-free, FPPHP can be filled with NCG (valves V2 and V3 are closed), the needle valve opens slightly to fill predefined quantity of gases (controlled with pressure sensor). Then pressure is reached necessary value, needle valve and valve V1 closed. Finally, previously explained last step of filling procedure can be done.

### *5.2.3. The cooling loop*

Since the developed FPPHPs were tested in two operating conditions: on ground and during parabolic flights, two different cooling sub-systems were used to ensure stable and efficient heat rejection from the condenser cooling plate.

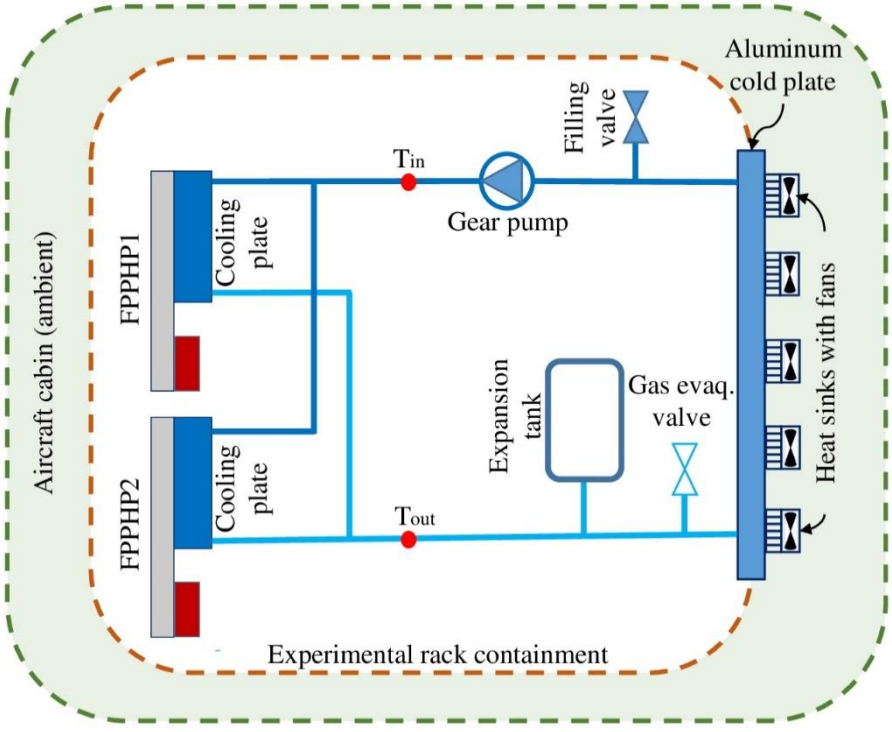


Figure 5.10. Parabolic flight cooling system description.

During ground-based tests, the condenser was directly connected to the open glycol-water mixture flow loop of the laboratory cryothermostat (Huber® CC 240wl, becoming a part of the cooling loop), insuring a constant temperature regulation in range of -20 ºC to 80 ºC (here, the condenser temperature ranges between 20 ºC and 40 ºC).

Due to security and electricity consumption limitation imposed for the tests inside aircraft, the thermostat-based cooling system cannot be used. So, it has been replaced by a water-based closed cooling loop. The parabolic flight configuration of the cooling system, described in Fig. 5.10, consists in an external massive aluminum plate with 15 embedded heat sinks (microprocessor heat sinks with equipped fans), a gear pump (Ismatec® Micropump) and an expansion tank. Connections have been realized via polypropylene tubes (8 mm of internal diameter) and quick connectors (Legris®).

Water has been used as secondary cooling fluid to transfer heat from the condenser to ambient (aircraft cabin). Initially heated in the condenser cooling plates of both FPPHPs, water flows in a copper tube crimped inside the massive aluminum plate (Fig. 5.11) by the gear pump and is cooled down thanks to the fifteen copper heat sinks with fans used to extract heat to external ambient air (at temperature around 20-25 ºC).

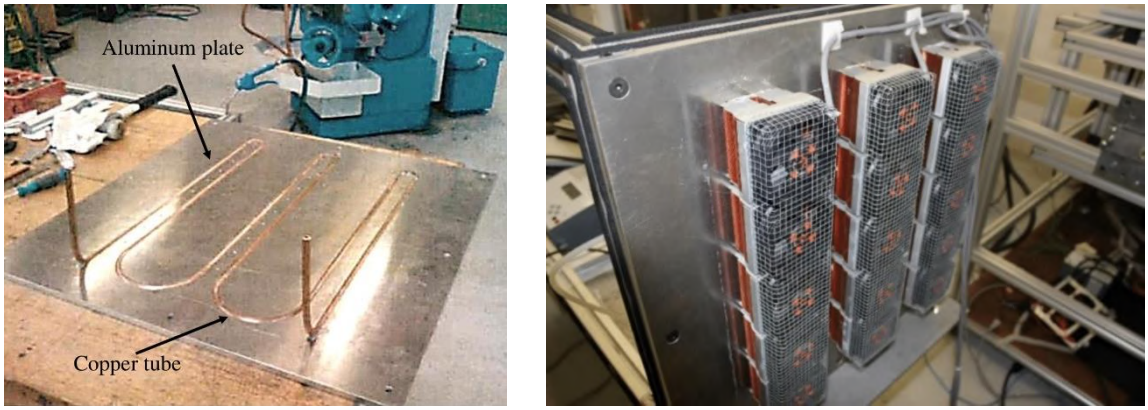


Figure 5.11. Aluminum cooling plate with fans.

Temperature variations causes pressure fluctuations and changes in fluid volume that are compensated by the expansion tank. Two thermocouples have been installed on the fluid line before and after condenser cooling plates to monitor the inlet and outlet cooling fluid temperatures ($T_{in}$ and $T_{out}$, see Fig. 5.10).

### 5.*2.4. Data acquisition and control*

On one hand, temperature measurements play a key role in the analysis of heat transfer devices. Due to some design differences, the number and positions of the thermal sensors varies from each tested pulsating heat pipe. Despite this, the quantity of thermocouples for each device (four in evaporation zone as minimum) is assumed to be sufficient for thermal performance characterization. As mentioned above, T-type thermocouples with accuracy of ±0.7 $^{o}$C have been used for the temperature measurements (their installation schema for each FPPHP presented in Fig. 5.12). A CompactRIO NI-9213 module have been used to record temperatures.

On the other hand, one of the most important PHP operational parameter is the absolute pressure and fluctuations. First, internal pressure monitoring makes possible to control the leaks and non-condensable gas presence inside the PHP by comparing it to the saturation pressure function of temperature. Then, pressure measurements allow to have an idea of the fluid flow behavior inside the PHP. A GE® PTX5076 pressure sensor (±200 Pa accuracy) is connected to connected to (or to one of) the central U-turn(s) of the evaporator zone (except for the 64$^{th}$ ESA PFC FPPHP where the pressure sensor was connected to the central surrounding U-turn of the condenser zone) (see figure 5.12 for positions). The sensor membrane was centered relatively to the middle of the device to prevent the liquid column pressure influence. Grabbing of the pressure values from the transducers were realized thanks to CompactRIO NI-9215 voltage measurement module.

Due to flight trajectory, the gravity levels are not permanent during whole tests, so measurements of the gravity acceleration become necessary to provide the adequate analysis of the obtained data. The measurements of the accelerations in three orthogonal directions are realized thank to a “homemade” accelerometer.

The heat load applied to the evaporators were ensured by two ELC® ALR3220 electrical power sources (DC, 0-30 V, 0-20 A; dV=0.03%, dI=0.05%). Measurement of the output electrical tension was done at both ends of the electrical heating resistant wire, whereas current was directly by the power source.

To improve the understanding of the two-phase flow inside flat plate pulsating heat pipes, visualization studies have been realized via a standard photo camera (Canon® EOS 100D and 550D, 50 fps) for ESA 64$^{th}$ and 69$^{th}$ PFCs and a high-speed camera (Mikrotron®

EoSens 4 CXP, 4 Mpx, 400 fps) for ESA 71st and74th PFCs, installed in front of the semi-transparent FPPHPs. Videos were directly transfered in the internal memory of the high-performance PC to ensure stable data collecting without any losses. Moreother, an infrared camera is used for IR thermography (FLIR® SC7200, wavelength band 1.5-5.1 μm, ±1K accuracy and 25 mK thermal sensitivity) during 69th and 71st PFCs. The synchronization module (trigger) was used in pair with NI-9402 output signal module to make the video registration in parallel with other parameters: data acquisition from all sensors, power sources and camera starts at the same time.

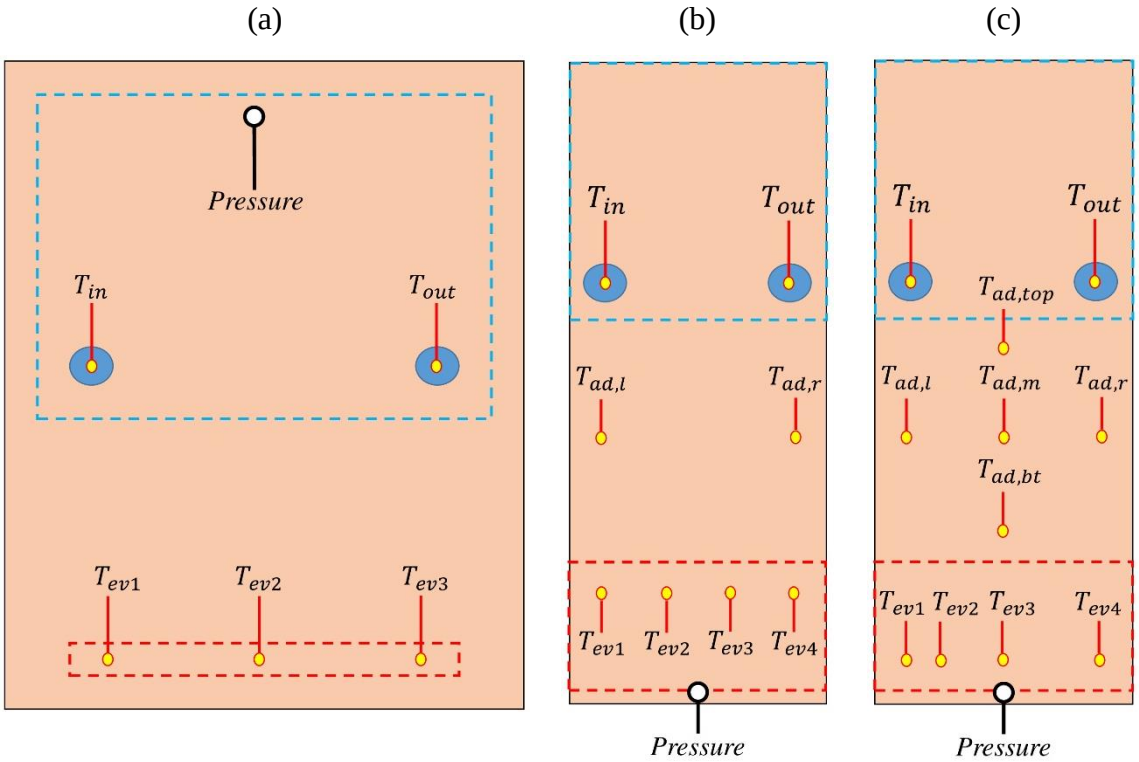


Figure 5.12. Temperature and pressure sensors placements in the FPPHPs tested during (a) 64th, (b) 69th and (c) 71st and 74th PFCs (blue and red lines correspond to condenser and evaporation sections, respectively).

All sensors described in the previous paragraphs are connected to a CompactRIO NI-cRIO 9074 controller via NI modules. This control unit scans all signals from each sensor (temperature and pressure) at regular time intervals (1 Hz for thermocouples and 50 Hz for pressure) and also sends the triggering signal to the camera. Accelerometer, power sources and controller are directly connected to the PC (vias USB and Ethernet connectors). All data manipulations (collecting, recording and processing) and device controlling (electrical heater power regulation and camera triggering) were ensured by a communication interface

provided by LabView® software, which also allows real-time visualization of the monitored parameters.

Moreover, this program interface ensures the system security provoking electrical heater shutdown if one or several measured temperatures reach a value higher than 115 $^{o}$C. This threshold value has been chosen to prevent from thermal stresses and deterioration of all the elements constituting the experimental bench and prevent from significant pressure augmentation inside PHPs (related to the design). According to Novespace's specifications, the experimental bench was also equipped by a redundant physical security box with maximum temperature set at 125 ˚C.

### *5.3. Working fluid*

The importance of the working fluid selection on the pulsating heat pipe operation has been mentioned in the previous chapter. This step is based on various parameters as well chemical compatibility with the device material, good thermal (high sensible and latent heat) and hydraulic (low viscosity and surface tension) properties ensuring high heat transfer rate and stable oscillatory flow. Also, due to peculiarities of this work related to the microgravity tests, low toxicity as well relatively low operational temperature and pressure are required.

According to the Merit number proposed by [4.19] and shown in Fig. 4.11b (see Chapter 4), the best fluids for PHPs are toxic and/or have a high saturation pressure in the tested temperature range (20-100 $^{o}$C) as well ammonia, R22 and R134a. These choices in this work have been made in favor of water, FC72, ethanol and methanol. Despite their low “ranking” related to other fluids, most of them correspond to the necessary requirements of design parameters, non-toxicity (except for methanol) and low pressure in the specified temperature interval. Moreover, these fluids have been widely used for electronic cooling (FC72), experimental studies (water and ethanol – classical fluids) and for space applications (methanol).

Additional attempt to improve heat transfer characteristics of the FPPHPs has been done, using different solutions of water and alcohol, and also with surfactant additives. The changes in the device heat transfer capability are expected mostly due to wettability improvement and rewetting phenomena (for self-rewetting fluids).

## 5.4. Experimental procedure

### *5.4.1. Ground tests*

Before every experimentations, the PHP had to be positioned in a predefined orientation – vertical or horizontal. Temperature of the secondary cooling fluid had also to be fixed thanks to the cryothermostat controller. Then, once the device temperature stabilized, a 50W-heat load level was applied. After a while (thermal regime establishment between 30 minutes and 1 hour), heat load was increased by steps of 50 W. Same procedure was repeated until 200 W. By the end of the test period with heat load of 200 W, it was then reduced down to 100 W to ensure repeatability tests.

Once the first test sequence is over, the condenser temperature or orientation could be changed for the following test.

### *5.4.2. Parabolic flight tests*

During parabolic flight campaigns, FPPHP have been tested with different heat loads for each series of parabolas. Before first set of parabolas, all systems need to be verified and previously determined heat load should be applied to reach the stable PHP operation. After announcement of the pull-up phase (beginning of the parabolic maneuver), data acquisition was started – temperature, pressure and heat load values recording, as well video from high-speed camera. Due to lack of time between parabola's sets to save recorded video on hard drive, the video registration was stopped just after the fourth parabola and saving procedure started. All other data continued to be registered until the end of the series of fifth parabolas. Immediately after flight stabilization, the acquisition was stopped and new values of heat load were set.

## 5.5. Data reduction and uncertainty analysis

Usually, experimental studies are accompanied by numerous measurements of different parameters, which can be difficult in the term of the widescale representation and thermal efficiency comparison. However, thermal resistance, as an important parameter indicating the device capability to thermal transport, and can be used for the FPPHP efficiency analysis. It is defined as follows:

$$R_{th} = \frac{\overline{T_{ev}} - \overline{T_{cool}}}{Q} \tag{5.2}$$

where $\overline{T_{ev}}$, $\overline{T_{cool}}$ and $Q=U\times I$ are, respectively, evaporator and cooling mean wall temperatures ($\overline{T_{ev}} = \sum_{i=1}^{N} T_{ev,i}/N$; $N$ being the number of thermocouples in the evaporator zone, and $\overline{T_{cool}} = (T_{c,e} + T_{c,s})/2$) both of them time-averaged over the successive recordings selected for the purposes of steady-state characterization, heat load, tension and current measured on the heater ends. As experimental measurements were conducted with certain accuracy and knowing the absolute error of each kind of measurements, uncertainties can be expressed as follows [5.3]:

$$\frac{\partial Q}{Q} = \sqrt{\left(\frac{dU}{U}\right)^2 + \left(\frac{dI}{I}\right)^2} \tag{5.3}$$

$$\frac{\partial R}{R} = \sqrt{\left(\frac{\delta T_{ev}}{T_{ev} - T_{cool}}\right)^2 + \left(\frac{\delta T_{cool}}{T_{ev} - T_{cool}}\right)^2 + \left(\frac{\delta Q}{Q}\right)^2} \tag{5.4}$$

Resulting uncertainty of the heat load varies in the range of 0.08% to 0.15%. The uncertainty for the thermal resistance has been found for the highest heat loads (with higher temperature differences between evaporator and cooling water) and was equal to 1.7%, whereas it reached values up to 26.7% for the lowest heat loads and temperature differences (complete range of uncertainties can be found in Appendix C).

### 5.6. Results presentation and test repeatability

To facilitate the understanding of the graphics on the temperature behavior presented in the next chapter, first results for the water-filled FPPHP tested on ground in vertical position (BHM) will be here described as an example. The temperature and pressure responses as functions of time and related to the heat load are shown in Fig. 5.13. Evaporator temperatures are plotted in different shades of red, adiabatic ones are in orange, the pressure curve is plotted in grey and heat load is represented by the dashed green line. Left ordinate-axes for temperature curves have the same scale for every graphs (0-120 ºC), while right one can vary depending on the pressure values (hPa or kPa) in order to improve graphics readability.

It seems that Fig. 5.13 can represent the main FPPHP operation conditions for major number of tested cases. For low heat load applied (50 W), the FPPHP filled with pure water operates in dry mode (liquid accumulates in the condenser zone). In these conditions, the FPPHP transfers heat mostly thanks to the device thermal conduction (discussed in the

previous chapter). With heat load augmentation, evaporator (and adiabatic) temperatures increases with significant pressure fluctuations, which means short-term "out" from stopover operational mode. Sometimes this phenomenon is observed for the FPPHP tested with other fluids, in different position and heat load.

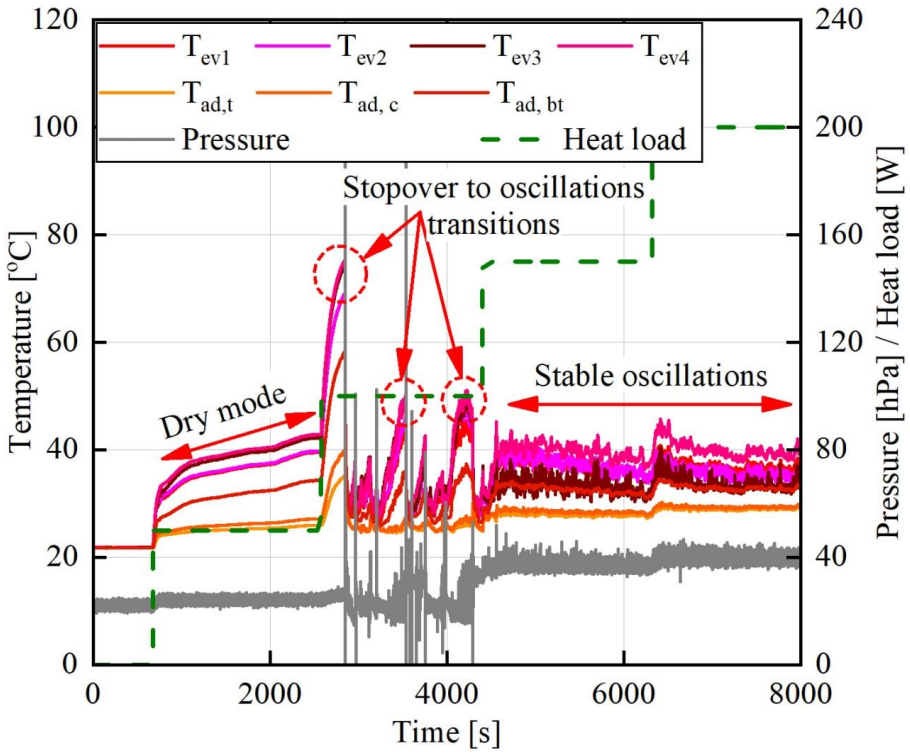


Figure 5.13. Transient temperature and pressure responses of the copper FPPHP (also ESA 71th PFC) related to the heat load increase (water, FR=50%, $T_{cool}$ = 20°C, vertical BHM).

The following increase of applied heat power (150 and 200 W) lead to the temperature and pressure stabilization. The amplitudes of these oscillations are significantly lower than for 100 W of heat load, which means a regular and frequent liquid flow fluctuations inside the FPPHP.

The test repeatability is a key factor of the experimental system reliability: if during repeated tests the same (or very similar) results are obtained, experimentation can continue to test other parameters. Fig. 5.14 represents the evaporator and adiabatic (one sensor in the center) temperatures and pressure for ethanol-filled FPPHP tested with a applied heat power of 100 W – left image represents test period before following heat load increasing step until 150 W; right image shows parameters after heat load decrease from 200 W to 100 W. It can clearly be seen that temperature and pressure oscillations amplitudes are almost the same for both cases, even the temperature average values are also equal.

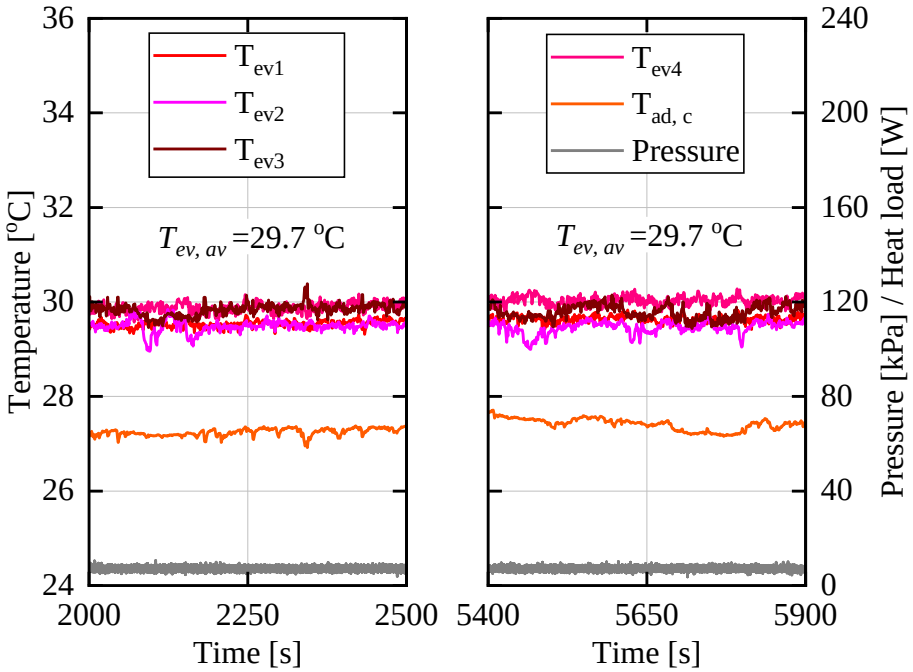


Figure 5.14. Temperature and pressure histories for FPPHP: (left) original and (right) repeated tests (ethanol, FR=50%, $T_{cool}$ =20 °C, vertical BHM)

The modifiable parameter during ground tests is the heat load, but for parabolic flight it is the gravity acceleration. So, results representation will be slightly different. Fig. 5.15 depicts the typical temperature, pressure and gravity profiles during one set of five consecutive parabolas. In analogy with Fig. 5.13, curves colored in shades of red, orange and grey are respectively representing evaporator, adiabatic temperatures and pressure. All parabola's set test are performed with the same heat load, so the curve of heat power is not necessary in the graphs, but the blue line, representing cooling water mean temperature, has been added due to the absence of precise cooling liquid temperature regulation (provided by thermostat during ground tests). The dashed grey curve shows the gravity variation during the five consecutive parabolas and allows to recognize all transitions caused by the gravity.

At the beginning of the parabola set, the FPPHP operates in vertical position (BHM) due to normal gravity onboard of aircraft. In Fig. 5.15, just after parabola starts, when microgravity conditions are reached, the evaporator temperatures drastically increase due to channel wall dry-out in the evaporator zone and liquid accumulation in the condenser zone (as already mentioned in section 3.2.4). This phenomena was observed for all pure fluids, tested during this work. Adiabatic temperatures smoothly increase in the microgravity phase beginning – and heat is transferred mostly by conduction. Similarly to the adiabatic

temperatures, pressure slightly increases probably due to evaporation of the residual liquid in the evaporator and vapor superheating. Sometimes, the evaporator temperature drops during parabola. At the same time, pressure and adiabatic temperature surges can be observed, which illustrates the sudden change of the FPPHP operational mode – transition from stopover to oscillations, due to the two-phase fluid flow "re-activation".

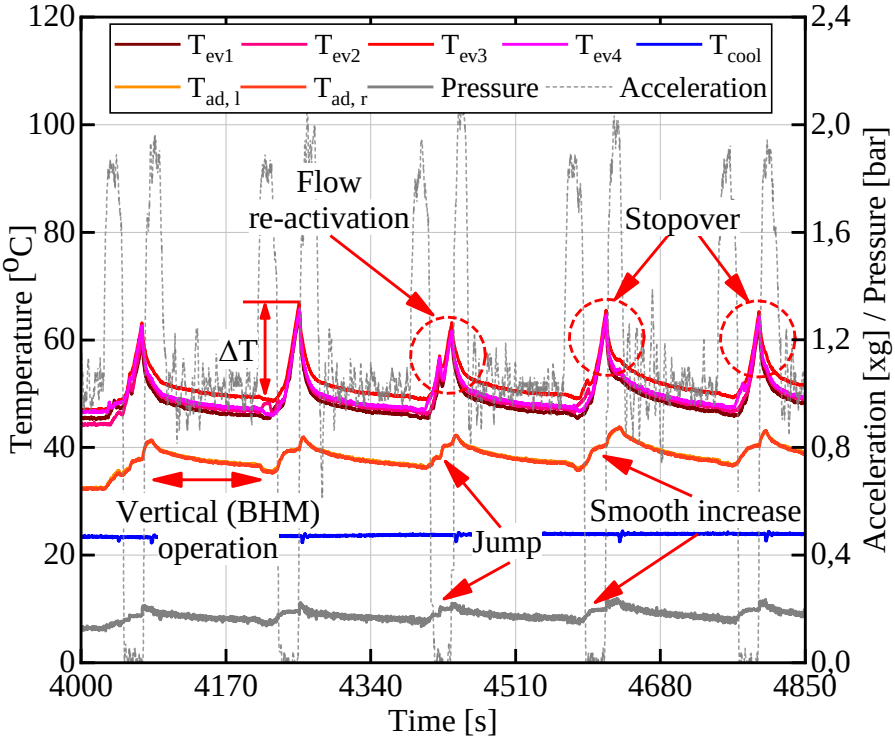


Figure 5.15. Transient temperature and pressure responses of the molybdenum FPPHP (used for ESA 69th PFC) related to the gravity acceleration changes (ethanol, FR=40%, Q = 100 W, vertical BHM during normal gravity).

## 5.7. Conclusions

The experimental system for ground and microgravity experiments, allowing both, qualitative and quantitative characterization of the flat plate pulsating heat pipe have been described in this chapter. The prototypes have been developed for the tests during four ESA Parabolic Flight Campaigns, based on the security requirements and zone of scientific interests – coupled thermal and hydraulic studies of the FPPHPs under different gravity conditions.

The uncertainty analysis also have been provided. The figures, used in following chapter are described during analysis of the first experimental results. Repeatability analysis provided, which also prove the system reliability.

**References**

[5.1] Poette C. and Reynier P., 2014. Evaluation of 3D Mapping Experimental Non-Intrusive Methods for Multiphase Flows. , Int. J. Multiphys 8, 69-90.

[5.2] Pletser V., Rouquette S., Friedrich U., Clervoy J.-F., Gharib Th., Gai F. and. Mora Ch, 2016. The First European Parabolic Flight Campaign with the Airbus A310 ZERO-G. Microgravity Sci. Tech. 28, 587–601.

[5.3] Kline S. and McClintock F., 1953. Describing uncertainties in single-sample experiments. Mech. Eng. 75,, 3–8.

# Chapter 6

## Ground Based and Parabolic Flight Tests Analyses

The data obtained during on-ground tests and parabolic flight campaigns (ESA 69th, 71st and 74th Parabolic Flight Campaigns) on flat plate pulsating heat pipe will be presented and analyzed in this chapter.

This chapter will be devised in two main parts:

- in the first one, results will be described for FPPHP tested on ground in order to evaluate the influences of orientation, operating conditions (condenser temperature, input heat load and filling ratio) and fluid thermophysical properties on both FPPHP behavior and thermal performance under normal gravity conditions;
- the second part will describe results for the FPPHP tested onboard of aircraft during parabolic flights under microgravity conditions (~0.01g) and filled with different fluids. In addition, results from specific ESA 74th PF campaign, for Lunar (~0.18g) and Martian (~0.38g) gravity conditions, will be briefly presented. Influence of non-condensable gases on FPPHP operation during normal gravity and microgravity periods will also be discussed.

### 6.1. Ground tests

As mentioned above (sections 3.2.4 and 4.2), the influence of gravity on the operation of a pulsating heat pipe is a crucial step in determining prospective applications for this device, especially for aerospace applications. This issue has been intensively studied to demonstrate gravity effects on PHP performances and overall operational behavior.

Previous studies on pulsating heat pipes have shown great influence of orientation (inclination) on both thermal transfer characteristics and operation behavior [6.1; 6.2; 6.3; 6.4; 6.5]: gravity assistance during vertical operation for bottom heated mode (BHM), as well as over inclinations of PHP (respecting BHM) [6.6], leads to significant decrease of

thermal resistance compared to horizontal FPPHP operation – in vertical orientation, gravity vector helps the liquid plugs to flow back to the evaporator zone.

In this section, ground based experimental results for the copper flat plate pulsating heat pipe, developed and described in Chapter 5, and tested in both BHM vertical and horizontal orientations are presented. Operating conditions, used working fluids and filling ratios are shown in table 6.1.

Table 6.1. Test operating conditions for ground tests.

| **Orientation** | **Fluid** | **Filling ratio** | **Applied power** | **Condenser temperature** |
|---|---|---|---|---|
| Vertical | Water | 50%<br>59% | 0 – 200 W | 20 $^{o}$C; 40 $^{o}$C |
| | Ethanol | 50% | 0 – 200 W | |
| | Methanol | 50%<br>59% | 0 – 200 W | |
| | Water – 20% ethanol | 50% | 0 – 200 W | |
| | Water – 28% methanol | 50% | 0 – 200 W | |
| | Water – 5% butanol | 50% | 0 – 200 W | |
| | Water – 0.5% Tween 40 | 50% | 0 – 200 W | |
| Horizontal | Water | 50% | 0 – 100 W | 20 $^{o}$C; 40 $^{o}$C |
| | | 59% | 0 – 150 W | |
| | Ethanol | 50% | 0 – 200 W | |
| | Methanol | 50% | 0 – 200 W<br>0 – 150 W | 20 $^{o}$C<br>40 $^{o}$C |
| | | 59% | 0 – 200 W | 20 $^{o}$C; 40 $^{o}$C |
| | Water - 20% ethanol | 50% | 0 – 200 W | |
| | Water – 28% methanol | 50% | 0 – 200 W | |
| | Water – 5% butanol | 50% | 0 – 200 W | |
| | Water – 0.5% Tween 40 | 50% | 0 – 150 W<br>0 – 200 W | 20 $^{o}$C<br>40 $^{o}$C |

*6.1.1. Results for the FPPHP tested in vertical BHM*

*6.1.1.1. Qualitative analysis of the FPPHP filled with pure fluids*

Here, in this first subsection, evolution of temperatures and pressure curves for the FPPHP varying heat load level will be studied. All tests were carried out for the heat load range from 50 W up to 200 W (if there is no system failure during tests) with 50 W-steps. Typical temperature and pressure responses as functions of time for the FPPHP filled with

pure water, ethanol and methanol in saturation state are presented in Fig. 6.1 – 6.3, respectivelly.

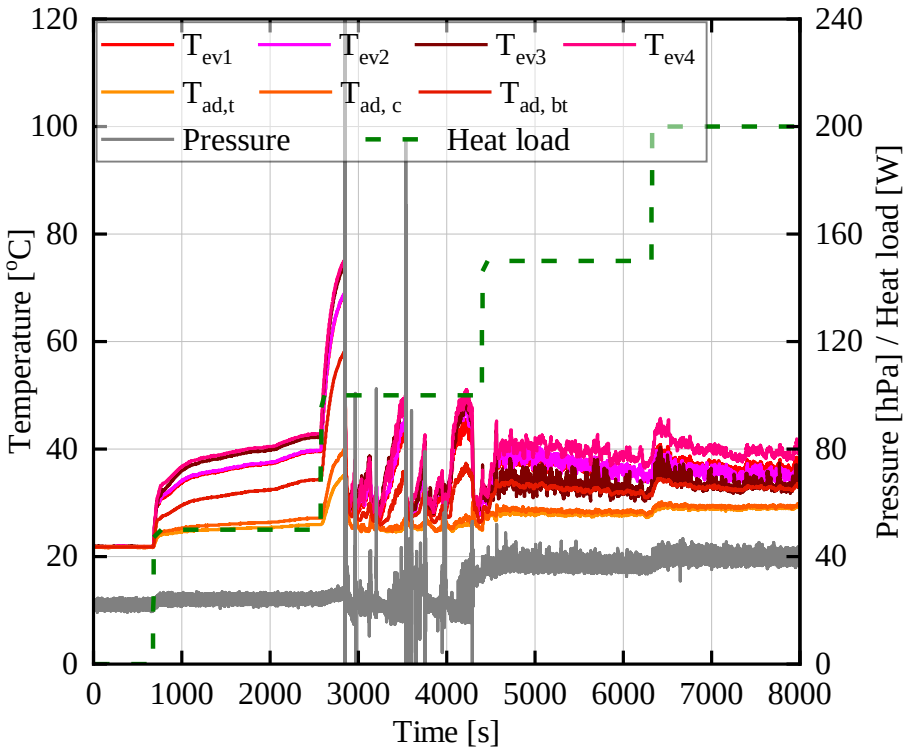


Figure 6.1. Temperature and pressure responses for FPPHP filled with water (FR=50%; $T_{cool}$ = 20 °C, vertical BHM).

As shown in Fig. 6.1, at the beginning of heating period (50 W of applied power), temperatures in evaporator zone of FPPHP filled with water (FR = 50%) drastically increase up to a value about equal to 32 °C (~12 °C higher than cooling water temperature, at t = 700 s). Smooth evaporator temperatures increase (until ~42 °C) is observed during almost all test period (~30 min) under this heat load. Following heat load increases up to 100 W leads to the short-term sharp evaporator temperatures rise till ~70 °C. After temperature values reach their maximum (at t = 2850 s), temperatures and pressure drops were observed with succeeding temperature high amplitude oscillations (peaks temperatures from 30 °C to 50 °C), corresponding to the beginning of fluid flow circulation in the separate form of liquid slugs and vapor bubbles. Next heat load increases of 150 W and 200 W lead to temperatures and pressure oscillations stabilization – frequency increase and amplitude decrease - accompanied with a maximum evaporator temperature value about 40 °C. It is noticeable that temperature oscillation amplitudes for 150 W and 200 W of applied power are almost the same.

Fig. 6.2 presents temperatures and pressure evolutions as functions of time for the FPPHP filled with pure ethanol (FR=50%) under saturation state. Period for 50 W of applied power is characterized by the presence of temperature peaks of ~37ºC and ~50ºC with following temperature decrease down to ~25ºC, accompanied by pressure drops. These periodical temperature variations report about dry-out occurrence during temperature increase with following start-up. This behavior is very similar to the one obtained for the case with water at 100 W of applied power.

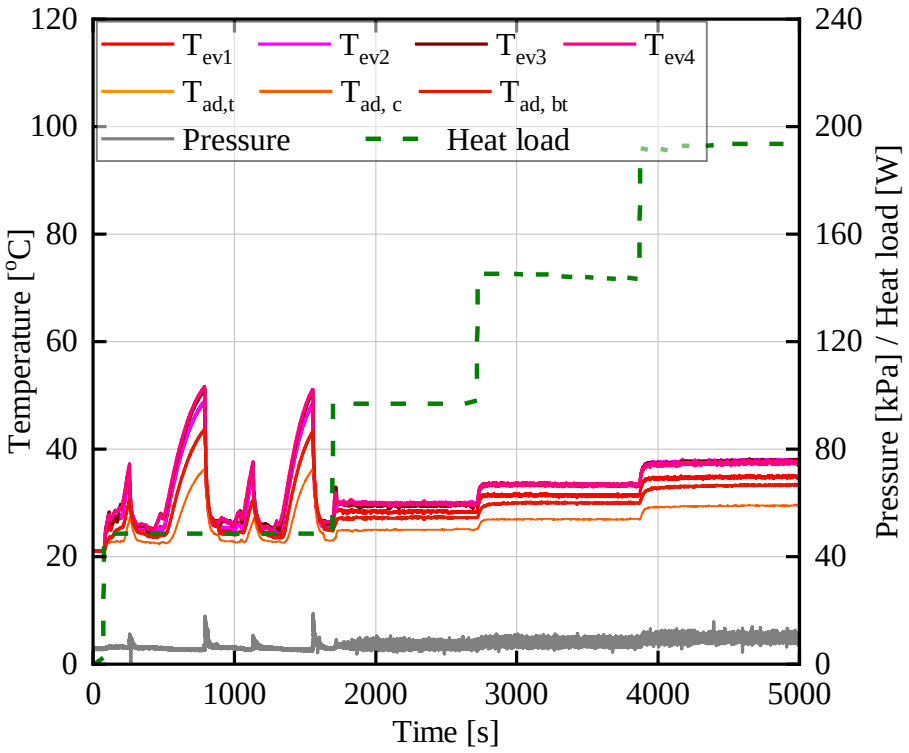


Figure 6.2. Temperature and pressure responses for FPPHP filled with ethanol (FR=50%; $T_{cool}$ = 20 ºC, vertical BHM).

Next augmentation of heat load up to 100 W leads to low temperatures (at the level of ~28ºC) and higher pressure amplitude oscillations during total period before next heat load step. Absence of significant temperature oscillations is due to gravitational forces dominance on surface tension forces and ensuing FPPHP operational changes – from slug/plug pulsating flow to annular, as previously observed and reported by [6.2]. FPPHP operational behavior for 150 W and 200 W of heat load is very similar to the case at 100 W of applied power with average evaporator temperature augmentations till ~33ºC and ~37ºC, respectively. One can argue that, at these operating conditions, the FPPHP operates very efficiently.

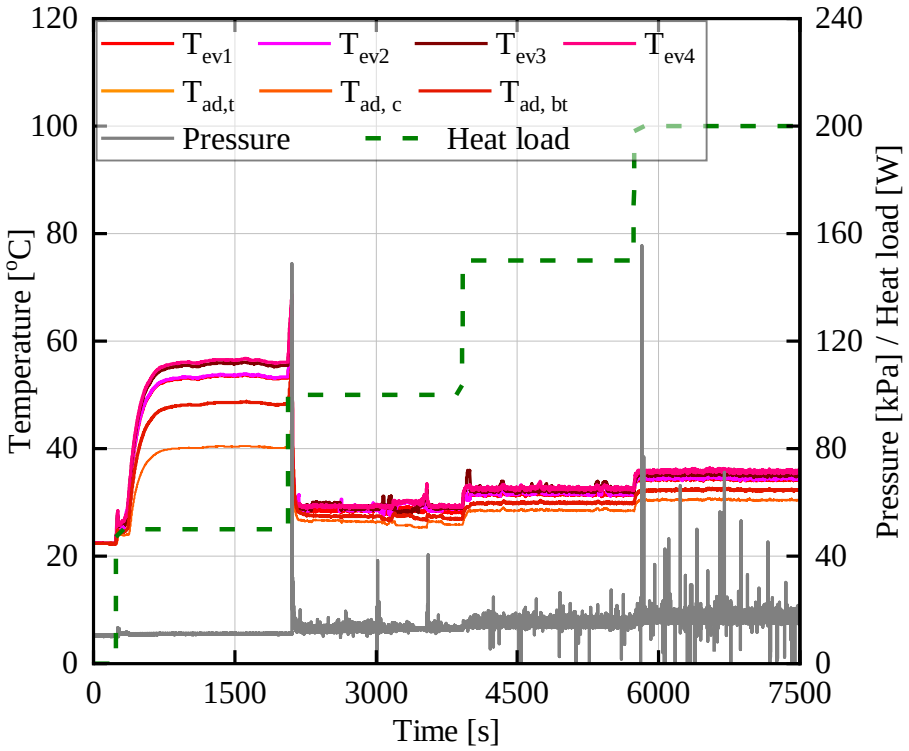


Figure 6.3. Temperature and pressure responses for FPPHP filled with methanol (FR=50%; $T_{cool}$ = 20 °C, vertical BHM).

For methanol-filled FPPHP (FR=50%), the temperature and pressure responses are presented in Fig. 6.3. Temperature behavior seems to be similar to the case of water-filled FPPHP for 50 W of applied power but with higher evaporator temperature increasement (temperature increase up to ~55°C). At the beginning of the period for 100 W, evaporator temperatures rise till ~70°C with following drop and temperature quasi-stabilization (with rare temperature leaps) on the level of ~28°C. Consequent heat loads of 150 W and 200 W lead to establishment of thermohydraulic behavior similar to the case of ethanol and temperatures of ~32°C and ~35°C (150 W and 200 W, respectively), which gives thermal performances slightly better than for the previous one.

*6.1.1.2. Influence of the condenser cooling fluid temperature*

Fig. 6.4 represents a comparison of thermal resistances as functions of applied heat power for FPPHP filled with water, ethanol and methanol, with filling ratio of FR = 50% at range of heat loads of 50 W – 200 W and condenser temperatures of 20 °C and 40 °C (Fig. A.1.6-A.1.8). Here, higher values of thermal resistance mean lower thermal performances and, so, lower values correspond to better heat transfer characteristics of FPPHP.

From Fig. 6.4, it seems that thermal resistance for methanol-filled device at 50 W of heat load and $T_{cool}$ = 20 °C is two times higher than for water-filled and three times higher than for ethanol-filled FPPHP, which seems to be in good accordance with evaporator superheats observed for this initial heat load in Fig. 6.3. Lower thermal resistance value at 50 W of heat load is observed for FPPHP filled with ethanol. Following heat load increase leads to thermal resistances decrease for all tested fluids at $T_{cool}$ = 20 °C. Then, their convergence almost at the same point ($R$ = 0.07 K/W) for 200 W of applied power is observed.

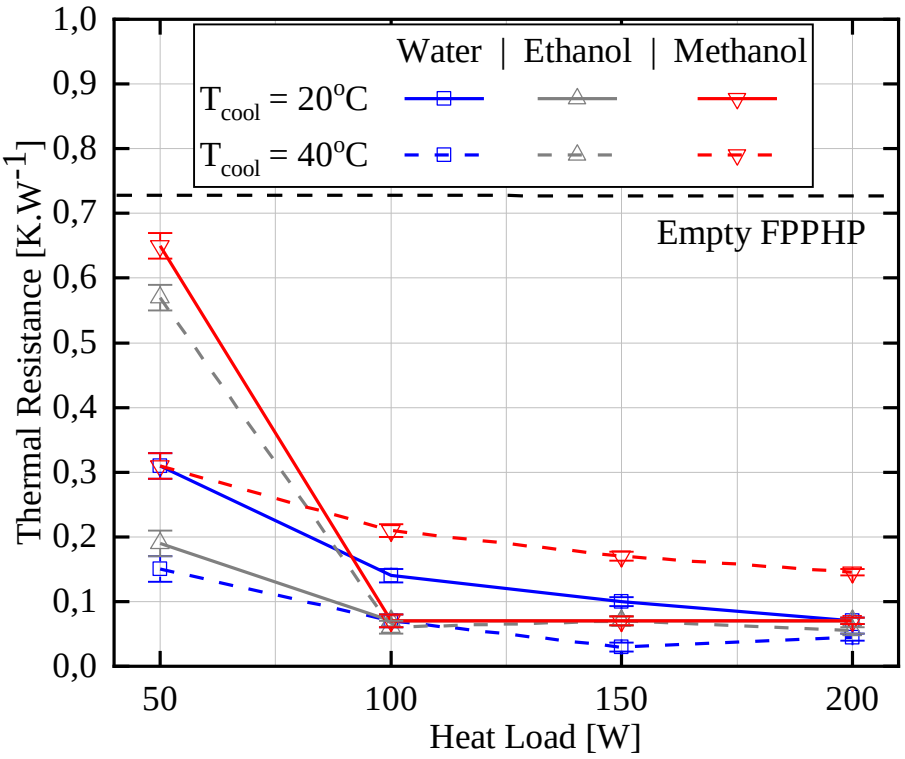


Figure 6.4. Thermal resistances for FPPHP tested at $T_{cool}$ = 20 °C and $T_{cool}$ = 40 °C of cooling water temperature (FR = 50 %, vertical BHM).

The overall values of thermal resistances for the same device filled with same fluids and tested at $T_{cool}$ = 40°C of cooling temperature are quite lower for all fluids in the entire range of heat loads, except cases with ethanol for 50 W and methanol in the power range between 100 W and 200 W. Thermal resistance values for water are varying from 0.15 K/W at 50 W to 0.07 K/W for 200 W; from 0.57 K/W at 50 W to 0,05 K/W at 200 W of applied power for ethanol; and from 0.31 K/W at 50 W to 0.15 K/W at 200 W of heat load for methanol.

*6.1.1.3. Influence of the filling ratio*

Some authors [6.7; 6.8] previously reported that filling ratio has significant influence on both pulsating heat pipe thermal performance and operation behavior. Usually, during the tests, flat plate pulsating heat pipe is filled with a filling ratio of FR=50%. Knowing that tested FPPHP is not symmetric (condenser is two time larger than evaporator) and that, during dry-out periods, liquid collects in the condensation zone, studied FPPHP with filling ratio of FR=59% allows to reach halfway between the condenser and the evaporator (Fig. 6.5), have been carried out.

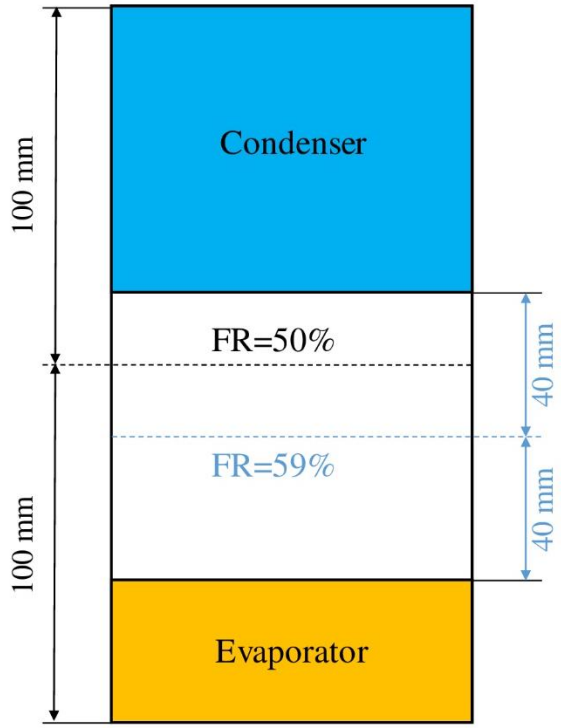


Figure 6.5. Schematic representation of the liquid level inside FPPHP (from the top condenser) for filling ratio of FR = 50% and FR = 59%.

Fig. 6.6 shows the comparison of thermal resistances for flat plate pulsating heat pipe filled with water at filling ratios of 50%, and 59%, respectively. First of all, in analogy with results for filling ratio of 50%, thermal resistances decrease with heat load augmentation for both cooling temperatures at filling ratio of 59%.

Thermal resistance of FPPHP filled with water for FR=50% and tested at condenser temperature of 20 $^{o}$C (solid blue line, Fig. 6.6) and heat load of 50 W is almost two times higher than for the case at FR=59% (dashed blue line, Fig, 6.6). Following increase of heat

load leads to the values alignment until almost fully coincidence of thermal resistance values at 150 W and 200 W of heat loads.

Condenser temperature rise shows opposite effect (for heat load equal to 50 W) – thermal resistance for higher filling ratio (dashed red line, Fig. 6.6) at 50 W of applied power is almost four time higher than value for FPPHP filled with lower amount of fluid. However, with heat load augmentation (in the range of 100 W to 200 W), any influence of filling ratio on FPPHP thermal performances has been noticed.

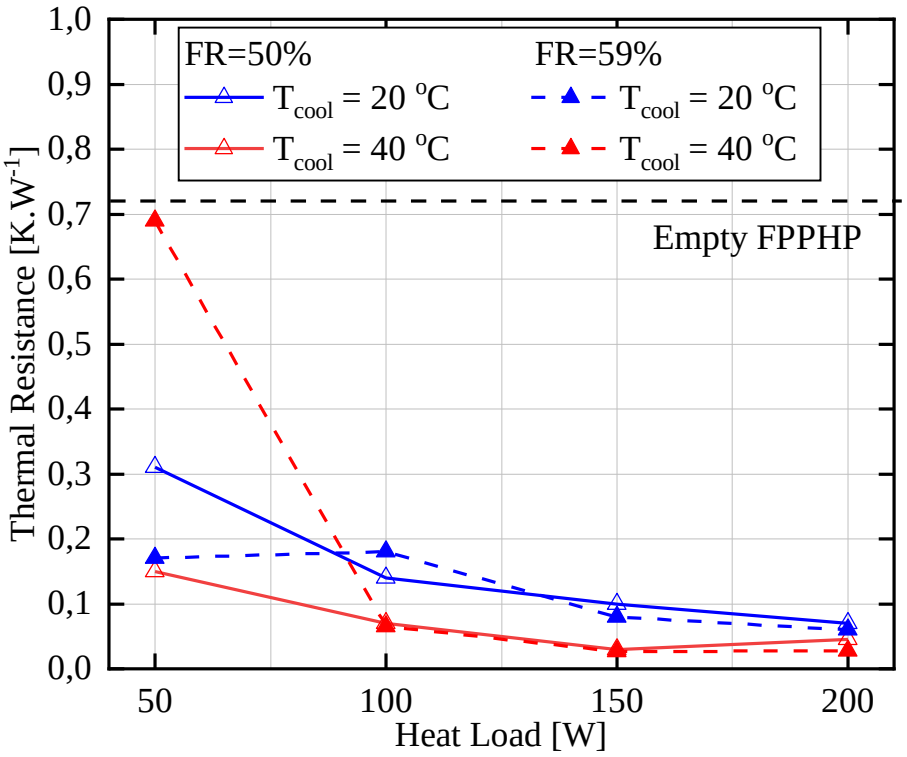


Figure 6.6. Effect of filling ratio on thermal resistances of FPPHP filled with water (vertical BHM).

These disagreements with thermal resistances at 50 W of heat load could be provoked by FPPHP unstable operation, but with heat load augmentation thermal responses seem to become more stable and reproducible.

*6.1.1.4. Influence of the binary mixtures*

Nowadays, many studies on enhancement of heat transfer performances of the pulsating heat pipes are carried out. Based on PHP working principles concerning liquid plug motions, wettability and surface forces can significantly affect the two-phase transfer characteristics

due to their high influence on flow resistance in mini- and microchannels. In addition, wettability has influence on liquid film formation close to the liquid plugs and can affect heat transfer performances.

Due to these facts, improvement of wetting properties relating to pulsating heat pipes becomes an interesting approach. Nowadays, many techniques are used to change wetting properties as well both solid surfaces and/or fluids modifications. Indeed, using fluids mixtures in the context of wetting and interfacial properties seems to be an interesting approach. This subsection will briefly present results for FPPHP tested with alcohol aqueous solutions, self-rewetting fluids and water-surfactant solutions. Thermal behaviors will be analyzed and compared with the ones obtained with pure water.

Fluids modification leads to changes of many thermo-physical parameters (thermal and transport properties) so, in this study, fluids with relatively close values of surface tension have been selected. Table 6.2 presents main thermophysical properties of tested fluids (density, viscosity and thermal conductivity of water - 0.5% Tween 40© solution assumed equal to pure water due to small amount of surfactant).

Table 6.2. Main thermophysical properties of the tested fluids at $T$ = 20 °C [6.9 – 6.11].

| | $\rho_l$ (kg.m$^{-3}$) | $\mu_l$ (kg.m$^{-1}$.s$^{-1}$) | $\sigma_l$ (N.m$^{-1}$) | $\lambda_l$ (W.m$^{-1}$.K$^{-1}$) | $\partial P_{sat}/\partial T$ (Pa.K$^{-1}$) |
|---|---|---|---|---|---|
| Water | 988 | $5\times10^{-4}$ | 0.068 | 0.604 | 609 |
| Water – 5% 1-butanol | 978 | $5.1\times10^{-4}$ | 0.034 | 0.595 | 605 |
| Water – 5% 2-butanol | 979 | $5.5\times10^{-4}$ | 0.032 | 0.564 | 619-639 |
| Water – 20% Ethanol | 943 | $5.2\times10^{-4}$ | 0.035 | 0.478 | 680 |
| Water – 28% Methanol | 943 | $4.9\times10^{-4}$ | 0.044 | 0.515 | – |
| Water – 0.5% Tween 40© | 988 | $5.4\times10^{-4}$ | 0.035 | 0.604 | – |

Results for FPPHP tested with water, water/ethanol and water/methanol mixtures as working fluids, are shown in Fig. 6.7 in the form of thermal resistances. As it could be seen, the thermal performances for FPPHP tested at $T_{cool}$ = 20 ºC are very similar for all tested fluids. Moreover, thermal resistances for water and water/ethanol cases are almost matching in the range of heat load from 50 W to 150 W. Despite this apparent similarity, real thermal behavior is very different - case with pure water as a working fluid accompanied with high temperature oscillations, contrary to water/ethanol and water/methanol cases, where very frequent and low amplitude temperature oscillations were observed (that could be seen in Fig. A.1.1, A.1.2, A.1.6, A.1.9 and A.1.10).

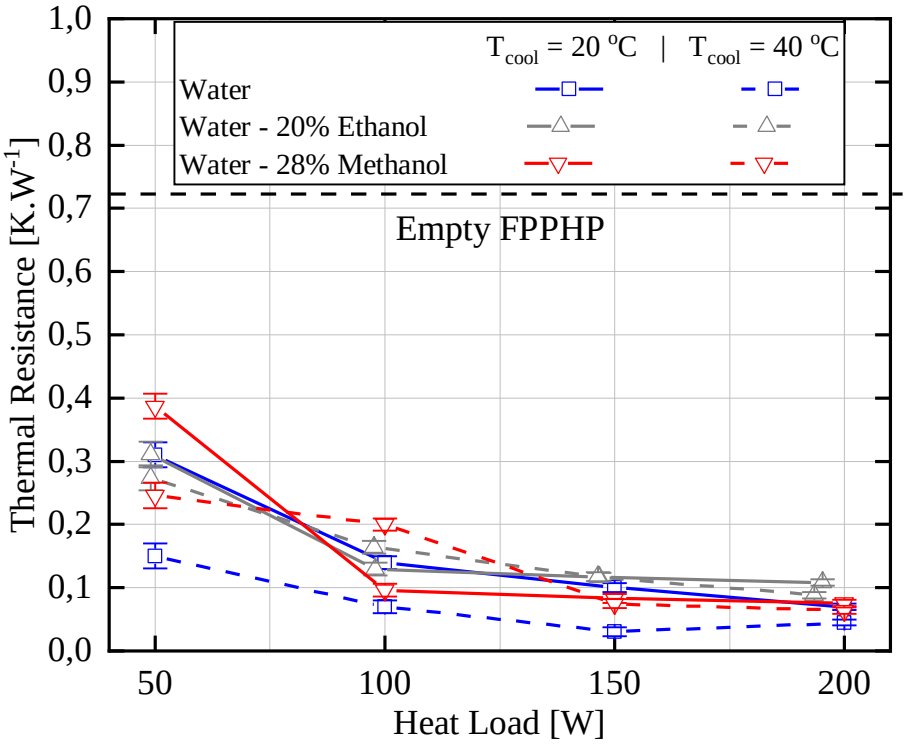


Figure 6.7. Thermal resistances for FPPHP filled with ethanol and methanol aqueous solutions at $T_{cool}$ = 20 ºC and $T_{cool}$ = 40 ºC (FR = 50%, vertical BHM).

It seems that FPPHP filled with pure water is almost two times more performant than the FPPHP filled with alcohol aqueous mixtures for tests at condenser cooling fluid temperature of $T_{cool}$ = 40ºC. Condenser temperature increase provokes a thermal behavior change for the FPPHP filled with pure water from rare high amplitude temperature oscillations to frequent and low amplitude temperature oscillations, which means the same two-phase flow behavior inside of the FPPHP. This fact, coupled with better transport characteristics of water, leads to overall thermal performance improvement.

Thermal resistances of FPPHPs filled with self-rewetting fluids and tested at condenser temperature of $T_{cool}$ = 20 ºC and 50 W of heat load (Fig. 6.8) are almost two times lower than thermal resistance for the FPPHP filled with pure water and tested at same conditions. With subsequent heat power augmentations, thermal resistances slightly decrease (more visible changes for case with water).

With augmentation of condenser temperature until *Tcool* = 40 ºC, thermal resistances for all fluids slightly decrease, comparing to the case with condenser temperature of *Tcool*

= 20 °C. No significant difference in thermal performance of FPPHP between the fluids was observed.

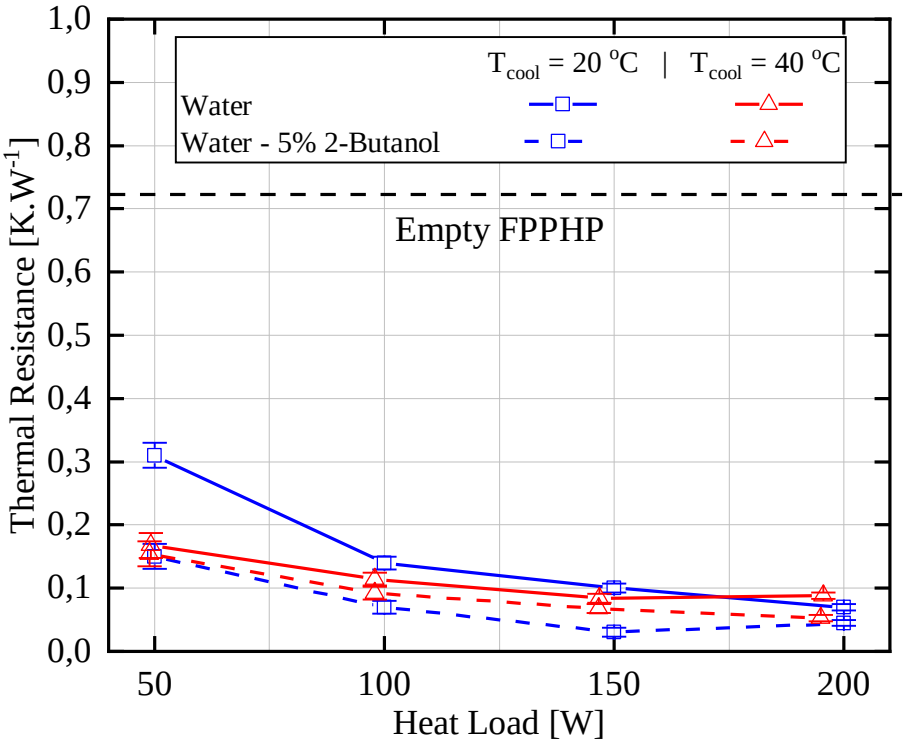


Figure 6.8. Thermal resistances for FPPHP filled with SRWFs at $T_{cool}$ = 20 °C and $T_{cool}$ = 40 °C (FR = 50%, vertical BHM).

Comparison of thermal performances for the FPPHPs filled with water and water surfactant solution (0.5% Tween 40©) is presented in Fig. 6.9. Thermal resistances for tests conducted at $T_{cool}$ = 20 °C of cooling water showed a lower thermal performance of water/surfactant solution than for pure water at the initial level of heat load (50 W). Following overall thermal performance changes accompanied with heat load augmentation have been observed.

Test case with $T_{cool}$ = 40 °C showed the same: higher thermal resistance value for water-filled FPPHP at initial heat load of 50 W. This can be explained by the temperature augmentation during non-oscillating device operation, which could be seen also for water-surfactant solution, but with much less temperature augmentation (temperature peak in Fig. A.1.13). Temperature high frequent and low amplitude oscillations take place with applied heat power increase (almost similar for two cases) which leads to the alignment of thermal resistance values.

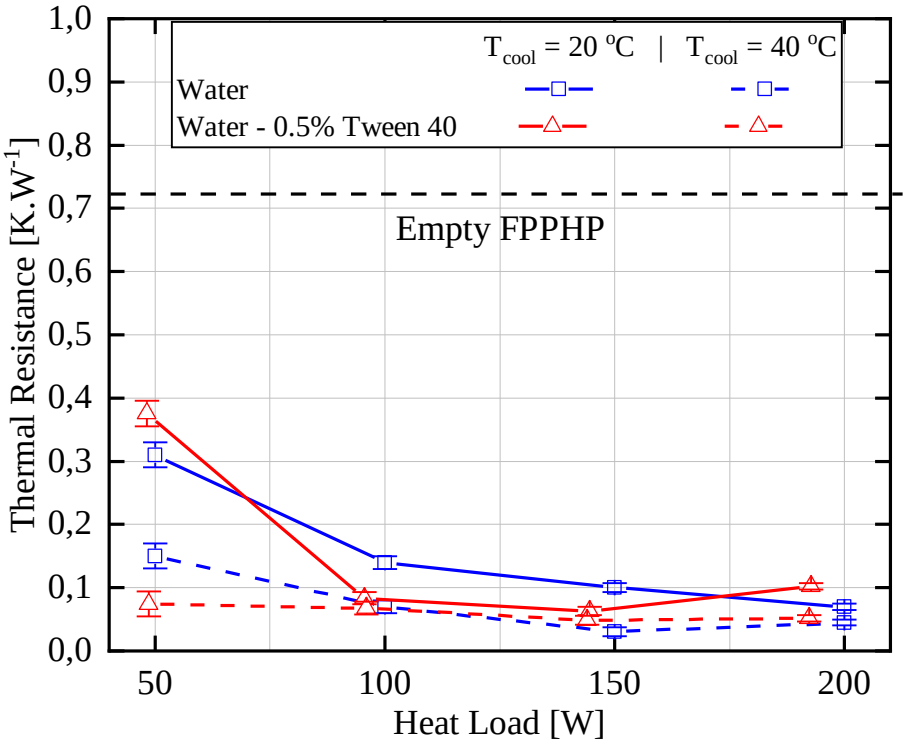


Figure 6.9. Thermal resistances for FPPHP filled with Tween 40© aqueous solution at condenser temperature of $T_{cool}$ = 20 °C and $T_{cool}$ = 40 °C (FR = 50%, vertical BHM).

*6.1.1.5. Influence of the non-condensable gas presence*

Generation of non-condensable gas inside two-phase heat transfer devices often occurs in a unpredictable way; it is mainly due to chemical reactions in liquid-solid interface, or to some some leaks through the soldered connections, etc. Non-condensable gas (NCG) presence inside two-phase heat transfer devices can become a crucial issue influencing the system operation and reliability [6.12]. NCG generation is one of the most important reasons of heat pipe heat transfer capability degradation and failure [6.13; 6.14]. However, not many papers exist concerning NCG influence on PHP operation. NCG amount directly influences the slug/plug flow dynamics and leads to a remarkable decrease of heat transfer capability with large amount of NCG [6.15; 6.16]. Injection of NCG in PHP does not prevent their operation, but produces a rise of overall system pressure, operational temperature resulting to thermal resistance increase [6.17]. Resulting system pressure and saturation temperature can be expressed as follow [6.18]:

$$P_{sys} = P_v + P_{gas} \tag{6.1}$$

where Pv and Pgas are the partial pressures of vapor (corresponds to the saturation pressure) and NCG gases, respectively. Finally, the real saturation temperature of the system consisting NCG will be:

$$T_{sat,sys} = T_{sat}[P_{sys}] \tag{6.2}$$

From Eq. (6.1) and Eq. (6.2) clearly seen, that internal pressure of the system increases with NCG presence, leading to the saturation temperature augmentation.

In this section will be discussed the effect of NCG on the flat plate PHP operation in vertical orientation (BHM). The system pressure with NCG addition corresponds to 15 kPa at 20 °C, contrary 2.3 kPa for pure water.

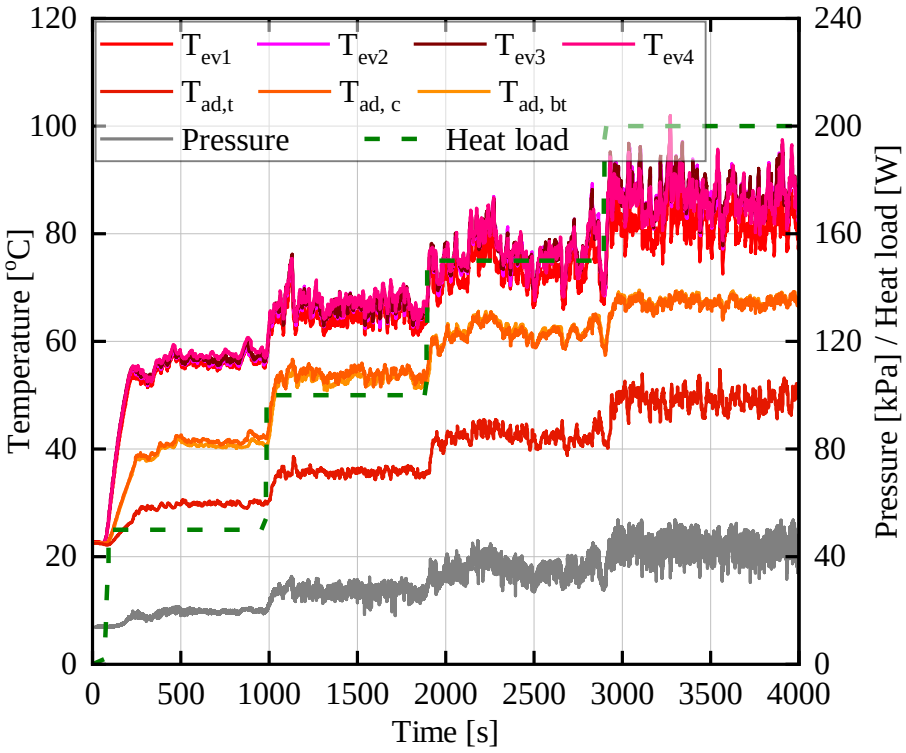


Figure 6.10. Temperature and pressure responses for FPPHP filled with water and NCG (FR = 50%; $P_{sys}$ = 15 kPa; $T_{cool}$ = 20 °C, vertical BHM).

Fig. 6.10 presents temperature and pressure behavior for FPPHP filled with NCG presence. The regular and high amplitude temperature oscillations can be seen starting from 100 W of heat load (low amplitude oscillations present at 50 W also), contrary case with pure water (Fig. 6.1), where temperature increases significantly during period for 50 W of applied power. Moreover, great oscillations of pressure values testifies the alternate presence of liquid and gaseous phases in the evaporation zone (near to the pressure sensor probe),

which can be caused by the liquid plugs separation with the NCG slugs. It should be noted that overall evaporator superheat (related to the case with pure water) is: ~18 $^{o}$C at 50 W; ~30 $^{o}$C at 100 W; ~38 $^{o}$C at 150 W and ~45 $^{o}$C at 200 W of heat load.

No significant changes in temperature and pressure behavior have not been found with liquid cooling temperature augmentation till $T_{cool}$ = 40 $^{o}$C (Fig. A1.16 – appendix A.1). However, average evaporator temperature increase have been found around ~10 $^{o}$C for heat loads in the range of 50 W – 150 W.

### *6.1.2. Results for FPPHP tested in horizontal position.*

The fact that, as previously mentioned, gravity effect on the FPPHP operation is minimal in horizontal orientation (gravity vector perpendicular to the flow direction) makes the tests in such position closer to the space conditions than tests in vertical BHM.

As mentioned in section 3.2.4, the fluid flow pattern in horizontal orientation can be only slug flow, and the motor of the fluid flow comes from the pressure instabilities in the various vapor bubbles. In such configuration, surface tension forces become significant in the momentum balance, and wettability also plays a role in heat and fluid flow behavior of PHPs.

In analogy with section 6.1.1, in this section results will be presented in form of temperature histories to evaluate a thermal transient behavior of the FPPHP and in form of thermal resistance curves to compare influence of different parameters (condenser cooling temperature, filling ratio, fluid properties etc.) on the FPPHP thermal transport efficiency.

#### *6.1.2.1. Qualitative analysis of the FPPHP filled with pure fluids*

Typical transient long-time test run results for the same working fluids tested under the same conditions presented in section 6.1.1.1, are presented in Fig. 6.11 – 6.13 in the forms of temperature and pressure histories. All data of this section can be found in appendix A.2 (Fig. A.2.1 to A.2.16).

For reported operating conditions, except for some oscillations noticed at the beginning of heat power level of 50 W, FPPHP filled with pure water operates “dry” after 800 s (Fig. 6.11), what can be provoked by liquid accumulation in the condensation zone (see Fig. 3.11c). During the beginning of heat power step of 150 W, evaporator temperature exceeds 100 $^{o}$C (highest possible operation temperature due to security reasons) and following tests

have been stopped. Anyway, presented cases could characterize an overall behavior of FPPHP operating with water in horizontal position.

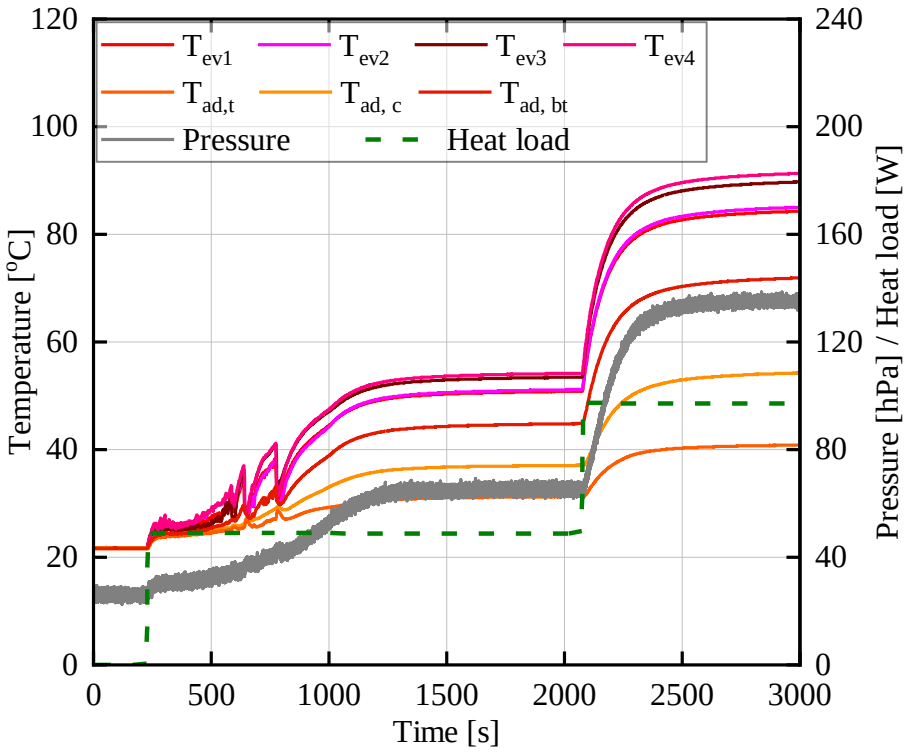


Figure 6.11. Temperature and pressure responses for FPPHP filled with water (FR = 50%; $T_{cool}$ = 20 °C, horizontal).

Temperatures and pressure behavior of ethanol-filled FPPHP are presented in Fig. 6.12. As for the case with water, some oscillations with following dry-out are noticed for first heat power load (50 W). Regular high amplitude and high frequency temperature oscillations can be observed for higher heat loads. It is interesting that sometimes high amplitude (~40-50°C) temperature oscillations alternate with lower ones (20-25°C) but with higher frequency. In such configuration, one can assess that the FPPHP filled with water operates at 40°C cooling temperature but in a degraded mode. Such high temperature oscillations are detrimental to prolongated and durable use of FPPHPs as heat transfer device.

Operation behavior for the FPPHP filled with methanol (Fig. 6.13) looks quite similar to the case of ethanol, except period for applied power of 50 W – if, for ethanol, dry-out has occurred, stable and low amplitude temperature oscillations have been observed for methanol, showing very good thermal operation in such conditions. Test periods for higher heat loads characterized by regular high frequency temperature oscillations and overall

evaporator temperature augmentation can be observed. Sometimes (especially for highest heat loads) higher temperature rises with following drops have been registered – this means a short-term periods of flow oscillations stopover.

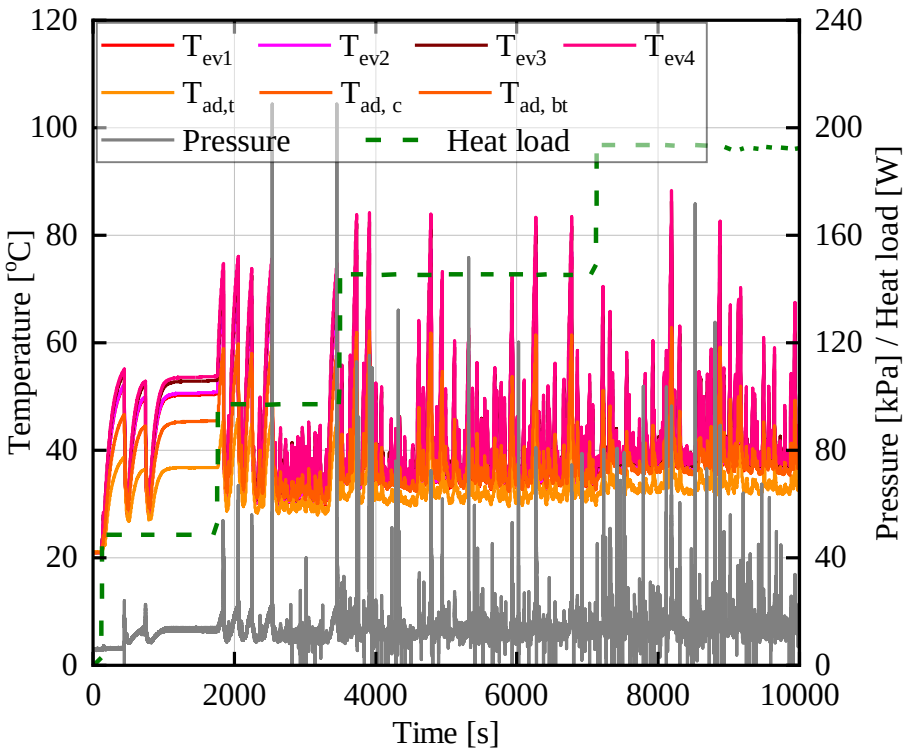


Figure 6.12. Temperature and pressure responses for FPPHP filled with ethanol (FR = 50%; $T_{cool}$ = 20 °C, horizontal).

In comparison with the FPPHP tested in vertical BHM (section 6.1.1), tests of the FPPHP in horizontal orientation showed completely different operational behavior. Indeed, in vertical position, with water as working fluid, the optimal operation mode has been reached for 150 W and 200 W of applied power but, in horizontal position operation of the FPPHP have failed (start-up not reached in the accepted temperature range); high amplitude temperature oscillations have been noticed for two other fluids in horizontal position, unlike almost smooth profiles in vertical position due to the gravity forces predominance compared to surface tension forces, helping the liquid plugs to flow back into the evaporator.

Comparing pressure curves for two tested positions (vertical and horizontal) and two tested liquids (ethanol and methanol), can be seen a significant difference in the amplitude and frequency of values oscillations. In vertical position, FPPHP filled with water show very rare pressure oscillations only at 100 W of applied power (from 3000 s to 4000 s) and

methanol-filled device show more frequent oscillations starting from 100 W (from 4000 s). These values mean the presence of the alternate slug-plug flow through pressure sensor in the center of evaporator. No significant pressure oscillation for FPPHP filled with ethanol and operated in vertical position was found – can be concluded that device working in thermosiphon mode. However, FPPHPs tested in horizontal orientation and filled with ethanol and methanol operated in clear oscillation mode starting from 100 W of heat load for both devices (high amplitude pressure oscillations can be found in Fig. 6.12 (starting from 1800 s) for ethanol and Fig. 6.13 (starting from 2200 s)).

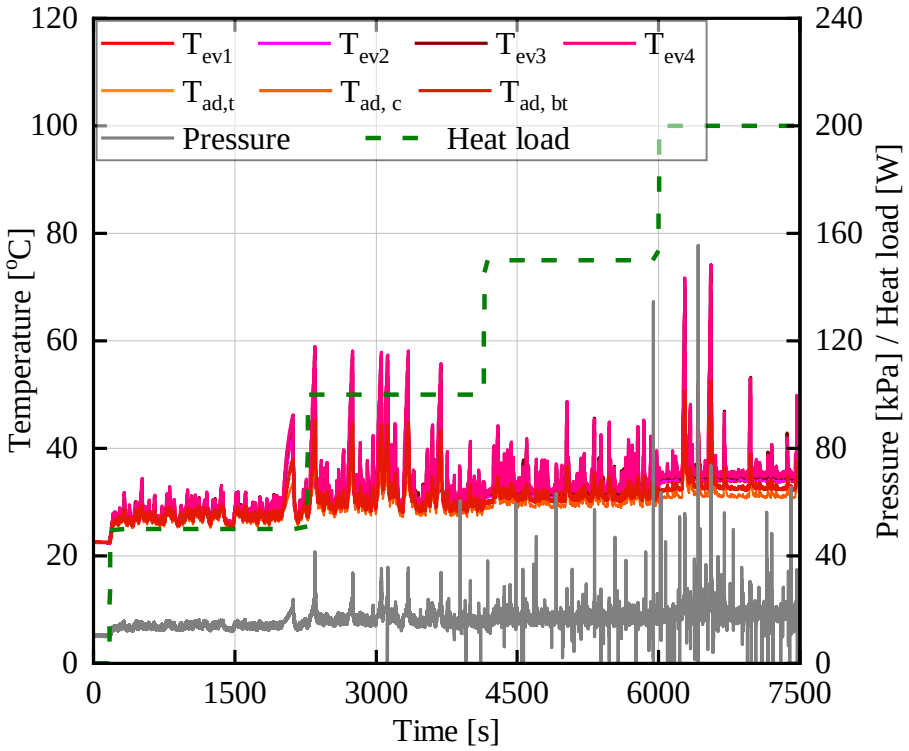


Figure 6.13. Temperature and pressure responses for FPPHP filled with methanol (FR = 50%; $T_{cool}$ = 20 °C, horizontal).

*6.1.2.2. Influence of the condenser cooling fluid temperature*

As shown in Fig. 6.11, FPPHP filled with water and tested at $T_{cool}$ = 20 °C of cooling water temperature operates in the "dry evaporator" mode and results have been obtained only for 50 W and 100 W of heat load. Thermal resistances for these two heat power are presented in Fig. 6.14 (blue solid line), where thermal performance of water-filled FPPHP slightly degrades with heat load augmentation, in contrast with case of ethanol and methanol filled devices.

If the thermal resistance for ethanol at the lowest heat load (50 W) is a bit higher than for water (0.55 K/W *vs.* 0.49 K/W), it significantly decreases with heat power augmentation. This is due to the transition from "dry" operating mode to "oscillatory" one which has not been reached for pure water.

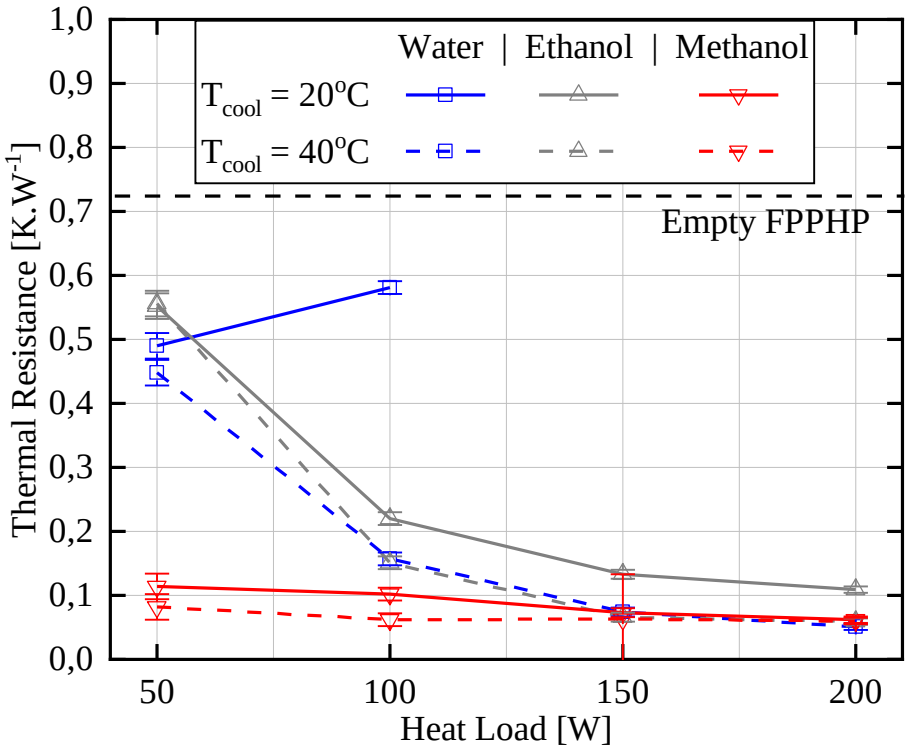


Figure 6.14. Thermal resistances for FPPHP tested at $T_{cool}$ = 20 °C and $T_{cool}$ = 40 °C of cooling water temperature (FR=50%, horizontal).

Due to presence of stable oscillations from the test beginning, *i.e.* for lowest heat load of 50 W, thermal resistance evolution for methanol-filled device for the same test conditions showed minor decrease in values, being the lowest ones compared to water and ethanol.

Very rare temperature drops could be seen in Fig. A.2.6 (Appendix A.2) for water at 50 W of heat load and cooling fluid temperature of 40°C which means a presence of occasional flow oscillations between dried evaporator periods. Despite these very rare reactivations, the thermal resistance value (Fig. 6.14 (red solid line)) is almost the same compared to the case with cooling fluid temperature of $T_{cool}$ = 20 °C. With heat load increase, thermal resistance significantly decreases due to "oscillatory" mode establishment.

Overall values of thermal resistance for methanol-filled FPPHP slightly decrease without any significant changes into operation behavior, confirming the best operating mode

for this fluid. For ethanol-filled device, any significant changes in operation have not been observed.

Better device performance for FPPHPs tested at $T_{cool}$ = 40 ºC can be explained by the higher value of driving pressure in Eq. (3.4) due augmentation of value of the vapor-liquid saturation line slope ($dP_{sat}/dT$) with operation temperature increase (Fig. 4.10a), and due to diminution of the capillary pressure drop and viscous friction caused by surface tension and viscosity decrease with higher temperature.

It is noticeable that thermal resistance almost converge until the same value for all three cases at highest heat loads (150 W and 200 W).

*6.1.2.3. Influence of the filling ratio*

Filling ratio influence on thermal resistance of the FPPHP filled with water and tested in horizontal position is presented in Fig. 6.15. Augmentation of filling ratio from 50% to 59% at cooling liquid temperature of 20 ºC leads to startup at 100 W of applied power with stable but high amplitude temperature oscillations up to ~70 ºC (Fig. A.2.14-Appendix A.2). From Fig. 6.15, it is clearly seen that thermal resistance for higher filling ratio decreases with heat load augmentation.

Also, higher filling ratio leads to temperature oscillations stabilization for higher cooling temperature ($T_{cool}$ = 40 ºC) which leads to higher thermal resistance decrease compared with FR = 50%. For $T_{cool}$ = 40 ºC, influence of filling ratio on thermal resistance is not as significant as for $T_{cool}$ = 20 ºC but stabilization of temperature oscillation has been observed (Fig. A.2.15 -Appendix A.2).

*6.1.2.4. Influence of the binary mixtures*

If for FPPHP tested in vertical orientation any significant effect of fluid thermophysical properties modification on thermal performance was not noticed (even for some cases FPPHP filled with water operated quite better than water-based mixtures), ethanol and methanol additives positively affected FPPHP operation in horizontal conditions.

FPPHP filled with alcohol aqueous mixtures operates stable with frequent and low amplitude temperature oscillations for both fluids and both cooling fluid temperatures, even

better than FPPHP filled with pure ethanol and methanol (Fig. A.2.1, A.2.2, A.2.9, A.2.10 – Appendix A.2).

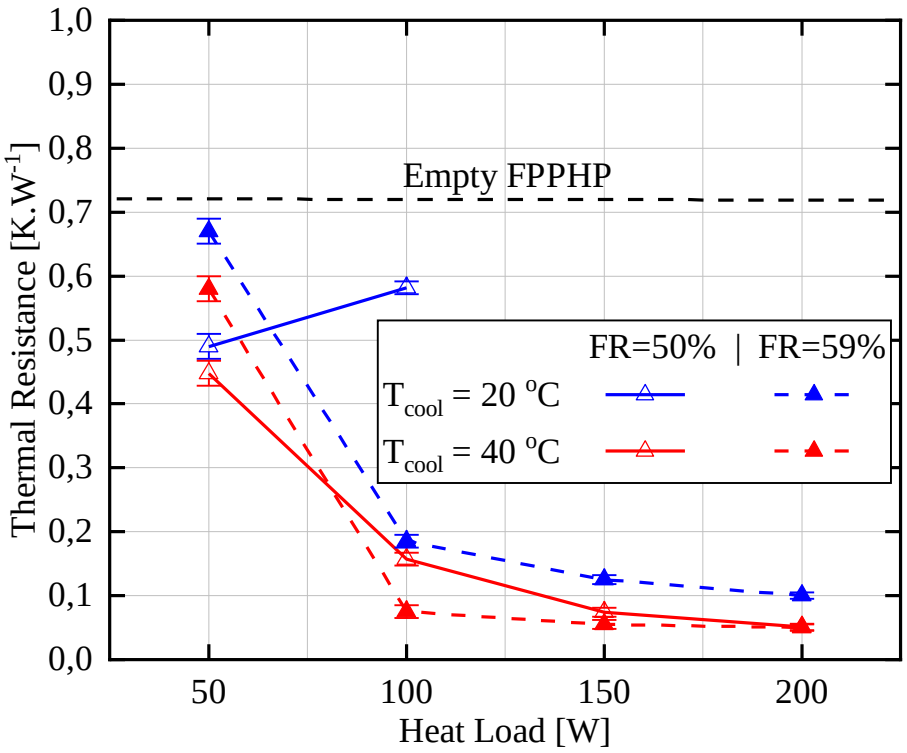


Figure 6.15. Effect of filling ratio on thermal resistances of FPPHP filled with water (horizontal).

As seen on Fig. 6.16, there are almost no difference in thermal performances for device filled with water/ethanol and water/methanol mixtures, especially for $T_{cool}$ = 40 °C, which can be explained by very close values of surface tension (table 6.2). Thermal resistance of water-filled device decreases down to values obtained for alcohol aqueous solutions with heat load augmentation (temperature of cooling fluid $T_{cool}$ = 20 °C).

Exactly same thermal resistance behavior with approximately the same values has been obtained for FPPHP tested with self-rewetting fluids (Fig. 6.17). Despite very close values of thermal resistances, 1-butanol based SRWF operates unstable in comparison with 2-butanol based aqueous solution. Device filled with 5% 2-butanol/water solution stably operates for all levels of applied power with low superheat and slight temperature oscillations during periods of 50 W of heat load.

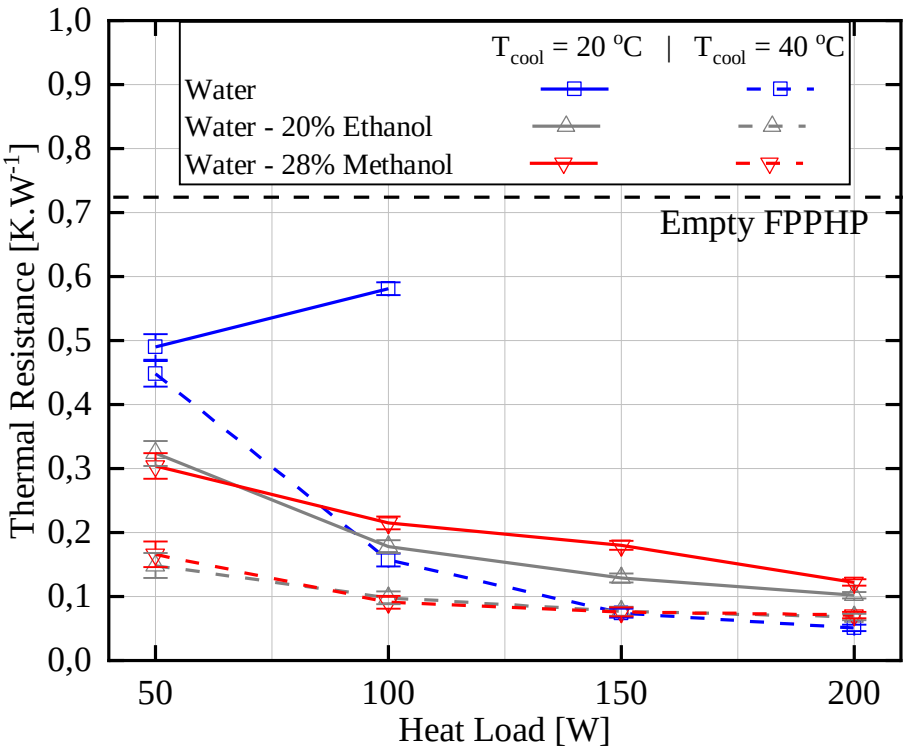


Figure 6.16. Thermal resistances for FPPHP filled with water, ethanol and methanol aqueous solutions at condenser temperature of $T_{cool}$ = 20 °C and $T_{cool}$ = 40 °C (FR = 50%, horizontal).

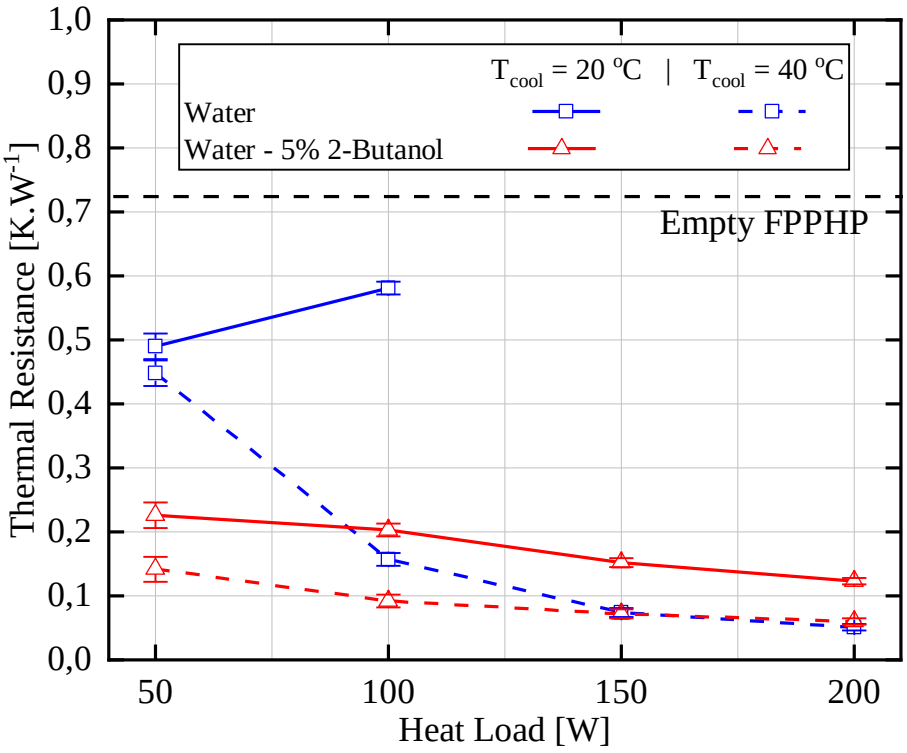


Figure 6.17. Thermal resistances for FPPHP filled with SRWFs at condenser temperature of $T_{cool}$ = 20 °C and $T_{cool}$ = 40 °C (FR=50%, horizontal).

In Fig. A2.4 and A.2.12 – Appendix A.2 – could be seen that, in horizontal position, FPPHP filled with self-rewetting fluid (2-butanol) operates in optimal mode with high frequent and low amplitude oscillations for both temperature levels of condenser cooling fluid. Heat load augmentation provokes overall non-significant evaporator temperature rise keeping the same operational mode. These evaporator temperature increases lead to smooth decrease of thermal resistance values.

Operation behavior and evaporator temperature evolution for the FPPHP filled with water/surfactant solution are almost the same as the case with pure water at 50 W of heat load and at cooling fluid temperature of 20º C (Fig. A.2.5 – Appendix A.2). But, contrary to the case of water-filled device, where heat load augmentation leads to total operation failure, startup is reached at 50 W of applied power for water/surfactant solution. Moreover, stable temperature oscillations have been observed only for 100 W of heat load (Fig. A.2.13 – Appendix A.2). Heat load increase up to 150 W led to temperature increase exceeding 100 ºC.

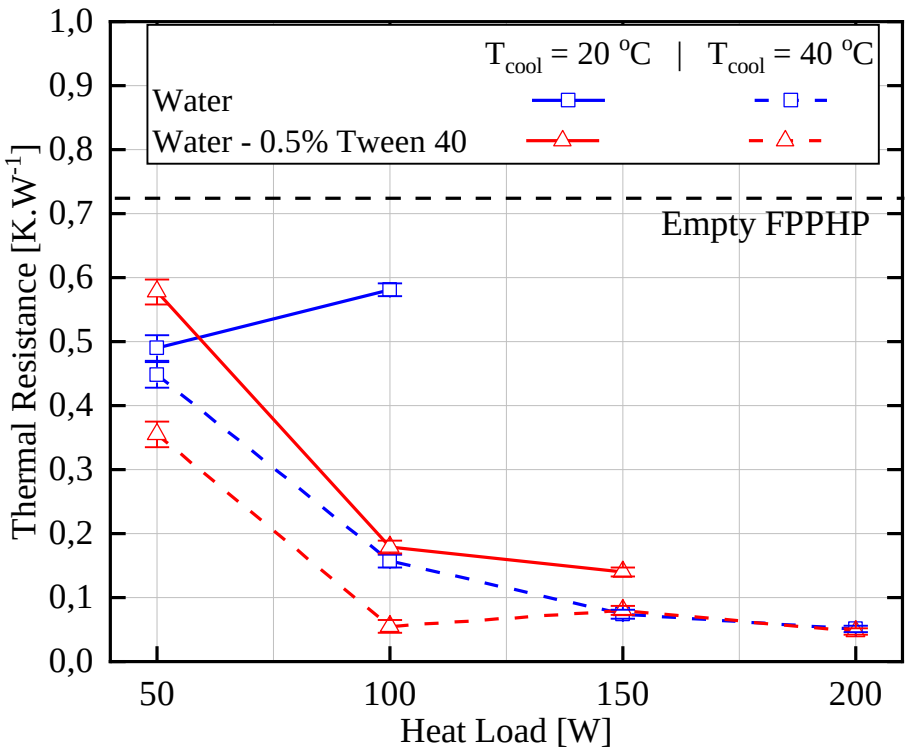


Figure 6.18. Thermal resistances for FPPHP filled with Tween 40© aqueous solution at condenser temperature of $T_{cool}$ = 20 ºC and $T_{cool}$ = 40 ºC (FR = 50%, horizontal).

With condenser cooling temperature of 40 ºC, the thermal resistance decreases (Fig. 6.18) with heat load increase for both fluids. But, if for water the FPPHP startup and stable "oscillatory" operation occurs at 100 W of applied power, for water/surfactant case, operation is not stable – with rare high temperature peaks and almost smooth –dried- periods, which could be provoked by foam generation (see section 4.6.3) and augmentation of flow resistance inside the channel.

*6.1.2.5. Influence of the non-condensable gases presence*

The temperature and pressure histories for water-filled FPPHP with non-condensable gases presence and tested at $T_{cool}$ = 20 ºC are presented in Fig. 6.19. Period for 50 W of heat load characterized by almost horizontal (500 – 800 s) pressure and temperature curves with values of ~30 kPa and ~72 ºC, respectively. Same behavior have been observed for the device filled without NCG presence (1100 – 3000 s in Fig. 6.11) but with lower pressure and evaporator temperature values (~6.5 kPa and ~50 ºC, respectively). However, with heat load augmentation till 100 W, start-up is reached and device operates with high amplitude and frequent pressure oscillations, contrary the case with pure water, where any oscillatory operation was not found.

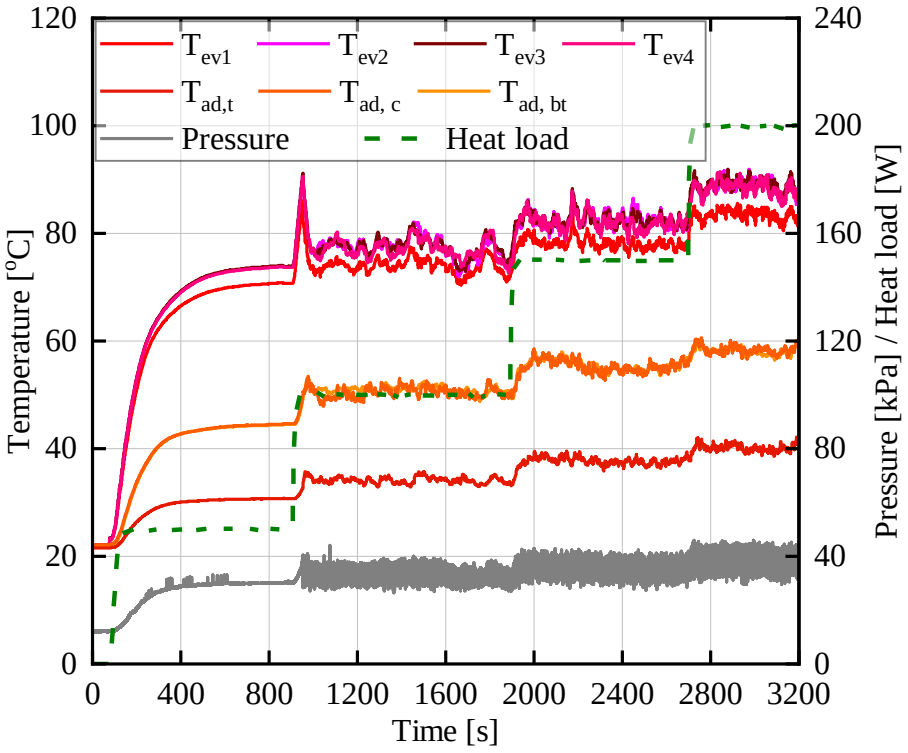


Figure 6.19. Temperature and pressure responses for FPPHP filled with water and NCG (FR=50%; $P_{sys}$ = 15 kPa; $T_{cool}$ = 20 ºC, horizontal).

Augmentation of the cooling temperature have not change significantly device operational behavior, except few temperature drops during period for 50 W of heat load (500 – 1100 s in Fig. A.2.16 – Appendix A.2) and overall system temperature increase.

### *6.1.3. Conclusions on ground tests*

During ground tests, the parametric study of the FPPHP filled with different fluids was provided. In vertical position, PHP operates almost all time as an interconnected thermosiphon. Device, operated in horizontal conditions operated in the oscillatory mode then star-up is reached (usually at 100 W of applied power), except water-filled FPPHP tested at $T_{cool}$ = 20 ºC, which has worse thermal performance in these conditions. Alcohol aqueous mixtures using as a working fluids lead to the thermal performance improvement, comparing to pure liquids (especially water). Condenser fluid cooling temperature augmentation also leads to FPPHP heat performance improvement. Device, filled with water-surfactant solutions shown very unstable operation despite lower thermal resistances compared with pure water. Non-condensable gases presence leads to overall system thermal performance degradation, but provokes stable oscillatory operation of tested FPPHP.

## 6.2. Parabolic flight tests

Characterization of the FPPHP for different gravity levels has been done during 69$^{th}$, 71$^{st}$ and 74$^{th}$ ESA Parabolic Flight Campaigns (PFC). Present section is focused on temperature and pressure signals analyses obtained during parabolic flight tests in the context of various gravity levels, heat load and working fluid thermodynamic properties influence on the FPPHP operation.

### *6.2.1. Experimental procedure*

Molybdenum FPPHP ($N$ = 7) covered with sapphire transparent plate and filled with ethanol has been tested during ESA 69$^{th}$ PFC. Several devices filled with water, water/5% 1-butanol mixture and water with presence of non-condensable gas (NCG) have been tested during ESA 71$^{st}$ PFC. Test parameters are presented in table 6.3. Note that only tests cases that could be exploited in this part are presented in this table.

Finally, FPPHP filled with water, water with 16% of ethanol and with 28% of methanol (in weight) solutions have been tested under Lunar, Martian and micro-gravity conditions (all parameters are presented in table 6.4) during ESA 74th PFC.

Table 6.3. Experimental matrix for microgravity tests (69th and 71st PFCs)

| **№ Parabola** | **PHP type** | **Working fluid** | **Heat Load** |
|---|---|---|---|
| Parabolic flight campaign 69th | | | |
| 16-20 | Mo/Sa | Ethanol FR = 40 % | 100 W |
| 26-30 | | | 150 W |
| Parabolic flight campaign 71st (day 1) | | | |
| 6-10 | Co/Sa | Water + NCG FR = 50% | 50 W |
| 10-15 | Co/Sa | Water + NCG FR = 50% | 100 W |
| 16-20 | Co/Sa | Water + NCG FR = 50% | 150 W |
| Parabolic flight campaign 71st (day 3) | | | |
| 6-10 | Co/Co | Water – 5% 1-butanol FR = 50% | 50 W |
| | Co/Sa | Water FR = 50% | |
| 10-15 | Co/Co | Water – 5% 1-butanol FR = 50% | 100 W |
| | Co/Sa | Water FR = 50% | |
| 16-20 | Co/Co | Water – 5% 1-butanol FR = 50% | 150 W |
| | Co/Sa | Water FR = 50% | |

Tables with experimental parameters provide following information about tested FPPHP and test conditions: metal-base plate material (Mo – molybdenum and Co – copper) in which channels are engraved and material of covering plate (sapphire – Sa, and copper – Co, for example); working fluid and filling ratio; applied heat loads, and gravity acceleration levels.

The FPPHP has initially been installed in a vertical position related to the floor of the aircraft. As it was previously discussed, in vertical position gravity vector assists the liquid plugs to flow back to the evaporator zone (in bottom heating mode) but, for parabolic flight tests, gravity level influences liquid plugs movements just during the periods between parabolas – during microgravity periods position of device is irrelevant. During this study, tests have been performed for FPPHPs in bottom heated mode (BHM) under different heating configurations.

After parabola “0” of each test day, power has been provided to the heaters. After the end of each set of five parabolas, value of heat load has been changed to planned one for next parabolas set (or kept the same if necessary) to reach quasi-established thermal regime. The detailed description of the parabolic flights and test procedure are presented in sections 5.1 and 5.4.2.

Table 6.4. Experimental matrix for 74th PFC tests (copper-copper FPPHP)

| **№ Parabola** | **Working fluid** | **Heat Load** | **Gravity level** |
|---|---|---|---|
| Day1 | | | |
| 0-5 | Water *FR*=50% | 50 W | Martian (*0.38g*) |
| 6-10 | | | Lunar (*0.18g*) |
| 10-15 | | | μ-gravity (*0.01g*) |
| 16-20 | | 150W | μ-gravity (*0.01g*) |
| 21-25 | | | Lunar (*0.18g*) |
| 26-30 | | | Martian (*0.38g*) |
| Day 2 | | | |
| 0-5 | Water – 16% Ethanol *FR* = 50% | 50 W | μ-gravity (*0.01g*) |
| 26-30 | | 150 W | μ-gravity (*0.01g*) |
| Day 3 | | | |
| 6-10 | Water – 28% Methanol *FR* = 50% | 50 W | μ-gravity (*0.01g*) |
| 21-25 | | 150 W | μ-gravity (*0.01g*) |

*6.2.2. Overall thermal behavior of the FPPHP tested during PFCs*

During the short periods of microgravity (~20 s), both thermal and hydraulic regimes are not established due to high thermal inertia of the FPPHPs. Fig. 6.20 presents typical temperature and pressure behavior for the FPPHP tested during five subsequent parabolas for the molybdenum-sapphire FPPHP filled with ethanol (ESA PFC 69). Although only one case is presented, the main behavior observed for microgravity conditions are representative of all other levels of heat power applied and all other tested fluids. Figures for all other tests conditions could be found in Appendix B (Fig. B.1.1 to B.3.3). Here will be presented mostly qualitative analysis of the FPPHP behavior for tests conducted during parabolic flights with explanation of the main related phenomena.

First of all, Fig. 6.20 represents temperature and pressure variations for the molybdenum device covered with sapphire plate, during a set of five consecutive parabolas inducing normal, hyper- and micro- gravity conditions, for 100 W of applied heat power. Evaporator temperature curves are colored in the shadows of red, adiabatic zone temperature is in orange and cooling one in blue. Gray curve represents values of the system pressure and dashed grey one level of gravity acceleration. First, it should be noted that hypergravity phases have practically not significant influence except a slight decrease of the temperature and pressure profiles compared to normal gravity conditions. A little difference between the evaporator temperatures can be observed for normal and hypergravity conditions. But, with the onset of microgravity, a decrease of this gap and a homogenization of the temperature profile occur, and is maintained until the gravity level normalization. Then, a temperature rise is observed

for the evaporator temperatures during each microgravity phases. The latter is due to all liquid collection in the condensation zone and so to evaporator dry-out (Fig. 6.21) – heat being transferred from evaporator to condensed only by FPPHP heat conduction through the metallic and sapphire plates.

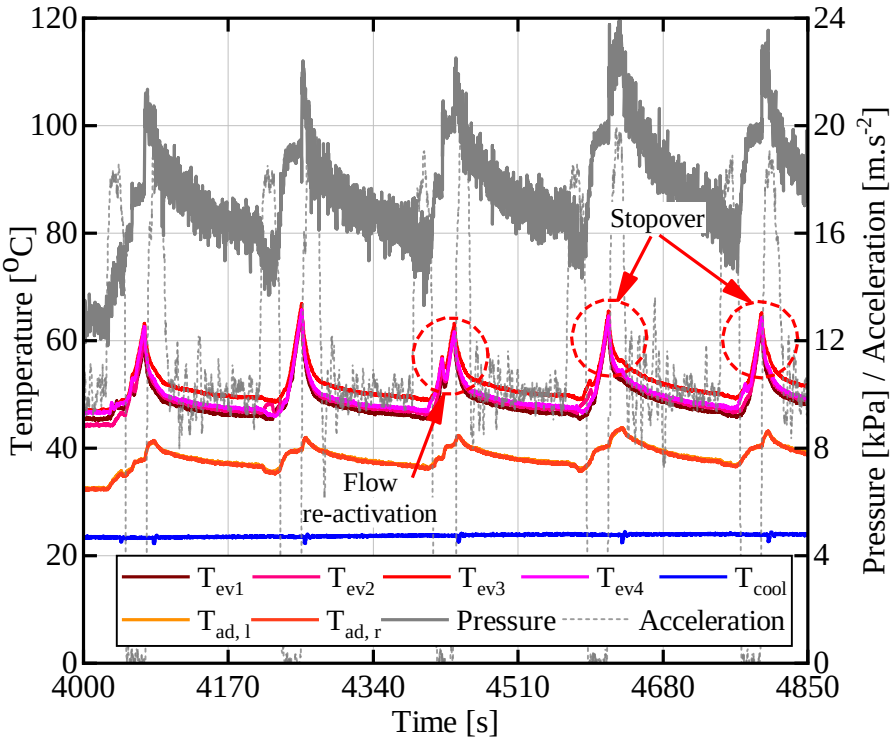


Figure 6.20. Transient temperatures, pressure and acceleration responses during a series of 5 successive parabolas for molybdenum-sapphire (Mo/Sa) FPPHP at heat load of 100 W (ethanol, FR = 40%, $T_{cool}$ = ~25 °C).

As could be seen in Fig. 6.21a, during normal gravity, semi-annular/annular flow patterns are predominant for ethanol-filled FPPHP, but during almost all parabolas (without temperature drops) liquid remains accumulated in the condenser zone in the form of liquid plugs. At the same time, without liquid re-flow into evaporator, dry-out occurs with low amplitude liquid plug oscillations.

Sometimes, evaporator temperatures suddenly and arbitrarily drops during microgravity periods, as well observable instantaneous pressure rise which corresponds to some changes in flow regime and fluid entering in the evaporator causing sensible and latent heat transfer between superheated walls and subcooled liquid also called “re-activation” phases (Fig.

6.20, parabola 3, indicated by a red circle). The mechanism of reactivations and fluid flow behavior during microgravity will be discussed in details in Chapter 7.

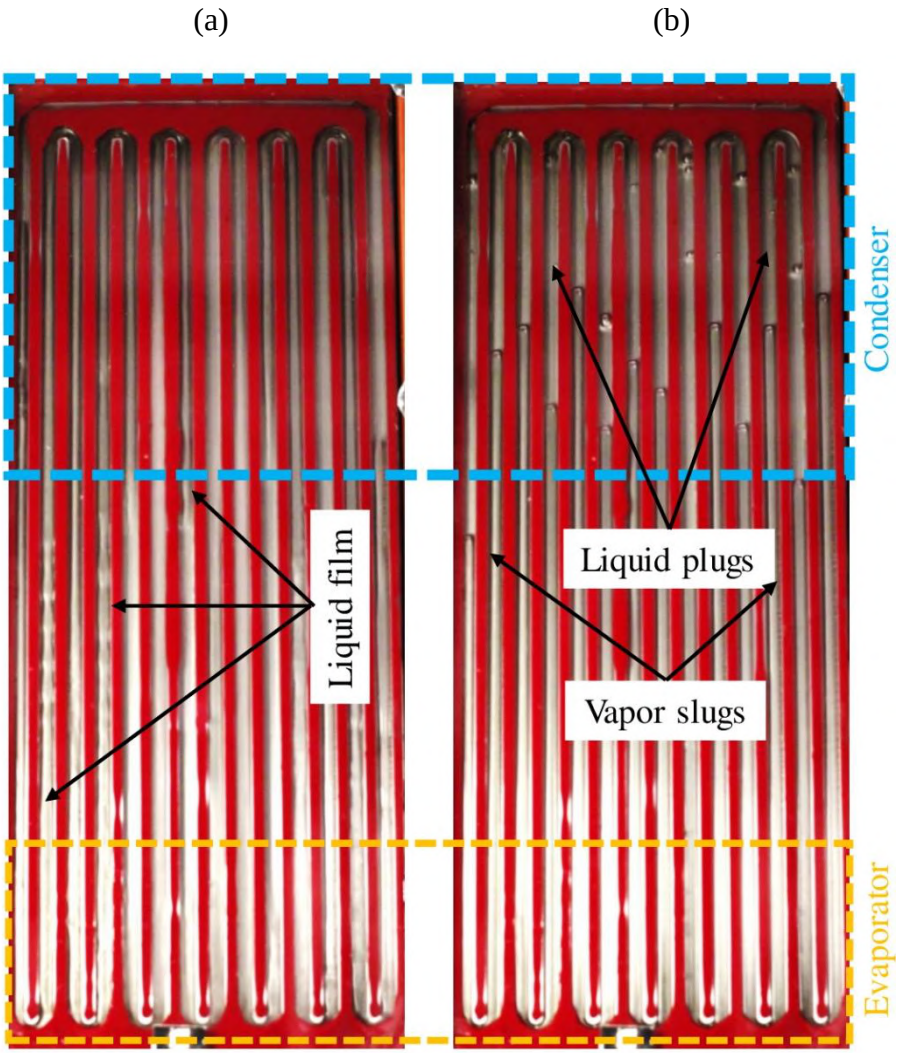


Figure 6.21. Flow pattern for FPPHP for (a) normal gravity and (b) microgravity.

*6.2.3. Influence of fluid thermodynamic properties on FPPHP behavior during parabolic flight campaign.*

Results for FPPHP filled with water, water/16% ethanol, water/28% methanol and water/5% 1-butanol solutions and obtained during 71$^{st}$ and 74$^{th}$ ESA Parabolic Flight Campaigns will be presented in this section. Note that only copper/copper FPPHPs have been used for these tests campaigns, so visualizations were obviously impossible. Thus, following analyses and explanations will be drawn based on our experience of previous visualization campaigns on such device. Fig. 6.22 – 6.25 represent temperatures and pressure

behaviors for all four tested cases at 50 W of applied power (figures for 150 W of applied power are available in Appendix B). In analogy with previous sections, curves, representing evaporator temperatures, are colored in the shadows of red, adiabatic – yellow and blue for secondary cooling liquid. Pressure is represented by grey curves and gravity acceleration by grey dashed curves.

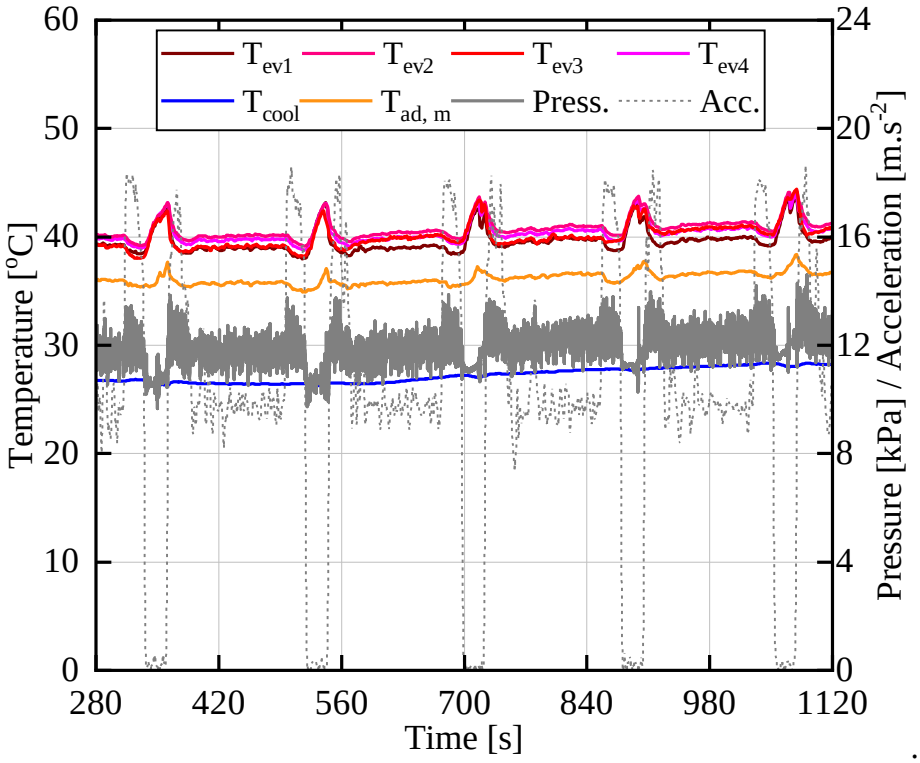


Figure 6.22. Temperature behavior of FPPHP filled with water (Co/Co, Q=50 W, $T_{cool}$ = ~25 °C, ESA PFC 74).

During normal gravity periods, FPPHP filled with water operates stably with low temperature oscillations (in the range of the measurements uncertainty). Some temperature changes have been observed due to changes of secondary cooling fluid temperature. Should be noted, that secondary fluid temperature is not constant, but slightly increases with time, due to heat sink direct link with ambient air in the aircraft – so, cooling temperature depends not only on heat load, but also on temperature of surrounding air. That said, hypergravity periods are accompanied with small temperature drops and pressure augmentation. Temperature augmentation, provoked by liquid accumulation in the condenser zone and by evaporator dry-out (explained in the beginning of this section), have been observed for all parabolas. Device operation reactivation phases, followed by temperature sudden decrease

and pressure drops, have been observed for first, fourth and fifth parabolas. Higher heat load does not almost influence temperature behavior during normal gravity (but with augmentation of overall evaporator temperature) and microgravity period are characterized by higher temperature peaks and rare reactivations (parabolas 1, 2 and 5 in Fig. 6.30).

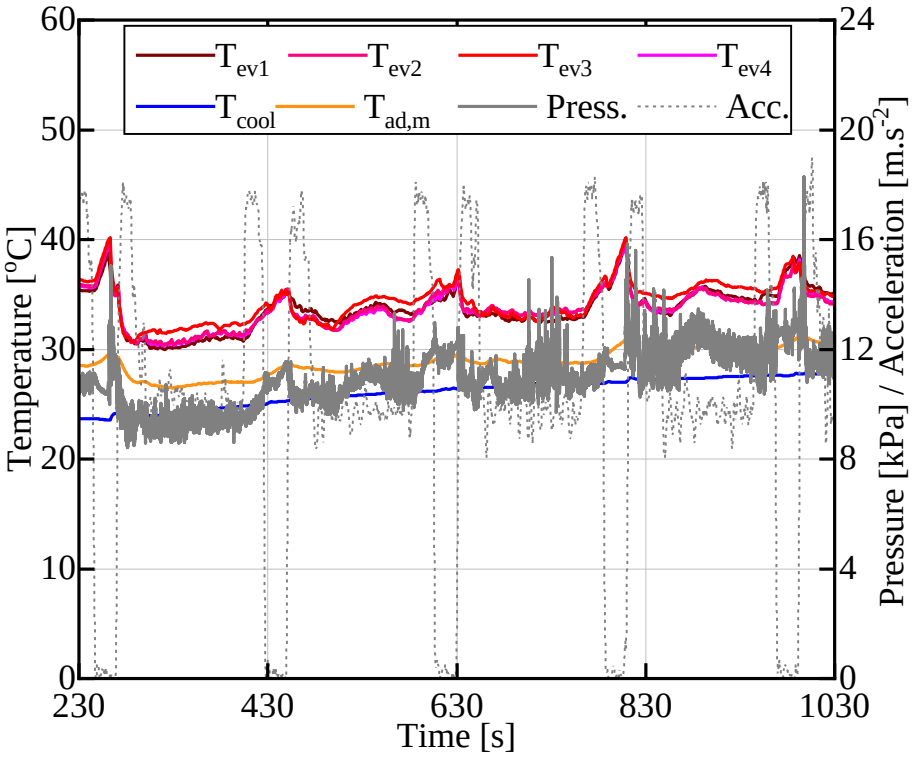


Figure 6.23. Temperature behavior of FPPHP filled with water/16% ethanol (Co/Co, Q = 50 W, $T_{cool}$ = ~25 °C, ESA PFC 74).

Temperature histories for device filled with water/ethanol mixture are presented in Fig. 6.23. Because it was the first test for the second day of flights and heat load has been applied just before end of parabola "zero", temperature increases in a similar way than the one observed in vertical on-ground tests – without oscillations, showing that the start-up did not really occurred. It seems that temperature level becomes stable just before first parabola, and the transition between microgravity and beginning of hypergravity phases provokes the change of device operation mode accompanied with temperature drop and following stabilization with lower temperature level and low temperature oscillations amplitude. Then, microgravity periods, are characterized by evaporator temperature augmentation but this time with more frequent temperature fluctuations, attributed to reactivations phases, than with water case. Probably, for this case, liquid was not accumulated in the condenser zone and dry-out was not reached, but FPPHP operates in the pulsating mode with reduced

oscillation frequency. Also, pressure oscillations during microgravity phases seem to confirm these trends.

Higher heat load level of 150 W leads to small temperature oscillations amplitude augmentation and overall evaporator temperature rise (as it is the case with water) during normal gravity. Note that despite significant evaporator temperature augmentation (normally states about dry-out) during microgravity periods, regular reactivation have been observed for all parabolas (Fig. B.3.3 – Appendix B.3) – it could be clearly seen with pressure oscillations, which mean oscillatory flow inside FPPHP.

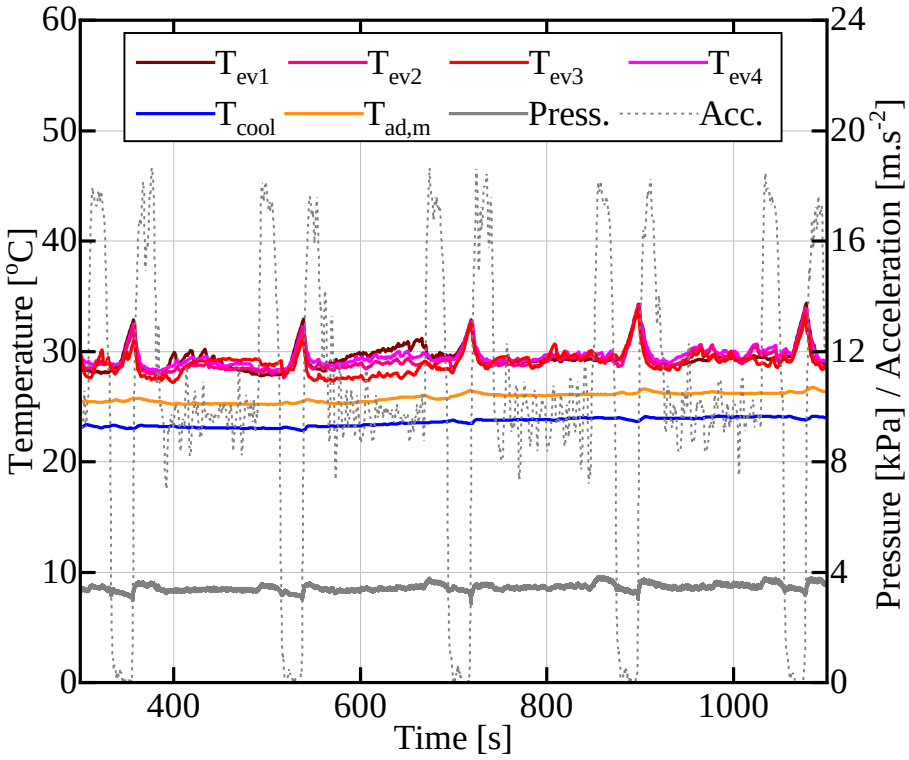


Figure 6.24. Temperature behavior of FPPHP filled water/28% methanol (Co/Co, Q=50 W, $T_{cool}$= ~25 °C, ESA PFC 74).

From Fig. 6.24 it could be seen that for FPPHP filled with water/methanol mixture, high amplitude fluctuations are present for normal gravity periods. However, and unfortunately, any temperature or pressure drops have not been observed for microgravity phases. This fact indicates that for this fluid at 50 W of applied power, dry-out without any flow reactivations takes place during each parabola.

Finally, last tested fluid is 5% 1-butanol aqueous solution, being a self-rewetting fluid. During ground tests, water/1-butanol filled FPPHP have shown pretty good performances

(Fig. 6.25), especially in horizontal orientation. Thermal behavior for the FPPHP filled with this solution and tested during parabolic flight at 50 W of applied heat power is very similar to the case with pure water - during normal gravity period any significant temperature and pressure oscillations were not observed. Moreover, during all five parabolas any fluid flow reactivation accompanied with temperature drop have not been registered.

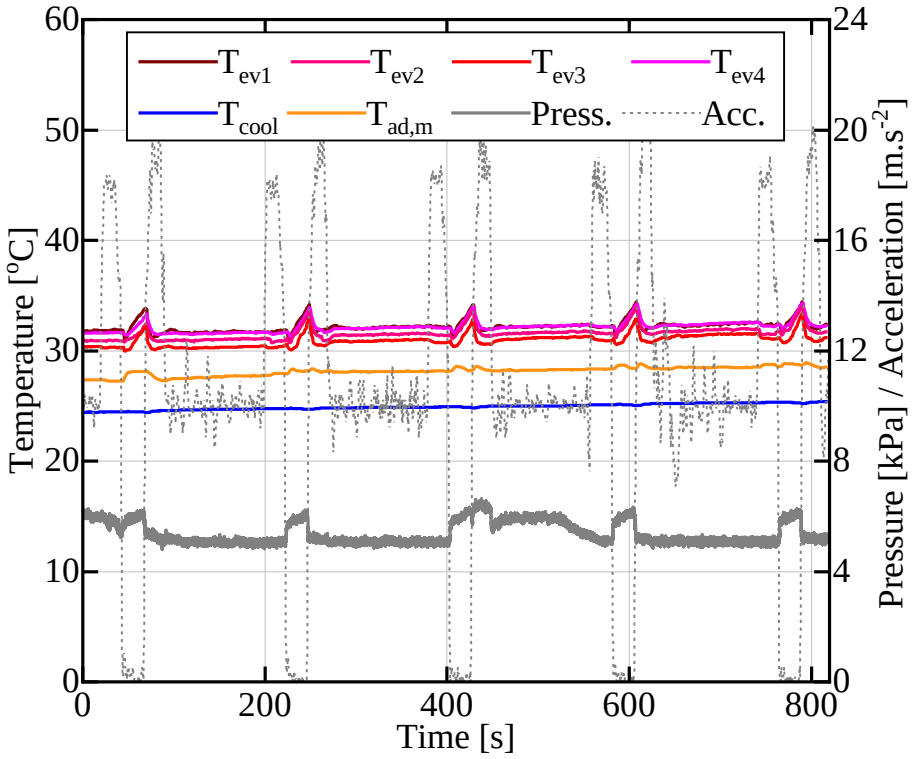


Figure 6.25 Temperature behavior of FPPHP filled water – 5% 1-Butanol (Co/Co, Q=50 W, $T_{cool}$ = ~25 °C, ESA PFC 71).

Nevertheless, despite similarities in behavior, the overall evaporator temperature is almost 10 °C lower for 1-butanol solution than for pure water. Better channel walls wetting and higher thin-film evaporation rate could have caused this. Heat load augmentation up to 150 W leads to overall evaporator temperature increase and provoke oscillations with higher amplitude during normal gravity periods. Note that for the other cases, temperatures peaks are almost equal for all parabolas (during one set), but for water/1-butanol solution, the peak temperature values varies from one parabola to another.

*6.2.4. Influence of the non-condensable gases presence on FPPHP operations under microgravity conditions*

All results obtained for copper – sapphire (Co/Sa) FPPHP during ESA 71st Parabolic Flight Campaign are presented in the form of temperatures and pressure evolutions, as well as differences between average evaporator temperature during normal gravity periods and peaks during parabolas, to explain FPPHP operating behavior for different gravity levels with and without non-condensable gas injection.

Temperatures, pressure and acceleration profiles for the FPPHP tested at 100 W applied heat load on a set of five subsequent parabolas are shown in Fig. 6.26 for the PHP filled with deionized water, and Fig. 6.27 for the PHP with water with NCG, respectively.

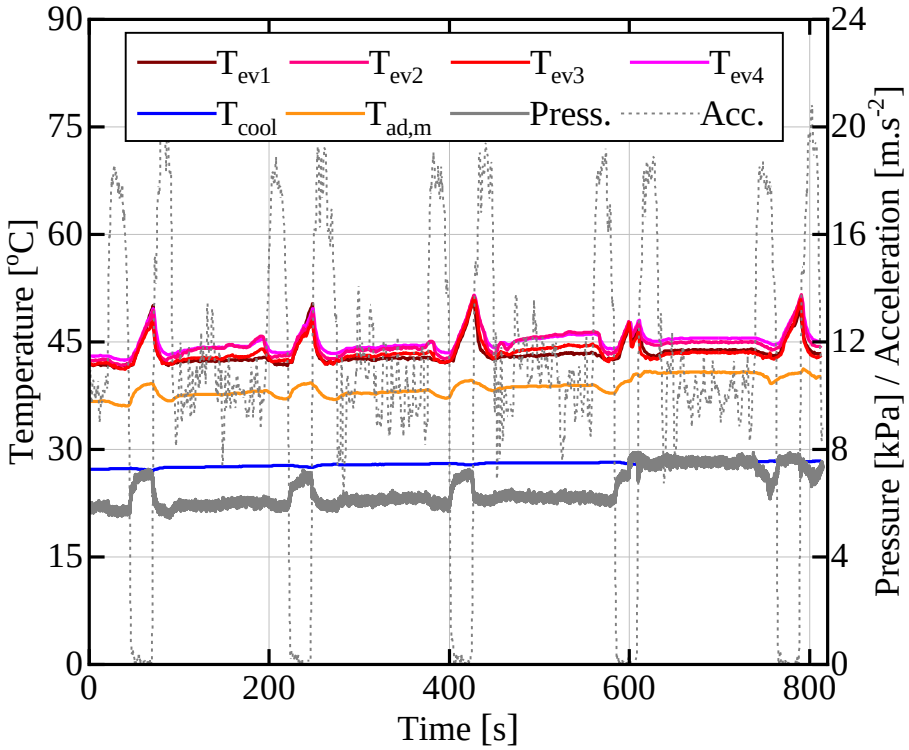


Figure 6.26. Test results for the FPPHP filled with deionized water (Co/Sa, Q = 100 W, $T_{cool}$ = ~27 °C, ESA 71st PFC).

Microgravity periods are characterized by significant temperature rises in the evaporation and adiabatic zones: they are due to a transition from nucleate boiling/annular flow pattern, under normal/hypergravity, to slug-plug flow pattern under microgravity. All microgravity phases are accompanied by a fast dry-out of the evaporator and the liquid accumulation in the condensation zone. Unfortunately, durations of such phases are too low

to reach fluid flow reactivation process, thus almost all parabolas are accompanied by smooth temperature peak curves. Nevertheless, some spontaneous hydraulic instabilities sometimes occur and following temperature drop could be observed due to initial fluid distribution in the beginning of microgravity phases and possibility on liquid plugs motions under influence of small pressure fluctuations. Temperature and pressure characterization of reached instabilities can be observed in Fig. 6.26(4th parabola) and in Fig. 6.29a.

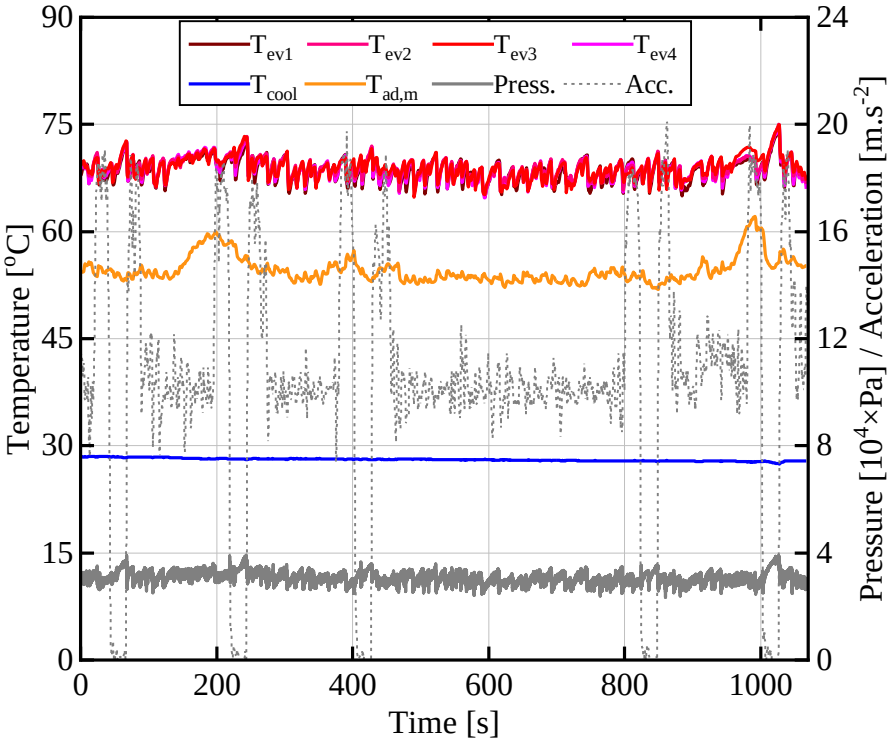


Figure 6.27. Test results for the FPPHP filled with water and NCG (Co/Sa, 100 W, $T_{cool}$ = ~28 °C, ESA 71st PFC).

On the other hand, under low heat load (50 W, Fig. B.2.5 – Appendix B.2), the FPPHP with presence of NCG seems to operate quite similarly to PHP with pure water, except that the overall system pressure remains higher and the following evaporator temperatures increase up to ~25 °C compared to the case with pure water (Fig. B.2.3 – Appendix B.2), leading to an overall system efficiency degradation. The temperature distribution along the adiabatic zone is quite close to a heat conduction profile. Several factors influence such thermal performances degradation: according to O'Connor *et al.* [6.18], NCG injection to the close equilibrium two-phase systems leads to total system subcooling, which means that boiling will start with higher surface superheat than for pure water. Gas presence in slug

form, in the evaporation and condensation zones, also reduces heat transfer effectiveness due to heat transfer surface occupation and liquid/vapor contact prevent with it.

For higher heat loads (100 W and 150 W, Fig. 6.27 and B.2.6), the presence of NCG seems to provoke regular temperature and pressure fluctuations, whatever the gravity levels, which means alternate movements of liquid and gaseous (vapor/air) phases in form of slug/plug flow, unlike the case with pure water (Fig. 6.26).

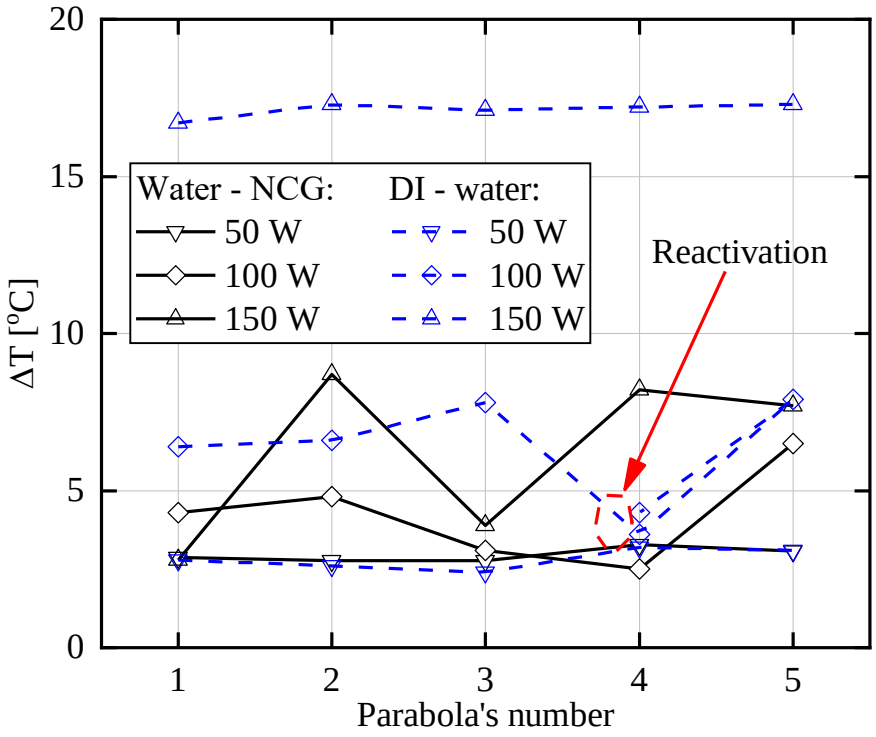


Figure 6.28. Temperature overshoots during parabolas.

Values of evaporator temperature differences ("$\Delta T$") between average temperatures during normal gravity and maximum temperatures during microgravity periods are presented in Fig. 6.28 as functions of parabola's number. Tests for low heat loads show almost the same values, with and without NCG, which can be explained by short microgravity periods and high PHP thermal inertia. Following power increase shows progressive and noticeable rise of temperature peaks for pure water (almost 7 times higher at 150 W than at 50 W); but these rises are much higher than those with NCG. Note that for the 4$^{th}$ parabola with instabilities, at 100 W, overshoot value is lower than for other peaks, but still higher than with NCG. On one hand, the curves of $\Delta T$ do not almost vary (horizontal line) for PHP with pure water, which demonstrates a certain regularity. On the other hand, for PHP with NCG,

the curves of $\Delta T$ show an unstable behavior but with much smaller values and distribution (some values at 100 W or 150 W are lower than at 50 W).

Fig. 6.29 presents pressure and temperature curves in the evaporator near pressure transducer location. Fig. 6.29a represents two consecutive parabolas (3rd and 4th) for pure water at 100 W applied of heat power. During the first one, smooth temperature peak and evaporator dry-out have been observed, while, during the second one, instabilities have been noticed. During normal gravity periods, pressure oscillations are relatively low (note that oscillations here correspond to the pressure transducer uncertainty range). Some pressure fluctuations are however noticeable just as temperature ones, due to some spontaneous fluctuations in gravity levels (see dotted grey curve). During microgravity periods (see first parabola), pressure reaches peak value with following sharp drop, but on the second parabola short pressure stabilization with subsequent increase until parabola's end can be noticed.

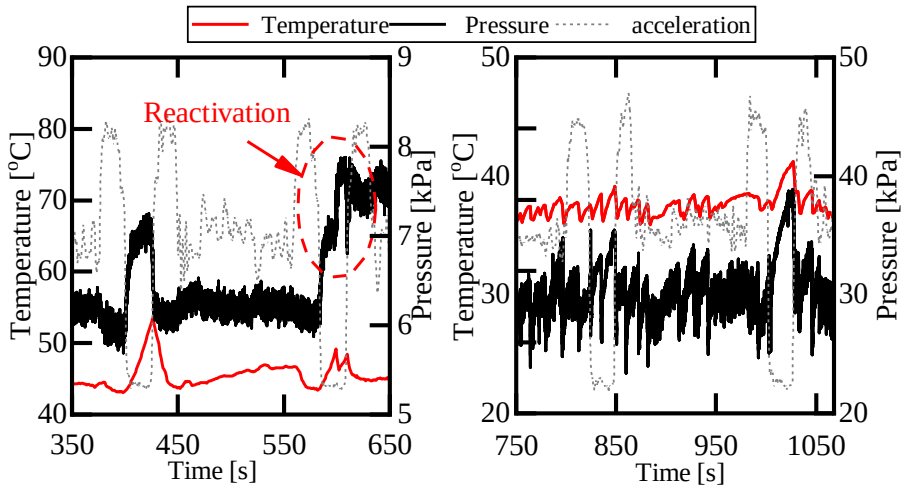


Figure 6.29. Pressure and temperature instabilities during two successive parabolas at 100 W for FPPHP filled with (a) DI water and (b) water - NCG.

Fig. 6.29b presents pressure and temperature oscillations for water and NCG during the same 3rd and 4th parabolas. No significant changes in temperature and pressure are noticeable for the three gravity levels during first parabola, which means continuous slug/plug flow motion. Temperature rise, such as pressure increase, can be observed during the second parabola. However, unlike case with pure water, a significant pressure surge happens before end of parabola, corresponding to a change of flow pattern.

*6.2.5. Results comparison for micro(μ), Lunar and Martian gravity levels.*

This subsection will present discussion on gravity level influence on water filled FPPHP operation behavior for 150 W of applied power, as a more representative case. All tests have been performed during the ESA 74$^{th}$ Parabolic Flight Campaign.

Thermal behavior of water-filled FPPHP tested under microgravity conditions (presented in Fig. 6.30) have been casually discussed in previous sub-section. As shown in Fig. 6.30, normal gravity conditions are characterized by evaporator temperature smooth oscillations. In the same way, during microgravity periods, FPPHP mostly operate in "dried" mode, accompanied with high temperature rise, with short-term reactivations (parabolas 2, 3 and 5).

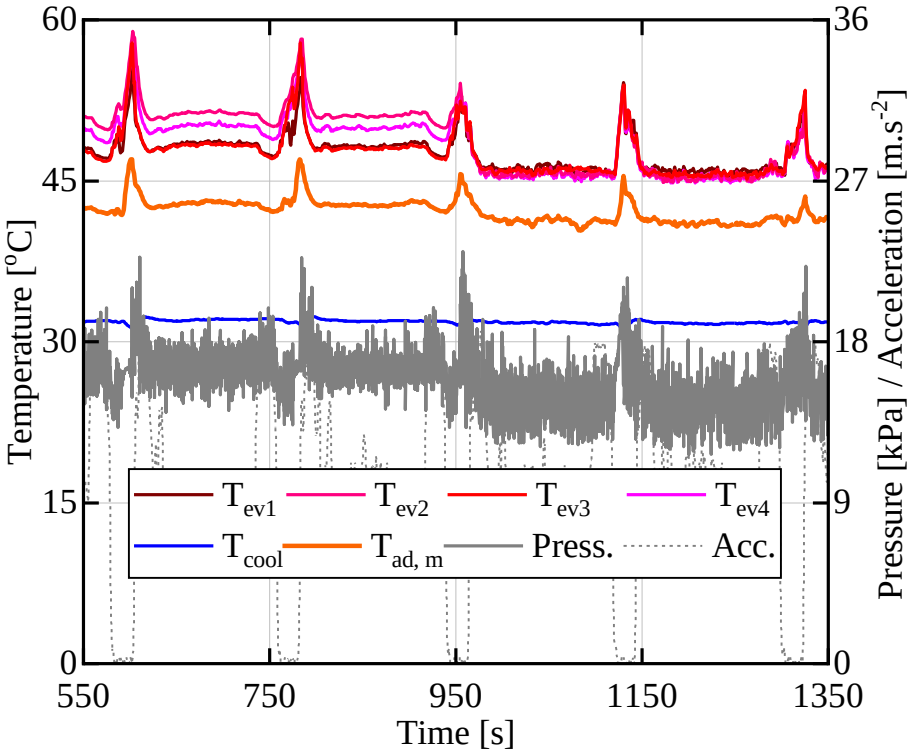


Figure 6.30. Transient temperatures, pressure and acceleration responses during a series of 5 successive parabolas for copper FPPHP at heat load of 150 W (water, microgravity, ESA PFC 74).

For lunar gravity conditions, evaporator temperature increases (~2-3 °C) are observed (Fig. 6.31). The maximum peak temperature is about three times lower than for microgravity. High and very frequent temperature oscillations, as well pressure oscillations, have been

registered during all parabolas and, probably, can be explained by absence of full stopover – present gravity force assists the liquid reflows back to evaporator.

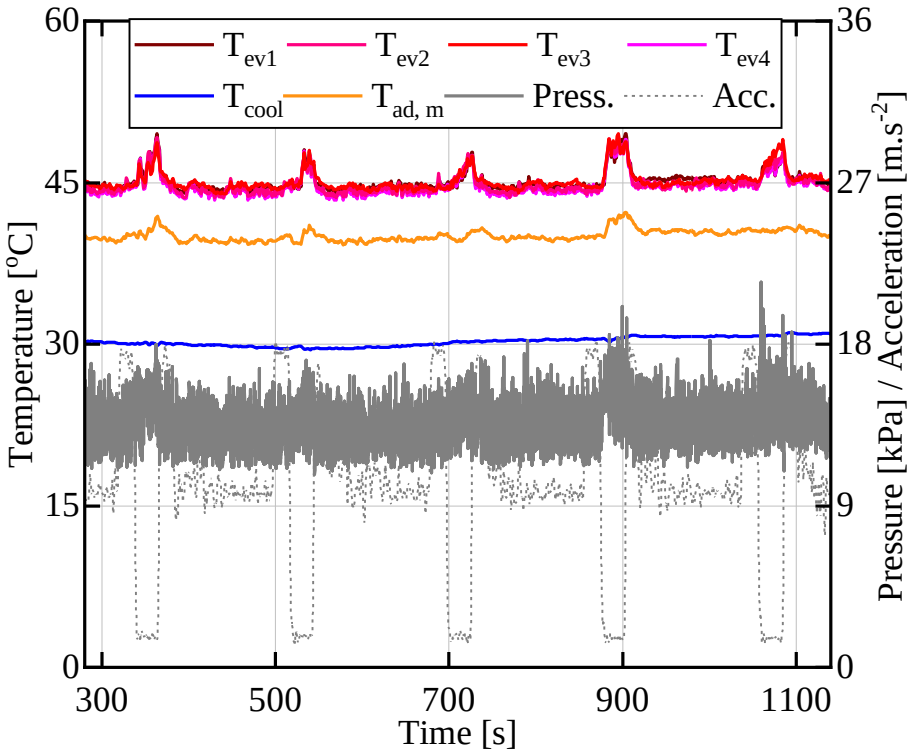


Figure 6.31. Transient temperatures, pressure and acceleration responses during a series of 5 successive parabolas for copper FPPHP at heat load of 150 W (water, Lunar gravity, ESA PFC 74).

Fig. 6.32 represents temperature thermal behavior of device tested under Martian gravity conditions. It is clearly seen that there are not any significant temperature or pressure changes caused by martian gravity. It seems that the level of gravity does not influence that much the operation of the FPPHP, at least on a range from the Martian (0.38 g) to the hyper (1.8 g) gravity levels. Unfortunately, this point has not been treated in the frame of this work, and would require further study.

### *6.2.6. Conclusion on parabolic flight tests*

Experimental results obtained for FPPHPs filled with different fluids and tested during parabolic flights have been analyzed in this section. During microgravity periods, temperature augmentation of evaporator temperature was observed for all tested cases. During most of parabolas, evaporator temperature augmentation was accompanied by a

smooth increase of the system pressure caused but evaporator dry-out and vapor superheating. However, some microgravity periods were accompanied with sudden temperature and pressure drops, which mean flow changes inside the PHP (will be analyzed in next chapter). For the device filled with water-ethanol mixture, these flow re-activations were observed much often than for other tested fluids.

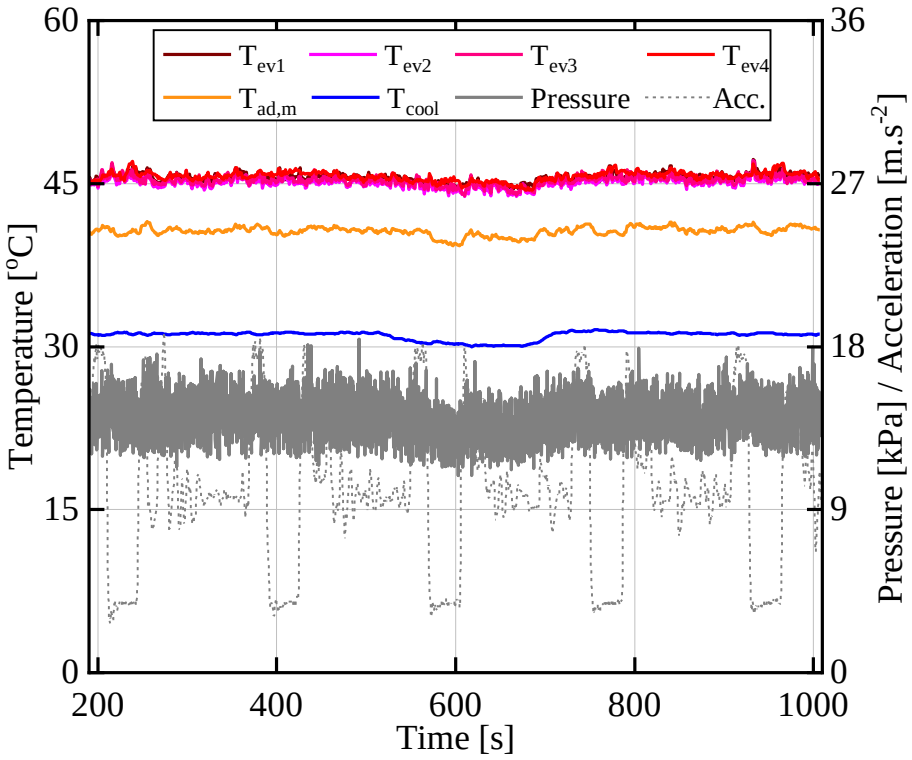


Figure 6.32. Transient temperatures, pressure and acceleration responses during a series of 5 successive parabolas for copper FPPHP at heat load of 150 W (water, Martian gravity, ESA PFC 74).

Presence of the NCG provokes not only the overall temperature augmentation, but also induces stable oscillatory operation of the device during both normal and microgravity phases with temperature increase (during microgravity) quite lower than for pure water (similarly to behavior observed and explained in section 6.1.2.5).

Finally, tests for three different levels of gravity (micro, Lunar and Martian) shown evaporator temperature increase during lunar gravity phases, but with frequent flow reactivations (unlike microgravity); and any difference for FPPHP operating behavior for Martian gravity, compared to the terrestrial.

## 6.3. Conclusions

In this chapter, influence of parameters on FPPHP operation, as well as orientation, cold source temperature, filling ratio, fluid thermodynamic properties and microgravity level, have been studied.

Main conclusions are the following:

Concerning ground tests in vertical position, any significant difference in operation behavior of FPPHP for all tested pure fluids has not been found (except different operational temperature ranges, and observed instabilities for device filled with 1-butanol and Tween 40 aqueous solutions). If for 50 W of applied power, thermal resistances greatly differ, no significant changes have not been observed for higher heat loads. Filling ratio augmentation has not a significant effect on FPPHP thermal performances.

Operation behavior of water-filled FPPHP in horizontal position is very different from vertical orientation, especially for low cold source temperature. If for vertical position, no start-up has been reached just for 50 W of applied power, FPPHP in horizontal position operates in “dry” mode for 50 W and 100 W of heat loads. Total system failure has been observed with heat load augmentation. On the contrary, other tested fluids show high amplitude and frequent evaporator temperature oscillations. Condenser temperature augmentation leads to start-up for water-filled FPPHP and temperature oscillations homogenization for heat load range from 100 W to 200 W for mixtures. Higher filling ratio also leads to stable oscillatory regime establishment for FPPHP tested at both temperatures of cooling liquid.

Concerning Parabolic Flight Campaigns, during microgravity periods, significant increase of evaporator temperature has been observed for all tested fluids. This could be a result of liquid accumulation in the condenser zone and of evaporator dry-out – heat being transferred just via thermal conduction through the FPPHP solid material plate.

Interesting results have been found for FPPHP filled with water when non-condensable gases are present- despite the overall thermal performances degradation (caused by system sub-cooling), pulsating heat pipe with NCG injection shows steady oscillatory operation with stable slug/plug flow pattern even during microgravity periods, unlike cases with pure liquids, with means absence of the stopover phenomena.

Using water/alcohol mixtures leads to more frequent fluid flow reactivations, accompanied with temperature drops, during microgravity phases, especially for higher values of heat load (150 W).

Brief analysis of the gravity level influence (tests for Lunar and Martian gravity levels) has shown that minor gravity values (0.18*g*) is enough to maintain continuous oscillation mode of FPPHP operation with some evaporator temperature augmentation (quite less than for microgravity periods) during reduced gravity phases. Almost any changes for FPPHP operation during Martian gravity phases, compared to normal gravity conditions, have not been observed.

**References**

[6.1] Yang H., Khandekar S. and Groll M., 2009. Performance characteristics of Pulsating Heat Pipes as integral thermal spreaders. Int. J. Th. Sc. 48, 815–824.

[6.2] Ayel V., Romestant C., Bertin Y., Manno V., Filippeschi S., 2014. Visualization of flow patterns in flat plate Pulsating Heat Pipe: influence of hydraulic behavior on thermal performances. Heat Pipe Sc. Tech.: an Int. J. 5, 377–384.

[6.3] Pagnoni F., Ayel V., Scoletta E., Bertin Y., 2018. Effects of the hydrostatic pressure gradient no thermohydraulic behavior of flat plate Pulsating Heat Pipe: experimental and numerical analyses. Proc. 16th Int. Heat Tr. Conf.. Beijing, China.

[6.4] Nekrashevych I. and Nikolayev V.S., 2019. Pulsating Heat Pipe Simulations: Impact of PHP Orientation. Microgravity Sci. Technol. 31, 241–248.

[6.5] Slobodeniuk M., Martineau F., Ayel V., Bertossi R., Romestant C. and Bertin Y., 2020. Thermal performance of flat plate Pulsating Heat Pipe using aqueous alcohol solutions. Proc. 28th Conf. Soc. Fr. Therm. (SFT), Belfort, France.

[6.6] Pagnoni F., Ayel V., Romestant C. and Bertin Y., 2021. Flat Plate Pulsating Heat Pipes with and without separating grooves: experimental investigation on adiabatic length, coolant temperature and orientation. IOP Conf. Ser.: Mater. Sci. Eng. 1139, 012005.

[6.7] Khandekar S., 2004. Thermo-hydrodynamics of Closed Loop Pulsating Heat Pipes. PhD thesis, University of Stuttgart.

[6.8] Shi W. and Pan L., 2017. Influence of filling ratio and working fluid thermal properties on starting up and heat transferring performance of closed loop plate oscillating heat pipe with parallel channels. J. Therm. Sci. 26, 73–81.

[6.9] Le Neindre B., 1998. Conductivité thermique des liquides et des gaz, Traité constantes physico-chimiques. Ed. Techniques de l'Ingénieur.

[6.10] Vazquez G., Alvarez E. and Navaza J., 2005. Surface tension of alcohol + water from 20 to 50°C. J. Chem. Eng. Data 40, 611-614.

[6.11] Green D. and Perry R., 2008. Perry's Chemical Engineers' Handbook. McGraw-Hill.

[6.12] Senjaya R. and Inoue T., 2014. Effects of non-condensable gas on the performance of oscillating heat pipe, part I: Theoretical study. Appl. Therm. Eng. 73, 1387-1392.

[6.13] Nikitkin M., Bienert W. and Goncharov K., 1998. Non-condensable gases and loop heat pipe operation. SAE Transactions 107, 394-399.

[6.14] Singh R., Akbarzadeh A. and Mochizuki M., 2010. Operational Characteristics of the Miniature Loop Heat Pipe with Non-Condensable Gases. Int. J. Heat Mass Transf. 23, 3471-3482.

[6.15] Qu W. and Ma T., 2002. Experimental Investigation on Flow and Heat Transfer of Pulsating Heat Pipes. Proc. 12th Int. Heat Pipe Conf., Moscow, Russia.

[6.16] Daimaru T. and Nagai H., 2015. Operational characteristics of the oscillating heat pipe with non condensable gas. J. Thermophys. Heat Transf. 29, 563-571.

[6.17] Taft B., 2013. Non-condensable gases and oscillating heat pipe operation. Fr. Heat Pipes 4, 013003.

[6.18] O'Connor J., You S. and Chang J., 1996. Gas-Saturated Pool Boiling Heat Transfer From Smooth and Microporous Surfaces in FC-72. ASME J. Heat Transf. 118, 662–667.

# PART III

## TWO-PHASE FLOW BEHAVIOR IN FPPHP IN MICROGRAVITY

# Chapter 7

## Definition of Flow Transition in Microgravity via High-Speed Visualization

The visual analysis of the two-phase flow inside the PHP could give some answers on the questions related to the flow behavior, the influence of sensible heat transfer on the overall performance of PHP, which is still contradictory [7.1; 7.2; 7.3; 7.4; 7.5; 7.6], the driving and flow transition mechanisms.

Complex mechanisms of thermo-hydrodynamic processes inside PHP are not yet fully studied, any general and suitable design recommendations are no available, together with some contradictory assessments from researchers [7.7; 7.8] and absence of universal flow transition criteria. Misunderstandings of the relation between velocity and flow pattern need regular experimental investigations to be carried out.

The visual investigations of the different flat plate pulsating heat pipes filled with different fluids have been performed during 64$^{th}$, 69$^{th}$ and 71$^{st}$ ESA PFCs. Note that the attempt to post-process the 71$^{st}$ parabolic flight data has been unsuccessful because the software could not recognize the menisci in the FPPHP channels due to the high contrast images from the IR camera and low quality of the high-speed camera video: interfaces were too thin to be captured by the trackers. Thus, only results obtained from 64$^{th}$ PFC for FPPHPs with two different channel diameters (1.5 mm and 3 mm) and filled with FC72, and from 69$^{th}$ PFC for the device with 3 mm channel diameter and filled with ethanol, respectively, are presented in this chapter.

Obtained images resulting from the recorded video during microgravity periods have been post-processed for the purpose of liquid/vapor interfaces tracking, particularly at the transition between dry-out and re-activation phases.

### 7.1. Two-phase flow determination inside the FPPHP during microgravity

The presence of the whole menisci in every channels and liquid accumulation in the condenser zone are clearly visible in Fig. 7.1b (left). Due to accumulation in the condenser zone, the fluid is separated separates in the form of liquid plugs and vapor bubbles by the menisci, and the vapor phase, remaining in the adiabatic and evaporation zones, provokes dry-out and failure operation of the FPPHP. In such a configuration, evaporator wall temperatures continuously rise due to a weak heat transfer with the non-moving fluid (until $t$ = 6221 s in Fig. 7.1a). Unlike the dry-out case, flow re-activation leads to a spontaneous rise of menisci oscillating amplitude, menisci deformation and a uniform fluid distribution inside the FPPHP in the form of a semi-annular/annular flow pattern. Flow pattern during this period is very similar to that observed for a FPPHP tested in the bottom heating mode under normal gravity conditions with ethanol [7.9].

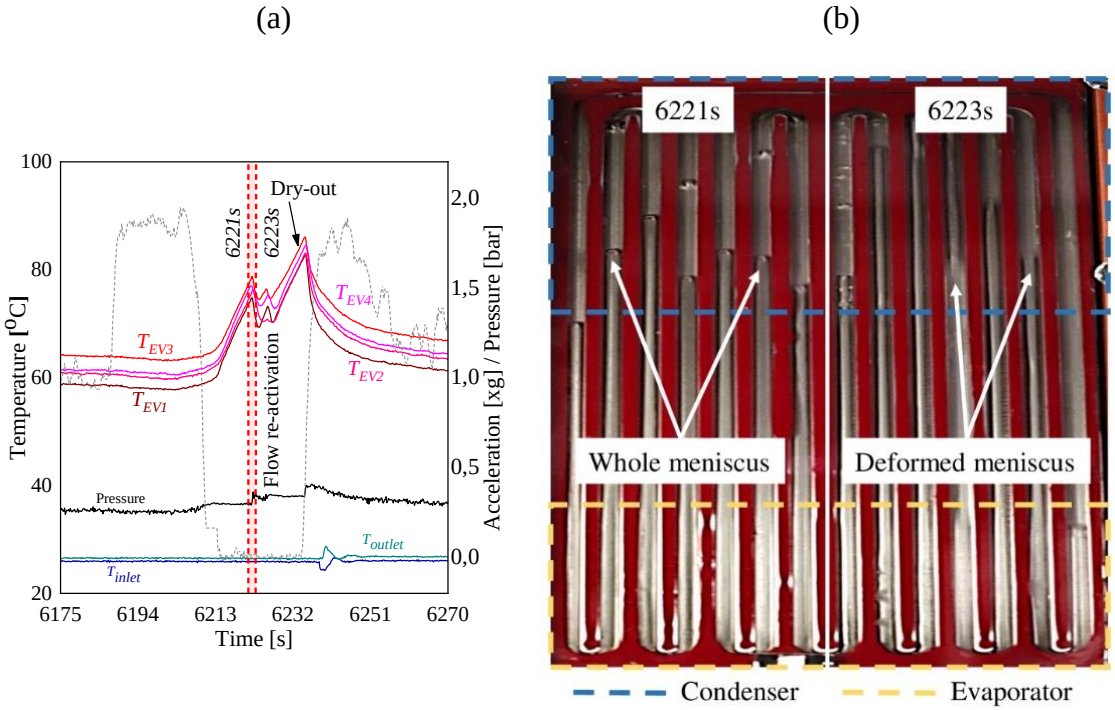


Figure 7.1. Transient operation during microgravity phase (ethanol; 3 mm; 69$^{th}$ ESA PFC): (a) temperatures profiles of flow reactivation during the 5$^{th}$ parabola of Fig. B.1.1; and (b) flow patterns one second before (left) and one second after fluid flow reactivation (right).

Synchronization of videos with temperature and pressure profiles have confirmed that the reactivation of fluid flow inside the PHP is at the origin of the observed evaporator

temperature decrease. Menisci movements and re-activation mechanisms, as well stopover mechanism, will be explained in the next sections.

### 7.2. Video post-processing tool

The general idea of the image post-processing in current work is the determination of the liquid-vapor interfaces position at each frame and other motion parameters extraction (velocity and acceleration) as derivatives. Knowing these values for each meniscus, the length, mass, velocity and acceleration of the liquid plugs can be easily found and will be used to establish the momentum equation of the liquid plugs (Eq. (7.7).

Particle image velocimetry (PIV) is a commonly used method for the flow direction and velocity determination from high-speed videos. Basically, fluid is seeded with tracer particles which are assumed to faithfully follow the flow dynamics. The laser-based illumination of the fluid with entrained particles is used to make the particles visible. As a result, the motion of the seeding particles is used to calculate speed and direction (the velocity field) of the flow. It is possible to use this method with the videos of the flow inside FPPHP without any tracer particles and illumination, replacing it by the visible reflection of the liquid-vapor interfaces. However, the overall fluid velocity for both liquid and vapor phases can be evaluated with this method and noise presence recognized as a "particle" to be traced that makes PIV unsuitable for the isolated menisci tracking.

A first attempt of the liquid-vapor interfaces detection in the channels has been done based on the infrared measurements [7.10]. Infrared image analysis is based on the different emissivity/transmissivity values between liquid and vapor phases: indeed, ethanol in vapor phase is transparent for the infrared wavelengths (between 1.5 µm and 5 µm), whereas in liquid phase the emissivity has been measured close to 1 for thicknesses above 2 mm thickness [7.11]. An example is given in Fig. 7.2 where darker lines in the left part represent part of the channels filled by vapor. This leads to the possibility to clearly distinguish the phase separation allowing to precisely define menisci positions. On the right-hand side of Fig. 7.2 are shown the temperature profile along a single channel (corresponding to the yellow line) on which the significant temperature drop, corresponding to the vapor-liquid interface, can easily be detected.

As the infrared data can be exported in numerical format (matrix of temperature values), the temperature drop can easily be recognized and position can be extracted in the form of

pixel's number. This procedure, repeated for every pictures in the matrix, allows to define the positions of menisci for the specified period in every channels.

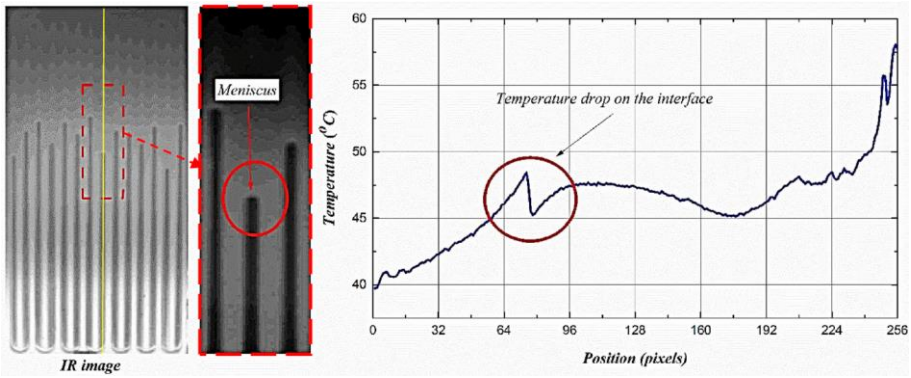


Figure 7.2. Infrared post-processing procedure on FlirIR software® (darker lines, and lighter lines on the left image correspond to the vapor and the liquid phase, respectively) [7.10].

Because the purpose was to visualize the whole channels of the entire FPPHP, the main disadvantage of this method is a very low resolution of the infrared camera (resulting resolution is 2-3 pixels for a 3 mm channel's width) which did not allow to provide the analysis for most of registered videos due to vibrations occuring during parabolic flights – sometimes zone of interests being displaced to the channel wall resulting in numerous parasitic interfaces detection.

On the basis of this observation, very similar approach has then been developed for visual images from high speed camera. As shown in fig. 7.3, the menisci are contrasting with channel (greyscale image with light intensity between 0-255) - interfaces exist as some change in intensity across the channel and their position can be extracted using the horizontal gradient filter.

The filtered image now contains interfaces, but other horizontal gradients caused by changes in lighting and general camera noise can also be observed. These have lower intensities than the interfaces and are mostly one or two pixels in thickness (similarly to some interfaces).

Finally, an approach based on the OpenCV [7.12] library has been implemented to track the menisci along the channels. OpenCV (Open Source Computer Vision Library) is a library of programming functions mainly aimed at real-time computer vision and consisting most

of basic image manipulation tools. The library is cross-platform and free for use under the open-source license.

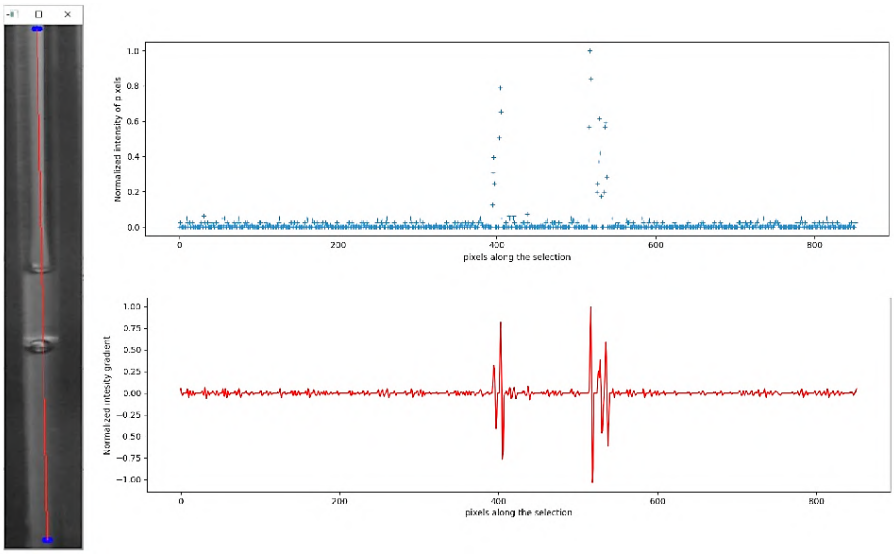


Figure 7.3. A cropped greyscale image of channel with vapor-liquid interfaces.

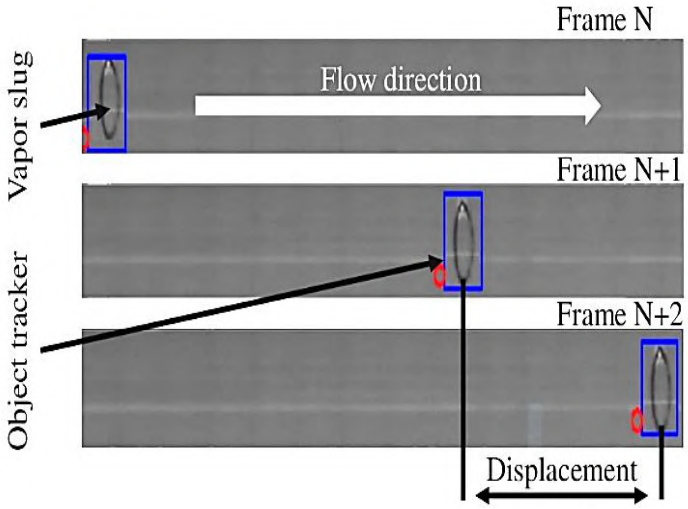


Figure 7.4. Definition of the menisci position: channel with menisci (images from [7.13]).

To process rough images, first, they have been extracted from raw videos in the form of image frames sequences and then converted to black and white. After that, feature definition and object tracking tools, available in the OpenCV® tool-set, have been used for the menisci tracking. The main purpose of these tools is the manual definition of the vapor/liquid interfaces and their following automatic tracking through time. One of the advantages of this approach is the possibility to define the flow transition from slug flow to annular flow pattern - or another one – if interface cannot be defined anymore (due to highly

deformed menisci). Therefore, in the following, critical velocities/acceleration values can be defined as the last values obtained before menisci "disappearance" or their deformation, corresponding to transitional flow patterns.

To validate the above developed approach, available images from previous studies of tubular pulsating heat pipe [7.13] have been used for the generation of the composite image (Fig. 7.4). Then, the image of menisci is isolated and placed over an extracted backdrop of the fluid regions in the image. The menisci are then moved with a given velocity profile (sinusoidal). The developed framework, used to determine menisci velocities from synthetic images, allowed comparing the latter with programmed velocity profile and showed great consistency in the results (see Fig. 7.5).

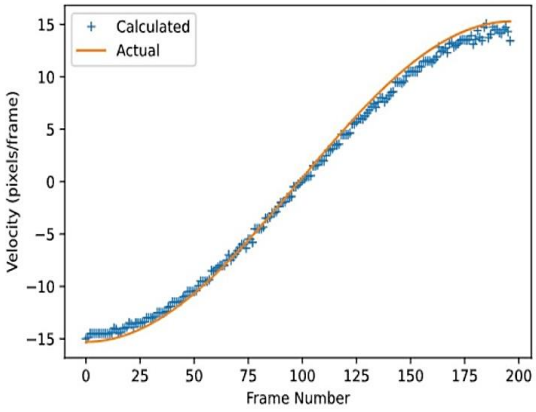


Figure 7.5. Developed tracking approach validation.

Despite the good agreement of the obtained velocity values with the programmed data, the maximum found deviation is 3 pix/frame, which corresponds to 20 mm/s (or 0.02 m/s), considering camera resolution and sampling frequency.

Unfortunately, it must be said that, during normal and hyper gravity conditions, analysis is impossible via all methods above due to the absence of menisci in such annular flow patterns. Thus, analysis could be done just for stopover and flow re-activation during microgravity periods.

### 7.3. Motion of liquid plugs

For better readability of the acquired data, an extra focus will be done on the examination of two nearby liquid plugs: LP67 and LP89, which are located in the center of the FPPHP. Fig. 7.6 depicts these two liquid plugs, as well as the channel numbers.

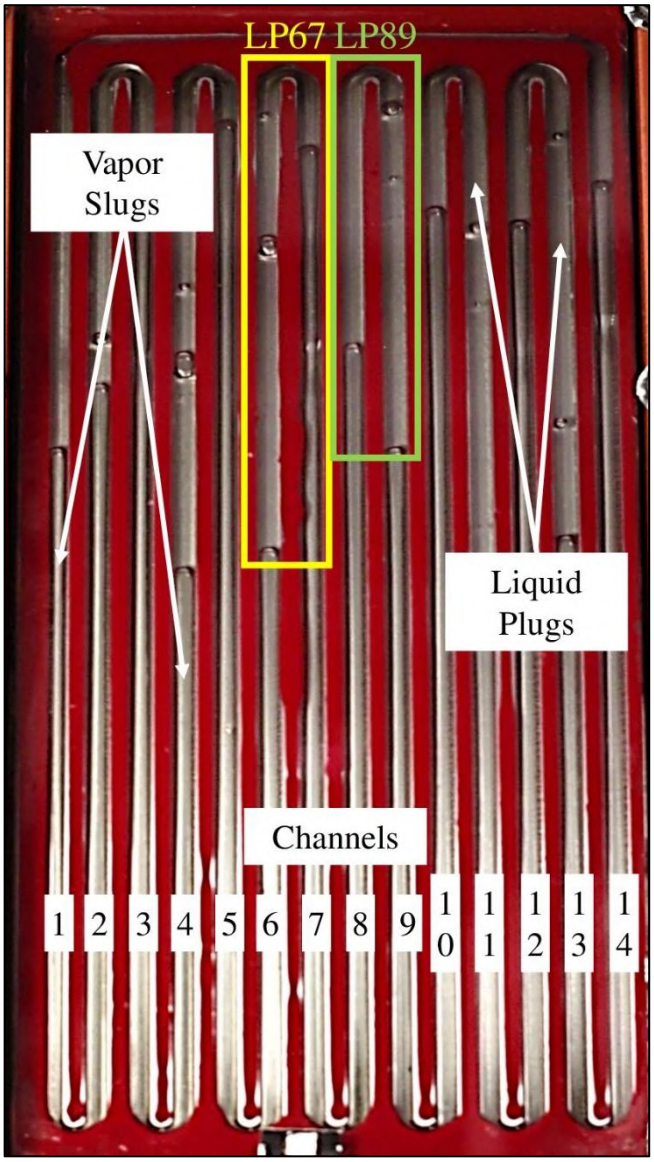


Figure 7.6. Representing liquid plugs and channels numbering (ethanol; 3 mm; 69$^{th}$ ESA PFC).

As the flow dynamics directly influence the re-activation phenomena, a study of the liquid/vapor interfaces displacements is presented in the following section. Menisci displacements of the two neighboring liquid plugs in the central zone of the FPPHP, for two tested cases (a first one for 100 W and a second for 150 W applied heat powers, respectively) are presented in Fig. 7.7. Microgravity phase turns fluid into slugs and plugs form and, once dried-out, the liquid plugs, accumulated in the condenser zone, are accompanied by low displacement interfaces movements (Fig. 7.7 (yellow section)) after flow stabilization due to influence of small pressure variations in the evaporator caused by vapor superheating, which was already observed and described in previous studies [7.14]. Note that the mirror

effect between the displacement of the left-hand side meniscus is well reproduced by that of the right-hand side one, corresponding to the same liquid plug, the latter being incompressible (a small difference can be attributed to measurement error and a very slightly higher velocity for the receding meniscus compared to the advancing one due to the downstream deposition of the thin liquid film which causes a local low loss of mass). However, at the beginning of microgravity phases, interfaces oscillations amplitudes are quite high due to influence of inertia forces and, after stabilization, surface tension became dominant.

Despite the rise of the interfaces motion amplitude during re-activation periods (Fig. 7.7, red field), liquid slugs do not attain the evaporator zone (due to the low filling ratio, *i.e.* 40%), which is not represented in the *y*-axis of Fig. 7.7 (situated between 0 cm and 4 cm positions). This means that the fluid flow transition is probably not triggered by evaporation in the evaporator but in the superheated adiabatic zone. On the other hand, high menisci motion amplitudes lead to the liberation of the wall surfaces in the condenser (located between 12 cm and 20 cm in *y*-axis of Fig. 7.7) and, as a result, to a higher condensation rate local pressure drop near liquid plug. Unlike case for 150 W of applied heat power, no frequent high amplitude movements of the central liquid plugs have been observed for 100 W.

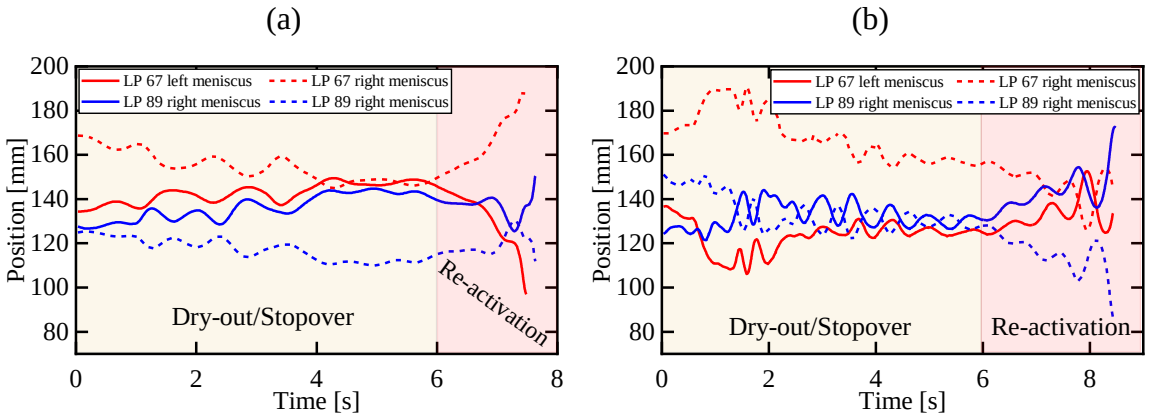


Figure 7.7. Displacement of the vapor/liquid menisci for two central liquid plugs during microgravity period from dry-out to re-activation phase (ethanol; 3 mm; 69$^{th}$ ESA PFC): (a) Fig. 6.20, third parabola (100 W); (b) Fig B.1.1, first parabola (150W).

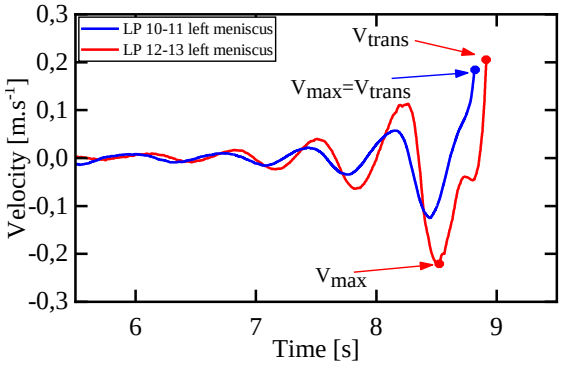


Figure 7.8. Transient velocities of two following liquid plugs menisci (Fig 6.20, parabola 1) (ethanol; 3 mm; 69th ESA PFC).

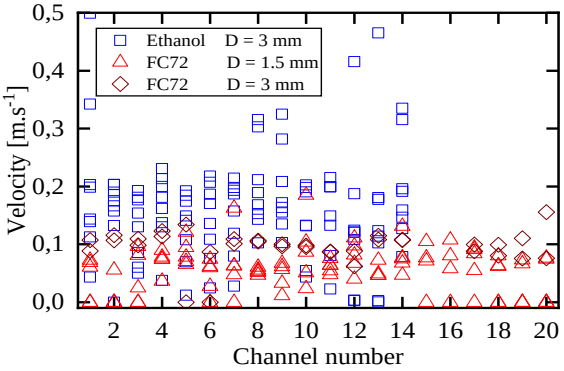


Figure 7.9. Channel distribution of $V_{trans}$. (65th and 69th ESA PFCs)

Values of velocities measured just before the flow pattern transitions ($V_{trans}$, see Fig. 7.8) during reactivation phases, are plotted in Fig. 7.9. In most cases, maximum oscillation velocities correspond to the transition velocities just before the flow pattern transition/menisci deformation. The average transition velocity for all presented conditions is equal to 0.15 m/s, which is one and half times higher than the commonly known operating velocity of 0.1 m/s in the literature [7.15]. It is also higher for ethanol compared ot the ones obtained with FC72. It must be noted that, sometimes "transition velocity" corresponds to the menisci deformation, but not to their total "disappearance". However, reaching these velocities gives us a flow pattern transition represented in Fig. 7.1b (right part).

### 7.4. Non-dimensional analysis of flow pattern transition

The obtained transition velocities allow evaluation of commonly used criteria for confined flow prediction: Weber ($We = \rho_l U_l^2 D/\sigma$) and Garimella ($Ga = Re\sqrt{Bo}$) numbers, as functions of the channel number are presented in Fig. 7.10 and Fig. 7.11, respectively. First observations show a distribution of Weber number ranging from 1 to 25, but most of the points (about 80%) for ethanol-filled FPPHP are gathered in the zone between 2 and 5, very close to the reference value of 4. The average value is 3. Value of the Weber number for FPPHP filled with FC72 and channel diameter of 1.5 mm varies in the range of 0.1 to 11 with concentration of the points majority between the values of 1.5 and 2.5 (with an average value of 2). For the device filled with FC72 and channel diameter of 3 mm, Weber number values are mostly in the range of 4-8 withan  average value of 6. All these values are quite

different, but not very far from the reference value. Note that any dependencies with applied power have not been founded.

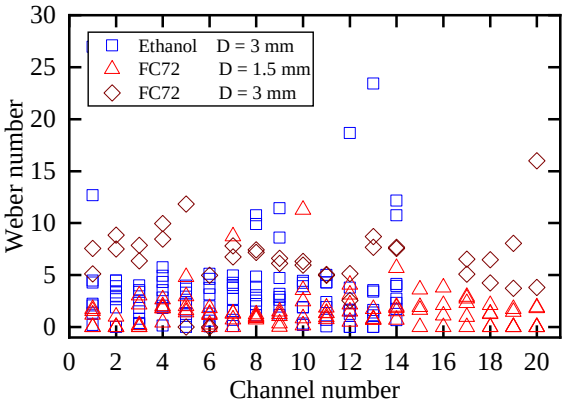


Figure 7.10. Weber number based on the transition velocity (65th and 69th ESA PFCs).

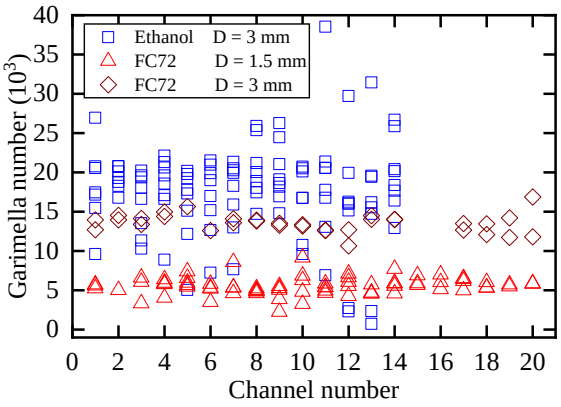


Figure 7.11. Garimella number based on the transition velocity (65th and 69th ESA PFCs).

The plot of the vise-channel Weber number does not show sharp breakdow associated with the different working fluids or diameters, finally distributed along the range starting from 1 to 6 (majority of values). Thus, a sharp transition criterion, based on Weber number, cannot be observed.

Almost the same behavior, as shown for Weber number, is observed for Garimella number (Fig. 7.11), but with much more higher values (up to two orders of magnitude) than the reference value of 160 mentioned in literature [7.16]. Most values are located in the range between $15\times10^3$ and $23\times10^3$ (average value of $18\times10^3$) for FPPHP filled with ethanol and channel diameter of 3 mm, then range from $11\times10^3$ to $17\times10^3$ (average value of $13\times10^3$) for FPPHP with same channel diameter filled with FC72. Finally, Garimella numbers values are found between $3\times10^3$ and $9\times10^3$ (average value of $6\times10^3$) for 1.5 mm diameter device filled with FC72. If, for Weber number, any valuable dependencies have not been found, Garimella number plot clearly shows separation in values for FPPHP with different diameters and slight difference in values for device with channel diameter of 3 mm and filled with FC72 and ethanol. However, these extremely high values (comparing to reference) and their great spreading make this criteria useless for flow mapping.

Earlier, modified non-dimensional numbers, based on operation limit map to quantify the effect of interface disturbance propagation and surface tension to actual flow conditions such as velocity and acceleration, have been proposed by [7.18]. This operation limit map is

based on following experimentally developed transitional correlations, found for a 3 mm tubular PHP (filled with ethanol and FC72):

Upper limit (coalescence):

$$Fr^{*0.25}We^{*0.25} = 12.42(Bo^{*0.5})^{-0.69} \tag{7.1}$$

Slug-plug dominant to transitional regime:

$$Fr^{*0.25}We^{*0.25} = 0.0059(Bo^{*0.5})^{2.45} \tag{7.2}$$

And transitional regime to annular dominant:

$$Fr^{*0.25}We^{*0.25} = 0.0009(Bo^{*0.5})^{2.02} \tag{7.3}$$

where terms (in conventional non-dimensional numbers) related to the gravity acceleration term $g$ have been replaced by the acceleration term of liquid plugs ($du_l/dt$). The modified numbers are calculated as follows:

$$Fr^* = \frac{u_l}{\sqrt{\left(\frac{du_l}{dt}\right)\cdot D}} \tag{7.4}$$

$$We^* = \frac{\rho {u_l}^2 D}{\sigma} \tag{7.5}$$

$$Bo^* = \frac{\rho}{\sigma}\cdot\left(\frac{du_l}{dt}\right)\cdot D^2 \tag{7.6}$$

On placing the non-dimensional numbers obtained through previous post-processing in the operation limit map and verifying with flow pattern correlations, all the points from post-processing are most likely to fall nearly to the upper coalescence and transition regions (Fig. 7.12) irrespective of the working fluid or channel diameter. This discrepancy may arise due to that estimated modified non-dimensional numbers did not account the bubble length to channel diameter ratio (used in [7.18]). However, more test points are necessary to determine their location in the flow map and to validate this approach.

### 7.5. Flow influencing forces analysis

The following momentum equation [7.19] could be used to calculate the magnitude of the driving pressure as well as the impact of the influencing forces on the motion of liquid plugs (Fig. 7.14):

$$m_l \frac{du_l}{dt} = F_{driv} - F_{vis} \tag{7.7}$$

where $F_{vis}$ and $F_{driv}$ are viscous, and driving forces, respectively. These forces are calculated with eq. (7.8). Gravity forces are not taken into account in this calculation due to the microgravity conditions.

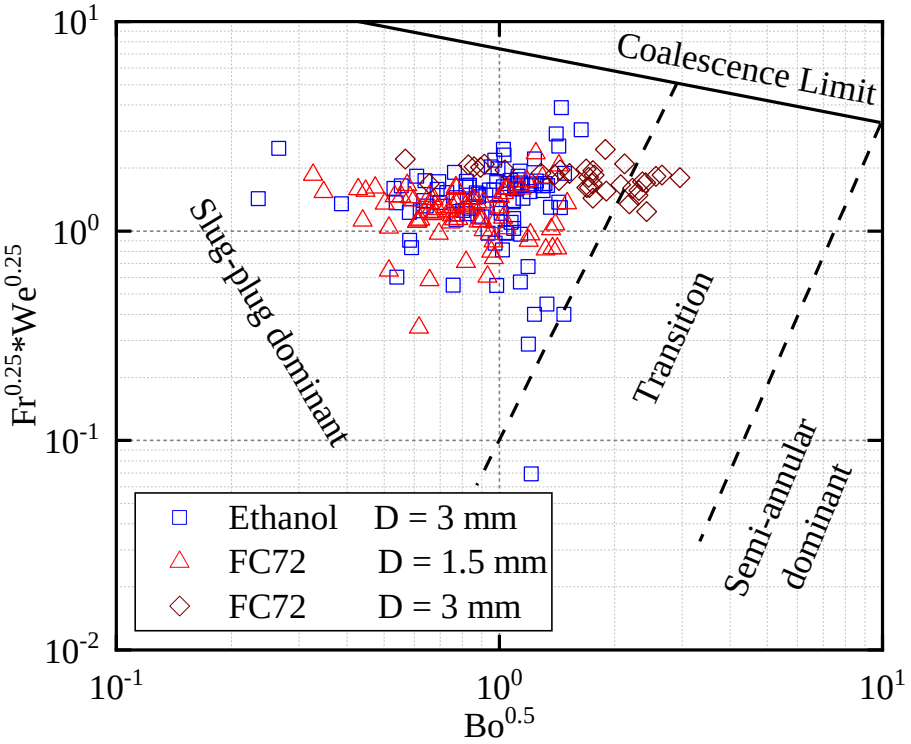


Figure 7.12. Flow map from [7.18] and adapted for the flow transition under microgravity for FPPHP with rectangular channels.

$$\begin{cases} F_{acc} = m_l \frac{du_l}{dt} \\ F_{vis} = A_{cs} \Lambda \cdot \left(\frac{L_p}{2R}\right) \cdot \left(\frac{1}{2}\rho_l u_l^2\right) \\ F_{driv} = A_{cs} \cdot (\Delta P_v - \Delta P_c) \cdot \end{cases} \tag{7.8}$$

where $m_l$, $L_p$, $u_l$ are respectively liquid plug mass, length and velocity; $\rho_l$ is the liquid density; $A_{cs}$ and $R$ are respectively the channel cross-section area and hydraulic radius; $\Delta P_v$ and $\Delta P_c$ are respectively the vapour pressure difference between two sides of each liquid plug, and the capillary pressure; and $\Lambda = 64/Re$ is the Darcy coefficient for viscous pressure losses for laminar flow (here, the flow is assumed to be developed laminar flow). Liquid plug mass is calculated as:

$$m_l = \rho_l A_{cs} L_p \tag{7.9}$$

As shown in Fig. 7.13, the length of liquid plug is defined from the knowledge of the positions (from top of each channel) of the two menisci located at both ends of liquid plug ($x_n$ and $x_{n+1}$):

$$L_p = L_{bend} + x_n + x_{n+1} \tag{7.10}$$

where $L_{bend}$ represents the length of the U-turn. Vapor pressure difference between two ends of liquid plug is given by:

$$\Delta P_v = P_{vr} - P_{va} \tag{7.11}$$

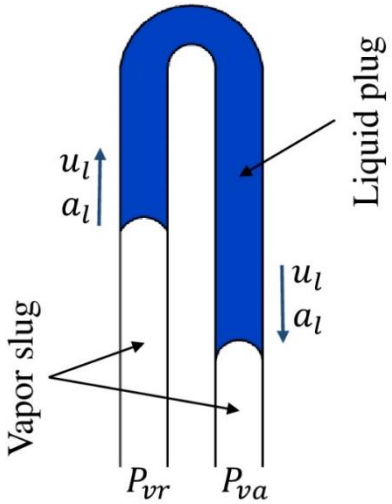


Figure 7.13. Schematic diagram of liquid plug movement.

Finally, from the knowledge of every post-processed parameters for every liquid plugs, it becomes possible to evaluate the driving force, $F_{driv}$, from Eq. (7.7) and (7.8).

Due to specific interest in flow transition and almost similar motion amplitudes and frequencies for all liquids plugs, calculated forces magnitudes just for one "surrounding" and two central liquid plugs (for channels 1-14, 6-7 and 8-9, see Fig. 7.6) are presented in Fig. 7.14.

Left-hand side of Fig. 7.14 represents forces magnitudes, obtained from Eq. (7.7) and (7.8), for a period, representing one second before transition, for 100 W (Fig. 6.20., third parabola), and right-hand side for 150 W (Fig. B.1.1, firth parabola) of applied powers, respectively. Fig. 7.14d, where forces are negative due to the opposite direction of the liquid plug movement, is presented with reversed *y*-axis for better comparison. Re-activation zones characterized by the significant amplitude rise of all forces oscillations for high heat loads,

which was also reported for the transition from the stopover period to a large-amplitude oscillations for horizontal micro FPPHP [7.20], but with quite higher values (which could be caused by the microscale channel dimensions, i.e. of 1×0.5 mm²). Fluctuations for lower heat powers are less noticeable.

It is important to note that the viscous forces are the weakest ones, while not being negligible for both cases during dry-out phases; but this influence comes out just before transition (as can be seen in Fig. 7.14d, e and f). Comparing presented cases, the acceleration and driving forces values on the transition line are very close from case to case. The low influence of the frictional part on the force balance and very close (almost equal) behavior of the accelerating and driving forces corresponding well to the results obtained in [7.21].

Interesting fact is that the transition takes place not at the same time for each liquid plugs, but with short time delay, that may be due to the vapor compressibility (dash line in Fig. 7.14).

Knowing the driving forces, the resulting values of the driving pressures $\Delta P_{driv}$ (eq. 7.12) are plotted in Fig. 7.15. Note that the capillary pressure drop, $\Delta P_c$, is directly included in the driving pressure term in eq. (7.12) due to the fact that its value is not estimable in these measurements. In analogy with the previous figures, driving pressures are plotted for the liquid plugs 6-7, and 8-9, in Fig. 7.15 for the periods from start of microgravity (at $t$ = 0 s) until the re-activation phase with applied power of 100 W (Fig. 7.15a) and 150 W (Fig. 7.15b), respectively. In parallel, the experimental absolute pressure ($P_{exp}$), in the evaporator zone between these two liquid plugs, is also plotted in the same graphs. One can see that the absolute pressure shows increased instabilities during the re-activation phases, synchronously with the calculated driving pressure fluctuations from the post-processing of the image analysis.

$$\Delta P_{driv} = \frac{F_{driv}}{A_{cs}} = \Delta P_v - \Delta P_c \tag{7.12}$$

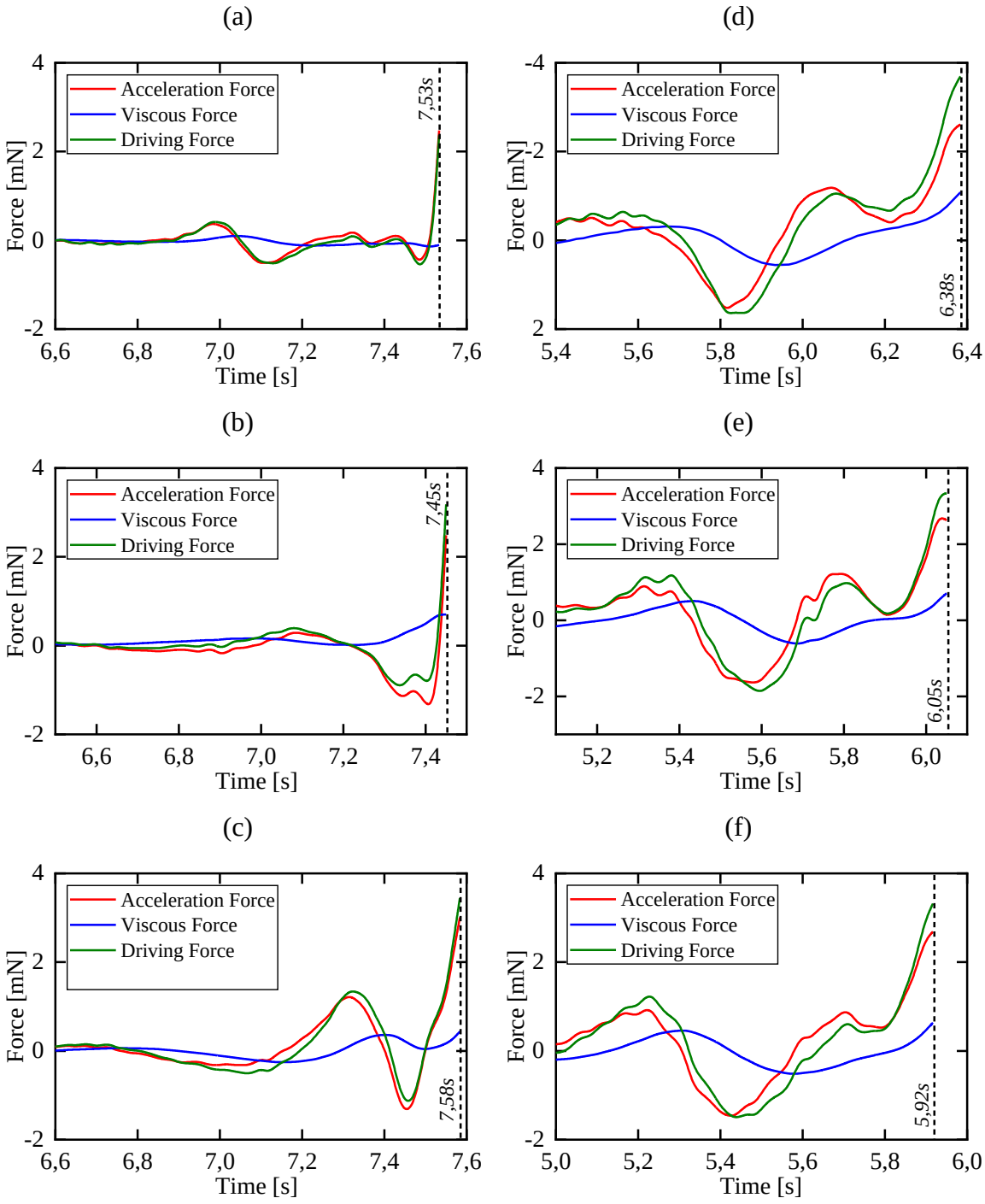


Figure 7.14. Forces influencing the liquid plugs motion during period prior to reactivation phases (ethanol; 3 mm; 69$^{th}$ ESA PFC): for 100 W (a) channels 1-14; (b) channels 6-7; (c) channels 8-9; and for 150 W (d) channels 1-14 ; (e) channels 6-7; (f) channels 8-9.

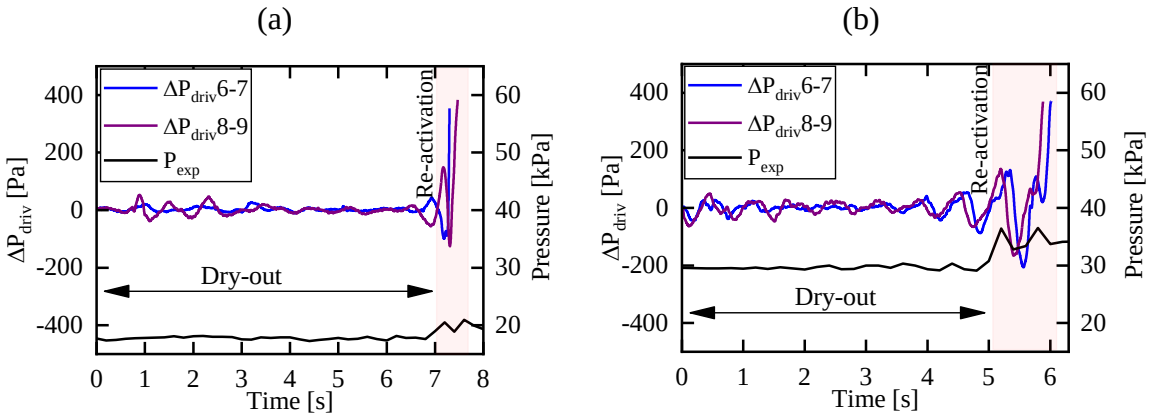


Figure 7.15. Comparison of driving forces values for two central liquid plugs (from Fig. 7, ethanol; 3 mm; 69$^{th}$ ESA PFC): (a) 100 W and (b) 150 W.

Here it can be seen that during total period until re-activation, values of driving pressure for the two liquid plugs seems to be almost similar with a slight time lag, due to the vapor compressibility (as shown previously). Amplitudes of pressure oscillations increase up to the value attained at the re-activation time and do correspond to significant absolute pressure surge between two liquid plugs. Interesting to note, that the final values of driving pressure ($P_{exp}$) (corresponding to the flow pattern transition) are almost similar for both values of applied heat power and are of about 350-380 Pa. Note that this pressure difference is one order of magnitude higher than the maximum capillary pressure drop, from minimum receding contact angle to maximum advancing contact angle ($\Delta P_{c,max} = 2\sigma/R$), of about 20-28 Pa when calculated in the temperature range of Fig. 6.20. This means that the driving pressure difference is largely counterbalanced by the inertial and viscous forces before the rupture of the menisci at the transition between slug flow and annular flow.

## 7.6. Conclusions

The object tracking based visual analysis methodology for liquid-vapor interfaces position determination has been developed, validated and implemented to study the flow behavior during stopover and re-activation periods under microgravity conditions. Experimental investigation of these phenomena inside flat plate pulsating heat pipes filled with ethanol (3 mm diameter) and FC72 (1.5 mm and 3 mm diameters) and operating under microgravity is also performed.

Microgravity periods, as previously reported [7.14], are accompanied by the stopover phenomena and evaporator dry-out that leads to overall thermal transport degradation. It was

found that, during some parabolas, stop-over periods occur and are sometimes interrupted by a flow pattern transition from slug flow to annular flow with uniform liquid distribution inside pulsating heat pipe, also called re-activation phases.

The motion of liquid/vapor interfaces, as well as the force influence on fluid flow and flow pattern change, have been analyzed. Despite the different amplitude and oscillation frequencies during microgravity start and stopover periods, the values of transition velocities appear to be very close to each other.

Frequently used non-dimensional criteria, based on Weber and Garimella numbers, have been evaluated for tested FPPHP under microgravity conditions. Experimentally obtained average values of *We* number for flow transition are very close to the reference critical value, whereas average values of *Ga* number are one-two orders of magnitude higher than reference critical value.

Adaptation of the flow map correlations (based on modified Bond, Weber and Froude numbers including the actual fluid acceleration than a constant gravity acceleration value) developed in [7.18] placed experimentally obtained in this work transitional points in the zone of slug-plug dominant flow pattern, nearly to the coalescence limit and zone of slug-plug to annular transition.

This work refers to few specific cases, and future complex studies are necessary to enhance the characterization of flow behavior and flow transition inside of PHP under both ground and microgravity conditions. The quantitative analysis of the flow transition mechanisms and forces influencing them can help in design of the stable functioning pulsating heat pipe without stopover phenomena and give the necessary data for the modelling.

**References**

[7.1] Shafii M. B., Faghri A., Zhang Y., 2001. Thermal Modeling of Unlooped and Looped Pulsating Heat Pipes. ASME. J. Heat Trans. 123, 1159-1172.

[7.2] Senjaya, R., Inoue T., Suzuki Y., 2010. Oscillating Heat Pipe Simulation with Bubble Generation. Proc. 15th Int. Heat Pipe Conf.

[7.3] Nikolayev V. S., 2011. A Dynamic Film Model of the Pulsating Heat Pipe. ASME. J. Heat Transf. 133, 081504.

[7.4] Jo J., Kim J., Kim S.J., 2019. Experimental investigations of heat transfer mechanisms of a pulsating heat pipe, Energy Convers. Manag. 181, 331-341.

[7.5] Jung C., Kim S., 2021. Effect of oscillation amplitudes on heat transfer mechanisms of pulsating heat pipes. Int. J. Heat Mass Trans. 165, 120642.

[7.6] Kamijima C., Yoshimoto Y., Abe Y., Takagi S., Kinefuchi I., 2020. Relating the thermal properties of a micro pulsating heat pipe to the internal flow characteristics via experiments, image recognition of flow patterns and heat transfer simulations. Int. J. Heat Mass Trans. 163, 120415.

[7.7] Tang X., Sha L., Zhang H., Ju Y., 2013. A review of recent experimental investigations and theoretical analyses for pulsating heat pipes. Front. Energy. 7, 161-173.

[7.8] Bastakoti D., Zhang H., Li D., Cai W., Li F., 2018. An overview on the developing trend of pulsating heat pipe and its performance, Appl. Therm. Eng. 141, 305-332.

[7.9] Ayel V., Romestant C., Bertin Y., Manno V., Filippeschi S., 2014. Visualization of flow patterns in flat plate Pulsating Heat Pipe: influence of hydraulic behavior on thermal performances. Heat Pipe Sci. Tech.: Int. J. 5, 377-384.

[7.10] Slobodeniuk M., Ayel V., Bertossi R., Romestant C., Bertin Y, 2019. Infrared thermography of fluid flow in flat plate pulsating heat pipes tested under microgravity conditions. Proc. 30th SFT.

[7.11] D. Brutin, B. Sobac, F. Rigollet, C. Le Nilliot, Infrared visualization of thermal motion inside a sessile drop deposited onto a heated surface, Exp. Them. & Fl. Sc., 35 (2011) 521-530.

[7.12] https://opencv.org/

[7.13] Pietrasanta L., 2018. Experimental analysis of two-phase flows in the context of Pulsating Heat Pipes for space applications. PhD Thesis, Brighton.

[7.14] Ayel V., Araneo L., Marzorati P., Romestant C., Bertin Y., Marengo M., 2018. Visualization of flow patterns in closed loop flat plate pulsating heat pipe acting as hybrid thermosyphons under various gravity levels. Heat Transf. Eng. 40, 227-237.

[7.15] Marengo M., Nikolayev V.S., 2018. Pulsating Heat Pipes: Experimental Analysis, Design and Applications. Encyc. Two-Phase Heat Transf. Flow IV, pp. 1-62.

[7.16] Harichian T., Garimella S., 2010. A comprehensive flow regime map for micro-channel flow boiling with quantitative transition criteria. Int. J. Heat Mass Transf. 53, 694-702.

[7.17] Pietrasanta L., Mameli M., Mangini D., Georgoulas A., Michè N., Filippeschi S., Marengo M., 2020. Developing flow pattern maps for accelerated two-phase capillary flows. Exp. Therm. Fluid Sci. 112, 109981.

[7.18] Bertossi R., Ayel V., Mehta B., Romestant C., Bertin Y., Khandekar S., 2017. Motion of liquid plugs between vapor bubbles in capillary tubes: a comparison between fluids. Heat Mass Transf. 53, 3315-3327.

[7.19] Jun S., Kim S-J., 2019. Experimental study on a criterion for normal operation of pulsating heat pipes in a horizontal orientation. Int. Jo. Heat Mass Transf. 137, 1064-1075.

[7.20] Yoon A., Kim S.J., 2017. Characteristics of oscillating flow in a micro pulsating heat pipe: Fundamental-mode oscillation. Int. J. Heat Mass Transf. 109, 242-253.

# Chapter 8

## Conclusions and Perspectives

### 8.1. Conclusions

The work presented here can be divided in two main parts respectively describing the parametric studies on the FPPHP and the analytical analysis of the hydraulic behavior of the FPPHP during stopover and flow re-activation periods. The parametric studies has consisted in the evaluation of the device orientation, gravity, working fluid, filling ratio, condenser temperature and non-condensable gases presence influence on the FPPHP operation. For the analytical part, only the videos obtained during 64$^{th}$ and 69$^{th}$ parabolic flight campaigns for three different FPPHPs filled with ethanol and FC72 have been used for analysis.

Related to the parametric studies, the following conclusions can be presented:

- The FPPHP tested in vertical orientation (bottom heating mode) mostly operates as an interconnected lopped thermosiphon (except water-filled device) due to relatively low surface tension and liquid stratification (hydraulic diameter is higher than static capillary limit, linked to the Bond number). Condenser temperature increase leads to significant temperature rise in evaporator zone. Higher filling ratio almost has no effect on the device performance. Non-condensable gases addition into the system leads to the total thermal performance degradation but also to the high-amplitude temperature and pressure oscillations appearances.
- Water-filled device tested in horizontal orientation at low cooling temperature has not reached start-up and operated in “dry” mode. Heat load increase leads to the total system failure. Other tested fluids show high amplitude and frequent evaporator temperature oscillations. Performance improvement and earlier start-up observed with condenser temperature increase as well for the case with higher filling ratio. Non-condensable gas presence provoked stable oscillatory operation for water-filled PHP, which was failed with pure water.

- Microgravity periods during parabolic flights are characterized by the significant increase of evaporator temperature for all tested fluids, which could be explained by dry-out and insufficient parabola duration for start-up (like temperature augmentation before start-up for horizontal orientation). The non-condensable gas addition leads to the continuous oscillatory operation, without significant difference in temperature and pressure amplitudes, comparing to the normal gravity periods.

In the last part of this thesis, post-processing of the video obtained during microgravity periods and its analysis has been presented. Evaporator dry-out starting at the beginning of parabola has been confirmed. However, during some parabolas, stop-over periods are interrupted by a flow pattern transition from slug flow to annular flow with uniform liquid distribution inside pulsating heat pipe. This flow pattern change is of particular interest to evaluate conventional criteria of flow transition regarding microgravity conditions. As a consequence, analyses performed for this particular case can be summarized as follows:

- Analysis of the liquid-vapor interfaces motions has shown very close values of the flow transition velocities for each studied PHP/fluid pair. No dependence of velocity on applied heat load has been found.
- Non-dimensional criteria, based on Weber and Garimella numbers, have been evaluated using experimentally determined velocities. Obtained *We* numbers are very close to the reference critical value but average values of *Ga* number are one-two orders of magnitude higher than critical one.
- Finally, proposed in [8.1] new flow pattern map with modified Bond and Froude numbers, including the actual fluid acceleration instead of a constant gravity acceleration value has been used to analyze the transitional points obtained in actual work. Their placement in this fluid properties independent map marks the distribution of the points in the zone of slug-plug flow dominant, nearly to the coalescence limit and zone of slug-plug to annular flow transition.

Generally speaking, this work gave some answer related, in particular, to the operational performances of the flat plate pulsating heat pipe under different working conditions, as well influence of filling liquid properties. Moreover, the visual analysis of the two-phase fluid flow and its transition can be used in future modelling tools development resulting to the engineering design approaches. Finally, presented results and analysis shed the light on further researches, proposed in the next section.

## 8.2. Perspectives

First, the accurate infrared measurements of the liquid bulk temperature should be realized in the context of the local heat transfer coefficient determination and liquid-vapor phase's separation detection (coupled with high-speed visualization).

Working on inverse heat conduction problem has already started in collaboration with partners from University of Parma. Knowing that external side of the FPPHP is affected by the flow temperature inside the device, it became possible to determine the wall-to-fluid heat fluxes using inverse heat conduction problem resolution approach, previously validated by numerical simulations. This methodology can provide a better insight into the oscillatory typical flow for such heat transfer devices (Fig. 8.1).

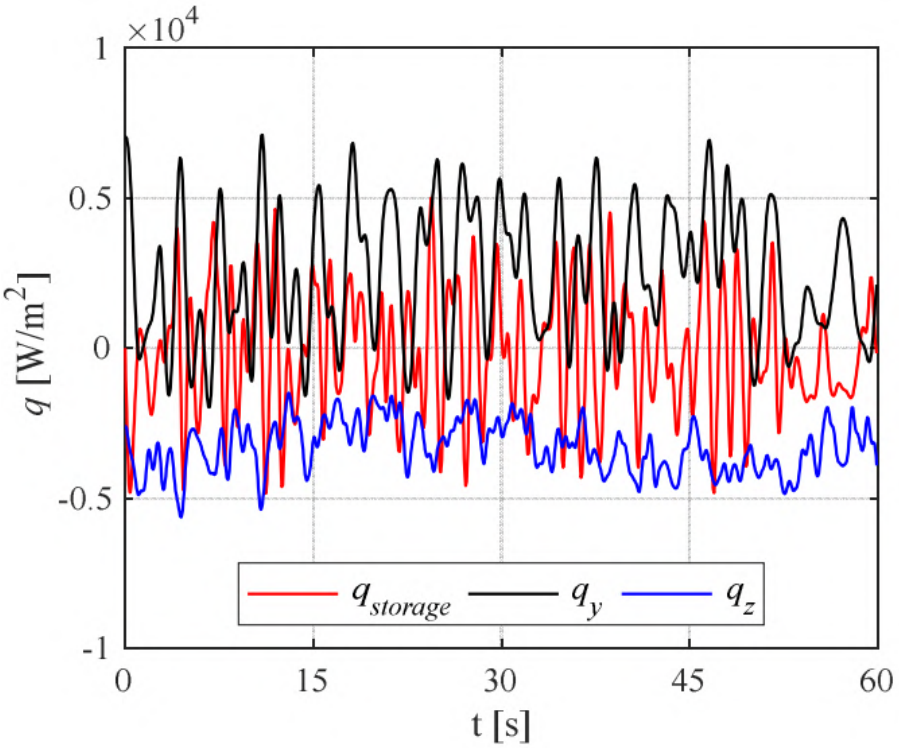


Figure 8.1. The evaluated heat flux adiabatic zone (ethanol, FR = 50 %, horizontal, 200 W) [8.2].

Finally, due to the significant prototype modification during experimental system development to be tested on-board of International Space Station, new ground-based experiments on new geometry are required to validate already selected working fluids and define the test conditions (heat load, condenser temperature etc.). Supplementary parabolic flight tests are also necessary to validate new device in microgravity conditions.

**References**

[8.1] Pietrasanta L., Mameli M., Mangini D., Georgoulas A., Michè N., Filippeschi S., Marengo M., 2020. Developing flow pattern maps for accelerated two-phase capillary flows. Exp. Therm. Fluid Sci. 112, 109981.

[8.2] Pagliarini L., Cattani L., Bozzoli L., Slobodeniuk L., Ayel A., Romestant C., Bertin Y. and Rainieri S., 2021. Study on the local heat transfer behaviour in a flat plate pulsating heat pipe, 38th UIT Int. Conf.

# Appendixes

# Appendix A

## Ground tests temperature and pressure responses

### A.1. Vertical position BHM

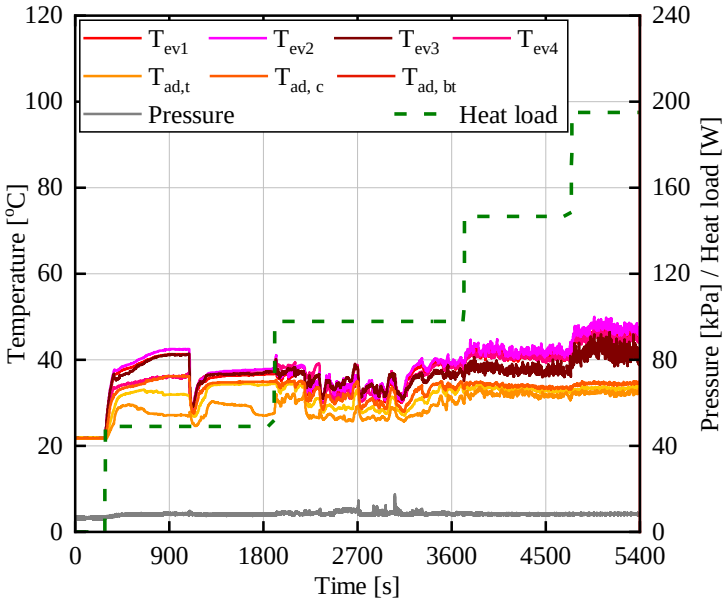


Figure A.1.1. Temperature and pressure responses for FPPHP filled with 20 % ethanol/water solution (FR = 50%, $T_{cool}$ = 20 °C, vertical BHM).

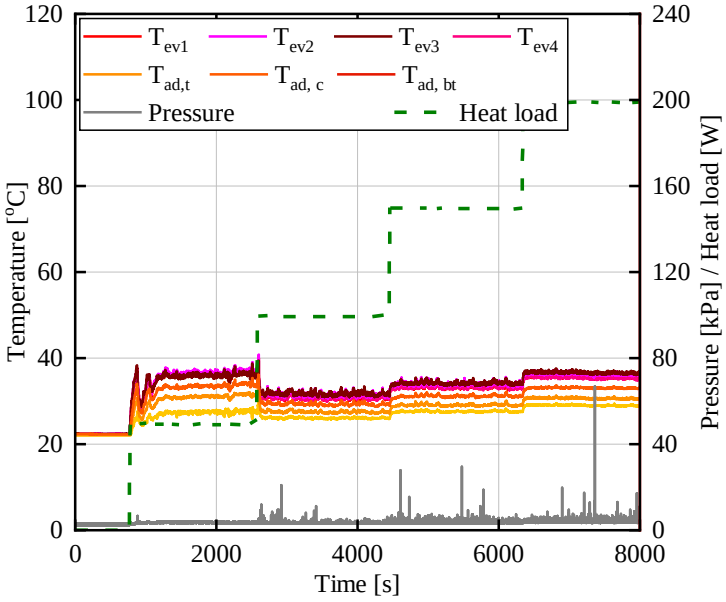


Figure A.1.2. Temperature and pressure responses for FPPHP filled with 28 % methanol/water solution (FR = 50%, $T_{cool}$ = 20 °C, vertical BHM).

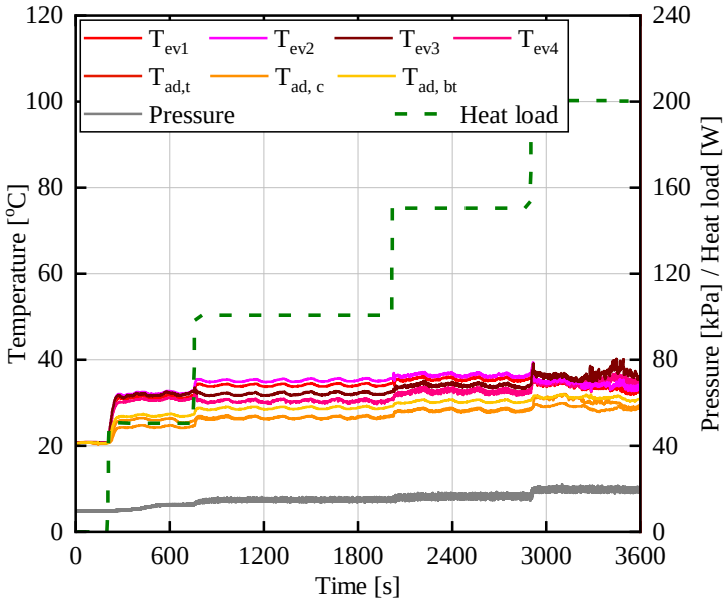


Figure A.1.3. Temperature and pressure responses for FPPHP filled with 5 % 1-butanol/water solution (FR = 50%, $T_{cool}$ = 20 ºC, vertical BHM).

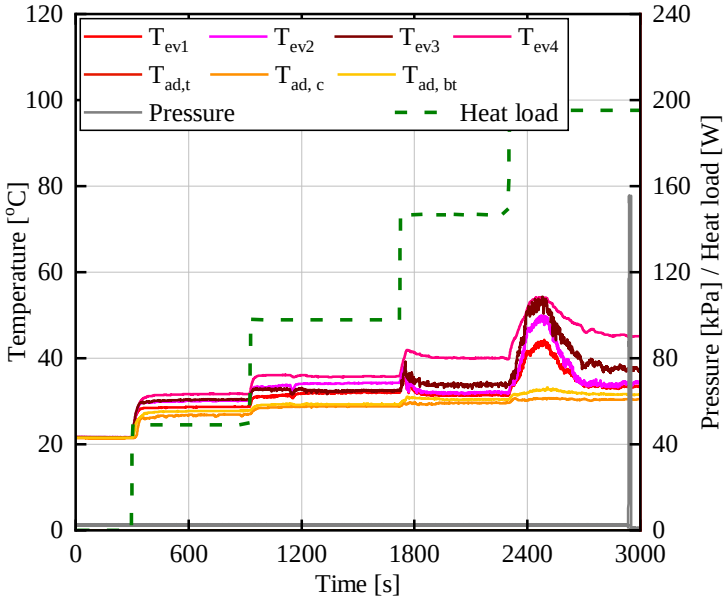


Figure A.1.4. Temperature and pressure responses for FPPHP filled with 5 % 2-butanol/water solution (FR = 50%, $T_{cool}$ = 20 ºC, vertical BHM).

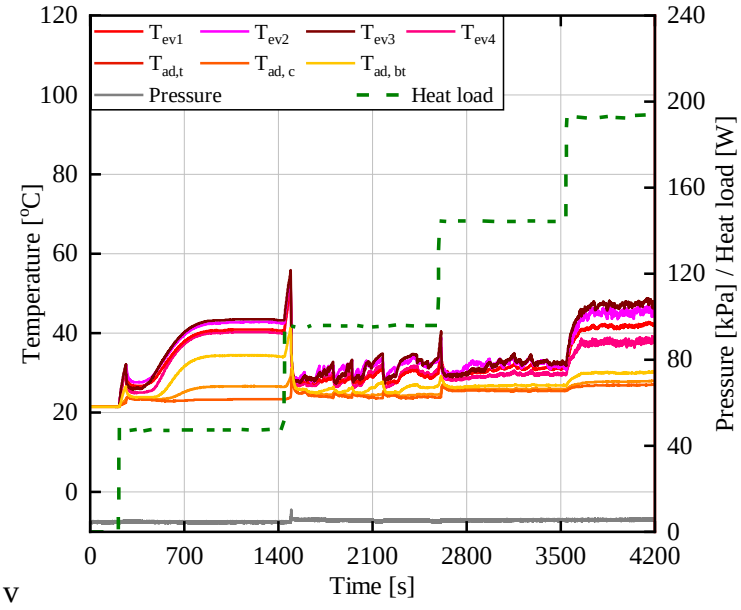


v

Figure A.1.5. Temperature and pressure responses for FPPHP filled with 0.5 % Tween 40/water solution (FR = 50%, $T_{cool}$ = 20 °C, vertical BHM).

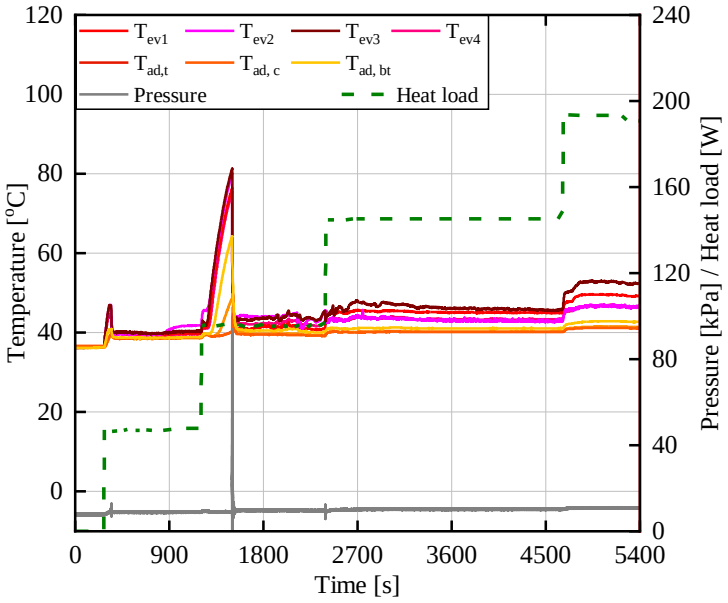


Figure A.1.6. Temperature and pressure responses for FPPHP filled with water (FR = 50%, $T_{cool}$ = 40 °C, vertical BHM).

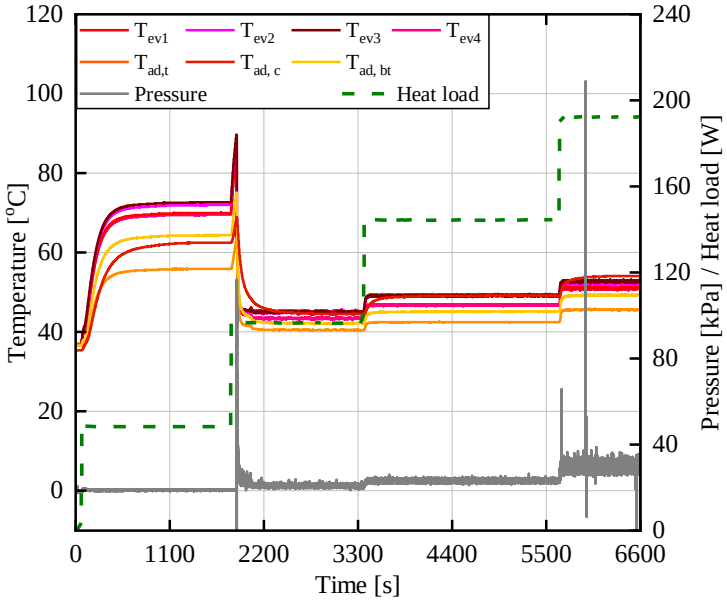


Figure A.1.7. Temperature and pressure responses for FPPHP filled with ethanol (FR = 50%, $T_{cool}$ = 40 °C, vertical BHM).

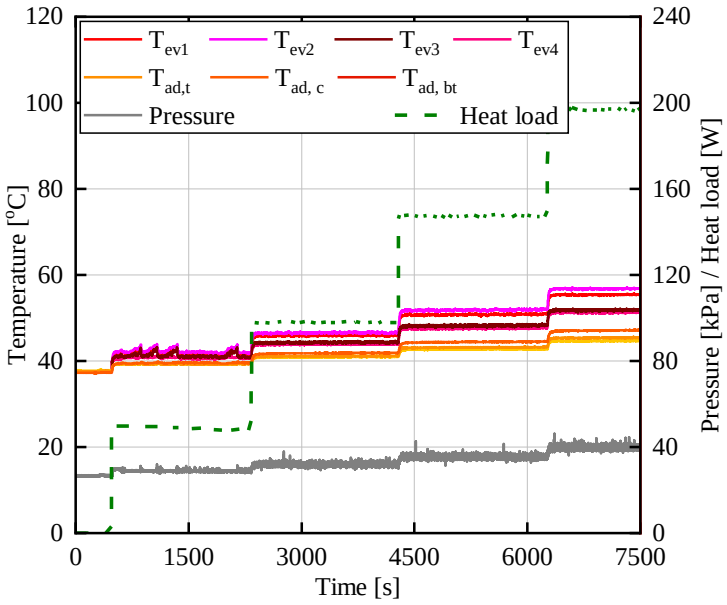


Figure A.1.8. Temperature and pressure responses for FPPHP filled with methanol (FR = 50%, $T_{cool}$ = 40 °C, vertical BHM).

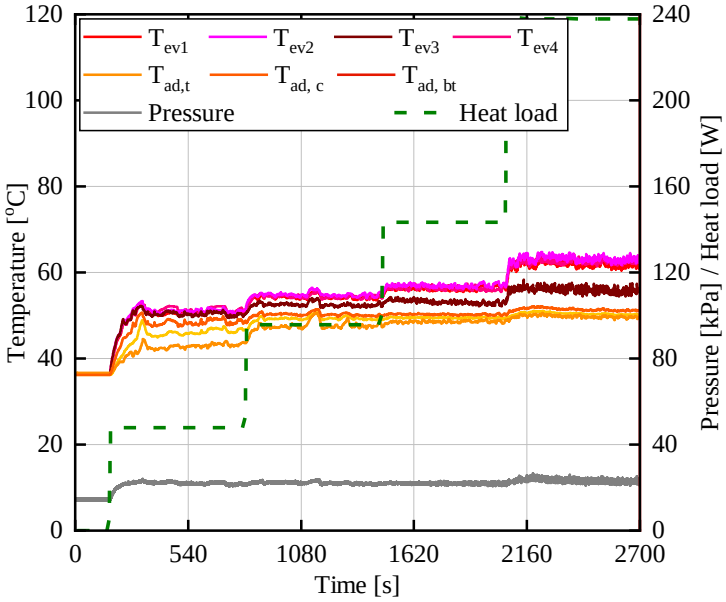


Figure A.1.9. Temperature and pressure responses for FPPHP filled with 20 % ethanol/water solution (FR = 50%, $T_{cool}$ = 40 °C, vertical BHM).

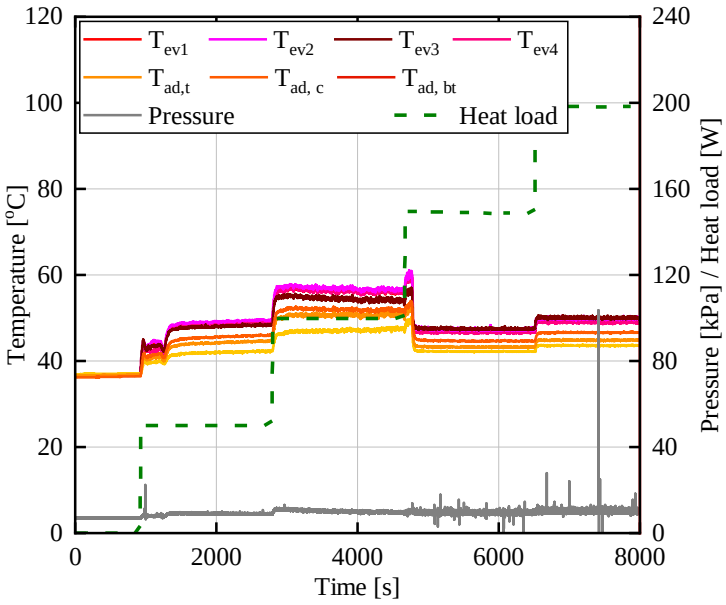


Figure A.1.10. Temperature and pressure responses for FPPHP filled with 28% methanol/water solution (FR =50 %, $T_{cool}$ = 40 °C, vertical BHM).

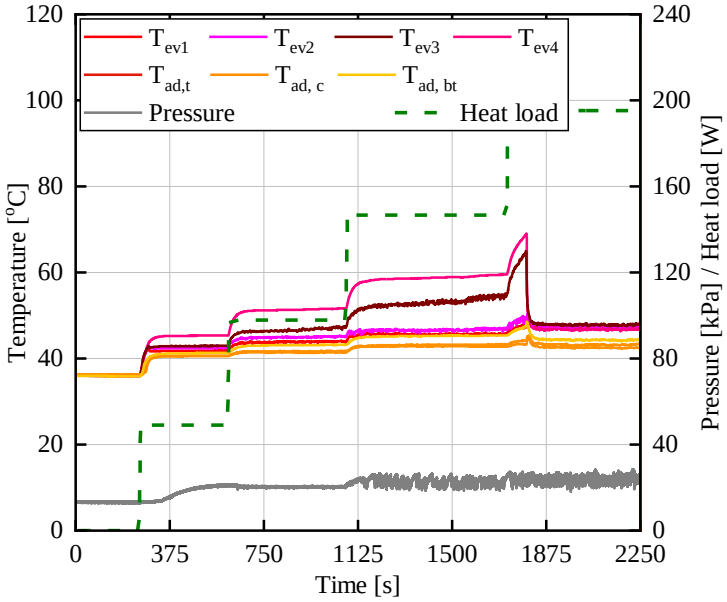


Figure A.1.11. Temperature and pressure responses for FPPHP filled with 5 % 1-butanol/water solution (FR = 50%, $T_{cool}$ = 40 °C, vertical BHM).

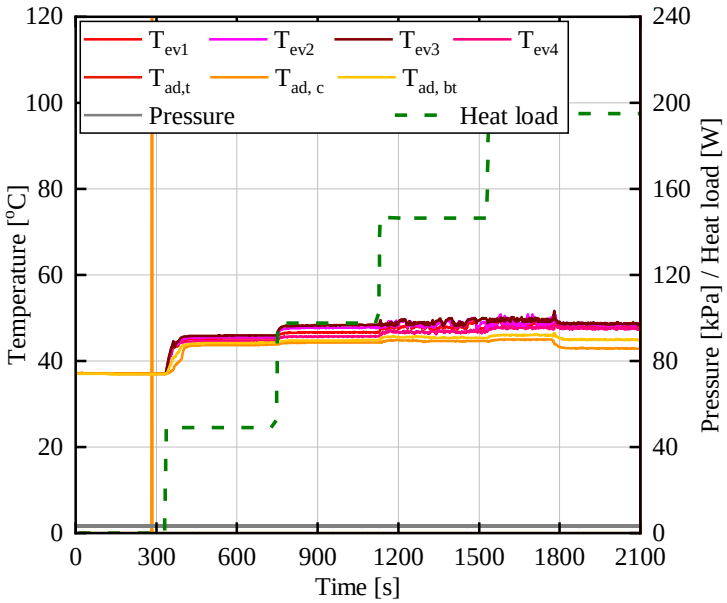


Figure A.1.12. Temperature and pressure responses for FPPHP filled with 5 % 2-butanol/water solution (FR = 50%, $T_{cool}$ = 40 °C, BHM).

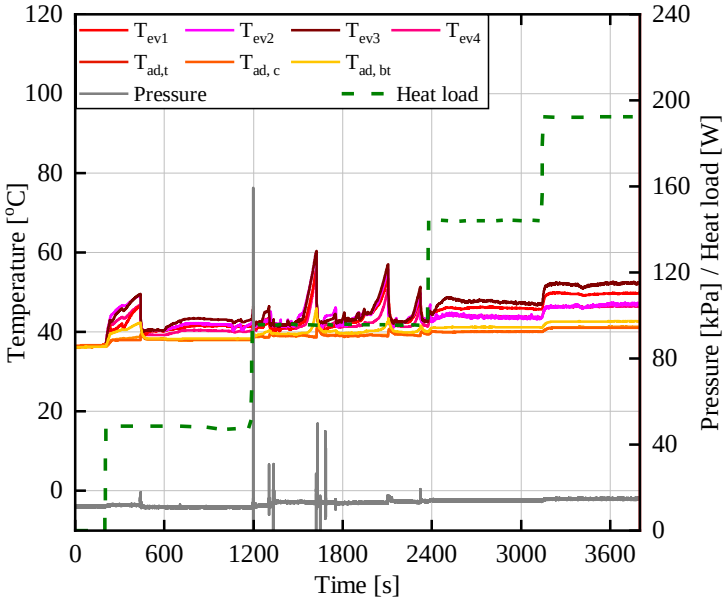


Figure A.1.13. Temperature and pressure responses for FPPHP filled with 0.5 % Tween 40/water solution (FR = 50%, $T_{cool}$ = 40 ºC, vertical BHM).

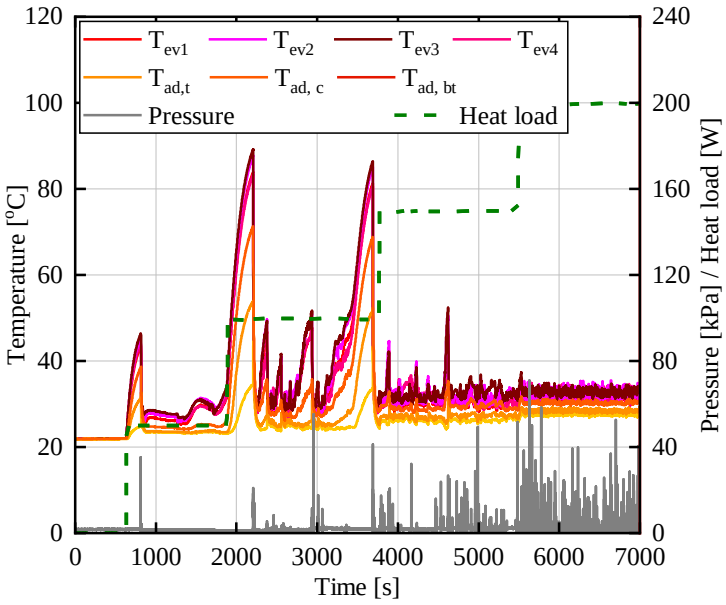


Figure A.1.14. Temperature and pressure responses for FPPHP filled with water (FR = 59%, $T_{cool}$ = 20 ºC, vertical BHM).

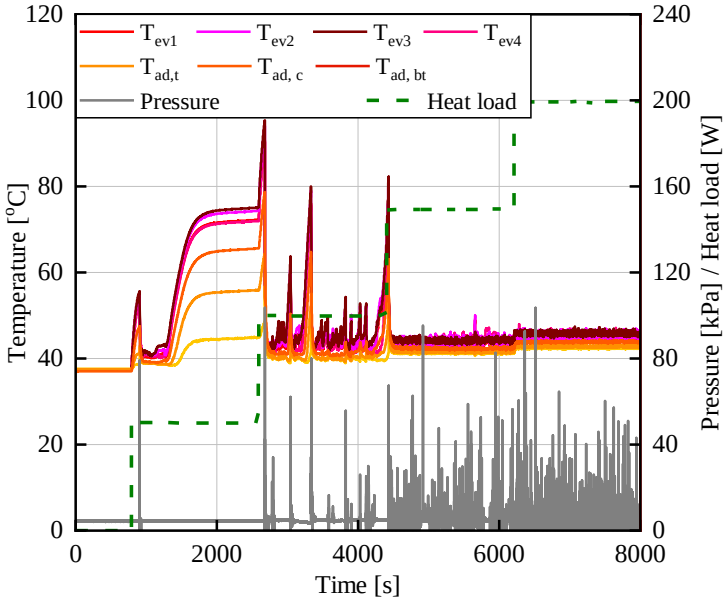


Figure A.1.15. Temperature and pressure responses for FPPHP filled with water (FR = 59%, $T_{cool}$ = 40 °C, vertical BHM).

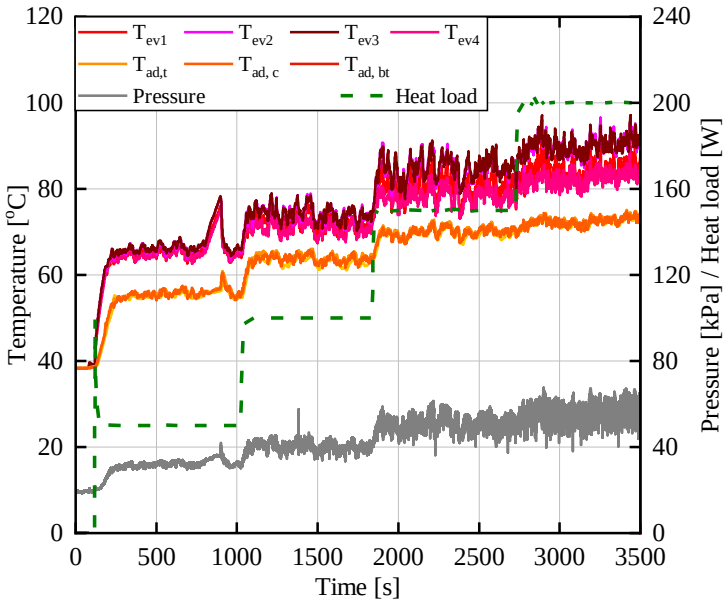


Figure A.1.16. Temperature and pressure responses for FPPHP filled with water + NCG (FR = 50%, $T_{cool}$ = 40 °C, vertical BHM).

## A.2. Horizontal position

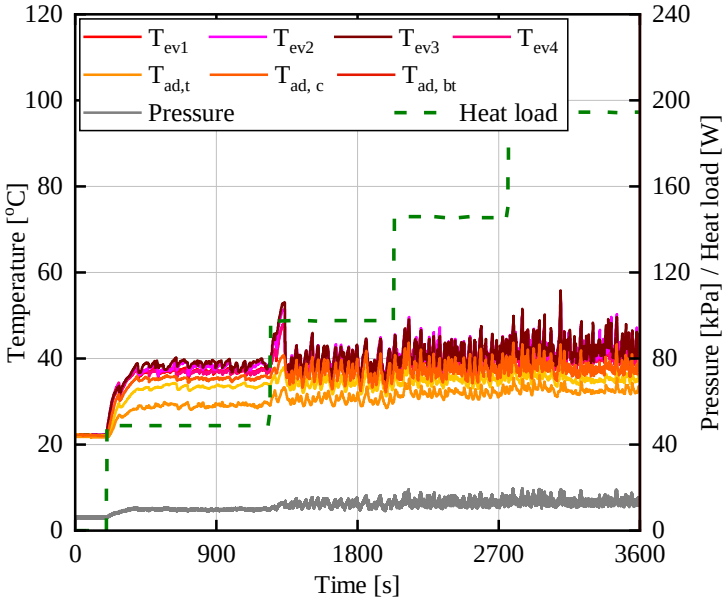


Figure A.2.1. Temperature and pressure responses for FPPHP filled with 20 % ethanol/water solution (FR = 50%, $T_{cool}$ = 20 ºC, horizontal).

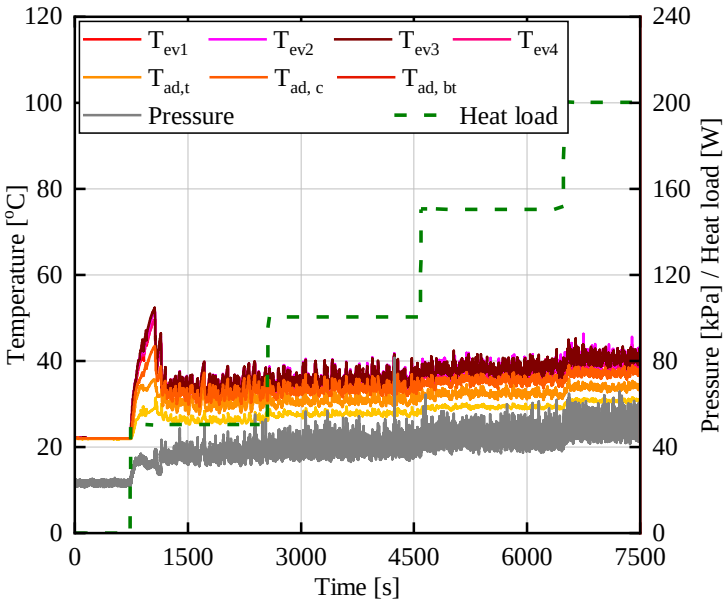


Figure A.2.2. Temperature and pressure responses for FPPHP filled with 28 % methanol/water solution (FR = 50%, $T_{cool}$ = 20 ºC, horizontal).

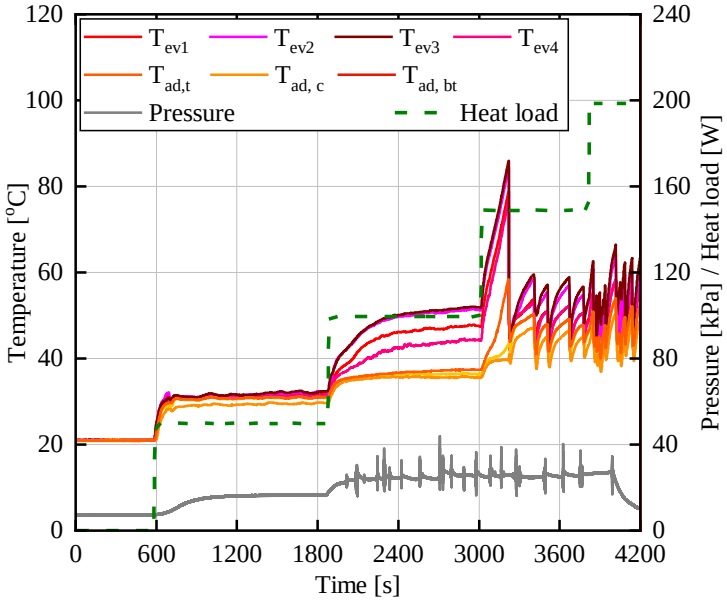


Figure A.2.3. Temperature and pressure responses for FPPHP filled with 5 % 1-butanol/water solution (FR = 50%, $T_{cool}$ = 20 ºC, horizontal).

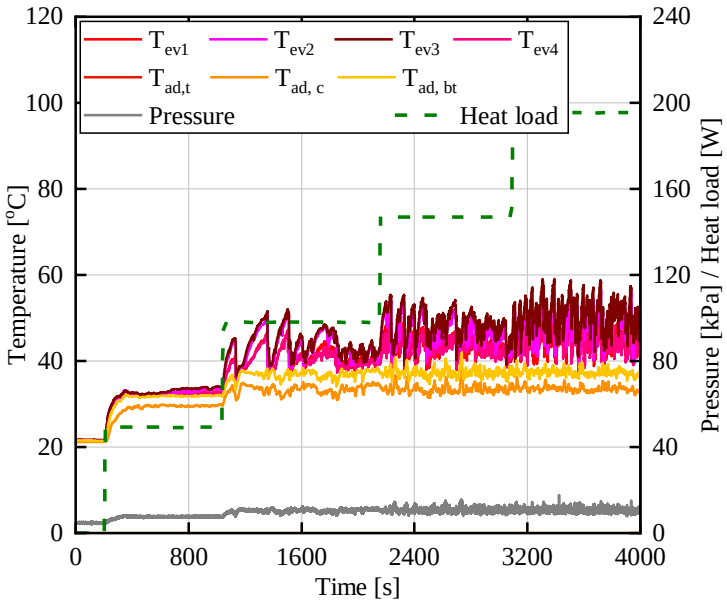


Figure A.2.4. Temperature and pressure responses for FPPHP filled with 5 % 2-butanol/water solution (FR = 50%, $T_{cool}$ = 20 ºC, horizontal).

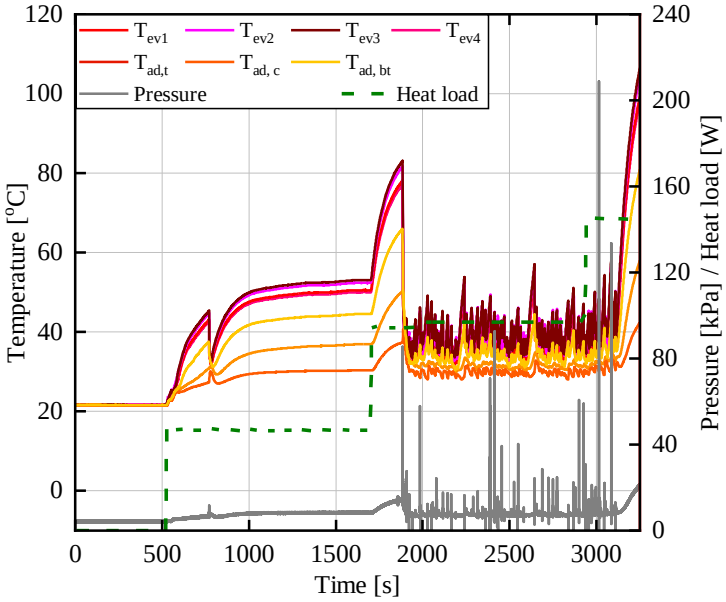


Figure A.2.5. Temperature and pressure responses for FPPHP filled with 0.5% Tween 40/water solution (FR = 50%, $T_{cool}$ = 20 ºC, horizontal).

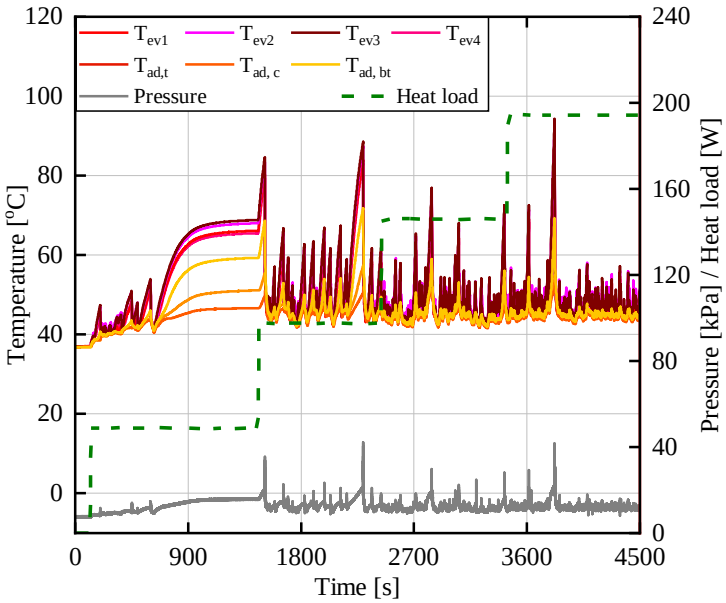


Figure A.2.6. Temperature and pressure responses for FPPHP filled with water (FR =50 %, $T_{cool}$ = 40 ºC, horizontal).

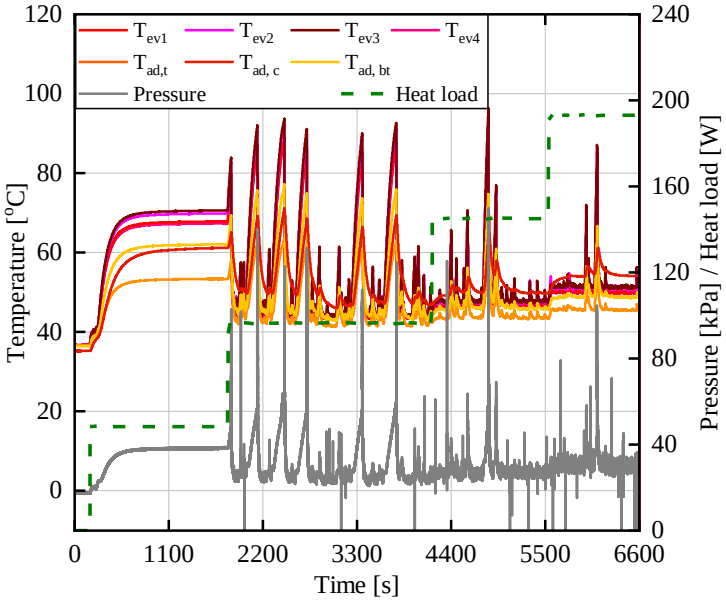


Figure A.2.7. Temperature and pressure responses for FPPHP filled with ethanol (FR = 50%, $T_{cool}$ = 40 °C, horizontal).

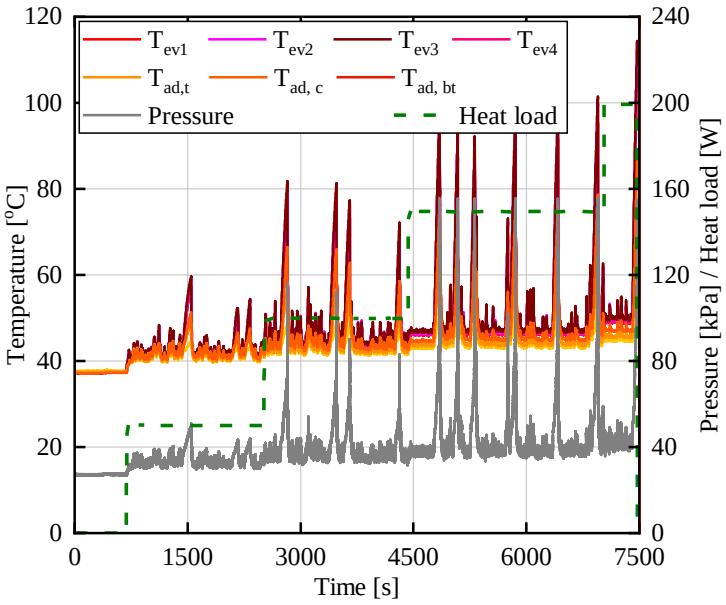


Figure A.2.78 Temperature and pressure responses for FPPHP filled with methanol (FR = 50%, $T_{cool}$ = 40 °C, horizontal).

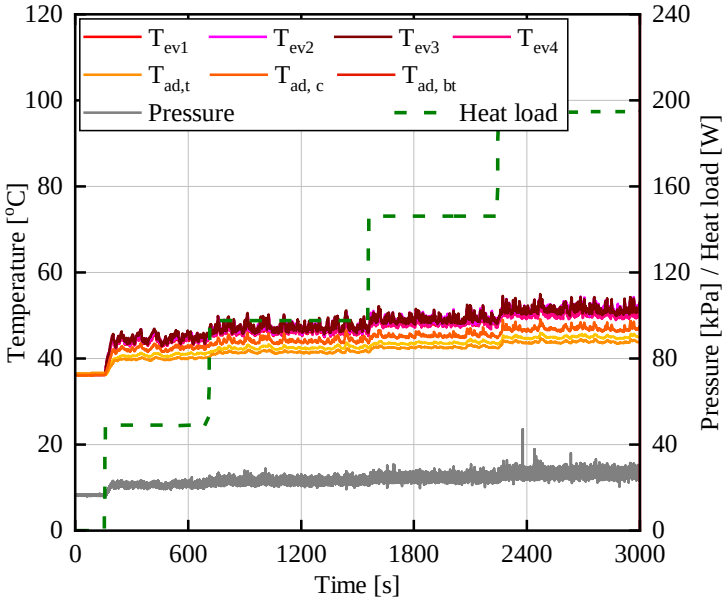


Figure A.2.9. Temperature and pressure responses for FPPHP filled with 20 % ethanol/water solution (FR=50%, $T_{cool}$ = 40 °C, horizontal).

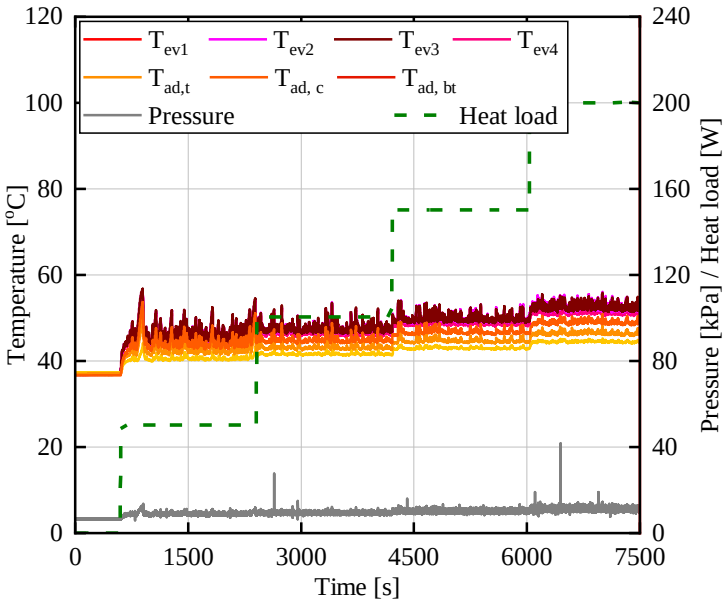


Figure A.2.10. Temperature and pressure responses for FPPHP filled with 28 % methanol/water solution (FR=50%, $T_{cool}$ = 40 °C, horizontal).

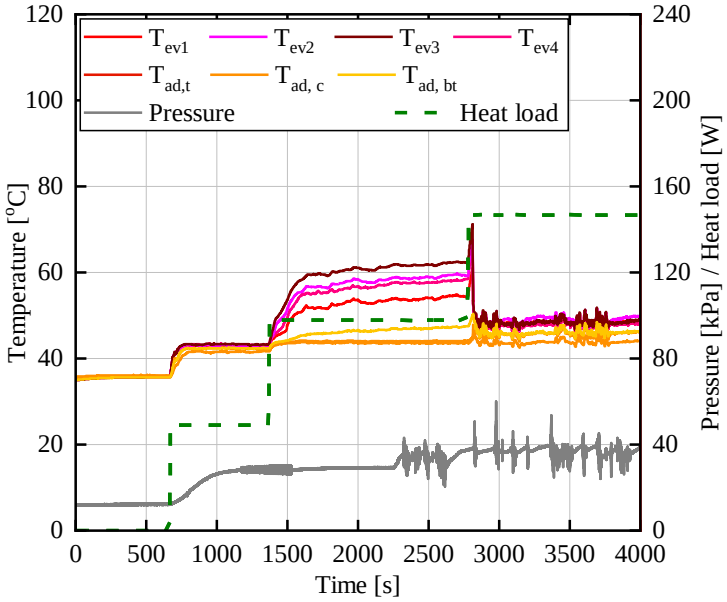


Figure A.2.11. Temperature and pressure responses for FPPHP filled with 5 % 1-butanol/water solution (FR=50%, $T_{cool}$ = 40 °C, horizontal).

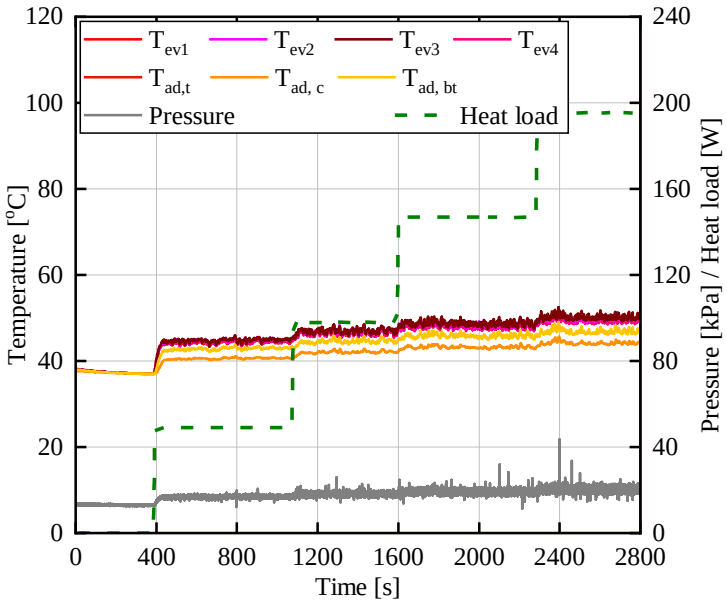


Figure A.2.12. Temperature and pressure responses for FPPHP filled with 5 % 2-butanol/water solution (FR=50%, $T_{cool}$ = 40 °C, horizontal).

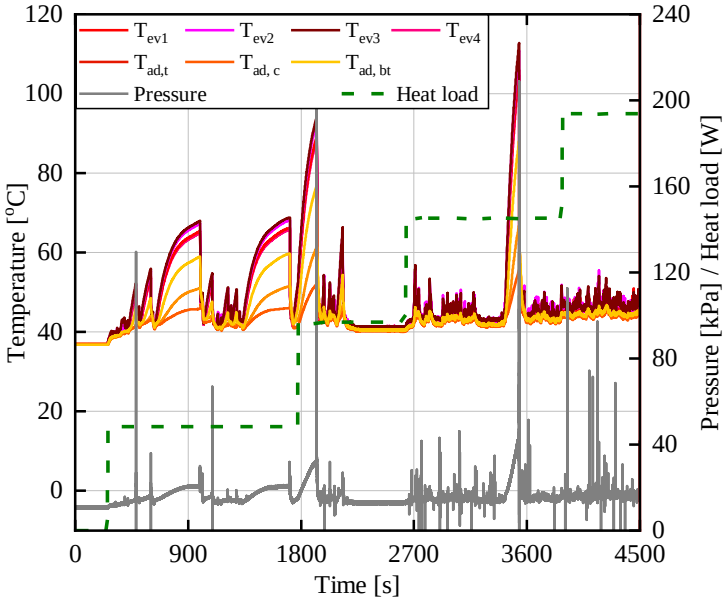


Figure A.2.13. Temperature and pressure responses for FPPHP filled with 0.5 % Tween 40/water solution (FR=50%, $T_{cool}$ = 40 ºC, horizontal).

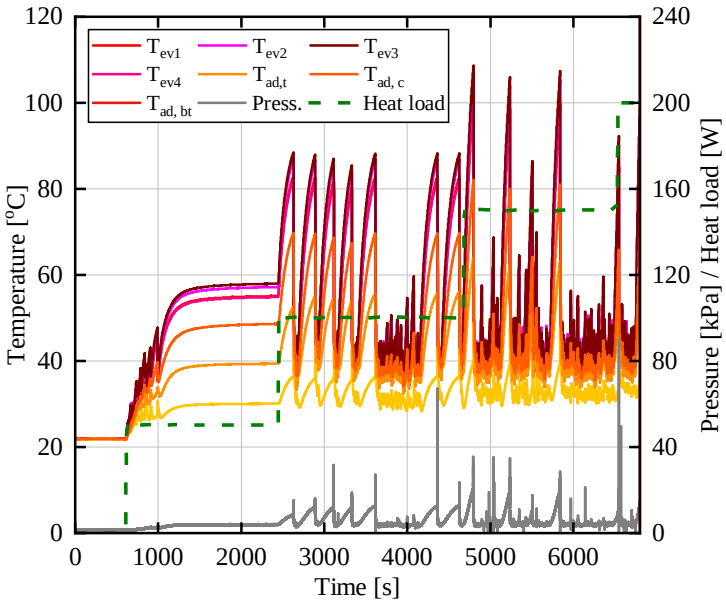


Figure A.2.14. Temperature and pressure responses for FPPHP filled with water (FR = 59%, $T_{cool}$ = 20 ºC, horizontal).

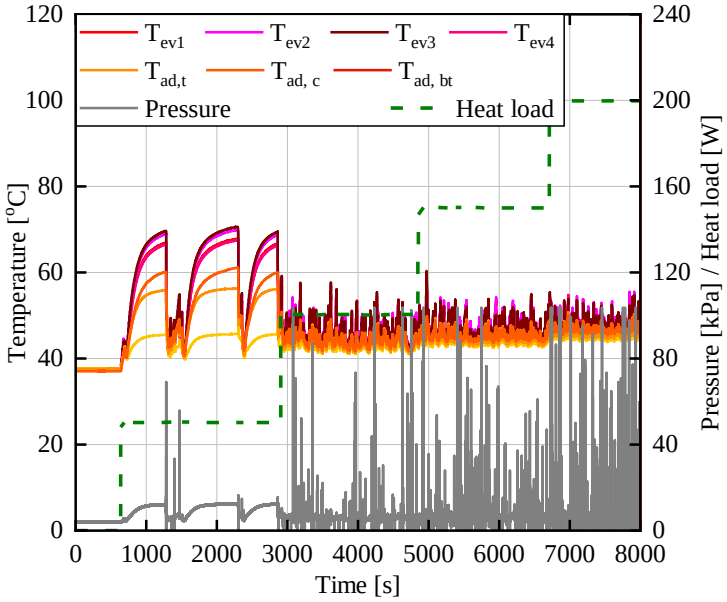


Figure A.2.15. Temperature and pressure responses for FPPHP filled with water (FR = 59%, $T_{cool}$ = 40 °C, horizontal).

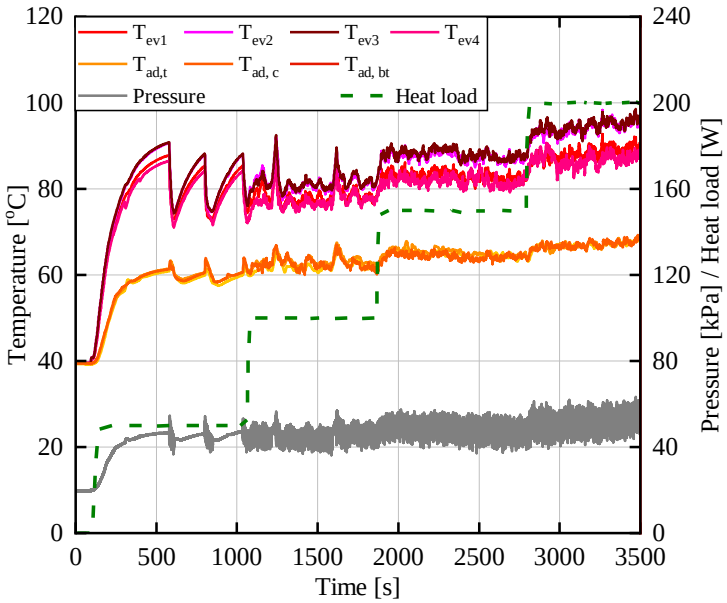


Figure A.2.16. Temperature and pressure responses for FPPHP filled with water + NCG (FR=59%, $T_{cool}$ = 40 °C, horizontal).

# Appendix B

## Parabolic flight tests temperature and pressure responses

### B.1. Results for 69th PFC

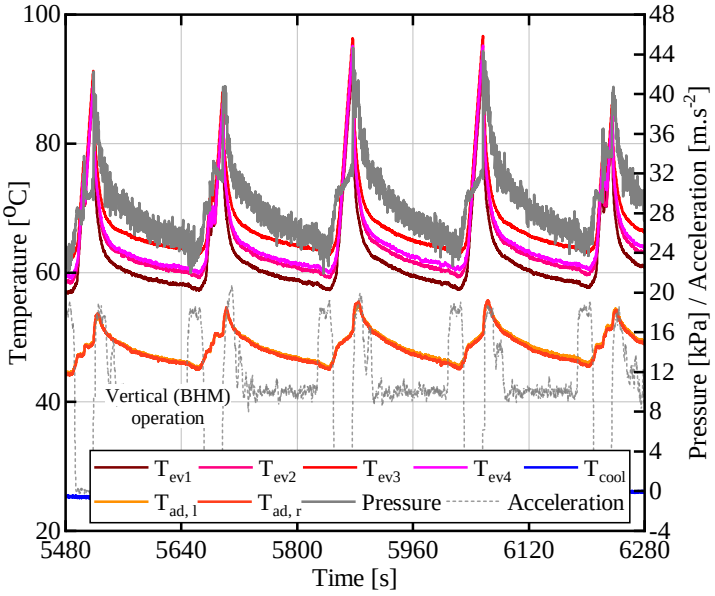


Figure B.1.1. Temperature and pressure responses for FPPHP filled with ethanol (Mo/Sa, FR = 40%, *Q* = 150 W, microgravity).

## B.2. Results for 71st PFC`

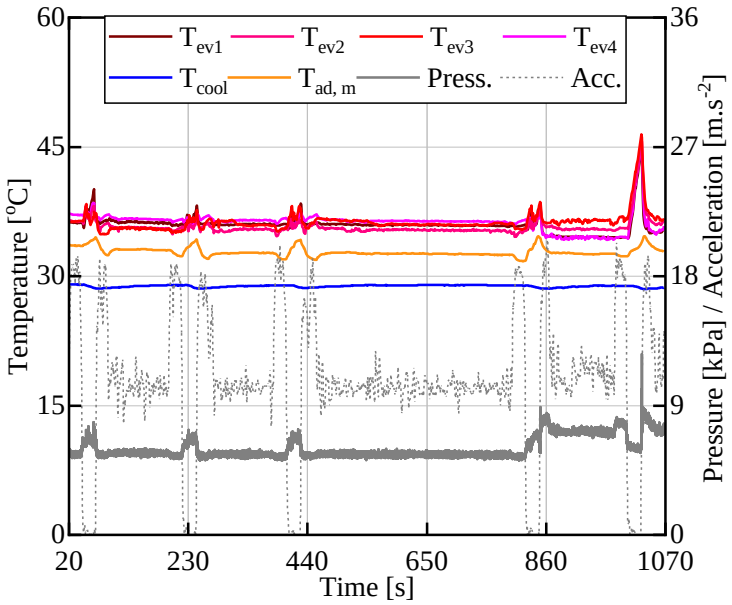


Figure B.2.1. Temperature and pressure responses for FPPHP filled with 5% 1-butanol/water solution (Co/Co, FR = 50%, *Q* = 100 W, microgravity).

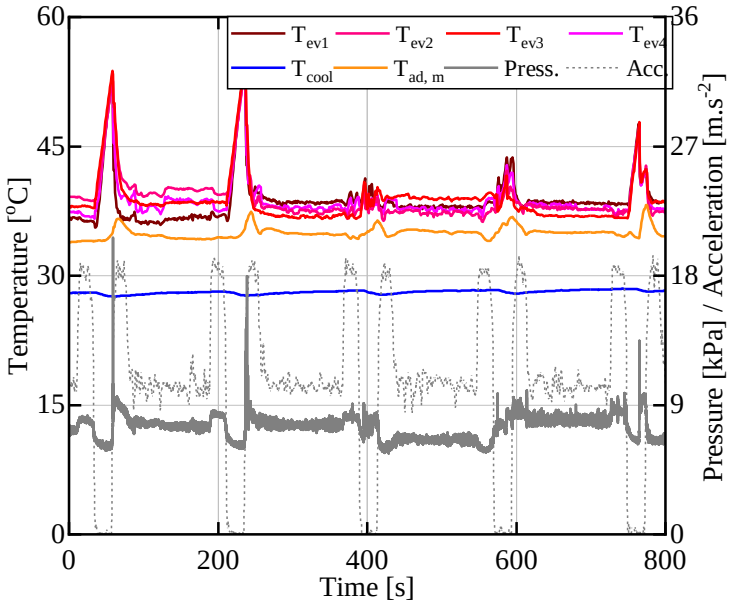


Figure B.2.2. Temperature and pressure responses for FPPHP filled with 5% 1-butanol/water solution (Co/Co, FR = 50%, *Q* = 150 W, microgravity).

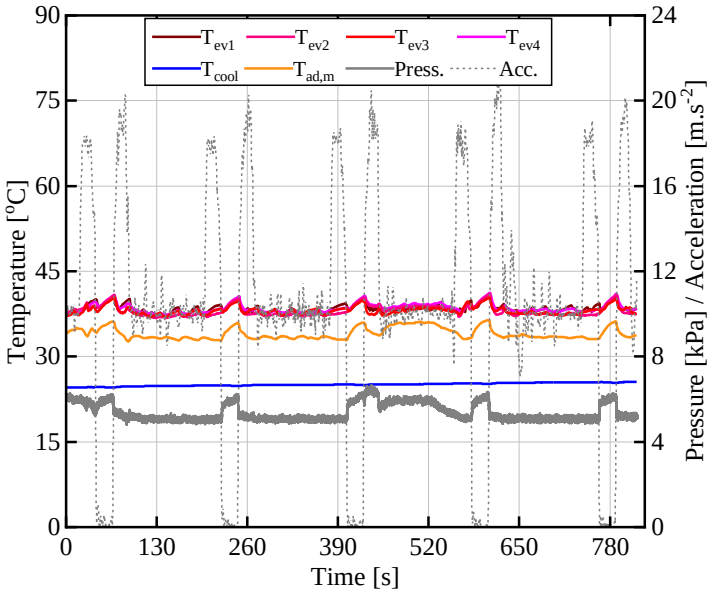


Figure B.2.3. Temperature and pressure responses for FPPHP filled with water (Co/Sa, FR = 50%, $Q$ = 50 W, microgravity).

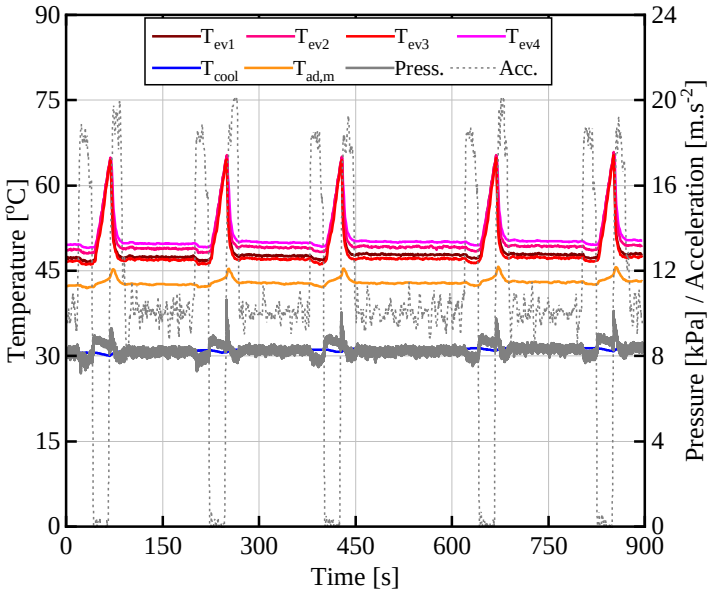


Figure B.2.4. Temperature and pressure responses for FPPHP filled with water (Co/Sa, FR = 50%, $Q$ = 150 W, microgravity).

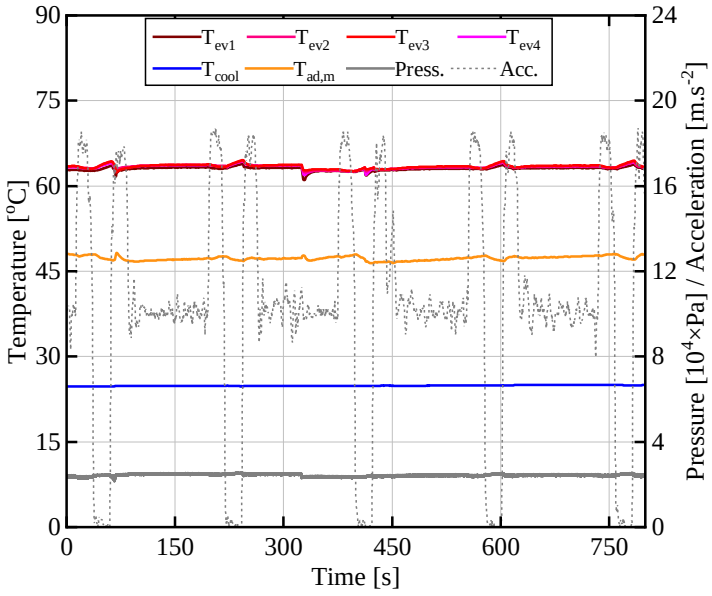


Figure B.2.5. Temperature and pressure responses for FPPHP filled with water + NCG (Co/Sa, FR=50%, *Q* = 50 W, microgravity).

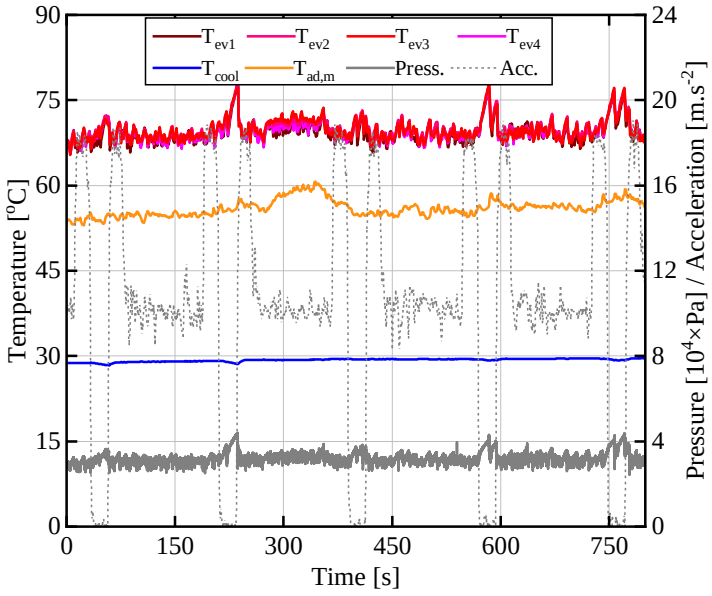


Figure B.2.6. Temperature and pressure responses for FPPHP filled with water + NCG(Co/Sa, FR = 50%, *Q* = 150 W, microgravity).

### B.3. Results for 74th PFC

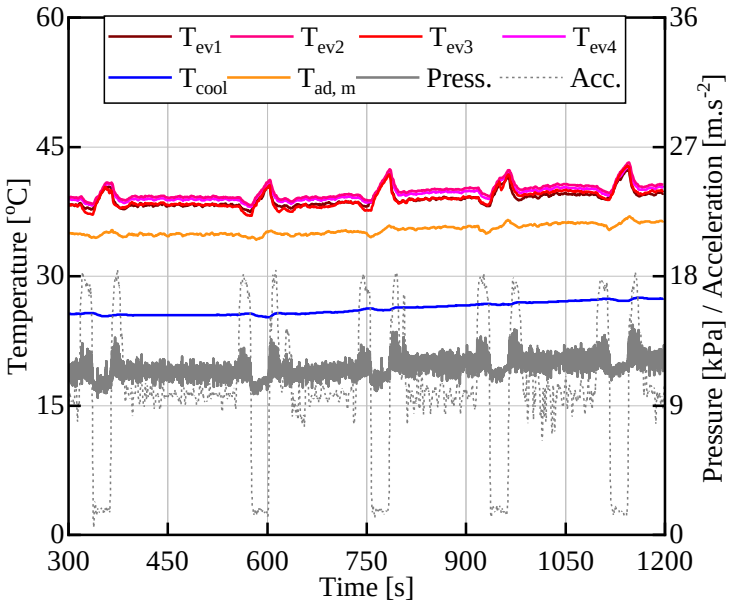


Figure B.3.1. Temperature and pressure responses for FPPHP filled with water (Co/Co, FR = 50%, $Q$ = 50 W, Lunar gravity).

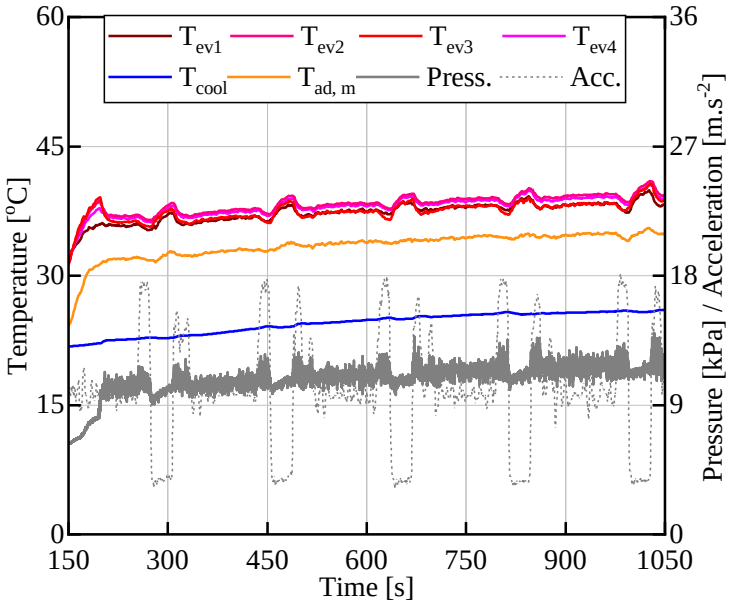


Figure B.3.2. Temperature and pressure responses for FPPHP filled with water (Co/Co, FR = 50%, $Q$ = 50 W, Martian gravity).

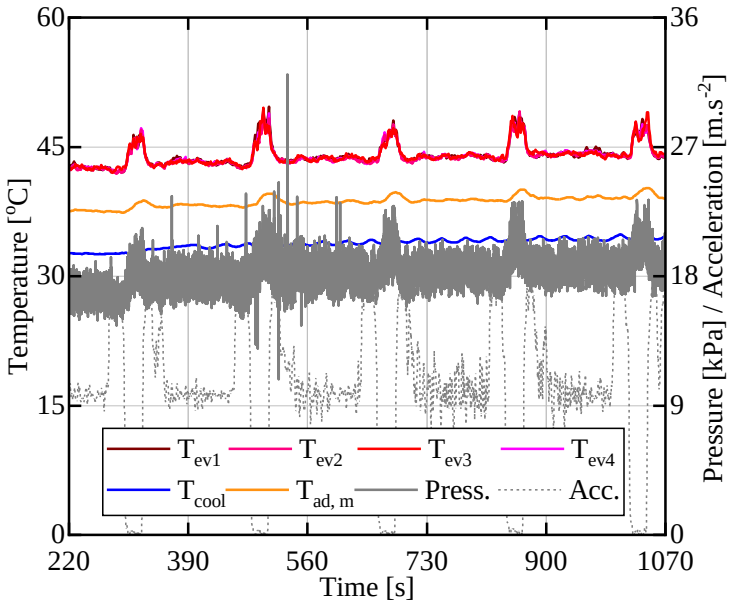


Figure B.3.3. Temperature and pressure responses for FPPHP filled with 20% ethanol/water solution (Co/Co, FR = 50%, *Q* = 150 W, microgravity).

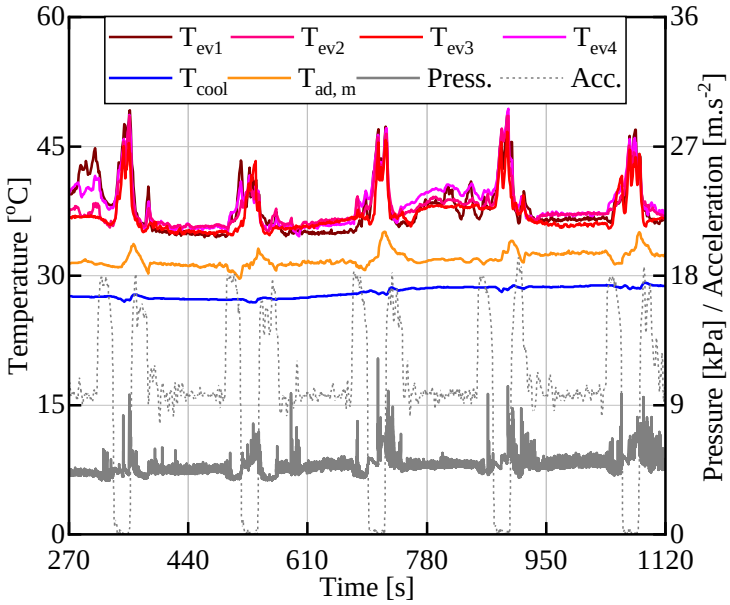


Figure B.3.3. Temperature and pressure responses for FPPHP filled with 28% methanol/water solution (Co/Co, FR = 50%, *Q* = 150 W, microgravity).

# Appendix C

## Thermal resistance relative uncertainties

Table C.1. Thermal resistance uncertainties for FPPHP tested in vertical orientation (BHM).

| Fluid | FR (%) | Condenser temperature (◦C) | **Error (%)** | | | |
|---|---|---|---|---|---|---|
| | | | Heat Load (W) | | | |
| | | | 50 | 100 | 150 | 200 |
| Water | 50 | 20 | 6.4 | 7.1 | 6.6 | 7.1 |
| | | 40 | 13.2 | 14.1 | 22 | 11 |
| | 59 | 20 | 11.6 | 5.5 | 8.2 | 8.2 |
| | | 40 | 2.9 | 15.2 | 24.4 | 17.7 |
| Ethanol | 50 | 20 | 10.4 | 14.1 | 9.4 | 7.1 |
| | | 40 | 3.5 | 16.5 | 9.4 | 9 |
| Methanol | | 20 | 6.4 | 4.7 | 3.9 | 3.4 |
| | | 40 | 24.1 | 16 | 10.5 | 8.2 |
| 20% ethanol / water | | 20 | 6.4 | 7.6 | 5.6 | 4.6 |
| | | 40 | 7.2 | 6 | 5.6 | 6.6 |
| 28% methanol / water | | 20 | 5.1 | 10.3 | 8 | 6.5 |
| | | 40 | 8 | 5 | 8.8 | 7.7 |
| 5% butanol / water | | 20 | 11.8 | 8.7 | 7.8 | 5.6 |
| | | 40 | 12.8 | 10.7 | 9.7 | 9.4 |
| 0.5% Tween 40 / Water | | 20 | 5.3 | 11.9 | 10.4 | 4.9 |
| | | 40 | 26.7 | 14.6 | 13.6 | 9.6 |

Table C.1. Thermal resistance uncertainties for FPPHP tested in horizontal orientation.

| Fluid | FR (%) | Condenser temperature (◦C) | **Error (%)** | | | |
|---|---|---|---|---|---|---|
| | | | Heat Load (W) | | | |
| | | | 50 | 100 | 150 | 200 |
| Water | 50 | 20 | 4 | 1.7 | - | - |
| | | 40 | 4.4 | 6.2 | 8.9 | 9.7 |
| | 59 | 20 | 3 | 5.4 | 5.3 | 4.9 |
| | | 40 | 3.4 | 13.2 | 12 | 9.9 |
| Ethanol | 50 | 20 | 3.6 | 4.5 | 5 | 4.5 |
| | | 40 | 3.6 | 6.6 | 10 | 8.4 |
| Methanol | | 20 | 17.4 | 9.7 | 9 | 8 |
| | | 40 | 24.1 | 16 | 10.5 | 8.2 |
| 20% ethanol / water | | 20 | 6.1 | 5.6 | 5.1 | 4.8 |
| | | 40 | 7.2 | 6 | 5.6 | 6.6 |
| 28% methanol / water | | 20 | 6.5 | 4.6 | 3.7 | 4 |
| | | 40 | 11.9 | 10.9 | 8.7 | 7 |
| 5% butanol / water | | 20 | 8.8 | 4.9 | 4.3 | 4 |
| | | 40 | 14 | 10.7 | 9.2 | 8.2 |
| 0.5% Tween 40 / Water | | 20 | 3.4 | 5.5 | 4.7 | - |
| | | 40 | 5.6 | 18 | 8.3 | 10.5 |

# Appendix D

## Résume entendu

### Chapitre 1

La première partie de la thèse décrit la motivation de l'étude des caloducs oscillants pour des applications spatiales parmi les autres systèmes de contrôle thermique diphasiques dans le cadre de deux projets MAP de l'Agence Spatiale Européenne (ESA).

Dans le cadre de projet ESA MAP INWIP, les travaux de recherche se concentrent sur les investigations numériques et expérimentales de trois dispositifs de transfert de chaleur diphasiques : les thermosiphons hybrides sans mèche poreuse, les caloducs rainurés et les caloducs oscillants. Les études paramétriques de ces systèmes incluent les évaluations des performances des différents fluides de travail, des surfaces fonctionnalisées (hydrophobes et hydrophiles), de l'influence de la gravité (différentes orientations lors des essais au sol et microgravité lors des vols paraboliques). Ce projet est une première étape préparatoire pour la poursuite d'expérimentation systématique sur la plateforme thermique TP1 à bord de la Station Spatiale Internationale, en étudiant notamment les caloducs rainurés et pulsés remplis de fluides ordinaires (FC72) et remouillant (mélange eau/butan-2-ol).

Ensuite, le projet MAP ESA TOPDESS vise à poursuivre le développement des travaux de recherche entamés dans le cadre du précédent projet INWIP, mais cette fois avec l'objectif ambitieux de traiter des systèmes diphasiques déployables et/ou flexibles pour développer les aspects applicatifs. Néanmoins, la déployabilité ou la flexibilité de tels systèmes ne seront pas étudiées dans le cadre de cette thèse.

Par conséquent, les principaux objectifs de cette thèse sont de caractériser les performances de transfert de chaleur de caloducs oscillants plats fonctionnant sous gravité normale et réduite, de comprendre le comportement des écoulements diphasiques à l'intérieur de ces systèmes et d'améliorer les performances de transfert de chaleur en utilisant des fluides caloporteurs  ayant différentes propriétés.

**Chapitre 2**

Le deuxième chapitre présente une revue des différents systèmes de refroidissement. Il n'existe pas de classification universelle des systèmes de contrôle thermique du fait de la complexité des différents principes de fonctionnement ainsi que de leur grand nombre. C'est pourquoi ici seuls les systèmes diphasiques sont présentés en tant que solutions de contrôle thermique parmi les plus efficaces et largement utilisées pour les applications terrestres et spatiales.

Les systèmes diphasiques peuvent être divisés entre systèmes actifs et passifs. Dans les systèmes actifs, l'utilisation d'une pompe est nécessaire pour forcer le mouvement du fluide caloporteur dans la boucle. En revanche, le mouvement du liquide dans les systèmes passifs est assuré par la gravité ou la capillarité. Dans les systèmes actifs, la pompe doit être complétée par un vase d'expansion permettant l'amortissement des instabilités éventuelles liées aux dilatations thermiques du fluide. Malgré un fonctionnement efficace, les composants supplémentaires et la consommation d'énergie entraînent une baisse de la fiabilité de ces systèmes.

En revanche, les sous-systèmes visant la fiabilité globale sont exclus dans les systèmes de refroidissement passifs, mais un autre moyen de mouvement de fluide est nécessaire – le fonctionnement des caloducs, LHP et CPL est permis grâce à la présence d'une structure capillaire ; les thermosiphons fonctionnant quant à eux grâce à la gravité (donc pas utilisables pour les applications spatiales malgré son efficacité).

Les caloducs présentent un avantage certain de par leur simplicité par rapport aux boucles diphasiques mais leur utilisation reste limitée à cause de leurs basses performances en termes de transfert thermique, elles-mêmes liées aux limites de transport du fluide par la structure capillaire. Une autre technologie récente dans la famille des caloducs est le caloduc oscillant. Dans ces systèmes, le transfert de chaleur par voies latente et sensible couplé aux transferts de masse provoqué par une différence de pressions entre les zones de condensation et celles d'évaporation, ce qui entraîne la mise en mouvement global du fluide caloporteur. Bien qu'offrant des performances limitées en termes de densité de flux par rapport à d'autres technologies, les caloducs oscillants ont l'avantage d'être des systèmes simples à réaliser et pouvant fonctionner sous différentes conditions de gravité.

**Chapitre 3**

Les principes de fonctionnement fondamentaux des caloducs oscillants, les particularités de ces dispositifs lorsqu'ils sont fabriqués à partir de plaques planes usinées, et leurs différences ainsi que les principaux paramètres d'influence sont abordés dans le troisième chapitre. Malgré différentes géométries, le point commun de l'ensemble de ces caloducs est la présence d'une zone d'évaporation au contact d'une source chaude, d'une zone de condensation (source froide) et d'une partie adiabatique entre ces deux zones.

Malgré le fait que les mécanismes physiques du fonctionnement des caloducs oscillants conventionnels (tubulaires) sont bien connus mais encore peu maîtrisés, des phénomènes particuliers et contradictoires se produisent dans les dispositifs à plaques planes (caloducs oscillants plats) en raison du lien thermique entre les canaux et de leur forme spécifique (la présence d'angles vifs conduit à une distribution non uniforme du film liquide lié au déséquilibre de pressions capillaires entre les coins et les bords de la section transversale).

Le fonctionnement d'un caloduc oscillant dépend d'une combinaison complexe entre différents paramètres, majoritairement couplés les uns aux autres. Un bon fonctionnement est obtenu lorsqu'un écoulement dit bulles/bouchons (slug flow) parcourt les différentes boucles du caloduc. Les transferts de chaleur se font à la fois par chaleur sensible dans les bouchons de liquide et par chaleur latente au niveau de l'évaporation ou de la condensation des films de liquide entourant les bulles de vapeur. Ces transferts sont sensiblement différents dans les caloducs plats avec une section carrée ou rectangulaire à cause de la présence des films liquides plus épais dans les coins et des liens thermiques entre les différents canaux. Aussi, le faible niveau de connaissance de ces systèmes ne permet pas encore de faire un dimensionnement pour un prototype industriel.

**Chapitre 4**

Une analyse bibliographique des différentes expériences réalisées sur les caloducs oscillants tubulaires et plats est détaillée afin d'évaluer l'influence des différents paramètres dans le quatrième chapitre. Pour des puissances moyennes à élevées, les performances des caloducs oscillants plats ayant des canaux à section carrée sont meilleures que pour ceux à section circulaire. L'orientation joue également un rôle important. La configuration verticale ou inclinée avec évaporateur en bas est plus favorable que la configuration horizontale. Une

faible longueur adiabatique entre l'évaporateur et le condenseur tend à diminuer la résistance thermique. Il en est de même avec l'augmentation du nombre de boucles. Le taux de remplissage doit aussi être optimisé pour favoriser les oscillations, éviter des frottements trop importants, mais aussi l'assèchement de l'évaporateur en cas de quantité trop faible. Les performances thermiques dépendent également des propriétés thermophysiques des fluidse et sont inversement proportionnelles à la pente de la courbe pression/température de saturation. Les mélanges binaires ont aussi largement été utilisés et certains comme le mélange eau-méthanol permettent d'améliorer les performances. L'amélioration de la mouillabilité des fluides en mélangeant l'eau à des alcools ou en utilisant des surfactants permet de réduire la formation de zones sèches au niveau de l'évaporateur. Plusieurs études ont été menées sur des caloducs dans des conditions de microgravité. Généralement les performances sont similaires en gravité normale ou microgravité en position horizontale si la taille des canaux est inférieure à la longueur capillaire. Les performances sont un peu réduites en microgravité par comparaison à la gravité normale en configuration verticale.

**Chapitre 5**

Le système expérimental, destiné aux expériences au sol et en microgravité, et permettant à la fois la caractérisation qualitative et quantitative des caloducs oscillants plats, est décrit dans le cinquième chapitre. Les prototypes ont été développés pour les expériences au sol et au cours de quatre campagnes de vols paraboliques de l'Agence Spatiale Européenne, sur la base des exigences de sécurité et de la zone d'intérêt scientifique - études couplées thermiques et hydrauliques des caloducs oscillants plats testés sous différentes conditions de gravité. Les caloducs testés sont soit ren cuivre, soit en molybdène et certains sont recouvert d'une plaque en saphir permettant les visualisations complètes de l'écoulement dans les canaux et des mesures de température par thermographie infrarouge.

Le système expérimental est équipé de thermocouples de type T permettant de mesurer les températures au niveau de l'évaporateur, de la zone adiabatique et du fluide de refroidissement secondaire. Un capteur de pression est également positionné soit en partie basse au niveau de l'évaporateur, soit en partie haute au niveau du condenseur.

Une estimation des incertitudes des mesures est présentée, ainsi que l'analyse de répétabilité, qui démontre également la fiabilité du système

**Chapitre 6**

Les résultats obtenus par les études expérimentales, s'intéressant à l'influence des différents paramètres (comme par exemple, la nature du fluide, le taux de remplissage, la présence de gaz incondensables, la température de la source froide, le positionnement du caloduc et le niveau de gravite) sont présentés dans le chapitre 6. Pour la plupart des essais, les évolutions temporelles des températures au niveau de l'évaporateur, de la zone adiabatique, du condenseur et de la pression sont présentées. Enfin, une notion importante est mise en évidence et représente un critère pour l'évaluation de performance des caloducs : la résistance thermique globale. Donc chaque configuration de caloduc a été évaluée et comparée grâce aux calculs de ces résistances thermiques en plus des évolutions temporelles des températures et pression.

Lors d'essais au sol, une étude paramétrique du caloduc oscillant rempli par des fluides de différentes natures a été menée. En position verticale, le caloduc oscillant fonctionne presque tout le temps comme un réseau de thermosiphons interconnectés. En orientation horizontale, le système fonctionne en mode pulsé puis le démarrage est atteint (généralement à 100 W de puissance appliquée), sauf lorsqu'il est rempli d'eau et testé à 20 $^{o}$C de source froide : il présente de moins bonnes performances thermiques dans ces conditions. Les mélanges aqueux d'alcool utilisés comme fluides de travail conduisent à une très nette amélioration des performances thermiques, par rapport aux fluides purs (en particulier l'eau). L'augmentation de la température de condenseur entraîne également une amélioration des performances thermiques du FPPHP, en raison d'un glissement des propriétés thermophysiques dans le bon sens pour la plupart. Le système, rempli avec des solutions eau-surfactant, a montré un fonctionnement très instable malgré des résistances thermiques plus faibles comparées à l'eau pure.

En revanche, il est aussi démontré que la présence des gaz non condensables dans le système, bien qu'entraînant une dégradation globale des performances thermiques du système, provoque un fonctionnement oscillatoire plus stable du fluide dans le caloduc testé. En effet, la présence de gaz incondensables provoque non seulement l'augmentation globale de la température du système en fonctionnement, mais induit également un fonctionnement oscillatoire stable du fluide aussi bien pendant les phases de gravité normales que de microgravité, avec une augmentation de température (en microgravité) bien inférieure à celle observée avec l'eau pure.

Pour finir, une campagne de vols paraboliques a permis d'effectuer une série de tests sur trois niveaux de gravité différents (microgravité, gravités lunaire et martienne). Les résultats ont montré une augmentation de la température de l'évaporateur pendant les phases de gravité lunaire, mais avec des réactivations de fluide fréquentes (contrairement aux phases de microgravité). En revanche, pour la gravité martienne, les performances obtenues restent tout à fait similaires à celles observées sous gravité terrestre, démontrant un niveau seuil d'influence de la gravité sur le fonctionnement des caloducs oscillants lorsqu'ils sont en position verticale favorable.

**Chapitre 7**

Le septième chapitre est dédié aux visualisations des écoulement réalisées en phases de microgravité, afin d'analyser plus spécifiquement les conditions de redémarrage du régime bulles/bouchons observé pendant certaines paraboles (phases de microgravité). La méthodologie d'analyse de visualisation, basée sur la technique de suivi d'objets pour la détermination de la position des interfaces liquide-vapeur (ménisques) a été développée, validée et mise en œuvre pour étudier le comportement de l'écoulement pendant les périodes de « stop-over » et de réactivations du fluide dans des conditions de microgravité. L'étude expérimentale de ces phénomènes à l'intérieur prototypes remplis avec de l'éthanol (diamètre des canaux : 3 mm) et FC72 (diamètres des canaux : 1,5 mm et 3 mm) et fonctionnant en microgravité est également présentée.

Les périodes de microgravité s'accompagnent de phénomènes d'assèchement de l'évaporateur qui entraînent une dégradation globale des performances thermiques. Il a été constaté que, pendant certaines paraboles, des périodes d'arrêt se produisent et sont parfois interrompues par une transition du mode d'écoulement bulles/bouchons à un écoulement de type annulaire, avec une distribution uniforme du liquide à l'intérieur du caloduc oscillant, également appelées « phases de réactivation ».

Le mouvement des interfaces liquide/vapeur, ainsi qu'un bilan des forces s'exerçant sur les bouchons liquides, et le changement de mode d'écoulement, ont été analysés. Malgré les différentes fréquences d'amplitude et d'oscillations pendant les périodes de « stop-over » et « startup » pendant les phases de microgravité, les valeurs des vitesses de transition semblent être très proches les unes des autres.

Des critères basés sur des nombres adimensionnels fréquemment utilisés pour ce type d'écoulement, les nombres de Weber et de Garimella, ont été évalués pour les caloducs oscillants testés lors des phases de microgravité. Les valeurs moyennes obtenues expérimentalement du nombre de Weber pour la transition d'écoulement sont très proches de la valeur critique de référence ($We_{,crit}$ = 4), tandis que les valeurs moyennes du nombre de Garimella sont supérieures d'un à deux ordres de grandeur à la valeur critique de référence ($Ga_{,crit}$ = 160).

L'adaptation des corrélations pour une tentative de cartographie d'écoulement (basée sur les nombres de Bond, de Weber et de Froude modifiés, incluant l'accélération réelle du fluide plutôt que l'accélération gravitationnelle constante), initialement développée par nos collègues de l'Université de Brighton, a permis de positionner les points de transition obtenus expérimentalement lors de ce travail dans la zone d'écoulement à dominante slug-plug, presque à la limite des zones de transition par coalescence et de transition d'écoulement slug-plug à annulaire.

Un bilan des forces entre l'accélération des bouchons liquides, les forces visqueuses et les forces motrices dues à la différence de pression entre deux bulles vapeurs de part et d'autre de ces bouchons a été effectué. La force visqueuse est estimée à l'aide d'une loi de Poiseuille en écoulement stationnaire, et la force motrice est ainsi identifiée à partir du bilan de quantité de mouvement par déduction des autres termes. La force visqueuse s'avère plus faible que la force de pression motrice calculée, cette dernière étant aussi supérieure d'un ordre de grandeur aux forces capillaires.

**Chapitre 8**

Cette thèse a été menée dans le cadre de deux projets successifs ESA MAP INWIP et ESA MAP TOPDESS, dédiés au développement des systèmes des transferts thermiques diphasiques et s'intéressant à la gestion thermique systèmes dissipatifs de haute puissance par caloducs oscillants, appliqués pour les vols hors gravité. Ce travail concerne les études expérimentales menés sur diffèrents caloducs oscillant dit plats testés sous différentes conditions opératoires incluant l'orientation, le taux de remplissage, la température de refroidissement, la nature du fluide, le niveau de puissance appliqué et le niveau de gravité.

Notons que de nouvelles expériences au sol sont programmées sur une nouvelle géométrie de prototype destiné à être testé à bord de l'ISS à l'horizon 2024-2026. De

nouveaux essais lors de campagnes de vols paraboliques seront également nécessaires pour valider le nouveau dispositif dans des conditions de microgravité.

# Résume

L'intégration de dispositifs électroniques de haute puissance et dissipant des centaines de watts par centimètre carré au sein des systèmes spatiaux provoque une hausse significative des besoins en systèmes de refroidissement de haute performance, légers et efficaces. En raison de ces exigences spécifiques, l'utilisation des systèmes de refroidissement diphasiques représentent un grand intérêt pour ces applications spatiales. Les caloducs oscillants, dispositifs passifs et simples de transfert de chaleur diphasique sont devenus une excellente solution pour les systèmes de management thermique spatiaux. Actuellement, le fonctionnement de ce type d'échangeurs de chaleur n'est pas entièrement étudié, notamment en conditions de microgravité. C'est pourquoi, dans le cadre des projets successifs INWIP et TOPDESS de l'ESA, l'évaluation des performances des caloducs oscillants plats et des spécificités opérationnelles sous différentes conditions de gravité a été défini comme principal objectif du présent travail de thèse.

Les études expérimentales menées au cours de ce travail ont porté sur la caractérisation thermique des différents caloducs oscillants testés au sol et au cours de quatre campagnes de vols paraboliques de l'ESA. Des études paramétriques des performances de ces systèmes ont été effectuées en configuration verticale et horizontale, en utilisant différents fluides de travail (mélanges alcool-eau, fluides remouillants ou solutions de surfactant), différentes températures de condenseur, plusieurs concentrations de gaz non condensables et différents niveaux de gravité (terrestre, martien, lunaire, hyper et microgravité). L'amélioration des performances, parfois inattendues, ont été observées sous certaines conditions opératoires. Les études analytiques de l'écoulement diphasique dans le caloduc oscillant, concernant notamment le passage de l'arrêt de fonctionnement aux oscillations de forte amplitude (« phases de réactivation ») ont été réalisées grâce à des visualisations haute fréquence. Pour finir, les critères de transition d'écoulement du régime bulles/bouchons au régime semi-annulaire/annulaire a été étudiée dans le cadre d'une l'analyse non-dimensionnelle des principaux paramètres de l'écoulement.



**Mots-clés:** Caloducs, Composants électroniques--Systèmes de refroidissement, Écoulement diphasique, Gravité réduite, Transfert de chaleur, Caloduc oscillant, Écoulement bulles/bouchons, Écoulement annulaire



# Abstract

Integration of high power and performance electronic devices in modern spacecraft systems with heat generation of hundreds of watts per square centimeter crucially increases needs in high performance, low weight, energy efficient and reliable thermal management systems. Due to these specific demands, two-phase heat rejection devices are of major interest for space applications. The Pulsating Heat Pipes, as simple passive two-phase heat transfer devices, have become an excellent solution for space cooling systems. Today, operation of this kind of heat transfer devices is not fully studied, especially in microgravity. So, in the context of ESA consecutive projects INWIP and TOPDESS, evaluation of the flat plate pulsating heat pipe performances and operational peculiarities under different gravity conditions has been defined as the main aim of the present PhD work.

Experimental studies conducted during this work concerned the thermal characterization of different flat plate pulsating heat pipes tested on ground and during four ESA Parabolic Flight Campaigns. Parametric investigations have been carried out for vertical and horizontal orientations of the device using different working fluids (including alcohol aqueous solutions, self-rewetting fluids and surfactant solutions), condenser temperatures, non-condensable gases concentrations and gravity levels (Earth, Martian, Lunar, hyper and microgravity). Obvious, and sometimes unexpected, performances improvement has been observed under certain conditions. Analytical studies of the two-phase flow inside the FPPHP, especially concerning the transition from stopover to high-amplitude oscillations (fluid flow "re-activation phases") have been done thanks to high-frequency visualizations. Finally, the flow transition criterion, from the slug-plug flow regime to semi-annular/annular flow, was studied thanks to dimensionless analyzes considering the main parameters of the flow.



**Keywords:** Heat pipes, Electronic apparatus and appliances – Cooling systems, Two-phase flow, Reduced gravity environments, Heat—Transmission, Pulsating heat pipe, Slug flow, Annular flow